TU/e EINDHOVEN UNIVERSITY OF TECHNOLOGY

Throughput and Link Design Choices for Communication over LED Optical Wireless Channels

Citation for published version (APA):
Mardanikorani, S. (2021). *Throughput and Link Design Choices for Communication over LED Optical Wireless Channels*. [Phd Thesis 1 (Research TU/e / Graduation TU/e), Electrical Engineering]. Eindhoven University of Technology.

Document status and date:
Published: 29/09/2021

Document Version:
Publisher's PDF, also known as Version of Record (includes final page, issue and volume numbers)

Please check the document version of this publication:

• A submitted manuscript is the version of the article upon submission and before peer-review. There can be important differences between the submitted version and the official published version of record. People interested in the research are advised to contact the author for the final version of the publication, or visit the DOI to the publisher's website.
• The final author version and the galley proof are versions of the publication after peer review.
• The final published version features the final layout of the paper including the volume, issue and page numbers.

Link to publication

General rights
Copyright and moral rights for the publications made accessible in the public portal are retained by the authors and/or other copyright owners and it is a condition of accessing publications that users recognise and abide by the legal requirements associated with these rights.

• Users may download and print one copy of any publication from the public portal for the purpose of private study or research.
• You may not further distribute the material or use it for any profit-making activity or commercial gain
• You may freely distribute the URL identifying the publication in the public portal.

If the publication is distributed under the terms of Article 25fa of the Dutch Copyright Act, indicated by the "Taverne" license above, please follow below link for the End User Agreement:

www.tue.nl/taverne

Take down policy
If you believe that this document breaches copyright please contact us at:

openaccess@tue.nl

providing details and we will investigate your claim.

Download date: 16. Nov. 2023

Throughput and Link Design Choices for Communication over LED Optical Wireless Channels

PROEFSCHRIFT

ter verkrijging van de graad van doctor aan de Technische Universiteit Eindhoven, op gezag van de rector magnificus prof.dr.ir. F.P.T. Baaijens, voor een commissie aangewezen door het College voor Promoties, in het openbaar te verdedigen op woensdag 29 september 2021 om 13:30 uur

door

Shokoufeh Mardanikorani

geboren te Farsan, Iran

Dit proefschrift is goedgekeurd door de promotoren en de samenstelling van de promotiecommissie is als volgt:

Voorzitter:	prof.dr.ir. A.B. Smolders
1e promotor:	prof.dr.ir. J.P.M.G. Linnartz
copromotor:	dr. X. Deng
leden:	prof. S. Hranilovic (McMaster University, Canada)
	dr. V. Jungnickel (TU Berlin, Institut für Telekommunikationssysteme)
	prof.dr. M. Matters- Kammerer (Technische Universiteit Eindhoven)
	dr.ir. C.W. Oh (Technische Universiteit Eindhoven)
Adviseur	dr.ir. C.W. Oh (Technische Universiteit Eindhoven)

Het onderzoek of ontwerp dat in dit thesis wordt beschreven is uitgevoerd in overeenstemming met de TU/e Gedragscode Wetenschapsbeoefening.

Throughput and Link Design Choices for Communication over LED Optical Wireless Channels / by Shokoufeh Mardanikorani, Lighting and IoT Lab, Signal Processing Systems, Eindhoven University of Technology, Eindhoven, the Netherlands, 2021.
A catalogue record is available from the Eindhoven University of Technology Library.
ISBN: 978-90-386-5360-0.

The research presented in this thesis has received funding from EU H2020 project ELIOT 825651 and from project Impulse II and was supported by Signify, Eindhoven, The Netherlands.

Cover design: Maryam Rashidkhan

© 2021 Shokoufeh Mardanikorani, The Netherlands. All rights reserved. Copyright of the individual chapters belongs to the publisher of the journal listed at the beginning of the respective chapters. No parts of this thesis may be reproduced, stored in a retrieval system or transmitted in any form or by any means without permission of the author.

To Ali, Nickan and Ayeen

Summary

The staggering growth in the demand for wireless bandwidth is putting stringent pressure on the Radio Frequency (RF) spectrum; high speed applications such as mobile phones or video streaming are demanding more bandwidth per single user while applications such as Internet of Things (IoT) are introducing more connection nodes to the network. Recently, Optical Wireless Communications (OWCs) using Infra-Red (IR) or visible light has shown great potential not only to support low to mid data rate required by the IoT but also to compete with the existing RF solutions in supporting growing data rate demands. Furthermore, OWC offers some great advantages compared to RF. Among other things, OWC offers license–free wide communication channels.

Thanks to the fast growing solid-state Light Emitting Diodes (LEDs), OWC links with several hundreds of Mbps data rates have been already commercialized. To further boost the throughput, several issues need to be addressed.

LEDs, particularly those used for Visible Light Communications (VLC), have a limited bandwidth, while above their 3 dB bandwidth, the roll-off is relatively gentle. If the modulation bandwidth would be limited to the 3 dB LED bandwidth, the throughput would be unacceptably constrained. Hence, effective communication systems need to optimize the use of bandwidth significantly above this 3 dB point, by employing techniques such as Orthogonal Frequency Division Multiplexing (OFDM). OFDM fine-tunes the amount of power and constellation as a function of the channel response over different frequencies. Various power and bit loading strategies have been proposed and simulated in literature, but their performance was not captured in expressions. This dissertation derives these for optimal waterfilling, uniform and pre-emphasized power loading for the LED channel, that severely attenuates high frequencies. Uniform power loading fixes the amount of power on each sub-carrier while the signal constellation is determined by the signal quality at the receiver. Pre-emphasis, on the other hand, fixes the signal constellation on all sub-carriers resulting a flat spectrum for the received signal. We also investigate the influence of practical discrete constellations and verify our new results experimentally.

Interestingly, simple uniform loading only falls less than 1$\sim$2% short of the through-

put achieved by waterfilling, but when we restrict OFDM to discrete QAM constellation sizes, the penalty for uniform loading is 1.5 dB. Inspired by the good performance of uniform power loading, we propose an algorithm with less complexity in the implementation compared to waterfilling approach to find the best discrete bit loading for uniform power within an optimized bandwidth. As pre-emphasis is nonetheless attractive because a flattened channel does not need adaptive sub-carrier loading, we quantify its penalty. This can be modest provided that the system can adapt its transmit bandwidth, thereby adaptively switching upper sub-carriers to zero power.

In a pre-emphasized channel, Pulse Amplitude Modulation (PAM) is also interesting. Next, in this thesis, we challenge whether OFDM large Peak-to-Average-Power Ratio (PAPR) and resulting large DC bias are justified. We compare systems using the same electrical power and derive how PAM and OFDM variants reach their optimum throughput at different bandwidths and differently shaped spectral densities, thus at very different Signal to Noise Ratio (SNR) profiles but nonetheless the same transmitter power. We argue that a mobile system that has to operate seamlessly in wide coverage and short–range high–throughput regimes, needs to adapt not only its bandwidth and its bit–loading profile, but also its DCO-OFDM modulation depth, and preferably falls back from OFDM to PAM.

LEDs, particularly those optimized for illumination, act as a non-linear low-pass communication channel. Next, in this dissertation, we translate the non-linear differential equations for the hole-electron recombination and photon emissions, into a discrete-time model with delay taps and non-linear coefficients. This LED model can be inverted, to actively eliminate or mitigate the non-linear dynamic LED distortion. We propose a further simplification of the compensation circuit that allows us to use a relatively simple structure with only a few parameters. We experimentally characterize and measure signals communicated via commercially available illumination LEDs that are also used for LiFi communication. In an Intensity Modulation Direct Detection (IM/DD) system employing PAM, we show that the proposed compensator can effectively widen the measured eye diagram, thereby reduce the error rate or can allow a larger constellation. For OFDM, the reduction in distortion allows at least a 50% increase in bit rate, even on measured noisy channels. This confirms the suitability of the LED model on which our non-linear compensator is based. We show how non-linear time-constants can be estimated from electrical measurements on the LED signal. With the proposed parameter estimation, the equalizer converges to appropriate compensation settings, in Minimum Mean Square Error (MMSE) sense.

List of Figures

1.1 Smart office lighting, LED lamp (data source) connected to mobile phones, personal computers, air conditioner , printer, laptops, etc. Source: Adapted from [25]. 4

1.2 Challenges and approaches addressed in this thesis. 8

2.1 LiFi communication downlink with detailed illumination LED structure. 15

2.2 Carrier transport by energy band in LED. EBL: Electron Blocking Layer. 17

2.3 (a) Qualitative normalized LED output power for two cases; slow and fast input current compared to the LED time constant. (b) LED output power using a square waveform of 5 MHz at the input. Rise and fall times of the LED are different. Eye-diagram for a 4-PAM input current with symbol rate 5 MSym/s, based on differential equation (2.4), (c) for LED parameters given in Table 2.1, (d) for $C = 10^{-28}$ and (e) for $t_w = 2 \times 10^{-4}$ cm and $C = 10^{-28}$. (f) Measured 4-PAM eye diagram at symbol rate of 5 MSym/s and 30 dB SNR. 22

2.4 Exponential (blue), 1^{st}–order (black) and experimental channel response (red). For the experimental channel model, a Luxeon Rebel LXML-PB02-0023 blue LED was biased at 350 mA. The 3 dB bandwidth for all three cases is 10 MHz. 24

2.5 (a) typical output spectrum emission of the blue and the yellow light and (b) normalized two-dimensional output optical intensity for an input impulse current. 29

2.6 (a) Normalized frequency response example for a blue emitter with $f_{3dB,b} = 15$ MHz (blue), phosphor coating with $f_{3dB,ph} = 3$ MHz (red) and warm white LED with $\alpha = 0.8$ and APD responsivity ratio of $G_B/G_Y = 0.5$. 30

2.7 (a) SNR vs frequency for cool white (4100K) LEDs with and without blue filter, (b) SNR vs frequency for Warm white (2700K) LEDs with and without blue filter. 33

2.8 Theoretical normalized optimum modulation BW, $f_{\max}$, and achievable date rate as a function of normalized power budget γ, defined in (2.56). 36

3.1 Block diagram of optical wireless system. In linear operation regime, the dashed box can be replaced by frequency dependent low pass transfer function $H(f)$. 41

3.2 The gap Γ as a function of $\log_2(M)$ for M-QAM modulation under different BER values. 51

3.3 Normalized rate (dashed curves) achieved by (a) uniform loading and (b) pre-emphasis versus the normalized modulation bandwidth ν for link NPB γ of 20, 30 and 40 dB. The dashed-grey curves are for the case of discrete constellation sizes i.e. M = 2, 4, 8, ... Normalized maximum throughput (solid) by (a) uniform and (b) pre-emphasized loading versus optimum modulation bandwidth ν_u and ν_p, respectively. Every point on this solid curve corresponds to a different γ. 56

3.4 Illustration of the different power loading strategies. (a) Channel response, (b) allocated power versus frequency and (c) PSD at the output of the LED for waterfilling, uniform loading and pre-emphasis. 57

3.5 Theoretical (normalized) optimum modulation bandwidth $\nu_x = f_{\max_x}/f_0$ (x refers to w, u or p) and (normalized) maximum throughput as a function of NPB γ in (3.30) for waterfilling (dark), uniform loading (red) and pre-emphasis (blue) for BER = 10^{-4}. The throughput of the channel (using waterfilling strategy with Γ= 1) and the corresponding bandwidth are shown using dashed lines. 60

3.6 (a) Relative rate difference between waterfilling and uniform loading (ΔR_{wu}), and between waterfilling and pre-emphasis (ΔR_{wp}), (b) relative optimum bandwidth difference between waterfilling and uniform loading ($\Delta f_{\max,wu}$) and waterfilling and pre-emphasis ($\Delta f_{\max,wp}$) as a function of NPB γ (normalized to LED 3 dB BW). 61

3.7 Measured response of the VLC link with Luxeon Rebel LXML-PB02-0023 blue LED (dark) and curve fitting (grey) with exponential curve (f_0 = 10.08 MHz), normalized to eliminate propagation attenuation ($H_0 = 1$). Channel response with a simple pre-emphasis (blue), given in (3.67), prior to the LED. 62

3.8 (a) Measurement Setup. (b) Schematic of the setup. 64

3.9 Experimental power (normalized to σ^2_{mod}) and number of bits loaded per sub-carrier for (a) waterfilling (HH algorithm [63]), (b) uniform loading after exhaustive search of the best $N_{\max}$ over VLC and (c) pre-emphasis employing strictly constant bit loading. For all three strategies BER = 10^{-4}. 65

3.10 Rate R_u for uniform loading of the modulation power versus the number of used sub-carriers N_{max} for different values of γ over the measured channel of Fig. 3.7. Sub-carriers were loaded with discrete QAM constellations. 66

3.11 Experimental results for the (a) maximum modulation bandwidth ($f_{\max}$) and (b) the rate as a function of modulation order M for the pre-emphasis algorithm and two different NPB values for BER = 10^{-4}. . . 71

3.12 Theoretical (solid) and measured (squares) bandwidth ν_x and throughput $\Re_x$ as a function of NPB γ in (3.30). All parameters are normalized to LED 3 dB bandwidth f_0, BER = 10^{-4} and are shown for waterfilling (dark), uniform loading (red) and pre-emphasis (blue). The throughput of the channel and the corresponding bandwidth are in dashed lines. 73

4.1 (a) (Optimum) normalized modulation bandwidth ($f_{\max_{PAM}}/f_0$, $f_{\max_p}/f_0$ and $f_{\max_w}/f_0$ for PAM, pre-emphasized OFDM and waterfilling, respectively) and (b) normalized throughput versus NPB used for modulation, γ, ignoring DC-bias power (VLC scenario). Dashed-red lines represent the performance for various constellation sizes M (for PAM and pre-emphasized DCO-OFDM) with the solid red being the choice of M optimized for maximum throughput. Solid blue and black lines represent the performance of OFDM with pre-emphasis and waterfilling, respectively, for continuous modulation order. For all plots BER_{M} = 10^{-4}. 86

4.2 PSD of an OFDM signal (black) and clipping noise (gray), for bias ratio of 0.5, 1 and 2. LED low-pass response not included. 93

4.3 Bias ratio z versus number of bits $b = \log_2 M$ per sub-carrier in one dimension. Noise-free ($r = 1$) and leaving a 3 and 6 dB power margin ($r = 2$ and $r = 4$, respectively) to operate over a noisy channel. Solid line: clipping limit. Dashed line: invertible distortion limit. For distortion–limited z, we used $r = 1$. 93

4.4 Normalized maximum modulation bandwidth and throughput for (a,b) waterfilling (W.F.), pre-emphasis (P.E.) with continuous (Cont.) and discrete (Disc.) modulation order M and (c,d) for pre-emphasis with discrete M, and different values of z as a function of γ. The BER is fixed at 10^{-4}. 99

4.5 (a,c) Optimum (normalized) modulation bandwidth and (b,d) throughput versus optical NPB γ_{opt} for PAM (red lines) and OFDM (with pre-emphasis and with waterfilling) with different z choices. For all plots BER = 10^{-4}. 100

4.6 Throughput versus distance for PAM (red), pre-emphasized OFDM with $z = 2.5$ (dashed-blue) and $z = 4$ (solid-blue) and waterfilling with $z = 2.5$ (dashed-black) and $z = 4$ (solid-black). The total electrical power is limited to 1 W. 105

5.1 Block diagram of optical wireless system including our non-linear equalizer. 113

5.2 Discrete-time non-linear LED model. For a DC-free modulation and for non-negative e.g. PAM, the same structure applies, but coefficients may take slightly different values. 117

5.3 (a) Exact inverse of LED model (post-distorter), (b) The proposed simplified structure. The input to the equalizer can be DC-free (s_r employing e.g. OFDM modulation scheme) or can be accompanied by a DC component (S_r employing e.g. PAM modulation). 118

5.4 (a) Normalized c_{2-4} using (5.35) to (5.37) (grey squares) and using (5.21) (solid dark curves). (b) Normalized (estimated) output signal, distortion and noise power at the equalizer output. 126

5.5 (a) Measurement Setup. (b) Schematic of the setup. 127

5.6 (a) Simulated SER performance for 4-PAM and 8-PAM signaling at 20 Msym/sec symbol rate. Red triangles (only for 8-PAM) show the SER for the case of no equalization at the receiver. Blue and dark triangles/squares show the SER for having a first–order linear equalizer and for having the proposed non-linear equalizer, respectively. The theoretical limit for uncoded SER for AWGN frequency–flat LTI channel is shown with a solid black line. (b) Simulated SER performance of 4-PAM for 20, 50 and 100 Msym/sec using the proposed non-linear equalizer (squares). Bound: SER for distortion-free frequency–flat (solid line) and distortion–free first–order low–pass LTI channel (dotted lines). 130

5.7 Simulated 4-PAM SER vs training sequence length for SNR of 15 dB (a) and 18 dB (b). 131

5.8 Simulated 4-PAM eye diagrams with rectangular waveform shaping and symbol rate of 20 Msym/s before (a), after linear (b) and non-linear equalization (c). The sample rate is taken 16x of the symbol rate, the training sequence includes 20 symbols (320 samples) and noise is absent. 132
5.9 Experimentally measured 4-PAM eye diagrams with raised cosine waveform shaping, symbol rate of 5 Msym/s and 30 dB SNR. before (a) with BER = 10^{-2} and after (b) non-linear equalization. The initial 25 symbols of the PAM signal was used to estimate the equalizer parameters. 132
5.10 (a) Measured SNR versus frequency for I_{IN} = 100 mA (dashed) and 350 mA (solid) with (W.) and without (W.o.) non-linear (N.L.) equalizer (EQ.), (b) Sub-carrier bit loading for I_{IN} = 350 mA to ensure BER $\leq$ 10^{-4} with (dark) and without (grey) enabling the non-linear equalizer. 135

List of Tables

2.1 Hypothetical LED parameters 22

3.1 OFDM parameters used for VLC measurements. 62
3.2 Comparison between the experimental results using proposed simplified algorithms for uniform loading, theoretical expectations and optimum experimental results for BER = 10^{-4}. 69
3.3 Comparison between the experimental results using proposed algorithms for the pre-emphasis loading and theoretical expectations for BER = 10^{-4}. 72

4.1 Current work in comparison with the previously published works. . . . 77
4.2 Required received average energy per dimension normalized to N_0 for different constellation size (M) and the minimum normalized bias requirement z at BER=10^{-4}. 85
4.3 Quick comparison of the linear and quadratic terms in the power consumption and a penalty on the SNR for flat channel (low NPB, small modulation bandwidth). 103

5.1 Summary of coefficient number for non-linear models in literature . . . 111
5.2 Parameters for the LED model 125
5.3 Measured harmonics of the LED output w/o non-linear equalizer and with non-linear equalizer for received SNR of 30 dB. 136

A.1 Estimation of $f(x) = \sqrt{x}$ with a second order polynomial and the residual error. 158
A.2 Estimation of $g(x) = x\sqrt{x}$ with a second order polynomial and the residual error. 159

Contents

Summary **i**

1 Introduction **1**
1.1 A Brief History of Lighting . . . 1
1.2 Optical Wireless Communication (OWC) . . . 2
1.2.1 Role of OWC as alternative to RF . . . 3
1.3 Challenges and Approaches . . . 4
1.3.1 LED Bandwidth Limitation . . . 5
1.3.2 LED Distortion . . . 6
1.3.3 Non-negativity and Clipping . . . 6
1.3.4 Power Constraints in OWC . . . 7
1.4 Thesis Outline and Contributions . . . 8

2 LED Communication Channel Model **13**
2.1 Introduction . . . 13
2.2 Intensity Modulated Optical System . . . 14
2.2.1 Electrical Driver . . . 15
2.2.2 Indoor Optical Propagation Channel . . . 16
2.2.3 Optical Detectors . . . 16
2.3 Physics of LED Junction . . . 16
2.3.1 Carrier Recombination Rate in QW . . . 17
2.3.2 QW Nonlinear Photon Emission Model . . . 18
2.3.3 QW Response to Step Function . . . 19
2.4 Linearized Small Signal QW Model . . . 23
2.4.1 Exponential Frequency Response Model . . . 24
2.5 Phosphor Coating . . . 25
2.5.1 Media with Photonic Conversion . . . 25
2.5.2 Typical Phosphor as the λ-Converting Media . . . 26

2.5.3 Visible Light Communication (VLC) Channel Through Media with Photonic Conversion . . . 27
2.5.4 Noise . . . 31
2.5.5 Optical Filtering and OFDM . . . 32
2.6 Throughput of First-Order Low-Pass LED Channel . . . 34
2.7 Conclusions . . . 36

3 DCO-OFDM Sub-carrier Loading Strategies 37
3.1 Introduction . . . 37
3.2 Optical Wireless System Architecture . . . 39
3.2.1 LED Non-linearity . . . 42
3.2.2 LED Channel model . . . 44
3.3 Power Consumption and Constraints . . . 44
3.3.1 Power Consumption for DCO-OFDM . . . 45
3.3.2 Power Constraint . . . 46
3.3.3 Power Consumption for ACO-OFDM . . . 47
3.3.4 Constrained IR Optical Power in ACO-OFDM . . . 48
3.4 Theoretical Throughout of the LED Channel . . . 48
3.4.1 Optical OFDM with Discrete Modulation . . . 49
3.4.2 Normalized LED Channel . . . 51
3.5 Power Loading Strategies . . . 52
3.5.1 Waterfilling . . . 52
3.5.2 Uniform power allocation . . . 54
3.5.3 OFDM with Pre-emphasis . . . 55
3.6 Comparison of Sub-carrier Loading Strategies . . . 57
3.6.1 Signal-to-Noise Ratio . . . 58
3.6.2 Example . . . 58
3.7 Experimental Verification . . . 61
3.7.1 Waterfilling . . . 63
3.7.2 Uniform power loading . . . 65
3.7.3 Pre-emphasis . . . 69
3.7.4 Experimental Comparison . . . 72
3.8 Conclusion . . . 73

4 Optimization and Comparison of M-PAM and Optical OFDM Modulation 75
4.1 Introduction . . . 75
4.2 OWC Power Constraints . . . 82
4.2.1 Channel Model . . . 82
4.2.2 Normalized Power Budget (NPB) Definition . . . 82

4.3 Pulse Amplitude Modulation (PAM) . . . 84
4.3.1 PAM Bias Penalty . . . 85
4.3.2 Throughput of DCO-PAM over Low-Pass Channel . . . 85
4.4 OFDM . . . 87
4.4.1 Throughput of DCO-OFDM over Low-Pass Channel . . . 88
4.4.2 OFDM with Waterfilling . . . 88
4.4.3 OFDM with Pre-emphasis . . . 89
4.5 Clipping and Distortion Model . . . 91
4.5.1 Current Clipping . . . 91
4.5.2 Invertible Distortion Model . . . 94
4.6 Effect of Clipping and Distortion on OFDM . . . 94
4.6.1 Conservatively Choosing Low Modulation Depth . . . 94
4.6.2 Optimizing for Throughput . . . 95
4.7 Comparison of DCO-PAM and DCO-OFDM . . . 98
4.7.1 Extra–Power Limited Channel . . . 99
4.7.2 Optical–Power Limited Channel . . . 101
4.7.3 Electrical–Power Limited Channel . . . 103
4.8 Computational Complexity . . . 105
4.9 Conclusions . . . 106

5 LED Nonlinear Distortion Mitigation 109
5.1 Introduction . . . 109
5.2 System Description and LED Model . . . 113
5.2.1 Low–Frequency (Quasi–Static) LED Model . . . 115
5.2.2 Discrete-Time LED Dynamic Model with Normalization . . . 116
5.3 Post-Distorter (Equalizer) Structure . . . 117
5.3.1 Single-Tap Second-Order Non-linear Equalizer . . . 118
5.3.2 Special Case: Very Small–Signal Excitation . . . 119
5.4 Training–Sequence Based Estimation . . . 120
5.5 Effect of Noise . . . 121
5.5.1 Estimation of Non-linear Equalizer Coefficients . . . 121
5.5.2 Summary of Equalizer Algorithm . . . 124
5.5.3 Noise and Signal Distortion Power . . . 125
5.5.4 A simulation Example . . . 125
5.6 Simulation and Practical Verification Setup . . . 127
5.7 Non-linear Equalizer in PAM Signaling . . . 128
5.7.1 Simulation Results . . . 129
5.7.2 Experimental Results . . . 131
5.8 Non-linear equalizer in OFDM Signaling . . . 133
5.9 Harmonic Distortion . . . 134

5.10 Conclusions 134

6 Conclusions and Recommendations for Future Research 137
6.1 Conclusions and Original Contributions 137
6.2 Recommendations for Future Research 139

A Equalizer Derivations 155
A.0.1 Zero Forcing (ZF) equalizer 155
A.0.2 The simplified equalizer structure 156

B Uniform Power allocation: Derivations 161

Acknowledgments 163

List of publications 165

Bibliography 165

Chapter 1

Introduction

1.1 A Brief History of Lighting

Looking back into the history of artificial lighting, a continuous effort in developing lighting sources can be recognized to make these more efficient and cheaper. The first human illumination discovery was likely a torch, while the first lamps looking like today's lamps were shells or hollow rocks filled with fuel or wood. The first electric lamps were fabricated in the early 1800s and the first light bulbs in the 1830s. In the early 1860s, fluorescent lights were introduced which were followed by the carbon-filament incandescent light bulbs in 1879 by Thomas Edison. These two latter light sources were the standard of lighting for decades. In 1891, Frederik Philips established a factory in Eindhoven manufacturing incandescent lamps which quickly became one of the largest producers in Europe.

In 1901, the mercury vapor light and following this, a vast variety of high-intensity discharge (HID) artificial light sources were developed; high-pressure sodium, mercury vapor, metal halide, neon and many others. Recently Light Emitting Diodes (LEDs) are popular which have some advantages over the predecessors. LEDs are semiconductor devices hence they exhibit long life time, become cheaper over time, are energy-efficient and environmentally friendly with no toxic mercury contained and they can be easily tuned, controlled and optimized for a target emission spectrum.

The first LEDs were commercialized in the late 1960s and were only available in red color. Since then an enormous progress could be recognized in color options, energy efficiency, output light intensity as well as in cost reductions. While off-the-shelf LEDs could already outperform incandescent and fluorescent light sources in efficiency and life time, the state-of-the-art High Brightness LEDs (HB-LEDs) by Philips could

provide more than 200 lumens-per-Watt[1] (lm/W) [1]. For more information, we refer the interested reader to [2–4].

1.2 Optical Wireless Communication (OWC)

The very first historical Optical Wireless Communication (OWC) system goes back to centuries ago when people were using smoke for long distance communications. The first OWC using artificial lights was by Alexander Graham Bell in 1880 [5], known as photophone. Photophone was used to transmit voice over hundreds of meters using a beam of light. The introduction of laser in 1960 and fiber optics one decade later, revolutionized OWC [6]. Today, fiber optics driven by lasers are the medium of choice for high speed data communications. Lasers have a narrow beam and not suitable for coverage of large areas such as rooms or offices. Therefore, WiFi signals were used by the end user in such scenarios. Most recently, commercialization of high speed and efficient LEDs has made it possible to use light for data transmission wirelessly.

With OWC, we refer to wireless communication technologies which utilize LEDs and optical carriers in infrared (denoted as IR), visible light (denoted as Visible Light Communication, VLC) or ultraviolet (UV) bands of electromagnetic spectrum. The work in this thesis focuses on IR and VLC communications.

An LED is basically a solid-state diode which can be switched rapidly with a rise/fall time in the order of several (tens) of nanoseconds. Such a fast response is tempting to utilize LEDs for data transmission. In 1979, infrared (IR) LEDs were used for wireless data transmission and soon after Infrared Data Association (IrDA) standardized IR wireless communications [7]. However, the applications were limited to special settings such as short range line-of-sight links and remote control applications.

The first communication link using visible light (Visible Light Communication, VLC) was demonstrated in 1999 to transmit audio signals [8]. In 2011, VLC protocols and PHY layer were standardized under IEEE standard 802.15.7, where the maximum data rate was limited to 96 Mbit/sec. The limitations on the VLC, such as limited data rate, were revised in a new version, IEEE 802.15.7r1. [12]. A topic interest group within IEEE 802.11 is also looking into the possibility of introducing OWC to 802.11 (denoted as 802.11bb). The IEEE 802.11bb will serve the mass market use-cases of OWC as the alternative to existing RF solutions. In fact, IEEE 802.11bb benefits from the 802.11 MAC and associated services that are already optimized for low cost wireless local area networks. G.vlc (G.9991) from ITU study group is also working on

[1] Lumen-per-Watt stands for the energy efficiency of lighting source. A traditional 60 watt incandescent bulb produces 860 lumens hence offers an energy efficiency of 14.3 lm/W. The energy efficiency of 200 lm/W means less than 5 watts of energy is required to produce the same brightness as the traditional 60W bulb.

physical layer (PHY) as a potential candidate for 802.11bb PHY. G.9991 was based on PHY's for base band communication such as ADSL (Asymmetric Digital Subscriber Line).

The emergence of fast IR and High Brightness white LEDs triggered a lot of attention from both academia and industry to OWC. In fact, the continual demand for high speed and secure data communication, the limited bandwidth resource for simultaneous connection of multiple devices and the increasing difficulties of electronic techniques within the Radio Frequency (RF) spectrum to handle these demands were the main drivers behind this attention. Yet, OWC offers some great advantages compared to its wireless RF alternative (WiFi) such as license free wide communication channels [13–18], enhanced security, ultra-dense cellular reuse and elimination of electromagnetic interference [16, 19].

IR or VLC LEDs require non-negative driving current to perform Intensity Modulation (IM) at the transmitter and Direct Detection (DD) at the receiver. In IR communication the signals are not visible by human eyes which allows for continuous operation while VLC operation is limited to the cases where illumination is required. For both applications, human eye safety limits the amount of optical power that can be emitted. The amount of eye-safe optical power at visible bands is much higher than that at the IR bands.

Figure 1.1 shows a smart office lighting scenario prototype using OWC. Electronic devices such as smartphones, computers, laptops as well as household appliances are connected to the network through the light. Some of the connection links in Figure 1.1, for example down(up)-link connection of laptops, require high speed data transmission rates. But for household appliances such as an air conditioner, a low throughput link can work quite well.

1.2.1 Role of OWC as alternative to RF

In the past few years, the data traffic has grown dramatically and there are several reasons to believe that there is far more growth yet to come. With each generation of mobile network introduced, the channel bandwidth has increased significantly, ranging from 200 kHz for the 2^{nd} generation to up to 20 MHz in the 4^{th} generation while the carrier frequency is in the sub-6 GHz range [20–23]. For the 5^{th} generation, which is still under development, to support bandwidth up to 400 MHz, the use of high frequency carriers in multi-GHz range, e.g. 26 GHz - 41 GHz, is unavoidable [24]. Next to the mobile network, there are other wireless applications evolving. Wireless Local Area Network (WLAN), also known as WiFi, is dominantly occupying Industrial, Scientific and Medical (ISM) band at 2.4 GHz (2.4 GHz - 2.5 GHz) and also utilizing 5 GHz - 6 GHz frequency range for enhanced data rate. While the sub-6GHz RF spectrum is occupied with bandwidth–hungry applications such as video-on-demand

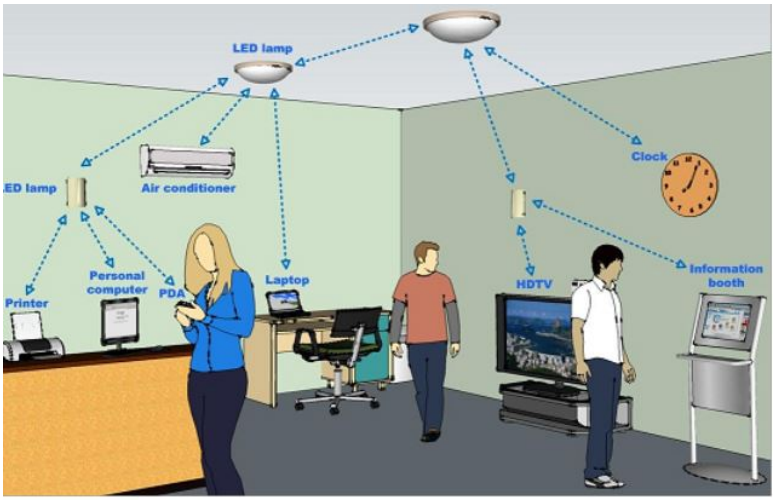

Figure 1.1: Smart office lighting, LED lamp (data source) connected to mobile phones, personal computers, air conditioner , printer, laptops, etc. Source: Adapted from [25].

services over WiFi or mobile networks, Internet of Things (IoT) is connecting more and more devices to the network everyday which are mainly operating at ISM band between 2.4 GHz to 2.5 GHz.

The emerging Optical Wireless Communication (OWC) is currently entering the market as an alternative to the RF communication providing significant relief from the over-crowed RF spectrum. OWC can fulfill the growing demand for the connectivity, e.g. for IoT applications and thanks to the vast amounts of unregulated spectrum of visible light or InfraRed (IR), it can also compete with high speed RF systems. New research activities have already started considering OWC to support 5^{th} generation of mobile network. OWC also offers strong advantages over its RF counterpart such as elimination of electromagnetic interference (suitable for EM wave restricted environments), ultra-dense cellular reuse and enhanced security [16, 19].

1.3 Challenges and Approaches

Despite the advantages of OWC, for widespread use, there are a number of challenges that need to be addressed. These challenges are mainly present at the transmitter side of an OWC link. In this section, we review the challenges and the solutions proposed in literature.

1.3.1 LED Bandwidth Limitation

The output light of an LED results from hole-electron recombinations which emit photons. The process of re-combinations is accompanied with a time constant that, in frequency domain, is equivalent to low–pass filtering.

Red/Green/Blue (RGB) LEDs show a 3 dB bandwidth of 10-20 MHz at a typical bias current of 0.5 A [26–29]. White light can be perceived from a combination of RGB-color light. Another approach to generate white light is to use Phosphor coated blue LEDs [26,28,29]. In these types of LEDs, a fraction of blue photos are converted to yellow by passing through a Phosphor layer and the white light is composed of the combination of blue and yellow photons. By controlling the yellow to blue photons ratio, warm, neutral or cold white light can be generated. In phosphor-coated LEDs, the slow time constant of the phosphor conversion limits the 3 dB bandwidth of the LED to about 3 MHz [28,31].

For IR applications, there is no illumination functionality required so the LEDs can be optimized just for communication. Commercial IR LEDs already exhibit fast switching behavior with 3 dB bandwidth which can easily reach to 40 - 50 MHz with a bias current of 50 mA [30]. Laser diodes can achieve a much higher bandwidth, several hundreds of MHz or multi-GHz [32]. However, the eye safety measures limit their application.

To tackle the LED bandwidth limitation, several techniques have been developed in the literature. Some techniques focused on LED design, e.g. the work in [33] used non-resonant cavity LEDs to achieve a 3 dB bandwidth of multiple hundreds of MHz. However, these techniques require an special LED design which increases the cost and in this thesis we focus on commercial LEDs. Blue filtering, i.e., passing on only the blue light and removing longer wavelengths, was shown to effectively remove the slower portion of the light at the receiver hence enhancing the 3 dB bandwidth of the LEDs [6,28,34]. This technique, however, removes part of the optical signal which could be used for improved detection performance at lower frequencies. Furthermore, depending on the nature of the ambient noise, blue filtering may in some cases counter-productively decrease the available system throughput [9]. In addition to blue filtering, pre or post equalization in both analog [35] or digital [26,36] domain can also be used to further extend the LED 3 dB bandwidth. One of the side effects of the post-equalization is noise enhancement. Using pre-equalization at the transmitter side avoids noise enhancement, but requires a larger input power to the transmit LED. Channel information is also needed for pre-equalization at the transmitter. Channel equalization techniques are necessary to reduce Inter-Symbol Interference (ISI) in OWC links employing Pulse Amplitude Modulation (PAM).

Orthogonal Frequency Division Multiplexing (OFDM) has the advantage of carrying multiple bits per symbol and allows frequency–adaptive subcarrier loading to

achieve decent OWC link throughput. Waterfilling accurately predicts the transmit Power Spectral Density (PSD) and optimizes the modulation bandwidth and the power and bit distribution over the sub-carriers to maximize the throughput [62]. However, applying an on/off power loading strategy comes with less complexity in the implementation. The complexity of implementation becomes important in, for example, a high speed data transmission where a large number of bits have to be distributed over a large number of sub-carriers. For the simpler implementations, the throughput penalty as well as the optimum modulation bandwidth w.r.t. the optimum waterfilling need to be understood. There are some literature on the comparison of the modulation schemes over OWC, e.g. [48,54,60]. However, the literature lacks a comprehensive platform considering many aspects such as application-specific power constraint or modulation-specific optimizations.

1.3.2 LED Distortion

It is often stated in literature that LEDs are non-linear devices. These nonlinearities degrade the performance by impairing the signal constellations. To tackle this issue, a simple primary approach could be to limit the driving current amplitude to the LED to prevent the distortion from happening [33]. In this case, a large bias current for the LED is required. Implementing a pre- [40] or post-distorter [41] at the transmitter or receiver side, respectively, is a more efficient approach to address this issue.

Different pre (post)-distorters have been reported previously. The generic Volterra series-based structures are typically highly complex and computational-intensive [42–44]. Simplified Volterra series with reduced complexity such as memory polynomial model [45–47] have been also reported. However, these simplified structures, which are not supported by with LED physics, are not reflecting the real system. Exploring physical model of LED junctions, a better and efficient pre(post)-distorter in terms of the number of unknown coefficients was implemented in our team [40,41]. Experimental results verified that the pre/post-distorter can boost the data rate substantially. Further investigations are also made in this thesis to simplify the pre/post-distorter structure reducing the number of coefficients and to estimate the optimum coefficient settings.

1.3.3 Non-negativity and Clipping

To generate a steady-state (DC) flow of photons, the LED needs a positive-valued current. It has been argued in literature , e.g. [48, 49], that if the driving current to the LED exhibits negative excursions, either a proper DC bias is needed to make the current strictly positive or the negative excursions have to be clipped at zero. However, the negative currents with short duration (compared to LED time constant) are

allowed as long as the quantum well of the LED is not fully depleted from the carriers [33]. Full depletion of the carriers slows down the LED limiting the modulation speed [33]. This was earlier understood by the work in [50] describing LED driver with active pull out. In this thesis, non-negative clipping of the LED current will be considered.

Moreover, in the early days, LEDs were designed for maximum power output and the current level was limited to prevent LED thermal break down. This justified a model in which the LED current is both non-negative and peak-limited [51]. Today's high brightness LEDs are operated at maximum energy efficiency point which is a set point where the photon output recombining electron-hole pair is the highest. This is far below any break-down rating. At higher currents, the LED efficiency only gradually reduces (LED droop) [52, 53]. This justifies a single-sided (non-negative) clipping model [49]. Furthermore, many practical electronic drivers do not allow a negative current through the LED.

Clipping the signal induces distortion that cannot be inverted. Frequency domain modeling of the clipping noise is necessary for link throughput calculations. In the literature, the distortion power, resulted from clipping, was considered to have a flat spectrum, similar to receiver noise [49, 54]. In this thesis we challenge this model. At this point a trade-off can be recognized between the LED DC power consumption (DC bias) and the clipping noise level. At a fixed LED DC current, for a large coverage in OWC, transmitter boosts the signal level causing the signal exhibit clipping and distortion hence limiting the link throughput for near–distant receivers.

1.3.4 Power Constraints in OWC

The capacity of a channel is calculated under a specific constraint on the channel. For example in RF communications, input power to the channel is constrained [61]. For OWC channels, the constraints differ per application and sometimes multiple constraints might be applied on a channel.

In a VLC channel, the target illumination level dictates the LED bias current and thus the LED DC power consumption. Modulation which is being considered as a secondary task consumes some extra power [51, 57]. LEDs have a relatively high optical efficiency. A minimum requirement on the overall system efficiency requires that the extra power due to modulation has to be limited. Then for VLC applications, the extra power consumed is the key constraint.

For IR applications, there is no illumination requirement and the total electrical power consumed is relevant. For both VLC and IR channels, the output average optical power (hence the LED DC current) might also be constraint, in VLC by the target illumination level and in IR, for human eye safety purpose.

In the past, the LED peak current was often constrained. However, in section

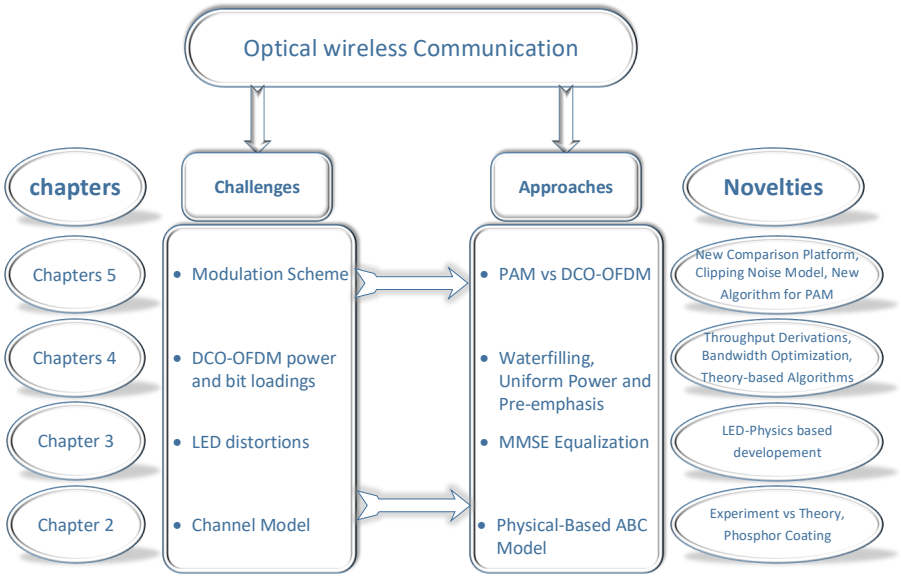

Figure 1.2: Challenges and approaches addressed in this thesis.

1.3.3, it was discussed that modern LEDs do not exhibit peak current clipping.

1.4 Thesis Outline and Contributions

The aforementioned challenges in OWC are addressed in this thesis, focusing on the promising approaches as reviewed in section 1.3. Fig. 1.2 gives an overview of this thesis with more details which follow.

In chapter 2, LED communication channel is discussed. We employ the newly proposed ABC model for hole-electron recombination in LEDs [33,52,53,67–70]. This model has been widely debated, matured and verified within our research group [40,71] and in this thesis we use this model to better analyze the system performance, to compare modulation methods and to design improved processing for receivers and transmitters. We show that the model suggests a first–order low–pass frequency domain channel model for LEDs when the modulation index is low enough to neglect LED–induced distortion. In this chapter, we also model the Phosphor-coating that is used to generate white light from blue LED source. For this, the dynamics of the photon conversion and the effect of blue filtering are investigated. Finally, the experimental channel model in comparison with the theoretical model is discussed. This chapter further reviews the OWC link throughput for the first–order low-pass channel model that appears to describe the LED junction capacity or the phosphor

coating well. For optimum waterfilling we derive new formulas, as well as for a uniform power distribution strategy.

To make the OFDM signal positive-only, different approaches have been introduced [57]; adding a DC offset, known as DCO-OFDM, or performing special amplitude-folding, Flip-OFDM, and clipping methods, Asymmetrically Clipped Optical OFDM (ACO-OFDM). The work in [59] has shown that typical Flip and ACO OFDM receivers loose 3 dB in signal-to-noise ratio by ignoring 50% of the signal energy, thereby jeopardizing a substantial part of their spectrum efficiency. Therefore, the focus of this thesis in chapters 3-5 will be on DCO-OFDM variant. A brief comparison between ACO-OFDM and DCO-OFDM will be provided in chapter 4.

For the high spectral efficiency variant (DCo-OFDM), distribution of power and bits over sub-carriers is still a challenge. Frequency-adaptive power and bit loading has been studied extensively for RF communications. In RF the channel frequency response is stochastically varying due to multipath. But in the line-of-sight LED channel, the transfer function exhibits a predictable roll-off [26, 58]. In RF channels, deep fades are rare and can be handled by interleaved coding. In fact, this is the main reason why frequency-adaptive power and bit loading was not adopted for RF standards.

The Shannon capacity expression in a flat frequency non-selective AWGN channel shows that the link throughput can be increased by increasing the modulation bandwidth in a constant energy per symbol thus in a constant Signal to Noise Ratio (SNR) over all frequencies [61]. To keep the symbol energy constant while increasing the bandwidth, the modulation power has to grow linearly with the bandwidth. Another approach could be to increase the power in a constant bandwidth to boost the SNR. Since throughput is proportional to the bandwidth but it depends to the SNR though a $\log_2(.)$ operation, it is far more attractive to increase the bandwidth than boosting the SNR. However, in a frequency–selective power-limited low–pass LED channel where the higher frequencies are severely attenuated, there is a trade-off between investing adequate power on high frequency sub-carriers (which due to channel attenuation result in a relatively low pay-load) and assigning the power to low frequency sub-carriers and accept the relatively lower throughput gain.

In chapter 3 different power and bit loading strategies of DCO-OFDM are discussed, waterfilling, uniform power and uniform bit loading (the latter being known as pre-emphasis) over the experimental channel model. Mathematical derivations are provided for the throughput and we show that for each strategy, there is a specific optimum bandwidth over which the modulation power is spread.

Waterfilling is a known strategy for optimum power loading to maximize link throughput. However, it requires a relatively complex and iterative algorithm [63,64]. We further show that it requires a high modulation bandwidth hence the highest sampling rate, higher than for uniform and pre-emphasis. In theory, uniform power

loading, which is used in ITU g.9991 standard, provides almost exactly the same rate as waterfilling in the LED low-pass channel. However, in practice, we show that uniform power loading wastes 1.5 dB of the modulation power due to the limitation of integer-bit constellation sizes on the sub-carriers of OFDM. Pre-emphasis simplifies the implementations by applying the same constellations on all sub-carriers. This is considered in the current standardization of IEEE 802.11bb, as it can reuse approaches designed earlier for RF channels. We show that, pre-emphasis requires the least bandwidth, compared to two other strategies, however, the sensitivity of throughput to link variations is relatively high. For both uniform power and pre-emphasis we present novel algorithms to achieve the theoretical throughputs.

Following IEEE 802.11bb to use uniform constellations over OFDM sub-carriers, one could pre-emphasize LED communication channel. Then, in a frequency–flat channel PAM could also be employed as the modulation technique. The question of which modulation scheme performs better requires a comprehensive modeling considering many aspects. Chapter 4 demonstrates such model, derives mathematical expressions for the throughput and optimum modulation bandwidth considering three different power constraints on the channel.

The presented model in Chapter 4 considers low–pass filtering by LED channel and some other extra modulation-specific constraints. We introduce a parameter, Normalized Power Budget (NPB), which is the available power budget of the transmitter multiplied by channel path loss and normalized to receiver noise power in channel 3 dB bandwidth. For PAM, modulation order and bandwidth are optimized for the given NPB and a new algorithm has been proposed for implementations. For DCO-OFDM, the limited DC-bias and the resulting clipping noise are considered and the existing clipping noise model of the literature has been refined for accurate modeling.

For an extra–power constraint, thus only for modulation on top of an already given LED DC power, we show that in a pre-emphasized channel there is no difference between DCO-OFDM and PAM in terms of throughput and the bandwidth occupied while DCO-OFDM with waterfilling provides the highest achievable throughput. In an LED channel with optical or electrical power constraint, PAM always performs better than DCO-OFDM with pre-emphasis. For channels with low NPB, PAM even outperforms DCO-OFDM with waterfilling. The results of this chapter show that for a simultaneously wide coverage and short–range high–throughput regimes, the bandwidth, bit–loading profile, DC bias optimization, and adaptive modulation schemes are the key.

Chapter 5 addresses the LED nonlinear distortion by introducing a novel, simple and practical non-linear equalizer at the receiver. For this, we take the LED model of chapter 2 and invert it to cancel the distortion in a Zero-Forcing (ZF) manner. The resulting model contains five unknown coefficients. We simplify the structure and

reduce the unknown parameters to three and develop a Minimum Mean Square Error (MMSE)-based approach to estimate those parameters. The effect of receiver noise on the equalizer parameter estimation algorithm is modeled which allows us to further simplify the parameters estimation. Both simulations and experimental results using PAM, DCO-OFDM and single-tone sinusoidal signals confirm the effectiveness of the proposed LED physics-based equalizer. For PAM, our equalizer widened the eye-diagram and improved Bit Error Rate (BER) performance, for OFDM, more than 50% improvement on the throughput for a fixed LED bias or equivalently more than 70% dc power was saved at a constant system throughput. Finally, for the single-tone sinusoidal input, the equalizer pushed the second and third harmonic power below receiver noise floor, more than 20 dB reduction on the second harmonic.

The research work described in this thesis has resulted in several publications, listed in the Appendix. In fact, Chapters 3-5 are the reformatted publications [72–74]. Finally, chapter 6 summarizes this thesis, with recommendations on the directions for future research.

Chapter 2

LED Communication Channel Model

2.1 Introduction

Optical Wireless Communication (OWC)[1], combined with full user mobility and wireless networking, is referred to as LiFi. The LiFi technology is progressing rapidly. In particular to increase bit rates further, it becomes increasingly important to have a reliable channel model. In fact, the LED optical channel differs substantially from the (typically stochastic) RF channel. A major challenge is the limited LED bandwidth, rolling off at only a few MHz with a mixture of low-pass, nonlinear and memory effects. Yet, tailored Digital Signal Processing (DSP) techniques can mitigate these effects [40]. Initially, the (static) nonlinearity and low-pass behavior have been modeled as separable mechanisms [42, 76]. However, the physics of photon generation in semiconductor junctions involves dynamic nonlinearities intertwined with electron-hole recombination latency effects [33]. Their models can inspire new non-linear equalizer concepts and can restrict their complexity.

In the visible light spectrum, a bandwidth of more than one thousand times of the total radio spectrum is available. However, current LED light sources emit a wide spectrum. For illumination, this is intentionally the case to provide an appropriate light rendering quality. Moreover, wide emission spectra also help to reach high efficiencies. Consequently, the bandwidth at which these LEDs can be modulated is not limited by constraints on the optical emission spectrum, but rather by the

[1]This chapter consists of materials previously published in IEEE Communications Magazine [75], International Society for Optics and Photonics (SPIE) [27] and European Conference on Optical Communication (ECOC) [9] and were re-structured for readability in thesis form.

recombination time constants and by speeds at which the hole-electron concentrations, thus the electrical charge in junction of the LED can be changed. This chapter reviews recent and ongoing advances in modelling LEDs peculiarities. As the LED technology has rapidly progressed towards higher photonic efficacies, we also observe significant differences in their response, compared to early-generation LEDs [75].

2.2 Intensity Modulated Optical System

Various scientific communities rely on different models for the LED channel. These models often focus on different challenges. In Intensity Modulated/Direct Detection (IM/DD) LED channels, photons are generated in integer numbers, according to Poisson statistics. Optimizing the throughput despite the associated shot noise is a key theme in some studies. However, in most practical systems, Additive White Gaussian Noise (AWGN), incurred during amplification of weak photo-diode signals, dominates. Moreover, light intensity is by definition real-valued and non-negative, so baseband LED signals are real, without quadrature phase components. This requires an adaptation of the signal waveform typically used in carrier-based RF channels.

The LED has repeatedly been mentioned to be a prime example of a peak-limited, rather than power-limited channel [77]. In an LED peak optical power limited channel, the maximum optical power (or equivalently the maximum LED current) is constrained while in an average optical/electrical power limited channel, the average LED current/average electrical power is of interest. According to the physics models behind photon generation, modern LEDs do not exhibit a hard saturation or abrupt clipping, but rather show a gradual reduction (droop) in efficiency [78]. In fact, in the early days, LEDs were operated near their maximum light output, even close to their thermal breakdown. Now with rapidly lowering LED prices, practical systems use LEDs much closer to their most power-efficient operation point, which corresponds to currents that are only a small fraction of the absolute maximum ratings. Although manufacturers specify absolute maximum currents for thermal reasons, LEDs have typical thermal time constants of tens or hundreds of milliseconds, so these are unlikely to be damaged by sub-microsecond modulation peaks from, e.g., Orthogonal Frequency Division Multiplexing (OFDM) running at sample frequencies far above 10 MHz. Hence, we increasingly see publications that treat the LED non-linearities as being invertible, while hard, non-invertible clipping only occurs at low or negative currents.

To elaborate on relevant effects of the Visible Light Communication (VLC) channel, the LiFi communication downlink cascaded with several analog functional blocks is shown in Fig. 2.1, including the electrical driving modulator. It generates the signal current through the Space Charge Region (SCR), and the Quantum Well (QW)

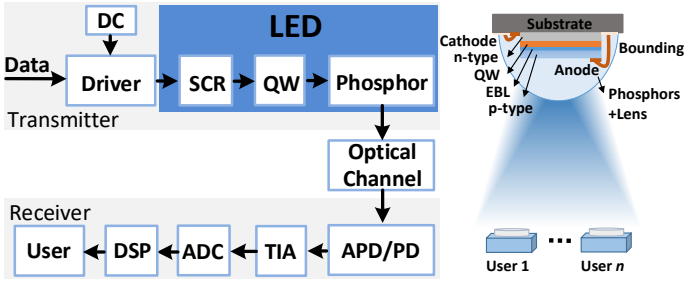

Figure 2.1: LiFi communication downlink with detailed illumination LED structure.

that actually emits photons. This optical signal possibly sees a phosphor coating (in VLC) and a lens, followed by the propagation channel, an optional receive optical filter or concentrator and detector lens, the Avalanche Photo Diode (APD) and the Trans-Impedance Amplifier (TIA). Throughout this thesis, we assume that, LED is the only that can non-linearly distort the signal while other blocks are operating in their linear regime with a possible (low–pass) filtering effect.

2.2.1 Electrical Driver

In a very crude simplification, the LED can be seen as a dynamic resistance in parallel with a QW capacitance. From this model, we can understand that the transfer behavior highly depends on the output impedance of the driver. In this thesis work, we consider bias-T configuration for the LED driver which can be simply assembled using off-the-shelf components [79]. There are other more efficient options, such as series modulator [50, 79], which requires special attentions in implementation which fall outside the scope of this thesis work.

In bias-T configuration, an amplifier is used to drive the LED and a bias-T is interposed between the amplifier and the LED to separate the LED DC current from the AC current of the amplifier. Typical RF amplifiers are designed to feed into 50 Ω. In particular, we distinguish between voltage driving (which enforces a voltage across the LED that is proportional to the signal to be emitted) and current driving, which enforces an LED current that is proportional to the signal to be emitted. Voltage driving can mitigate the low-pass effect of the LED capacitor. Regrettably, many previously reported experimental studies do not explicitly mention the real output impedance of the driver. Nonetheless, in some cases typical 50 Ω bias-T components are used to drive the LED.

In fact, 50 Ω would be very large compared to the dynamic resistance of the LED and would lead to current driving. Our result can be applied to voltage driving, but this requires elaboration of the dynamic I - V relation of the entire LED, which is

outside the scope of this thesis. In the remainder of the thesis we focus on current driving. An appropriate circuit for this purpose can be found in the literature [79,80].

2.2.2 Indoor Optical Propagation Channel

In many papers, the first-order Lambertian radiation pattern is repeated to describe the angular directivity of illumination light. Yet, in practice LED optics use different radiation patterns, in particular to optimize the uniformity of lighting coverage [81]. In an indoor setting, light may reflect against walls which leads to a Ricean signal distribution [82, 83]. Delayed paths have been reported with excess delays of 10 nsec (3 meter extra path length, first dip at 50 MHz modulation bandwidth) for office and 70 nsec for industrial settings. Yet for ceiling-to-table paths, such reflections mostly are too weak to cause significant nulling [84]. Overall, we believe that the bandwidth limitations of LEDs are more significant than multipath dispersion, so reference models preferably emphasize LED limitations. Interference spillover into neighboring cells decays much faster in typical VLC or IR networks than in RF networks [85, 86]. This helps to achieve denser reuse.

2.2.3 Optical Detectors

The received information by the APD/PD (in the optical domain), is converted into electrical current. PDs also have a relatively large junction capacitance, that can act as a low-pass filter. In particular it has to capture signals from a wide variety in angles, the junction area, thus also its capacitance is large. This large junction capacitance together with an amplifier input impedance creates a low-pass frequency response with a bandwidth which normally, but depending on the APD/PD, is an order of magnitude larger than the LED bandwidth [87]. Yet, usually a Trans-Impedance Amplifier (TIA) is used to compensate the effect of the PD capacitance and to remove the LPF cut-off, but at the cost of a sharp rise of the noise levels at high frequencies [88]. The received power by the APD is (normally) small, and thermal noise limits the link performance. Yet distortion caused by the APD or TIA modules is usually negligible.

2.3 Physics of LED Junction

The LEDs non-linear operation and their limited bandwidth are two critical limitations in high speed VLC. Several models have been previously proposed to describe or to simplify the LED response. In a simple approximation the LED can be seen as a first-order low-pass filter, composed of the driver output impedance, differential resistances and the junction Quantun Well (QW) capacitance. A more sophisticated model, representing an LEDs small-signal electrical equivalent circuit is discussed

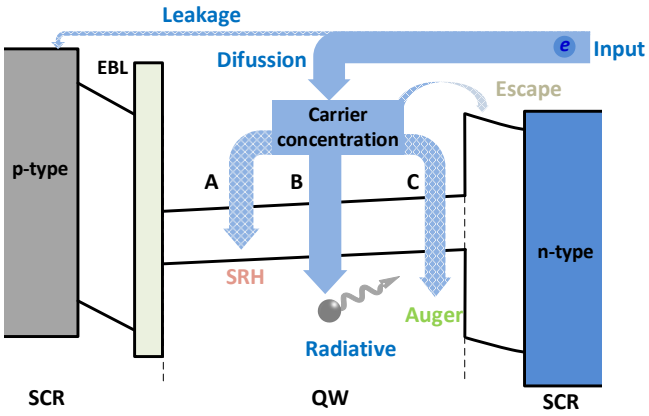

Figure 2.2: Carrier transport by energy band in LED. EBL: Electron Blocking Layer.

in [89]. To account for the nonlinear operation, a separate memoryless non-linear function was used by in [46]. However, the work in [40], discussed that the LED operation can not be modeled by a linear low-pass filter followed by a non-linear operation.

In this section we briefly review the LED physics and discuss the important phenomenon laying behind the relation between the input current to the LED and the carrier concentration in the QW and the output optical power.

2.3.1 Carrier Recombination Rate in QW

As shown in Fig. 2.1, charge carriers, i.e., electrons and holes injected into the LED junction, initially arrive at the SCR, and then diffuse into the QW. Carrier storage, transport and recombination mechanisms [90] are depicted in Fig. 2.2. These affect the bandwidth and the nonlinear distortion of the light output. The rate at which the carrier concentration N_c in the QW changes depends on the provided rate of the carriers by the input current I_{in} minus the rate of the hole-electron recombinations:

$$\frac{dN_c}{dt} = \frac{I_{in}}{qA_w t_w} - R_{rec} \tag{2.1}$$

Where A_w and t_w are the QW area and thickness, q is the unit electron charge and R_{rec} is the recombination rate of hole-electrons. As we know from the ABC-model [33, 52, 53, 67–70], the carrier recombination can occur either as radiative recombination with rate $R_{r,rec}$ or as the non-radiative recombination of $R_{nr,rec}$. Thus, the rate equation for carrier recombination in the LED can be expressed as

$$
\begin{aligned}
R_{rec} &= R_{r,rec} + R_{nr,rec} \\
R_{r,rec} &= B(p_0 N_c + N_c^2) \\
R_{nr,rec} &= AN_c + CN_c^3
\end{aligned} \tag{2.2}
$$

where A, B and C are Shockley-Read-Hall (SRH), radiative and Auger recombination coefficients, and p_0 is the active region doping concentration, respectively. Some LEDs have significant doping levels of the active region and $p_0 > 0$, yet most illumination LEDs have $p_0 = 0$.

Note that the recombination rate, given in (2.2), is valid for a p-doped active layer with $p_0 \gg n_0$ and $N_c \gg n_0$ where n_0 is intrinsic carrier concentration. For LEDs with n-doped active layer, a similar relation can be derived. A model for an LED with an intrinsic active region can be easily found from (2.2) by nullification of p_0.

The output luminescence intensity of the LED is proportional to the radiative recombination rate $R_{r,rec}(t)$ in (2.2). Thus, the optical output power is calculated as

$$
S_o(t) = \langle E_p \rangle A_w t_w B[p_0 N_c(t) + N_c^2(t)], \tag{2.3}
$$

where $\langle E_p \rangle$ is the average photon energy. The relation between $N_c(t)$ and the input current $I_{in}(t)$ is given in (2.1). From (2.1) and (2.3), the LED output power $S_o(t)$ is a nonlinear function of the input current $I_{in}(t)$.

2.3.2 QW Nonlinear Photon Emission Model

Inserting (2.2) into (2.1), the time-domain transient (dynamic) memory behavior of LED is expressed as

$$
\frac{dN_c(t)}{dt} = \frac{I_{in}(t)}{qt_w A_w} - (Bp_0 + A)\, N_c(t) - BN_c^2(t) - CN_c^3(t), \tag{2.4}
$$

This model is particularly suited to study the LED behavior in response to PAM-like signals. To have a discrete time representation, suitable for signal processing, (2.4) can be converted into discrete time n, sampling at T_s; $N_c[n+1]$, corresponding to $N_c(t)$ at $t = (n+1)T_s$ can be adaptively described by the previous states, as

$$
N_c[n+1] = \frac{T_s I_{in}[n]}{qt_w A_w} + [1 - (Bp_0 + A)\, T_s]\, N_c[n] - BT_s N_c^2[n] - CT_s N_c^3[n] \tag{2.5}
$$

where T_s is the sampling period. Note that this numerical model can approximate the LED rate equation in (2.4) accurately when T_s is sufficiently small. The output optical power in discrete domain is

$$
S_o[n] = \langle E_p \rangle A_w t_w B[p_0 N_c[n] + N_c^2[n]] \tag{2.6}
$$

2.3.3 QW Response to Step Function

Finding a general closed–form solution to (2.4) to express the carrier concentration for an arbitrary input signal can be cumbersome (even if a closed–form solution exists), particularly if $C > 0$. In fact typically, Auger recombination, via C compose about 10-20% on emitting recombinations.

In fact, [33] derived a closed–form analytical solution for a special case of $A = C = 0$ and for the step function input current to the LED. Such analysis are relevant for instance for OOK or PAM signaling without pulse shaping. In this chapter, we extend the solution to account for the non-zero A and for PAM signaling. A solution for non-zero C can be found by numerical solution of the differential equation.

For the PAM signaling with rectangular pulse shapes, the input current has K equidistant DC levels $I_k, k \in \{0, 1, ..., K-1\}$, $I_0 = 0$ and $I_{k+1} > I_k$. The input signal I_{in} in (2.4) toggles between these K levels with a pulse width T_{Sym}. Let us assume that at $t = (t_0 - \epsilon)$ the LED current was at I'_k (for any arbitrary $k' \in \{0, 1, ..., K-1\}$), shown in Fig. 2.3(a). The carrier concentration at this time moment is assumed to be $N_{c,k'}$. At $t = t_0$ the current level changes to I_k for $k \in \{0, 1, ..., K-1\}$ and for two equal successive symbols $k = k'$.

The time domain closed form equation for the carrier concentration can be obtained by solving the first order non-linear equation (2.4). For $C = 0$, the differential equation is simplified into a Riccati differential equation [91]. In general, we can use separation of variable to solve this differential equation given that I_{in} is a constant PAM level, $I_{in} = I_k$,

$$\int \frac{dN_c}{CN_c^3 + BN_c^2 + (A + p_0 B) N_c - \frac{I_k}{qt_w A_w}} = -\int dt. \tag{2.7}$$

Next, we need to find the roots of the denominator, then,

$$CN_c^3 + BN_c^2 + (A + p_0 B) N_c - \frac{I_k}{qt_w A_w} = 0. \tag{2.8}$$

For $C = 0$,

$$BN_c^2 + (A + p_0 B) N_c - \frac{I_k}{qt_w A_w} = 0$$

$$\rightarrow N_{1,2} = \frac{-(A + p_0 B) \pm \sqrt{(A + p_0 B)^2 - \frac{4BI_k}{qt_w A_w}}}{2B} = \frac{-(A + p_0 B) \pm \omega}{2B}.$$

where ω depends on the current level I_k in the next symbol k, namely

$$\omega = \sqrt{(Bp_0 + A)^2 + \frac{4BI_k}{qt_w A_w}} \tag{2.9}$$

and Equation (2.7) can then be written as

$$\int \frac{dN_c}{B\left(N_c - N_1\right)\left(N_c - N_2\right)} = -\int dt,$$

$$\rightarrow \frac{1}{B\left(N_1 - N_2\right)} \int \left(\frac{1}{N_c - N_1} - \frac{1}{N_c - N_2}\right) dN_c = -\int dt,$$

$$\rightarrow \frac{1}{\omega} \ln\left(\frac{N_c - N_1}{N_c - N_2}\right) = -t + r, \tag{2.10}$$

where r is a constant. Then,

$$\frac{N_c - N_1}{N_c - N_2} = Re^{-\omega t} \rightarrow N_c = \frac{N_1 - Re^{-\omega t} N_2}{1 - Re^{-\omega t}}, \tag{2.11}$$

where $R = e^{\omega r}$. Replacing N_1 and N_2,

$$N_c = \frac{1}{2B} \frac{\left[-\left(A + p_0 B\right) + \omega\right] - Re^{-\omega t}\left[-\left(A + p_0 B\right) - \omega\right]}{1 - Re^{-\omega t}} = \frac{-\left(A + p_0 B\right)}{2B} - \frac{\omega}{2B} \frac{1 + Re^{-\omega t}}{1 - Re^{-\omega t}}, \tag{2.12}$$

Writing $R = e^{\omega r}$,

$$N_c = -\left(\frac{p_0}{2} + \frac{A}{2B}\right) + \frac{\omega}{2B} \frac{e^{-\omega t + r} + 1}{e^{-\omega t + r} - 1} = -\left(\frac{p_0}{2} + \frac{A}{2B}\right) + \frac{\omega}{2B} \tanh\left(\frac{-\omega t}{2} + \frac{r}{2}\right). \tag{2.13}$$

We called $r/2 = \theta_k^{'}$ and our reference time is t_0, then,

$$N_c\left(t > t_0\right) = -\left(\frac{p_0}{2} + \frac{A}{2B}\right) + \frac{\omega}{2B} \tanh\left(\frac{-\omega\left(t - t_0\right)}{2} + \theta_k^{'}\right) \tag{2.14}$$

$\theta_k^{'}$ depends on the initial condition at t_0, $N_c(t_0) = N_{c,k'}$. For $t < t_0$, the PAM current level was $I_k^{'}$ which resulted in $N_{c,k'}$. Having the carrier concentration, the output optical power can be readily obtained from (2.3).

We consider two different cases, low (large T_{Sym} compared to LED time constant) and high (small T_{Sym} compared to LED time constant) bandwidth inputs $I_{in}(t)$. These two cases are illustrated in Fig. 2.3(a). For the low bandwidth input current, $N_c(t)$ (as well as the output power) is able to settle to its final value (steady state response), $N_{c,k}$, obtained by solving the equation (2.4) for $I_{in} = I_k$ and $dN_c(t)/dt = 0$. Also, the initial condition $N_c(t = t_0) = N_{c,k'}$ can be obtained by solving the equation (2.4) for $I_{in} = I_k'$ and $dN_c(t)/dt = 0$. For two equal successive symbols, the output power (for $t \in (t_0 + 3T_{Sym}, t_0 + 4T_{Sym})$) is already at the steady state and there is no transient response.

For the high bandwidth input current, $N_c(t)$ (as well as the output power) at $t = t_0$ has not yet settled to its final value, the LED input current $I_{in}(t)$ toggles to a new value. In this case the carrier concentration $N_c(t)$ for the symbol $I_{in}(t) = I_k$ and

$t_0 \geq t < t_0 + T_{Sum}$ depends on $N_c(t = t_0)$. For ($\geq$) two equal successive symbols, the LED has more time to catch with the steady state.

Consider a hypothetical LED with the parameters given in Table 2.1. For our theoretical plots in this section we assume that $C = 0$. The case $C \neq 0$ can be captured in simulations, nevertheless, the conclusions remain intact. We consider two inputs, an OOK current with amplitude levels $I_0 = 0$ and $I_1 = 0.3$A and a 4 level PAM signal with levels $I_0 = 0$, $I_1 = 0.1$A, $I_2 = 0.2$A and $I_3 = 0.3$A and the symbol duration is $T_{Sym} = 0.2$us.

Fig. 2.3(b) shows the two levels of the (normalized) input current and the output optical power versus time. It can be seen that the output optical power is much slower than the input current, showing a limited frequency bandwidth for the LED, and the rise time for the output power is smaller than the fall time. This non-equal rise and fall time is due to the non-linear operation of the LED. For $I_{in}(t) = I_1 = 0.3$A, the number of the carriers in the QW increases and as a result LED response is enhanced.

The eye-diagram of the output optical power for the 4 level (PAM) input current is shown in Fig. 2.3(c). Different eye openings can be distinguished at different PAM levels. The eye is wider at higher levels due to increased carriers in the QW which results in a faster LED response. For the non-zero parameter $C = 10^{-28}$, the corresponding eye-diagram is shown in Fig. 2.3(d). For this plot we used the discrete time LED equations (2.5) and (2.6) in a numerical solver. A non-zero C reduces both the rising and falling time, affecting the rise time more, resulting in a wider eye. Also, it affects the (PAM) levels of the output optical power; higher levels are closer.

The parameter ω, given in (2.9), determines the LED time constant; larger ω (due to a larger A, B, p_0 and I_k or smaller t_w and A_w) results in a faster LED. The eye-diagram for the LED parameters in Table 2.1 and for $t_w = 2\times10^{-4}$ cm and $C = 10^{-28}$ is shown in Fig. 2.3(e), showing a slower response compared to that shown in Fig. 2.3(d) (for $t_w = 5 \times 10^{-5}$ cm). Finally, a comparison with real measured data shows that this model can describe typical properties of the PAM eye-diagram, experienced by typical LEDs. Fig. 2.3(f) shows the eye diagrams of the PAM-4 modulating signal for 5 Msym/s. It can be seen that due to the nonlinearity, the eye closing is more pronounced for low signal levels.

This section showed that the LED non-linearity can cause different rise and fall times at different signal levels and different eye openings. If Nyquist pulse shaping is used, the non-linearity causes a signal-level dependent right-skew that compromises a well-defined optimum sampling moment.

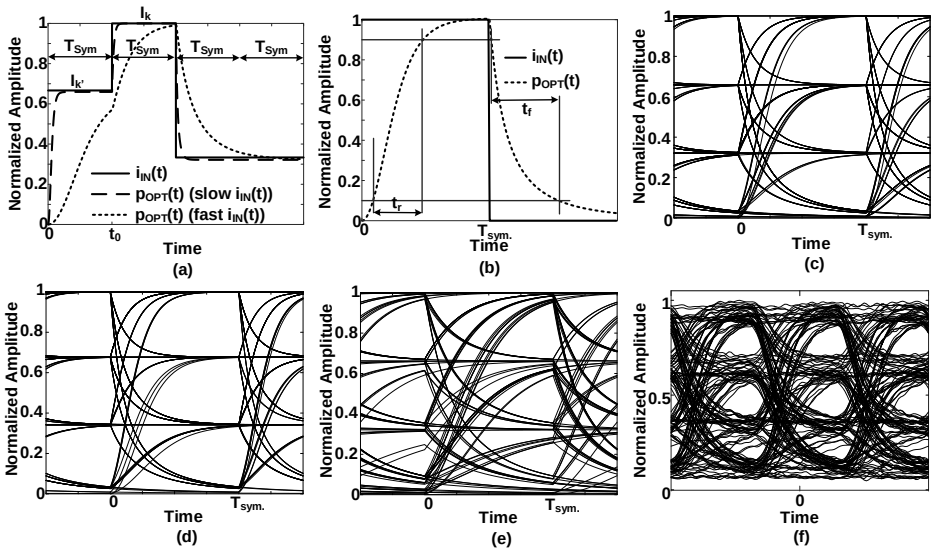

Figure 2.3: (a) Qualitative normalized LED output power for two cases; slow and fast input current compared to the LED time constant. (b) LED output power using a square waveform of 5 MHz at the input. Rise and fall times of the LED are different. Eye-diagram for a 4-PAM input current with symbol rate 5 MSym/s, based on differential equation (2.4), (c) for LED parameters given in Table 2.1, (d) for $C = 10^{-28}$ and (e) for $t_w = 2 \times 10^{-4}$ cm and $C = 10^{-28}$. (f) Measured 4-PAM eye diagram at symbol rate of 5 MSym/s and 30 dB SNR.

Table 2.1: Hypothetical LED parameters

Parameter	Interpretation	Value
q	Charge of Electron	1.6×10^{-19} C
A	SRH recombination coefficient	$1 \times 10^{6}\ s^{-1}$
B	Radiative recombination coefficient	$1 \times 10^{-10}\ s^{-1}cm^{3}$
C	Auger recombination coefficient	$0\ s^{-1}cm^{6}$
t_w	Active layer thickness	5×10^{-5}cm
A_w	Active layer area	0.01cm^2
p_0	Doping concentration	0 No./cm^3
E_p	Energy of photon	4.31×10^{-19}J
T_s	Sampling period in simulation	1ns

2.4 Linearized Small Signal QW Model

The LED current is composed of a DC current I_{in} and AC fluctuations i_{in}, i.e. $I_{in} = \mathrm{I}_{in} + i_{in}$. For a small modulation index, $\max\{i_{in}/\mathrm{I}_{in}\} \ll 1$, we can linearize (2.3) and (2.4) and get

$$\frac{dn_c(t)}{dt} = \frac{i_{in}(t)}{qt_w A_w} - \left(A + p_0 B + 2B\mathrm{N}_c + 3C\mathrm{N}_c^2\right) n(t) \tag{2.15}$$

$$s_o(t) = \langle E_p \rangle A_w t_w B \left(p_0 + 2\mathrm{N}_c\right) n_c(t) \tag{2.16}$$

where N_c is the DC component of N_c depending on LED properties and DC level of input current.

Doing a Fourier Transform, $n_c <-> X_N(f)$, $i_{in} <-> X_I(f)$ and $s_o <-> X_S(f)$, gives

$$\frac{X_I(f)}{qt_w A_w} = \left[j2\pi f + \left(A + Bp_0 + 2B\mathrm{N} + 3C\mathrm{N}^2\right)\right] X_N(f) \tag{2.17}$$

$$X_S(f) = \langle E_p \rangle A_w t_w B[(p_0 + 2\mathrm{N}_c)\, X_N(f) \tag{2.18}$$

The frequency domain channel model, in this case assuming injection current as the input and LED optical power as the output, becomes

$$H(f) = \frac{X_S(f)}{X_I(f)} = \frac{\langle E_p \rangle A_w t_w B[(p_0 + 2\mathrm{N}_c)}{2\pi f_{3dB}} \cdot \frac{1}{1 + j\frac{f}{f_{3dB}}} \tag{2.19}$$

where the LED functions as a linear first-order low-pass filter with 3 dB cut-off frequency of

$$f_{3dB} = \frac{1}{2\pi}\left(A + p_0 B + 2B\mathrm{N}_c + 3C\mathrm{N}_c^2\right). \tag{2.20}$$

For the case $C = 0$, in chapter 5, we derive that

$$\mathrm{N}_c(C=0) = \frac{-(A + p_0 B) + \sqrt{(A + p_0 B)^2 + 4\frac{B\mathrm{I}_{in}}{qA_w t_w}}}{2B} \tag{2.21}$$

hence

$$\omega_{3dB}(C=0) = 2\pi f_{3dB} = \sqrt{(A + p_0 B)^2 + 4\frac{B\mathrm{I}_{in}}{qA_w t_w}} \tag{2.22}$$

Interestingly, the 3dB cut-off frequency of the LED for small signal excitation depends on the parameter ω in (2.9) by the scaling factor 2π. It can be concluded that for small signal excitations, the LED exhibits a first order low-pass frequency response with a 3 dB bandwidth which is an increasing function of input DC current.

2.4.1 Exponential Frequency Response Model

Although the low-pass model described above has been confirmed by many experiments, also alternative models have been proposed. A commonly referred front-end channel model is the exponential decay [26, 58],

$$|H(f)|^2 = H_0^2 2^{-\frac{f}{f_0}}, \tag{2.23}$$

where f_0 is the 3 dB cut-off frequency, and H_0 is the low frequency channel gain that also includes effects such as distance, angle and beam width. It is known from the theory of RLC networks that a network with a finite number of elements always give a finite number of 3 dB cross-over points that connect sections with a slope that is an integer multiple of 6 dB per octave, thus straight lines on a log-log Bode diagram. Yet, a behavior as in (2.23) is a straight line on a log-lin plot.

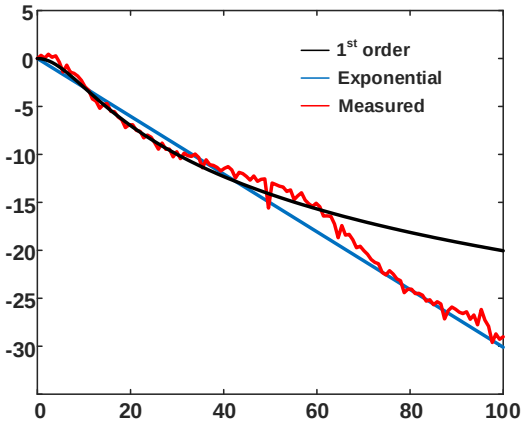

Figure 2.4: Exponential (blue), 1^{st}–order (black) and experimental channel response (red). For the experimental channel model, a Luxeon Rebel LXML-PB02-0023 blue LED was biased at 350 mA. The 3 dB bandwidth for all three cases is 10 MHz.

Fig. 2.4 compares the exponential channel model described in (2.23) for f_0 =10 MHz (blue) to the 1^{st}–order channel model with the same 3 dB bandwidth and to experimental channel model using a Luxeon Rebel LXML-PB02-0023 blue LED biased at 350 mA of DC current. It can be observed that up to 40 - 50 MHz, the 1^{st}–order channel model can very well describe the experimental LED channel while above 60 MHz the deviation from the experimental model is considerable. The effects of wiring start to play a role. For the frequency range above 60 MHz, the limited bandwidth of APD and TIA and furthermore, second–order effects inside the space charge region

of the LEDs [89] cause the experimental response decay faster compared to 1^{st}–order model.

The exponential model of (2.23) is a better fit to the experimental channel response in a wide frequency range of 0 - 100 MHz. Some deviations occur around 20 MHz and 60 MHz, but overall it can closely predict the channel response. In fact with the exponential model, we do not limit our channel model to the LED response when the modulation bandwidth can easily extend to the range that other mechanisms such as APD/TIA frequency response play roll.

2.5 Phosphor Coating

In illumination, LEDs are used in two ways, namely as Phosphor Coated LEDs (PC-LEDs) and as the Red-Green-Blue LEDs (RGB-LEDs). To produce white light, the PC-LED utilizes a blue emitter in combination with a yellowish phosphor while the RGB-LED combines three LED chips that emits white lights. While the RGB LEDs follow the ABC model, the phosphor coating further limits the modulation bandwidth to only a few MHz [26, 28, 29, 31]. In this section, the impulse response of a PC-LED as a function of time and wavelength is studied for the first time and the effect of optical filtering in presence of the background light is discussed. More generally, we see is as a communication channel with photonic conversion.

The transmitted signal in the form of the current offered to a blue LED is described in the electrical domain by $I_{in}(t)$ and by its Fourier transform $I_{in}(f)$. We describe the optical signal intensity (blue output light) by $S_o(\lambda, t)$ such that $S_o(\lambda, t)d\lambda dt$ (with unit w/m^2) amounts to the optical energy per unit area in a two dimensional interval $(\lambda, \lambda + d\lambda)$ and $(t, t + dt)$. Transforming time axis into frequency axis gives $S_o(f, \lambda)$, so we use the term *frequency* for the frequency contributions in the modulated data signal and we explicitly call the *photon* frequency $f_\phi = \frac{c}{\lambda}$ where, c is the speed of the light.

2.5.1 Media with Photonic Conversion

Photon (or wavelength) conversion is used in e.g. white LEDs where a fraction of the blue light is converted to yellow and the white light is the combination of those two [92]. Let's assume that the emitted blue light, after passing through a medium with photonic conversion is denoted as $S_{o,c}(\lambda, t)$, i.e. $S_{o,c}(\lambda, t) = \mathbb{H}(S_o(\lambda, t))$. We define a linear photon-converting medium as one in which, if

$$\begin{aligned} \mathbb{H}(S_{o,1}(\lambda, t)) &= S_{o,c,1}(\lambda, t) \\ \mathbb{H}(S_{o,2}(\lambda, t)) &= S_{o,c,2}(\lambda, t) \end{aligned} \tag{2.24}$$

then for any arbitrary constants a and b, we have

$$\mathbb{H}\left(aS_{o,1}(\lambda,t)+bS_{o,2}(\lambda,t)\right)=aS_{o,c,1}(\lambda,t)+bS_{o,c,2}(\lambda,t)$$

We further assume that the medium is time-invariant but due to λ-conversion it can be wavelength-variant. For such a linear medium, we can define a single wavelength impulse response $h(\lambda,\lambda_x,t)$ which is the response to an input signal of the form of the two-dimensional delta function $\delta(\lambda-\lambda_x,t)$. The latter function being defined as a function that realizes the following sampling and shifting property

$$\int_t\int_\lambda f(\lambda,t)\delta(\lambda-\lambda_x,t-t_x)d\lambda dt=f(\lambda_x,t_x) \tag{2.25}$$

Then, for any input $S_o(\lambda,t)$, we have

$$S_{o,c}(\lambda,t)=\mathbb{H}\left(\int_{\lambda_x}\int_{t_x}S_o(\lambda_x,t_x)\delta(\lambda-\lambda_x,t-t_x)d\lambda_x dt_x\right) \tag{2.26}$$

$$=\int_{\lambda_x}\int_{t_x}S_o(\lambda_x,t_x)\mathbb{H}\left(\delta(\lambda-\lambda_x,t-t_x)\right)d\lambda_x dt_x \tag{2.27}$$

$$=\int_{\lambda_x}\int_{t_x}S_o(\lambda_x,t_x)h\left(\lambda,\lambda_x,t-t_x\right)d\lambda_x dt_x \tag{2.28}$$

where, in transition from (2.26) to (2.27) we used the linear property of the medium described by (2.24) and in transition from (2.27) to (2.28) we used the time invariant property of the medium and the definition of the single wavelength impulse response. Eq. (2.28) can be considered as the two-dimensional convolution integral.

Energy of a photon is proportional to the inverse of its wavelength; $E_\lambda=\frac{h_p c}{\lambda}$ where E_λ is photon energy with wavelength λ, h_p is the Planck constant and c is the speed of light in vacuum. Therefore, an inherent loss is associated with the wavelength conversion when converting a photon with wavelength λ_x to a photon with wavelength λ ($\lambda>\lambda_x$). This phenomena is called quantun difict or Stokes shift [92].

Some materials such as quantum-splitting phosphors [93] absorb a short-wavelength photon with wavelength λ_x and re-emmit two longer-wavelength photons with wavelength λ_1 and λ_2 such that (ideally) $E_{\lambda_x}=E_{\lambda_1}+E_{\lambda_2}$. However, there is always some energy that is dissipated to excite the molecules and to re-emit the photons. Then, the loss in photon conversion implies that for any λ_x, we have

$$\int_\lambda\int_t h\left(\lambda,\lambda_x,t\right)d\lambda dt\leq 1 \tag{2.29}$$

2.5.2 Typical Phosphor as the λ-Converting Media

The state of a phosphor layer can be described by the density of the molecules $m(t)$ that are in excitation state. The optical intensity of the re-emitted yellow photons is

proportional to $m(t)$, i.e. $\int_\lambda S_{o,c}(\lambda,t) \propto m(t)$. The dynamic of the molecules density ($\frac{dm(t)}{dt}$) can be written as

$$\frac{dm(t)}{dt} \propto \int_\lambda \frac{S_{o,c}(\lambda,t)}{dt} d\lambda \propto \int_\lambda w(\lambda) S_o(\lambda,t) d\lambda - \int_\lambda S_o(\lambda,t) d\lambda \tag{2.30}$$

where the first and the second terms at the right hand side of (2.30) describes the flow of the incoming (blue) photons respectively, re-emitted (yellow) photons and the weight factor $0 \leq w(\lambda) \leq 1$ is the probability that a photon with wavelength λ excites the molecules.

Assuming τ_Y as the time constant of the phosphor layer and applying Fourier (Laplace) transform, (2.30) can be written as

$$\int_\lambda \psi(\lambda,t) d\lambda = \int_\lambda w(\lambda) \left(\int_{t_x} \phi(\lambda,t_x) e^{-\frac{t-t_x}{\tau_Y}} dt_x \right) d\lambda \tag{2.31}$$

Similar to [94], for a hypothetical monochromatic phosphor layer assume that the single wavelength impulse response can be written as

$$h(\lambda,\lambda_x,t) = h_Y(t) f_Y(\lambda,\lambda_x). \tag{2.32}$$

Using (2.31) for $S_o(\lambda,t) = \delta(\lambda-\lambda_x,t)$, we have

$$h_Y(t) = e^{-\frac{t}{\tau_Y}} \tag{2.33}$$

$$\int_\lambda f_Y(\lambda,\lambda_x) d\lambda = w(\lambda_x). \tag{2.34}$$

According to the impulse response, phosphor as a media conversion acts as a first order low–pass filter.

2.5.3 Visible Light Communication (VLC) Channel Through Media with Photonic Conversion

In this section we discuss the channel model that is developed to include the the effect of the blue filtering, APD responsivity and signal-dependent shot noise in the optical wireless communication systems. Consider a VLC link where an LED is used as the transmitter and an APD detects the received signal from the LED. At the transmitter side, an electrical current $I_{in}(t)$ derives the blue-emitting junction that generate blue photons. A fraction of the blue photons (α) is converted to yellow due to the phosphorescent layer while the fraction $1-\alpha$ passes through the layer without being affected. The combination of these blue and yellow photons creates the white light.

For the blue-emitting junction let's assume that

$$S_o(\lambda,t) = (I_{in}(t) \otimes h_B(t))\, L_B(\lambda) \tag{2.35}$$

where $h_B(t)$ is the optical output power of the junction for an input impulse current, $L_B(\lambda)$ describes the spectrum emission in λ domain and $\otimes$ stands for the convolution operation. For a blue-emitting junction with instantaneous action ($h_B(t) \propto \delta(t)$), from (2.35) the output optical intensity of the blue photons, $S_o(\lambda, t)$, can be written as

$$S_o(t, \lambda) \propto (I_{in}(t) \otimes \delta(t))\, L_B(\lambda) = I_{in}(t) L_B(\lambda) \tag{2.36}$$

Phosphor layer converts a fraction of the blue photons to yellow. Therefore, from (2.28), the output optical intensity of the yellow photons can be written as

$$S_{o,c}(t, \lambda) \propto \int_{\lambda_x} \int_{t_x} \alpha I_{in}(t_x) L_B(\lambda_x) h\left(\lambda, \lambda_x, t - t_x\right) d\lambda_x dt_x \tag{2.37}$$

For the hypothetical phosphor with single wavelength impulse response given in (2.32), (2.37) can be simplified to

$$S_{o,c}(t, \lambda) \propto \int_{t_x} \alpha I_{in}(t_x) h_Y(t - t_x) dt_x \int_{\lambda_x} L_B(\lambda_x) f_Y(\lambda, \lambda_x) d\lambda_x = \alpha \left(I_{in}(t) \otimes h_Y(t)\right) L_Y(\lambda) \tag{2.38}$$

where $L_Y(\lambda) = \int_{\lambda_x} L_B(\lambda_x) f_Y(\lambda, \lambda_x) d\lambda_x$ is the output spectrum emission of the yellow light. The total output optical intensity of the white light is the combination of the blue and the yellow optical intensities as

$$S_{o,w}(\lambda, t) \propto (1-\alpha) S_o(\lambda, t) + \alpha S_{o,c}(\lambda, t) = (1-\alpha) I_{in}(t) L_B(\lambda) + \alpha \left(I_{in}(t) \otimes h_Y(t)\right) L_Y(\lambda) \tag{2.39}$$

where $S_{o,w}$ is the output optical intensity of white light. The parameters $L_B(\lambda)$ and $L_Y(\lambda)$ for a typical commercial LED is shown in Fig. 2.5 and the normalized $S_{o,w}(\lambda, t)$ for an input impulse current is shown in Fig. 2.5 (similar impulse response plots for a different application can be found in [94]).

At the receiver, due to the loss of the free space, only a fraction of the transmitted white light is received as $S_{r,w}(\lambda, t) = h_{fs} S_{o,w}(\lambda, t)$ where h_{fs} is the free space loss factor,

$$I_r(t) = \int_{\lambda} S_{r,w}(\lambda, t) F(\lambda) R(\lambda) d\lambda \tag{2.40}$$

where $I_r(t)$ is the APD output (current), $R(\lambda)$ is the APD responsivity, $F(\lambda)$ is the gain of the (optional) optical (blue) filter prior to the APD.

Using (2.39), the detected signal by the APD, can be written as

$$I_r(t) = \int_{\lambda} S_{r,w}(\lambda, t) F(\lambda) R(\lambda) d\lambda \propto h_{fs} G_B (1 - \alpha) I_{in}(t) + h_{fs} G_Y \alpha (I_{in}(t) * h_Y(t)) \tag{2.41}$$

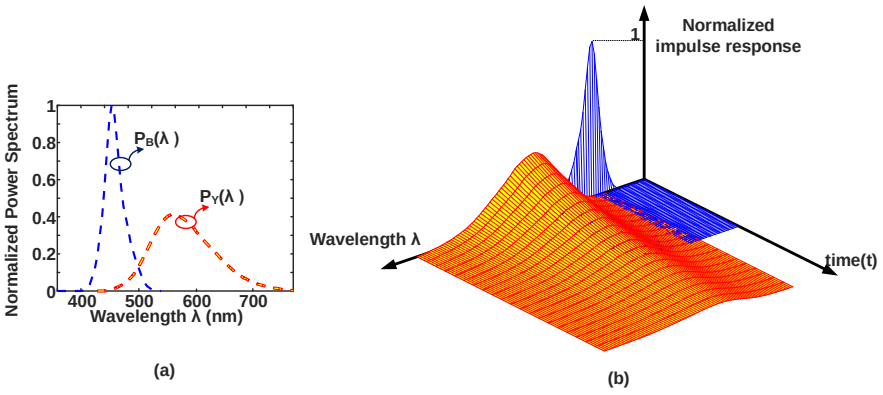

Figure 2.5: (a) typical output spectrum emission of the blue and the yellow light and (b) normalized two-dimensional output optical intensity for an input impulse current.

,

$$G_Y = \int_\lambda L_Y(\lambda)F(\lambda)R(\lambda)d\lambda \tag{2.42}$$

$$G_B = \int_\lambda L_B(\lambda)F(\lambda)R(\lambda)d\lambda \tag{2.43}$$

where G_Y and G_B are the average gain of the optical (blue) filter in combination with the APD for the yellow and blue lights, respectively.

The frequency domain transfer function is calculated using Fourier transform,

$$H(f) = \frac{I_r(f)}{I_{in}(f)} \propto h_{fs}\left(G_B(1-\alpha) + \frac{\alpha G_Y}{j2\pi f\tau_Y + 1}\right). \tag{2.44}$$

The transfer function can be written in a standard format as,

$$H(f) = H_0 \frac{1 + j\frac{f}{f_{z,ph}}}{1 + j\frac{f}{f_{3dB,ph}}}, \tag{2.45}$$

where H_0 is the transfer function at DC, $f_{z,ph}$ and $f_{3dB,ph}$ are the zero and pole (3 dB bandwidth) of the transfer function and are equal to,

$$f_{z,ph} = \frac{1}{2\pi\tau_Y}\frac{G_B(1-\alpha) + \alpha G_Y}{G_B(1-\alpha)}, \tag{2.46}$$

$$f_{3dB,ph} = \frac{1}{2\pi\tau_Y}, \tag{2.47}$$

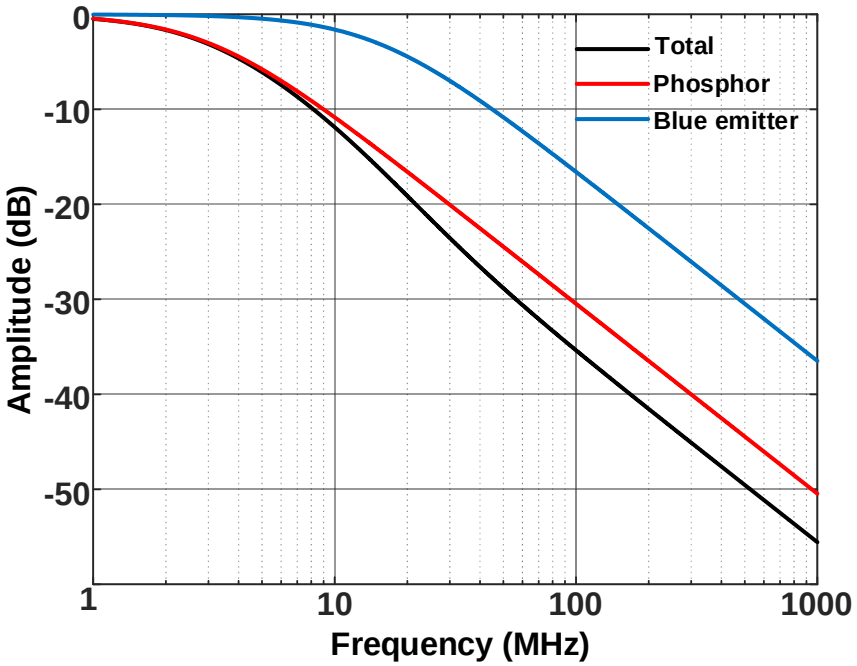

Figure 2.6: (a) Normalized frequency response example for a blue emitter with $f_{3dB,b} = 15$ MHz (blue), phosphor coating with $f_{3dB,ph} = 3$ MHz (red) and warm white LED with $\alpha = 0.8$ and APD responsivity ratio of $G_B/G_Y = 0.5$.

respectively. The transfer function of (2.45) does not include the low-pass behavior of blue emitter that follows ABC model. To find the total frequency response including the blue emitter frequency response, we can simply write,

$$H(f) = H_0 \frac{1 + j\frac{f}{f_{z,ph}}}{1 + j\frac{f}{f_{3dB,ph}}} \cdot \frac{1}{1 + j\frac{f}{f_{3dB,b}}}, \tag{2.48}$$

where $f_{3dB,b}$ is the 3 dB bandwidth of the blue emitter calculated in (2.20); the subscript $_b$ was added to distinguish blue emitter 3 dB bandwidth from that for phosphor. Fig. 2.6 depicts an example of the channel for the case of $f_{3dB,ph} = 3$ MHz, $f_{3dB,b} = 15$ MHz, $\alpha = 0.8$ (warm white) and $G_B = 0.5G_Y$ [87]. With $f_{3dB,ph} < f_{3dB,b}$, the 3 dB bandwidth is dominated by the phosphor coating response and the black curve in Fig. 2.6 follows the red curve. For frequencies above 5 MHz, blue emitter further limits the frequency response and black curve deviates from red curve. At higher frequencies, the yellow photons re-emitted by the phosphor layer do not have a considerable energy and the frequency response is dominated by the blue photons, for $f > f_{z,ph} = 27$ MHz.

For Pulse Amplitude Modulation (PAM), typically, a blue filter is used to filter out the slow portion of the white light, that is yellow photon flow [10]. This is equivalent to force $G_Y = 0$ in (2.46) which results in $f_{z,ph} = f_{3dB,ph}$ hence the total frequency response (2.48) reduces to blue emitter frequency response but at the cost of reduced signal strength. Other techniques such as equalizers are used to further boost the 3 dB bandwidth [26,35,36]. Note that a flat frequency response is necessary for ISI-free communication of PAM signals.

Formularization of the frequency response can be used to design pre- or post equalizers such as the work in [101] which has only used experimental frequency response for the design of the equalizer without providing any theoretical background. Furthermore, the provided channel model (2.48) can be used to calculate the SNR for PAM at various speeds with or without the optical blue filter.

2.5.4 Noise

The noise sources of a wireless optical link are the major factors in determining the performance [95]. Determination of noise sources in the input of communication link is critical since the incoming signal has the least power at this point.

Thermal noise due to resistive elements in the pre-amplifier is major source of noise which modeled as as being white, signal independent and having a Gaussian distribution ($n_{th} \sim N(0, \sigma_{th}^2)$) [10].

$$\sigma_{th}^2 = \frac{4k_bT}{R_L}BW \tag{2.49}$$

where k_b, T , R_L, and B are Boltzman constant, absolute temperature, load resistance, and the equivalent noise bandwidth of the system respectively [10].

At the receiver, signal level dependent shot noise is also present which is coming from the Poisson nature of the arrived photo-electrons. This noise source is modeled by the Poisson distribution with the (Poisson) parameter proportional to the input signal intensity. For Poisson distribution, the fluctuations (noise variance) around the mean value is proportional to the Poisson parameter. That makes the variance of the shot noise to be dependent on the received signal intensity. The shot noise is due to both the ambient light (shown by ξ) and the transmitted signal [95]. Intensity shot noise approaches a Gaussian distribution at high intensities [96–98]. Since the noise power due to the pre-amplifier (thermal noise), and due to shot noise, is uncorrelated, the total noise is

$$n(t) = n_{th}(t) + n_{shot}(t). \tag{2.50}$$

For our study in this thesis, we assume that the total noise $n(t)$ is a random i.i.d. Gaussian signal with noise power distributed over the modulation bandwidth.

2.5.5 Optical Filtering and OFDM

Previously published works in literature have different conclusions on the effectiveness of blue filters in systems employing OFDM. The work in [102] concludes that blue filters are not necessary and may even degrade the performance of the link. On the other hand, the work in [103] claims 40% improvement in link bit error rate when using blue filters. The different conclusions come from lack of proper modeling which is missing in the literature considering different aspects such as light nature, warm of cold, and ambient noise. Also the impact of the blue filter highly depends on whether appropriate signal processing is used, such as equalizers or OFDM with adaptive bitloading to separately optimize for each frequency bin.

Using (2.44), the frequency–dependent Signal–to–Noise Ratio (SNR) at the output of the detector is

$$\mathrm{SNR}(f) \propto \frac{|G_B(1-\alpha) + \frac{\alpha G_Y}{j2\pi f \tau_Y + 1}|^2 S(f)}{N_{th} + N_{shot}}, \tag{2.51}$$

where $S(f)$ is the power spectral density of input current to the LED, $\propto$ is the proportionality symbol and N_{th} and N_{shot} are the power spectral density of thermal and shot noise at the output of the detector, both having a flat spectrum over the modulation bandwidth. The spectral density of N_{shot} is depending on the background light and the received desired signal intensity.

When using a blue filter in front of photo detector at the receiver, the factor G_Y is negligible ($G_Y = 0$). Furthermore, the blue filter, filters only passes the blue component of desired signal as well as the background light reducing the noise PSD N_{shot}. Depending on the factor α and the receiver thermal noise floor N_{th}, the blue filter might improve or degrade the performance.

For an LED with cold output light (small yellow portion) in the presence of ambient noise, using blue filters is suggested. In this case, in (2.51) the coefficient α is small and attenuating the yellow portion of the light at the receiver, by having $G_Y = 0$, will not affect the numerator considerably. Looking at the denominator, the blue filter mitigates the shot noise coming from the yellow component of the background light and from the desired signal. At low frequencies, both the numerator and the denominator are attenuated and depending on the fraction α, the N_{th} and the background light, the SNR might increase or reduce. But at high frequencies, where the contribution of the yellow component to the SNR is already attenuated (due to the low frequency response of the phosphor), using blue filters, it is expected that SNR improves.

For warm LEDs, the blue portion is small and α is large. At low frequencies, the numerator of (2.51), in the presence of blue filters, will be attenuated considerably, reducing the SNR. The reduction could be more significant when the denominator in (2.51) is dominated by N_{th} (no background noise and low level of signal dependent

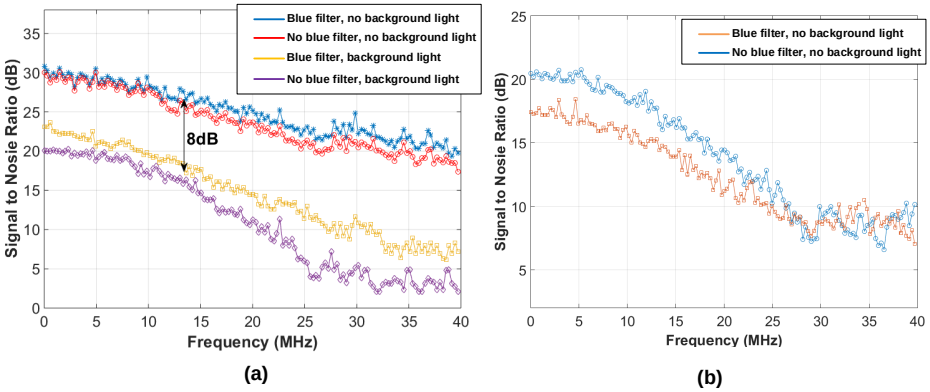

Figure 2.7: (a) SNR vs frequency for cool white (4100K) LEDs with and without blue filter, (b) SNR vs frequency for Warm white (2700K) LEDs with and without blue filter.

shot noise) while using blue filter attenuates the numerator. At high frequencies, the contribution of yellow photos to SNR reduces and filtering the shot noise can improve the SNR. The overall effect of blue filters, however, requires some information on the factor α, N_{th} and background light.

Fig. 2.7 shows the effect of blue filter on received SNR for various cases using experiments. We measured the SNR by directly modulating the LEDs with an OFDM-BPSK signal having 128 sub-carriers within a bandwidth of 40 MHz. We used both cool white and warm white LEDs (Philips luminaire) as a transmitter, and extract the SNR from the error vector magnitude of the received constellation. A dichroic blue filter is used to evaluate its effect on the SNR performance for both types of LEDs. A second neutral white illumination LED was used to add some background ambient light/noise.

For the case of cool white LED, blue filter improves the SNR, the improvement is more noticeable when the background noise is present, 2 - 5 dB. Adding the background noise attenuates the SNR considerably, around 8 dB with blue filter. When the background light is turned off, the improvement is minor and mainly at higher frequencies thanks to the filtering of some sun light which leaks to the measurement room as well as filtering signal dependent shot noise, which was expected according to our model.

For the case of a warm white LED (2700K), the SNR vs frequency with and without the blue filter is presented in Fig. 2.7(b). Since the warm white LED has a smaller blue component, the blue filter does not improve the SNR, in fact the SNR is degraded at low frequencies due to the filtering of the yellow component that mainly contribute to the SNR at low frequencies.

2.6 Throughput of First-Order Low-Pass LED Channel

The previous sections show that if a basic LED model is needed, a simple first order low-pass channel model may be used. The 3 dB frequency of this channel can be in the order or several MHz. To achieve high data rates, say, several hundreds of MHz with an LED with such a small bandwidth, OFDM modulation is normally employed. Yet, the need to optimize the data rate by adaptively assigning a specific power and also the number of bits on each sub-carrier of the OFDM modulation scheme depending on the channel properties is important.

In this section we use the 1^{st}–order model for the channel frequency response

$$|H(f)| = H_0 \left(1 + \frac{f^2}{f_0^2}\right)^{-\frac{1}{2}} \tag{2.52}$$

where H_0 is the DC channel gain and f_0 is the 3 dB cut-off frequency of the channel. The dominant noise is assumed to be additive white Gaussian noise (AWGN) which is independent from the transmitted signal [10].

Using the Shannon capacity expression under a constraint on the modulation power

$$\begin{aligned} &\max \tfrac{1}{2} \int_f \log\left(1 + S(f)\tfrac{|H(f)|^2}{N_0}\right) \\ &s.t. \int_f S(f)df \leq P_{mod} \end{aligned} \tag{2.53}$$

where N_0 (Watts/Hz) is the AWGN spectral density, $S(f)$ is the allocated power over the frequency f and P_{mod} is the total (available modulation) power to be distributed. Using the Lagrangian method, a general closed-form solution (known as waterfilling [62]) can be derived for the throughput [56, 99, 100]. The allocated power on each frequency f should adhere to

$$S(f) = \left[\upsilon - \frac{N_0}{|H(f)|^2}\right]^+ \tag{2.54}$$

In general, there is no guarantee that $H(f)$ is monotonic. Yet, for a low-pass LED channel (2.52), this is the case, so we can relate υ to a specific maximum frequency, where $S(f)$ in (2.54) is non-negative. In fact, for the given power budget P_{mod}, we calculated $f_{\max_w}$ [99] as the maximum (or optimum) frequency (or modulation bandwidth) which has nonzero power level, with

$$\gamma = \frac{2}{3}\left(\frac{f_{\max_w}}{f_0}\right)^3 \tag{2.55}$$

where the power budget parameter γ is the normalized power P_{mod} via the definition

$$\gamma = \frac{H_0^2 P_{mod}}{N_0 f_0} \tag{2.56}$$

The unique relation between the normalized maximum throughput R_w (for waterfilling) and the power budget γ is derived as [99]

$$\frac{R_w}{f_0} = 2\left(\frac{3}{2}\gamma\right)^{(1/3)} - 2\tan^{-1}\left(\left(\frac{3}{2}\gamma\right)^{(1/3)}\right) \tag{2.57}$$

The normalization strategy used in (2.55) and (2.57) makes the derivations generic hence not dependent on any specific LED channel properties.

The throughput, given in (2.57) and also denoted as the capacity of the first order low-pass channel, require the specific waterfilling power loading strategy, given in (2.54). In practice, complex algorithms such as Hughes-Hartogs [63] are used to implement a discretized version of the Lagrangian method to resemble waterfilling power loading strategy.

The simplest way to load the OFDM sub-carriers would be to load them all with the same power. Assuming $f_{\max_u}$ as the maximum frequency that is assigned with power, the power allocation is

$$S(f) = \frac{P_{tot}}{f_{\max_u}} \tag{2.58}$$

The normalized throughput for this power loading can be derived as [99]

$$\frac{R_u}{f_0} = \nu_{\max_u} \ln\left(\frac{1+\gamma+\nu^2}{1+\nu^2}\right) + 2\sqrt{1+\gamma}\tan^{-1}\left(\frac{\nu_{\max_u}}{\sqrt{1+\gamma}}\right) - 2\tan^{-1}(\nu_{\max_u}) \tag{2.59}$$

where $\nu_{\max_u} = f_{\max_u}/f_0$ is the normalized modulation bandwidth for the uniform power loading strategy. Using Leibniz rule, the $\nu_{\max_u}$ that optimizes the throughput can be obtained from $\frac{dR_u}{d\nu_{\max_u}} = 0$.

The throughput and the optimum modulation bandwidth for the two power loading strategies and as a function of the normalized power budget γ are compared in Fig. 2.8. It can be seen that both the algorithms achieve almost the same performance in terms of the throughput. Waterfilling is outperforming the simplest uniform power loading at best by less than 2%. As a conclusion, a much simpler bit and power loading algorithm (based on the uniform power loading) can be implemented with a small loss in the throughput. Furthermore, waterfilling demands more bandwidth (almost 25%). This makes the waterfilling to employ higher sampling frequency in the digital domain for the signal processing that compromises the throughput for the given power budget. In chapter 3 we will consider a more practical channel model and back up our derivations with experimental results.

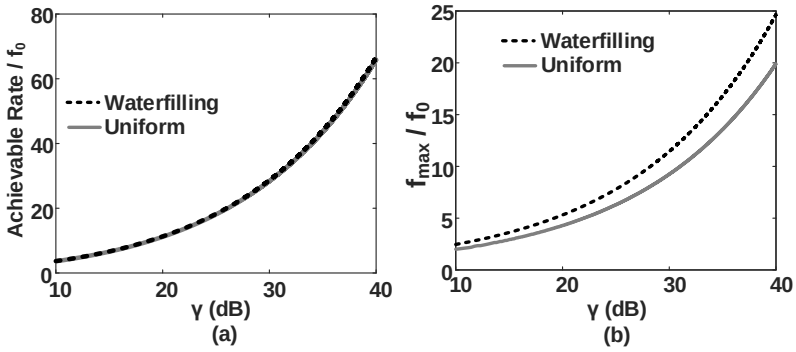

Figure 2.8: Theoretical normalized optimum modulation BW, $f_{\max}$, and achievable date rate as a function of normalized power budget γ, defined in (2.56).

2.7 Conclusions

This chapter discussed the communication channels using LEDs. We presented the LEDs non-linear dynamic electron-hole recombination mechanism and derived time domain first-order non-linear differential equation to capture the behavior. The response of the LED to PAM signaling was discussed and the effect of different mechanisms on the response was described. In chapter 5, we will use this non-linear LED model to design a compensator to mitigate the LED induced distortions.

This chapter also discussed the frequency–domain linear channel model (when the distortion is negligible). Experimental channel model was also discussed in comparison to the theoretical first-order model obtained from the LED differential equation. In chapters 3 and 4, we will use the experimental model to calculate system throughput and compare different modulation schemes over the LED channel.

The effect of a phosphor coating in VLC white LEDs was modelled and was used to discuss the effect of blue filtering. It was shown that, blue filters might improve or degrade the system performance depending on LED night nature, cold or warm LED, and background noise. In the remainder of the thesis, we focus on IR or blue-chip LEDs and neglect the effect of phosphor coating.

Chapter 3

DCO-OFDM Sub-carrier Loading Strategies

This chapter includes discussions for different power and bit loading strategies for DCO-OFDM. The optimum strategy to maximize the throughput is presented and compared to the other simpler (in the implementation) strategies, namely, uniform power and constant modulation over all sub-carriers. Experimental results are provided to backup the presented theory.

3.1 Introduction

[1]Optical Wireless Communication (OWC) employs the infrared (IR) or Visible Light (VLC) spectrum for data transmission that can be used license free. OWC attracted a lot of attention as it promises to become a key solution to mitigate the congestion on the radio spectrum for IoT applications [17]. The Intensity Modulation / Direct Detection (IM/DD) signal, which is the mode of operation in VLC, has to be positive. The information rate of an IM/DD channel, in which the non-linearity has been modelled as a hard limiting (clipping) level has been previously evaluated under various constraints. Pioneering work on constraints on the peak and average signal power was conducted in [111]. Optical power constraints were considered in [112, 113], with peak-limited LED currents [114]. The electrical power is constrained in [51], which also addresses distortion and clipping caused by the transmitter [51].

Yet, the low-pass nature is a further essential design aspect that is not always considered simultaneously. To achieve a reasonable throughput, the LED channel

[1]This chapter consists of material previously published in IEEE Transactions on Communications [72] which was re-structured for readability in thesis form.

must also be used at several tens or hundreds of MHz, one or two order of magnitude beyond the 3 dB frequency bandwidth, which may be as low as a few MHz. Orthogonal Frequency-Division Multiplexing (OFDM), yet either with a DC-bias [55, 115, 116] or with a unipolar amplitude transformation [57, 113], is popular to accommodate the low-pass nature of the channel, as it allows the selection of an optimized bit and power density on every sub-carrier of its intensity-modulation frequency spectrum. Heavily attenuated portions above the LED 3 dB bandwidth can still be used though with lower bit rates per Hz. This motivated us to study adaptive loading for VLC, and based on benchmarking in [57], focusing on DC Offset (DCO) OFDM. Yet, as we will show, new results can also be applied for other constraints than VLC and for other forms of OFDM.

Frequency-adaptive bit loading has been studied extensively for RF, but, to our knowledge, closed-form mathematical solutions, similar to our new results, cannot exist for RF. In fact, in RF the transfer function is stochastically varying due to multipath. In contrast to this, the line-of-sight LED channel exhibits a predictable roll-off [26], [58]. A second difference is that, in RF deep fades are rare and can often adequately be handled by interleaved coding, as the bulk of the probability mass of the amplitude lies near a fairly constant value. This is seen as an important reason why adaptive channel loading was not adopted for RF standards such as IEEE 802.11 (WiFi), but rely on interleaved coding. In contrast to this, our results show that in LED communication, it is advantageous to adapt the constellation and preferably also the power on each sub-carrier. However, adaptive bit loading can be highly compute and memory intensive, and may cause significant signalling overhead. This motivated us to further study adaptive sub-carrier loading for the specific LED channel transfer. Our findings recommend to adapt at least the total transmit bandwidth according to the link NPB, i.e., to dynamically set upper sub-carriers to zero power, particularly in pre-emphasized LED systems.

Waterfilling [62] is known to be an optimum strategy for loading power and choosing constellations in every frequency bin. The iterative Hughes-Hartogs (HH) loading algorithm approaches it in practical implementation [63, 64]. Yet, expressions for the throughput have not been reported before for the VLC channel with the exponential frequency response. Other practically relevant strategies are simple uniform power loading and uniform bit-loading with a pre-emphasis, which are also considered in this work.

Uniform loading transmits the same power on all frequencies but adapts the constellation, while the pre-emphasized power loading transmits the same number of bits per sub-carrier but adapts the power to invert the channel attenuation. These two practical strategies also appear to be relevant to current standardization, in particular ITU g.9991 [65] and IEEE 802.11bb [66], respectively. In fact, the recently released ITU g.9991 (or g.vlc) applies a uniform loading, such that OWC can reuse chipsets

that already exist for communication over a power line, where the main constraint is the Power Spectral Density (PSD) to satisfy EMI regulations. Alternatively, IEEE 802.11bb tends to opt for reusing its legacy Physical Layer (PHY), which was designed for radio systems that do not require adaptive power loading. In fact, deep fades are narrow if the multipath reception has a sufficiently long delay spread (thus a small coherence bandwidth), so the frequency selectivity can in RF be overcome by appropriate error correction coding and interleaving but with a fixed constellation on all frequencies. Yet, when used over an LED channel, adaptive bit-loading is needed as wide portions of the channel are heavily attenuated.

The outline of this chapter is as follows: We lay the model foundation for our findings in Sections 3.2 and 3.3. To check its validity beyond VLC with shallow (energy-conserving) modulation, we revisit the Lagrangian optimization to show by transformation of constraints that a waterfilling approach, is valid for a much broader range of signal constraints and also for unipolar variants of OFDM, or channels subject to clipping. In Section 3.4, we propose an appropriate link power budget normalization that, as we show later, leads to generic curves, irrespective of the LED choice. In Section 3.5 and 3.6, we show that for the commonly reported exponential LED transfer, closed–form expressions for throughput exist, not only for waterfilling but also for uniform loading and pre-emphasis, extending our findings in [117]. Such new, generic results, which do not exist for stochastic RF channels, facilitate the creation of adaptive loading schemes and their signalling protocols. Section 3.7 compares our theoretical expressions, with the performance of practical optimization algorithms that are limited to practical discrete constellation sizes. While Hughes-Hartogs (HH), Levin-–Campello (LC), and Chow target a (general) waterfilling distribution [63, 64, 118–122], we propose simplified algorithms. Conclusions are drawn in Section 3.8.

3.2 Optical Wireless System Architecture

To our knowledge, the capacity of a channel that has both time-domain constraints (such as a peak limitation or non-negativity) and frequency-domain challenges (attenuation of higher frequencies) is not yet generically known. A well-known exception is a variance-constrained Additive White Gaussian Noise (AWGN) Linear Time Invariant (LTI) channel. As we discuss in Section 3.3.A, that models reasonably well the challenges in VLC, limited by allowing only a small amount of extra power on top of the illumination power [57]. Yet, it does not capture further limitations of the IR LED channel. The works [111, 114] focus on the most suitable signal distribution for a peak-limited, non-negative channel, but do not indicate how the result can be applied on a severely selective channel, driven one or two orders of magnitude above the 3 dB

low-pass frequency. In fact, optimized distributions apply in time domain, but not necessarily for parallel signals, each in narrow frequency bins. The composition into a frequency multiplexed wide-band signal will anyhow give a Gaussian time-domain signal, according to the Central Limit Theorem (CLT). Unipolar OFDM examples in the overview [49, 113] decompose the user signal via an IFFT (giving a Gaussian PDF), followed by a post-process $x(t) \rightarrow i_{LED}(t)$ to satisfy amplitude constraints i_{LED} over all frequency dimensions jointly, as illustrated in Fig. 3.1. Practical examples are DCO-OFDM or forms of (polarity-flipping and) clipping, as in Flip OFDM, or ACO-OFDM [57]. That poses questions, such as

- What is the optimum spectral composition $\mathbf{E}\{|X_n|^2\}$ and are practical simplifications still effective? This is the main focus of the chapter, and elaborated in Sections 3.4 and 3.5.

- How to map the Gaussian pdf of $x(t)$ most power-effectively to the non-negative $i_{LED}(t)$? This has been addressed extensively in literature [49, 113, 123, 124]. Yet, as we will show, within the scope of our spectral analysis, it induces a non-unity gain and a consumed power penalty, both of which are equivalent to a transformation of the link power budget axis.

- Is the optimization of spectral decomposition different for different power constraints on i_{LED} or ϕ_{TX} (output optical flux from the LED)? It appears that one generic Lagrangian approach, constraining $\sigma_x^2 = \mathbf{E}\{x^2(t)\}$, applies not only for DCO-OFDM but also for other OFDM variants, if appropriate mapping functions are used. To this end we introduce, mapping function $g(\sigma_x^2)$, that maps any power constraint into a constraint on σ_x. Clipping noise requires a further adaptation of the Lagrangian evaluation, but leaves the most favorable spectral composition unaltered.

- What is the best signal constellation or pdf that we should offer to the IFFT inputs X_n? It would be straightforward to prove that Gaussian IFFT inputs need to be chosen if a time-domain $\mathbf{E}\{x^2(t)\}$ is constrained. However, we follow the common OFDM practice, also in ACO-OFDM [49,113,123,124], to use discrete (mainly rectangular) constellations, and quantify its penalty Γ in Section 3.4.A.

- As the adaptive bit loading for LED reduces to that of a variance-limited AWGN LTI channel, hasn't the radio community solved all problems already? LEDs attenuate high-frequencies in a specific way, subject to e.g. the time constants of (photonic) hole-electron recombination in the LED junction. Results comparable to our derivations, e.g. in (3.38), (3.39), (3.46), (3.49) do not exist for RF channels. Moreover, we exploit monotonicity of the LED channel attenuation to

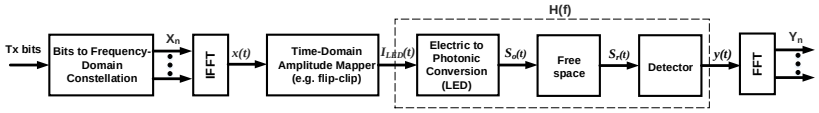

Figure 3.1: Block diagram of optical wireless system. In linear operation regime, the dashed box can be replaced by frequency dependent low pass transfer function $H(f)$.

define a maximum non-zero loaded frequency f_{max} below which all sub-carrier powers are strictly positive. This appeared a critical step to finding expressions for the throughput. In RF, such an approach would fail.

The received VLC signal Y_n at sub-carrier frequency $n\Delta f$, after the receive FFT in Fig. 3.1, is

$$Y_n = H_n X_n + n_n + d_n, \quad 0 \leq n \leq N_s - 1, \tag{3.1}$$

subject to a pronounced frequency roll-off H_n, with noise n_n, and distortion or clipping d_n. In (3.1), N_s is the number of sub-carriers. We focus on the optimization of the vector $\mathbf{E}\{|X_n|^2\}$ subject to a constraint

$$\sum_{n=0}^{N_s-1} \mathbf{E}\{|X_n|^2\} = \mathbf{E}\{x^2(t)\} = \sigma_x^2 \leq \sigma_{mod}^2 = g^{-1}(P_{constr.}), \tag{3.2}$$

where σ_x^2 is the variance of the signal at the output of the IFFT and σ_{mod}^2 is the translated constraint to the IFFT output. Without loss of generality, the constraint $\sigma_x^2 \leq \sigma_{mod}^2$ can also be applied at the input of the LED hence in current domain. According to Parseval, σ_x^2 equals to the (normalized) power in frequency domain. $P_{constr.}$ is the system constraint in power, amplitude or light flux on the LED, or in the power amplifier, which we translate into a σ_x^2-constrained IFFT output, via $g^{-1}(.)$.

Moreover, non-linearity causes an extra noise term with variance σ_D^2, yet being subject to the LED response H_n, it has non-white spectrum at the detector. We will use this in our Lagrangian optimization of the spectral composition.

Next, we will compare a number of mapping schemes such as DCO or ACO-OFDM, and derive the corresponding $g(.)$, the distortion PSD N_D and a resulting effective power for communication, as a gain correction G. As any signal gain in the mapper can be translated to a scaling of X_n's, without loss of generality for DCO-OFDM, the amplitude mapper in Fig. 3.1 performs

$$I_{LED}(t) = \mathrm{I}_{LED} + x(t). \tag{3.3}$$

In (3.3), I_{LED} and $I_{LED}(t)$ are the bias current and total current of the LED, respectively. From a communication perspective, the relevant DCO mapping is $i_{LED}(t) = x(t)$, where $i_{LED}(t)$ is the modulation current. The relative modulation depth and the trade-off with clipping can be reflected as a constraint in $\sigma_x^2 = \sum_n \mathbf{E}\{|X_n|^2\}$. For ACO-OFDM, the input signal $x(t)$ of the mapper is clipped at zero level to ensure non-negativity of $I_{LED}(t)$ to be fed to the LED. We define $x(t)$ such that we can use the generic expression

$$I_{LED}(t) = x^+(t), \tag{3.4}$$

where the notation + stands for clipping at zero. However, this leads to an attenuation of the communication signal, $G = 1/4$, while DCO-OFDM would have unity gain ($G = 1$) for the mapper.

3.2.1 LED Non-linearity

Signals with larger variations at the LED input (large $\mathbf{E}\{i_{LED}^2(t)\}$) cause the LED to operate in non-linear regime. Two options to cope with nonlinearity are 1) to see it as an invertible artefact that can be pre-compensated [47, 51] or post-processed [41], or 2) to model it as a form of extra hard clipping [49] or distortion noise [113], [45].

Invertible Non-linearity

In chapter 2, it was discussed that LEDs exhibit both static and dynamic non-linearities. For simplicity of discussion, in this section we only consider static distortions. Considering up to 3^{rd}-order non-linearity term (the validity of this assumption is discussed in chapter 5), the optical power can be expanded as

$$S_o(t) = a_1 I_{LED}(t) + a_2 I_{LED}^2(t) + a_3 I_{LED}^3(t), \tag{3.5}$$

where $S_o(t)$ is the total output optical flux consisting of a DC term and a modulated part as $S_o(t) = \mathrm{S_o} + s_o(t)$.

In the range of validity of (3.5), $S_o(I_{LED})$ is monotonic and invertible. The latter is confirmed by progress in non-linear equalization for LED communication [40,47,51]. A pragmatic and simple equalizer to invert this nonlinearity can be of the truncated form

$$I'_{LED}(t) = b_1 I_{LED}(t) + b_2 I_{LED}^2(t) + b_3 I_{LED}^3(t), \tag{3.6}$$

where the optimum value of the coefficients b_i is beyond the scope of the chapter. When we feed this pre-distorted signal $I'_{LED}(t)$ into the LED, with power

$$\mathbf{E}\{I_{LED}^{'2}\} = \mathbf{E}\{I_{LED}^2\}[b_1^2 + 3(b_2^2 + 2b_1 b_3)\mathbf{E}\{I_{LED}^2\} + ...], \tag{3.7}$$

in its relevant range, it is a monotonous function of $\mathbf{E}\{I_{LED}^2\}$, thus, as the above expression shows, can be written as an invertible function of σ_x^2. That is, LED

distortion can be handled by our optimization in Section 3.5 if we consider a $g({\sigma_x}^2) = \mathbf{E}\{I'^2_{LED}\}$ to address also the power needed to pre-compensate distortion.

Non-Invertible Distortion

The non-negativity nature of the optical channel causes hard clipping if signal amplitude falls below zero. It is not invertible and results in extra noise. Bussgang's theorem has been employed to model such nonlinearities [45], by introducing a further channel gain change and extra uncorrelated noise, as in Eq. (3.33). Yet, we challenge the popular assumption that all LEDs also exhibit hard clipping for (short) high currents ($I_{LED} > I_{peak}$). In fact, because of rapidly lowering LED prices, practical systems are no longer operated near their maximum light output but rather near their most efficient point, which corresponds to much lower currents, far below values where hard clipping or thermal breakdown occurs. Secondly, although manufacturers specify absolute maximum current ratings, for thermal reasons, the LEDs having typical thermal time constants of tens or hundreds of milliseconds, are not likely to be damaged by sub-microsecond modulation peaks from OFDM running at sample frequencies far above 10 MHz. Hence, we tend to conclude that a saturating peak limit does not accurately model modern LED behavior. For instance, data sheets for a LUXEON Rebel state a maximum current $I_{MAX} = 1000$ mA to avoid thermal damage after sustained periods of high current. Yet, it is usually biased only around 350 mA for decent efficiency but can handle occasional peaks of 5 amps, where the light output is still growing with current. Yet, we do acknowledge that the electronics driving the LEDs have peak limitations.

If we assume that the signal is only clipped at low levels (near zero due to a non-negativity constraint or LED turn-on effects) while there is no limit at high levels, clipping noise power can be expressed as a closed-form monotonous function of signal power ($\sigma_D^2(\sigma_x)$) [49]

$$\begin{aligned}\sigma_D^2(\sigma_x) = \mathrm{I}_{LED}^2 \left[\alpha_x^2 + \left(1-\alpha_x^2\right) Q\left(\alpha_x^{-1}\right) - \alpha_x q\left({\alpha_x}^{-1}\right)\right] \\ - \alpha_x^2 Q^2\left(-\alpha_x^{-1}\right) - \left[\alpha_x q\left(\alpha_x^{-1}\right) - Q\left(\alpha_x^{-1}\right)\right]^2,\end{aligned} \tag{3.8}$$

where $q(.)$ and $Q(.)$ are the probability density function (pdf) and the tail distribution function of the standard normal distribution, respectively, and $\alpha_x = \sigma_x/\mathrm{I}_{LED}$ is the relative rms modulation depth. A similar expression can be derived for hard-clipping at the high side [126]. Since each instance of clipping, creates an error that is a delta function in time domain, each clipping event creates equal amounts of noise power on all sub-carriers in the emitter, denoted as power spectral density $N_D = \sigma_D^2/BW_X$ where BW_X is the signal bandwidth at the IFFT input. However, this white current-clipping noise is subject to the same LED-junction frequency-dependent photon response $H(f)$ as the wanted signal [49].

3.2.2 LED Channel model

In chapter 2, two different LED channel models in frequency domain were discussed; first-order, derived from LED physical behavior, and experimental exponential channel model including all imperfections. In this chapter we opted for the experimental model and for simplicity of referring, we bring it here,

$$|H(f)|^2 = H_0^2 2^{-\frac{f}{f_0}}, \tag{3.9}$$

where H_0 and f_0 are the channel gain at DC and the 3 dB cut-off frequency, respectively.

3.3 Power Consumption and Constraints

The Shockley diode equation expresses the LED voltage as

$$V_{LED} = n_{LED} V_T \left(\ln \frac{I_{LED}}{I_s} + 1 \right) + R_s I_{LED}, \tag{3.10}$$

where n_{LED} is the LED ideality factor, V_T is the thermal voltage ($V_T \approx 26$ mV at room temperature), I_s is the reverse bias saturation current and R_s is parasitic resistance of the LED. The electrical power consumed by the LED, which in many applications is an important link budget constraint, is

$$\begin{aligned} P_{DC} = g(\sigma_x^2) &= \mathbf{E}\{V_{LED} I_{LED}\} \\ &= \int_0^\infty \left[n_{LED} V_T \ln \left(\frac{I}{I_s} + 1 \right) + R_s I \right] I f_{I_{LED}}(I) dI, \end{aligned} \tag{3.11}$$

where $f_{I_{LED}}$ is the pdf of I_{LED}, with σ_x^2 as a parameter. In the next sections, we discuss various mapper, modulation and application solutions. For all cases known to us, but in particular for DCO and ACO-OFDM, the constraint $g(.)$ is an invertible, monotonous function of σ_x, i.e., $dg(.)/d\sigma_x > 0$, which is an essential property needed for our further analysis.

Various LED models are used in scientific literature. This section elaborates on our LED model, that considers non-negativity, junction voltage and LED junction capacitance and resistances. So, in fact we consider LED low–pass nature and one–sided clipping. We model that electrical power consumption not only grows with the DC bias, but also with the modulation variance. In contrast to this, the average optical power only relates to the biasing, while modulation comes for free, in the sense that DC-free modulation does not affect the average current. We denote the LED current to consist of $I_{LED}(t) = \mathrm{I}_{LED} + i_{led}(t)$, where $i_{led}(t)$ is the zero–mean (AC) modulation current and I_{LED} is the DC current of the LED to ensure $I_{LED}(t) \geq 0$.

Here, the DC voltage V_{LED} can be expressed as

$$\mathrm{V}_{LED} \approx \mathrm{V}_0 + R_{LED}\mathrm{I}_{LED}, \tag{3.12}$$

where V_0 can be interpreted as the turn-on limit and R_{LED} is the dynamic plus parasitic resistance of the LED [79, 132].

3.3.1 Power Consumption for DCO-OFDM

Using (3.3), the emitted electrical *communication* power per frequency bin of width Δf is

$$S(n\Delta f)\Delta f = \mathbf{E}\{|X_n|^2\} \text{ for DCO} - \text{OFDM}, \tag{3.13}$$

where $S(f)$ is the spectral power density in $f = n\Delta f$. In this section, we also address the consumed power to create this signal, by inserting a Gaussian PDF with, for DCO-OFDM, a mean $\mathrm{I}_{\mathrm{LED}}$ and variance σ_x^2 in (3.11). This defines the function $g(.)$ mapping a power constraint on total power consumption for DCO-OFDM into a constraint on σ_x. Its dependency on σ_x^2 can intuitively be explored by approximating it as

$$g(\sigma_x^2) \approx \mathrm{V}_{LED}\mathrm{I}_{LED} + \frac{1}{\eta_{PA}} R_{LED}\sigma_x^2. \tag{3.14}$$

Here, the first term is the illumination power P_{lumen}, while $P_{extra} = R_{LED}\sigma_x^2$ with dynamic resistance $R_{LED} = nV_T/\mathrm{I}_{LED} + R_s$, is the extra power consumed by the LED for communication. The efficiency η_{PA} of the OFDM linear Power Amplifier in the mapper is notoriously low, $\eta_{PA} \leq \mathrm{PAPR}^{-1}$ where PAPR is the peak-to-average-ratio [79]. For IR channel, total consumed power is relevant, for VLC, only the extra power.

Using (3.12), the total electrical power consumed by the LED is,

$$\mathrm{P}_{tot} = \mathrm{V}_0\mathrm{I}_{LED} + R_{LED}\mathrm{I}_{LED}^2 + \frac{1}{\eta_{PA}} R_{LED}\sigma_x^2. \tag{3.15}$$

An extensive study [50] into the power efficiency of a series transistor modulator revealed a total power consumption of $P_{tot} \approx (\mathrm{V}_0 + 2R_{LED}\mathrm{I}_{LED})\mathrm{I}_{LED}$ where factor 2 is due to an extra voltage headroom $R_{LED}\{\max I_{LED}(t)\}$ required to operate the modulating series transistor [50]. More generically, a versatile power constraint is the weighted sum of moments of the probability of the signal

$$\mathrm{P}_{tot} = \mathrm{P}_{DC} + \mathrm{P}_{ext} = \beta_1\mathrm{I}_{LED} + \beta_2\sigma_x^2 + \beta_3\mathrm{I}_{LED}^2, \tag{3.16}$$

where P_{ext} is the extra power on top of the DC power consumed by the LED due to modulation and the β-weights may also depend on the electronic topology and the use case (VLC vs IR). In fact, various works take different interpretations of β_1, β_2 and β_3, as we will discuss in the next sections.

3.3.2 Power Constraint

For IR and VLC communication, the power can be constrained either in the optical or the electrical domain, which may lead to different optimizations.

1) Optical Power Constraint: Optimizations for the optical domain, for instance dictated by eye-safety in IR or illumination level in VLC, basically limit the average (or DC-bias) LED current I_{LED}: $(\beta_1 > 0, \beta_3 = 0)$, but do not impose a power penalty for modulation ($\beta_2 = 0$). As we will quantify in section 3.4, the DC current I_{LED} needs to accommodate the LED input current AC excursions. Hence, it nonetheless becomes an indirect function of σ^2_{mod} to ensure a sufficiently low clipping distortion.

2) Electrical Power Constraint in IR: The associated electrical power also depends on the variance via $\beta_2 = R_{LED}$. For a constrained total electrical power, in (3.15), $\beta_1 = V_0$, $\beta_2 = \beta_3 = R_{LED}$. In fact, the non-linear current-voltage curve, approximated in (3.12), was further simplified by omitting the photonic junction voltage ($V_0 = 0$) in [49], taking $\mathrm{P}_{tot} = R_{LED}(\mathrm{I}^2_{LED} + \sigma^2_x)$, thus $\beta_2 = \beta_3$ and $\beta_1 = 0$. Yet, V_0 dominates the voltage across the LED ($V_0 > R_{LED}\mathrm{I}_{\mathrm{LED}}$). Hence, OWC sees a large β_1, so that $P_{tot} \approx V_0\mathrm{I}_{\mathrm{LED}}$ may be reasonable as a first-order estimate, particularly if V_0 is adjusted for typical biased V_{LED} voltages.

3) Extra Power Constraint in VLC: The primary function of VLC is illumination, so the DC current of the LED is determined by the target illumination level [51], and is not subject to a communication optimization ($\beta_1 = 0, \beta_3 = 0$). As communication is a secondary function, the illumination system is expected to deliver a high lumen-per-wall-socket-watt. Consequently, any additional consumption of power just for modulation deteriorates the energy efficiency and may even jeopardize the 'green' certification of the LED lighting product. Hence, an important VLC design objective is to get the highest possible throughput for the least amount of extra power, in a regime where DC bias is not the dominant scarce resource. In fact, modulating the LED current consumes extra power $\mathrm{P}_{ext} \approx R_{LED}\sigma^2_x/\eta_{PA}$, as reflected in $\beta_2 = R_{LED}/\eta_{PA}$ [57]. An (in-) efficiency of the amplifier (LED driver) can be reflected in η_{PA}. If we are only interested in the LED power, we take $\eta_{PA} = 1$. However, inefficient (linear) modulator amplifiers in VLC make the overall LED lighting product less efficient, even to the extend that it fails lighting energy conservation regulations. Hence, VLC optimizations on P_{ext} are highly relevant (thus with $\beta_1, \beta_3 = 0$). In this chapter, we evaluate systems limited by extra power.

DCO-OFDM in VLC

In [57], we discussed that VLC often is used in applications where communication is just a secondary function on top of a primary illumination function, thus $g(\sigma^2_x) = \eta^{-1}_{PA}P_{extra} \approx \eta^{-1}_{PA}R_{LED}\sigma^2_x$ is relevant if the extra electrical power $\eta^{-1}_{PA}R_{LED}\sigma^2_x$ (due to modulation) must be almost negligible compared to $P_{lumen} = \mathrm{V}_{LED}\mathrm{I}_{LED}$. Modu-

lation deteriorates the wall-plug-to-lumen efficiency by a factor of

$$\Delta_\eta = \frac{P_{extra}}{P_{lumen}} \approx \frac{\eta_{PA}^{-1} R_{LED} \sigma_x^2}{\mathrm{V}_{LED}\mathrm{I}_{LED}} = \mathrm{PAPR}\frac{\sigma_x^2}{I_{LED}^2}\frac{R_{LED}\mathrm{I}_{LED}}{\mathrm{V}_{LED}}. \tag{3.17}$$

For a typical lighting LED (e.g. Luxeon Rebel LXML-PB02-0023 blue LED), typically $\mathrm{V}_{LED} \approx 3V$ for a bias current $\mathrm{I}_{LED} \approx 0.35A$ and $R_{LED} \approx 1\Omega$, so $R_{LED}\mathrm{I}_{LED}V_{LED}^{-1}$ is in the order of 0.12 (12%). If we would allow full modulation, i.e., $\sigma_x^2/\mathrm{I}_{LED}^2 = \mathrm{PAPR}^{-1}$, the VLC product would consume 12% more power per illumination lumen. This even is highly optimistic, as signal processing and effective matching to a 1 Ω load with typical transistors and PCB lines is prone to further losses. State-of-the-art lighting achieves a wall-plug electrical power effectiveness above 90% and deliver more than 120 lumens per watt. So a deterioration above a few percent would jeopardize the promise of LEDs being energy efficient. Regulations, e.g. [127] or the Single Lighting Regulation (SLR) increasingly mandate higher lumen-per-watt efficacy. Then, (3.17) forces us to use $\sigma_x^2 << \mathrm{I}_{LED}^2$, certainly $\sigma_x^2/\mathrm{I}_{LED}^2 < \mathrm{PAPR}^{-1}$ and reaching clipping levels realistically does not happen. That makes the DCO VLC σ_x^2 limited. Furthermore, unipolar OFDM (such as ACO-OFDM) is less attractive for VLC, as Δ_η (defined in (3.17)) would be too large [57].

DCO-OFDM in IR

In IR, the power budget contains both DC and modulation power. In fact, if one would make the IR signal fully clip-free, one would presumably overspend power in the bias. Although, the prime focus of this chapter was on energystar compliant VLC [127], for the reader interested in cases where the total power, including DC bias is relevant, we refer to chapter 4. This chapter further includes an evaluation of the impact of clipping noise on the optimum channel loading (in Section 3.5), in particular Eq. (3.33).

3.3.3 Power Consumption for ACO-OFDM

One can argue that for IR communication, thus constrained by *total* power, DCO-OFDM is not preferred because of its poor power efficiency. In this section, we show how our frequency-loading results can be applied for Flip and ACO-OFDM. Importantly, these unipolar modulation methods, despite their truncation, preserve the property that each X_n sees a narrowband channel in a frequency bin around $n\Delta f$. So, we now obtain $g(.)$. Because the truncation $i_{LED}(t) = x^+(t)$, a one-sided Gaussian is transmitted, with mean value $\mathbf{E}\{i_{LED}\} = \sigma_x/\sqrt{2\pi}$ and $\mathbf{E}\{i_{LED}^2\} = \sigma_x^2/2$. We insert

$$f_{I_{LED}}(I) = \frac{\delta(I)}{2} + \frac{U(I)}{2\sqrt{2\pi}\sigma_x}\exp\left(-\frac{I^2}{2\sigma_x^2}\right), \tag{3.18}$$

in (3.11) to obtain the (extra) power of the LED. This is a monotonous, invertible function of σ_x, that we use in the Lagrangian optimization in Section 3.5. For a linearized LED model, this can be approximated as [57]

$$g(\sigma_x^2) \approx \frac{\mathrm{V}_J}{\sqrt{2\pi}}\sigma_x + \frac{1}{2}R_{LED}\sigma_x^2 \text{ for ACO} - \text{OFDM}, \tag{3.19}$$

where before the truncation, we assumed a unity gain for the mapper. The emitted communication power per frequency bin is [128]

$$S(n\Delta f)\Delta f = \frac{\mathbf{E}\{|X_n|^2\}}{4} \quad \text{for ACO} - \text{OFDM}, \tag{3.20}$$

where the factor $G = 1/4$ results from the removing 50% of $x(t)$. As ACO-OFDM is guaranteed non-negative, ignoring clipping noise $\sigma_D(\sigma_x) = 0$ becomes reasonable, but a non-linear compensation (3.7) is recommended.

3.3.4 Constrained IR Optical Power in ACO-OFDM

While electrical power is relevant to battery life time, eye safety in IR can constrain optical power. For ACO-OFDM, the optical power is proportional to the $\mathbf{E}\{I_{LED}\}$. So the mapping function $g(.)$ to relate a constraint on the average optical power to σ_x^2 is [57]

$$g(\sigma_x^2) = \sigma_x/\sqrt{2\pi} \quad \text{for ACO} - \text{OFDM}, \tag{3.21}$$

which is optically constrained. That is, even for an optical power constraint, an appropriate translation of the σ_x^2 constraint exists. To mitigate the penalty of a factor of 2 in the throughput, caused by only loading odd sub-carriers, various hybrid unipolar and biased schemes exists. Also for such schemes, an invertible $g(.)$ can be found by interpreting pdfs in [57].

3.4 Theoretical Throughout of the LED Channel

Using the channel model in 3.9, we evaluate the throughput. Communication over a general frequency selective channel requires the choice of an appropriate frequency-dependent constellation size $M(f)$ on all dimensions. For a band-limited channel with frequency response $H(f)$, experiencing AWGN with spectral density N_0, the throughput (in bits per second) is integral of all rate contributions at frequency f, so, if no clipping noise occurs

$$R = \int_f \log_2\left(1 + \frac{S(f)|H(f)|^2}{\Gamma N_0}\right) df, \tag{3.22}$$

where $S(f)$ is the transmit spectral density as dictated by the choice of $S(n\Delta f)\Delta f = G\mathrm{E}\{|X_n|^2\}$ values, where G is the gain of the mapper, thus $G = 1$ for DCO-OFDM and

$G = 1/4$ for ACO-OFDM. While (3.22) resembles the Shannon capacity expression for power limited LTI AWGN channels, the next section describes how this is appropriate for practical OFDM systems with commonly-used constellations, where Γ can be interpreted as the distance to the bound for an ideal LTI AWGN channel ($\Gamma \geq 1$).

The received signal $y(t)$ in Fig. 3.1 is de-mapped in the receiver chain and its DC bias level is removed. It is transformed into frequency domain Y_n by a receive FFT, where $\mathbf{E}\{|Y_n|^2\} = G\mathbf{E}\{|X_n|^2\}|H(n\Delta f)|^2$. ACO-OFDM only loads odd sub-carriers, thus the achievable throughput is divided by 2. Our objective is to find the signal spectral distribution $\mathbf{E}\{|X_n|^2\}$ for all n to maximize R.

3.4.1 Optical OFDM with Discrete Modulation

Practical systems use (real or complex) amplitude modulation, such as the one-dimensional PAM or two-dimensional QAM. For OWC, PAM may be applied directly in base-band, but, to account for the frequency–selectivity in the channel, usually these are translated onto sub-carriers in a form of OFDM.

So, throughout this chapter, we interpret M-QAM as an amplitude modulation for two orthogonal symbols, each carrying $0.5 \log_2 M$ bits. Because of OFDM, the constellation size can be made as a function of frequency, $M = M(f)$. Since M constellation points can carry $b = \log_2 M$ bits, the achieved rate (expressed in bits/s) across the modulation spectrum $[0, f_{\max}]$ is

$$R = \int_0^{f_{\max}} \log_2(M(f))df, \tag{3.23}$$

where the optimization challenge is to choose $M(f)$. While our theoretical analysis optimizes (3.22), our algorithmic sections optimize (3.23), but reach an equivalent objective of maximizing the rate.

The spectrum efficiency of OFDM on OWC, including the impact of the real-valued nature of the LED channel has been widely debated. This section intends to clarify our throughput calculation of OFDM. A bandwidth of df and the time duration T_s can accommodate $2T_s df$ dimensions [100]. So every dimension occupies a footprint that satisfies $T_s df = 1/2$. This can be mapped in various ways, e.g, by (DC biased) M-PAM, or in fact bandpass M-ASK, or by (DC-biased) M-QAM with Hermitian symmetry to adapt to the real-valued light intensity channel. In fact, the FFT even with Hermitian mapping is a unitary operation, that conserves power levels between input and output, but only rotates the base of the dimensions. The invertability of the operation proves that optical OFDM addresses exactly the same number of dimensions and is equally spectrum efficient as ASK or PAM. Obviously, in carrier-based RF communication, QAM results in different lower and upper side bands, thus carries twice the number of dimensions of a double-sized bandwidth, but these are

not accessible in baseband LED communication. For a two-dimensional QAM signal in an OFDM grid where $H(f)$ being moderately selective, the footprint is $T_s = 1/df$, so its Signal to Noise Ratio (SNR) per symbol is

$$\frac{\epsilon_s}{N_0} = \frac{P_r(f)T_s}{N_0} = \frac{P_r(f)}{N_0 df} = \frac{S(f)|H(f)|^2}{N_0}. \tag{3.24}$$

where $P_r(f) = S(f)|H(f)|^2 df$.

For QAM-OFDM over an AWGN channel, the probability P_N of an error in the data load is tightly upper-bounded by [100]

$$P_N = 4Q\left(\sqrt{\frac{3\epsilon_s}{(M-1)\,N_0}}\right) \tag{3.25}$$

where Q is the tail distribution function and ϵ_s is the average symbol energy. Enforcing that the probability of errors is less than a certain value of P_N and using the decreasing property of $Q^{-1}(.)$ function, we invert (3.25) to get a minimum required ϵ_s/N_0. Inserting (3.24) into (3.25), M and subsequently the rate (from (3.23)) appears to result in a formula of the form of (3.22), namely

$$R = \int_0^{f_{\max}} \left\lfloor \log_2\left(1 + \frac{S(f)|H(f)|^2}{\Gamma N_0}\right)\right\rfloor df, \tag{3.26}$$

that is, with a rounding down to an integer number of bits per constellation and with a modulation (or SNR) gap of [129, 130]

$$\Gamma = \frac{1}{3}\left(Q^{-1}\left(\frac{P_N}{4}\right)\right)^2, \tag{3.27}$$

where the modulation gap Γ is a decreasing function of symbol error rate P_N and it takes values of 7.39 dB and 6.06 dB for $P_N = 10^{-4}$ and $P_N = 10^{-3}$, respectively. In our theoretical evaluation, we omit the floor function to allow analytical expressions, while our experiments inherently model such a discretization.

The optimization in which all sub-carriers have the same symbol error rate can be seen as a discrete optimization of the Shannon expression with a gap of Γ. Yet, most of practical use is an optimization with equal Bit Error Rate (BER) across the entire OFDM block. Considering $P_N \approx \mathrm{BER}\log_2 M$ [100], thus, the modulation gap for a constant BER can be derived as

$$\Gamma(BER) = \frac{1}{3}\left(Q^{-1}\left(\frac{\log_2(M)BER}{4}\right)\right)^2. \tag{3.28}$$

The gap Γ for a constant BER depends on the modulation order M, and is a decreasing function of M, as shown in Fig. 3.2 for different BER values. It is about

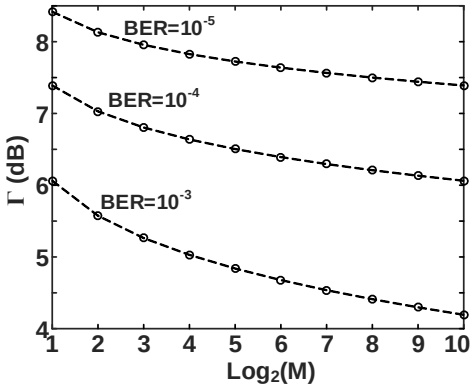

Figure 3.2: The gap Γ as a function of $\log_2(M)$ for M-QAM modulation under different BER values.

1.3 dB lower for large M than for $M = 2$ when $BER = 10^{-4}$. The bit-power loading algorithm can take this into account to effectively distribute the power among the subcarriers of OFDM, however, in practice and to simplify the algorithm the maximum value (for the worst case of $M = 2$) is more suitable. This simplification, however, underestimates the throughput.

3.4.2 Normalized LED Channel

The throughput over the channel response approximated in (3.9), calculated from (3.26), is

$$R = \int_0^{f_{\max}} \log_2 \left(1 + \frac{H_0^2 S(f)}{\Gamma N_0} 2^{-f/f_0}\right) df. \tag{3.29}$$

Although it is a common engineering practice to define an SNR over the relevant bandwidth $f_{\max}$ occupied by the signal, in our optimization $f_{\max}$ is a system choice, subject to optimization for different bit and power loading strategies. This prohibits the definition of an SNR that pre-assumes a certain bandwidth. Moreover, the SNR would not be constant across the receive band. We adopt the recommendation in [117] to normalize the SNR, or in fact the link power budget, to the 3 dB bandwidth f_0 of the LED, even though the practical and optimal signal bandwidth may be an order of magnitude larger:

$$\gamma = \frac{\sigma_{mod}^2 H_0^2}{N_0 f_0}. \tag{3.30}$$

We denote γ as the link Normalized Power Budget (NPB).

Similarly, we normalize the rate also to the LED bandwidth, as $\Re = R/f_0$. In fact, using this more appropriate normalization (3.30), we are able to create generic

curves for the throughput and the corresponding optimum bandwidth to be used that are not restricted in validity for specific values of H_0, f_0, N_0 or σ_{mod}.

3.5 Power Loading Strategies

This section evaluates different power loading strategies. Interestingly, we arrive at generic, though implicit, solutions for the optimum bandwidth to be used and for the throughput, depends only on the link NPB γ, but if appropriately corrected for, not on any other link parameters.

3.5.1 Waterfilling

Waterfilling [62] optimizes the transmitted spectrum $S(f)$ allocated to each frequency component to maximize the throughput. This chapter extends the results of our previous work in [117], and we derive new elegant, tractable theoretical expressions for the LED channel (3.9). We optimize

$$\max \int_f \log_2 \left(1 + \frac{S(f)|H(f)|^2}{\Gamma\left(N_0 + N_D|H(f)|^2\right)}\right) df, \tag{3.31}$$

constrained by $g(\sigma_x^2) \leq P_{constr.}$.

We transfer the Lagrangian constraint by applying the inverse mapping function $g^{-1}(.)$, provided that it exists and is unique, i.e. $\sigma_x^2 \leq g^{-1}\left(P_{constr.}\right)$. We defined $g^{-1}(P_{constr.}) = \sigma_{mod}^2$, so we require $\sigma_x^2 \leq \sigma_{mod}^2$. Using the gain G of the mapper,

$$\frac{1}{G}\int_f S(f)df = \sum_n \mathbf{E}\{|X_n|^2\} \leq \sigma_{mod}^2. \tag{3.32}$$

The optimization covers the (DCO, ACO, or other) signal mapping, but also a predistortion power penalty as in (3.7). Thus, the optimization objective translates into

$$\begin{aligned}\lim_{\Delta f \to 0} \frac{1}{\Delta f} \sum_n \log_2 \left(1 + \frac{G|H(n\Delta f)|^2 \mathbf{E}\{|X_n|^2\}}{\Gamma(N_0 + N_D|H(n\Delta f)|^2)}\right) \\ + \lambda\left[g^{(-1)}\left(g\left(\sigma_x^2\right)\right) - g^{(-1)}\left(P_{constr.}\right)\right].\end{aligned} \tag{3.33}$$

Taking the derivative w.r.t. $\mathrm{E}\{|X_n|^2\}$ on every frequency bin n, and setting these to zero lets the mapping effect of $g(.)$ vanish. Yet, it gives an expression with a correction for N_D:

$$\begin{aligned}\mathrm{E}\{|X_n|^2\} &= \frac{S_w(n\Delta f)\Delta f}{G} \\ &= \frac{\Delta f}{G}\left(\tau - \frac{\Gamma\left(N_0 + N_D|H(n\Delta f)|^2\right)}{|H(n\Delta f)|^2}\right)^+,\end{aligned} \tag{3.34}$$

where τ is a constant and $S_w(f)$ is the optimum power spectral density. While the above expression is suitable to load FFT inputs, for our analytical evaluation, we take $\Delta f \to 0$, thus

$$S_w(f) = \left(\tau - \Gamma\left(\frac{N_0}{|H(f)|^2} + N_D\right)\right)^+. \tag{3.35}$$

The above optimal solution (3.35), or pragmatic alternatives, can be inserted in e.g. (3.22) to obtain the throughout. In radio communication, where the channel transfer $H(f)$ is dominated by the stochastic effects of multipath wave cancellation, the bandwidth integral (3.22) can not be evaluated generically with (3.35). Yet, the LED channel (3.9), is different in the sense that the transfer function caused by hole-electron time constants and can be covered in a generic mathematical expression. In the next sections, which are not valid for a radio channel, we derive this solution for the LED low-pass channel. In particular, we exploit the fact that $H(f)$ in (3.9) is monotonously decreasing, which would not hold for an RF channel. But, for any LED channel, there exists $0 < f < f_{\max_w}$, where $S_w(f)$ is non-zero, while $S_w(f)$ is zero beyond $f_{\max_w}$. The parameter $f_{\max_w}$ depends on P_{constr} and is denoted as the optimum $f_{\max}$ required by waterfilling (w) strategy. This yields

$$\tau = \Gamma\left(\frac{N_0}{|H\left(f_{\max_w}\right)|^2} + N_D\right). \tag{3.36}$$

Interestingly, N_D cancels in (3.35), thus clipping noise does not affect the optimum spectral composition of the modulation or its bandwidth. To find the maximum throughput of the waterfilling, R_w, as a function of the NPB γ, we express R_w and the modulation budget σ^2_{mod} (or γ) both as a function of $f_{\max_w}$. Then, $f_{\max_w}$ is eliminated as the intermediate variable. Using (3.35), we have

$$\begin{aligned}\sigma^2_{mod}(f_{\max_w}) &= \frac{1}{G}\int_0^{f_{\max_w}} S_w(f)df \\ &= \frac{\Gamma N_0}{GH_0^2}\int_0^{f_{\max_w}}\left(2^{\frac{f_{\max_w}}{f_0}} - 2^{\frac{f}{f_0}}\right)df.\end{aligned} \tag{3.37}$$

In the next section, we present DCO VLC results, but leave it to the reader to map G and $g(.)$ for ACO-OFDM in the final results. Solving (3.37) uniquely expresses the optimum modulation bandwidth ($\nu_w = f_{\max_w}/f_0$) as a function of γ, by inverting

$$\gamma = \frac{\Gamma}{\ln(2)}\left(1 + (\ln(2)\nu_w - 1)\,2^{\nu_w}\right). \tag{3.38}$$

Noteworthy, $f_{\max_w}$ appears to be independent of any clipping noise N_D. However, it causes a throughput penalty, that we quantify by inserting (3.35) and (3.36) into

(3.31). The normalized maximum throughput for waterfilling, denoted as $\Re_w = R_w/f_0$, can be found by splitting the integral:

$$\begin{aligned}\Re_w &= \frac{1}{f_0}\int_0^{f_{\max_w}} \log_2\left(\frac{|H(f)|^2}{|H(f_{\max})|^2}\right)df \\ &+ \frac{1}{f_0}\int_0^{f_{\max_w}} \log_2\left(\frac{N_0+N_D|H(f_{\max_w})|^2}{N_0+N_D|H(f)|^2}\right)df. \\ &= \frac{\nu_w^2}{2} + \Delta_{R_w}\left(\nu_w, \frac{N_D}{N_0}\right)\end{aligned} \tag{3.39}$$

The second integral Δ_{R_w} is rate loss due to clipping (or distortion) noise at the transmitter. Using a similar approach as in the appendix, it can be expressed as a function of optimum bandwidth ν_w and the ratio N_D/N_0. For $N_D = 0$, $\Delta_{R_w} = 0$. To avoid unnecessary complication, we further focus on optimal loading schemes for the clipping free cases, such as energy-regulation constrained VLC. Since γ and $\Re_w$ are monotonous functions of ν_w, this gives a unique, though implicit but simple relation between throughput $\Re_w$ and the available NPB γ:

$$\gamma(\Re_w) = \frac{\Gamma}{\ln(2)}\left(1 + \left(\ln(2)\sqrt{2\Re_w} - 1\right)2^{\sqrt{2\Re_w}}\right). \tag{3.40}$$

Since an expression of the generic form of $\gamma = x\exp(x)$ is known not to have an analytical solution (here, $x = \sqrt{2\Re_w}$ with some constants), there is no closed form solution to invert (3.40), that would express the throughput as a function of the link NPB γ.

3.5.2 Uniform power allocation

For a modulation bandwidth of $f_{\max}$, the transmit power spectral density of uniform power allocation is

$$S_u(f) = \frac{\sigma_{mod}^2}{f_{\max}}. \tag{3.41}$$

The throughput of this uniform loading, denoted as R_u, is calculated by replacing $S(f)$ of (3.29) with that given in (3.41), so

$$R_u = \int_0^{f_{\max}} \log_2\left(1 + \frac{H_0^2\sigma_{mod}^2}{\Gamma N_0 f_{\max}}2^{-\frac{f}{f_0}}\right)df. \tag{3.42}$$

Denoting the normalized modulation bandwidth by $\nu = f_{\max}/f_0$ and using the definition of link NPB γ in (3.30), (3.42) can be written as the normalized generic result

$$R_u = f_0\int_0^{\nu} \log_2\left(1 + \frac{\gamma}{\Gamma\nu}2^{-x}\right)dx. \tag{3.43}$$

Using a numerical solver such as Matlab, Fig. 3.3(a) depicts the rate achieved by the uniform loading strategy as a function of normalized modulation bandwidth (ν), shown with dashed-dark lines for 3 different link NPB values of 40 dB, 30 dB and 20 dB. It can be seen that the rate as a function of modulation bandwidth exhibits a single extermum, $\nu = \nu_u$ with $dR_u/d\nu_u = 0$. Also for $\nu \to \infty$, $dR_u/d\nu$ =0. The effect of a discrete constellation size, reflected in the floor function in (3.26), (dashed-grey lines in Fig. 3.3(a)) will further be discussed in our experimental discussions.

To find the maximum throughput, again, we first calculate the optimum $f_{\max}$ (denoted by $f_{\max_u}$) by taking the derivative of (3.43), and then get the maximum throughput by employing Leibniz's rule as in Appendix A. We define the normalized optimum modulation bandwidth $\nu_u = f_{\max_u}/f_0$. Using the definition of the link NPB (3.30), Appendix A shows that γ dictates an optimum ν_u governed by

$$(\ln(2)\nu_u + 1)\log_2\left(1 + \frac{\gamma}{\Gamma\nu_u}2^{-\nu_u}\right) = \log_2\left(1 + \frac{\gamma}{\Gamma\nu_u}\right). \tag{3.44}$$

To have a closed-form expression for the normalized maximum throughput $\Re_u = R_u/f_0$, we express it as a Spence's function $Li_2(.)$, with

$$Li_2(z) \triangleq \int_0^z \frac{\ln(1-u)}{-u}du. \tag{3.45}$$

Rearranging (3.42), we can also express the rate as a function of γ and $\nu_u(\gamma)$, namely

$$\Re_u(\nu_u) = \frac{1}{(\ln 2)^2}Li_2\left(-\frac{\gamma}{\Gamma\nu_u}2^{-\nu_u}\right) - \frac{1}{(\ln 2)^2}Li_2\left(-\frac{\gamma}{\Gamma\nu_u}\right). \tag{3.46}$$

Thus, via (3.46) and (3.44), the rate can be expressed as a function of the link NPB γ. The detailed calculations are given in Appendix A. Fig. 3.3(a) shows (with a solid line) the normalized throughput as a function of optimum normalized modulation bandwidth (ν_u). At the crossing point between the solid line and the dashed lines, $dR_u/d\nu = 0$, hence the rate is at its maximum for the corresponding link NPB (γ varies along the solid line). A bandwidth far from the optimum has a very pronounced impact, particularly for pre-emphasized systems, as we will see in the next section. While we quantify these effects in Fig. 3.3, We do not show non-optimum bandwidths for waterfilling, since a waterfilling strategy only yields one, optimum solution.

3.5.3 OFDM with Pre-emphasis

A pre-emphasis boosts high frequencies such that the output spectrum of the LED channel, thus also the signal-to-noise ratio, is uniform across $[0 - f_{\max}]$. Applying the

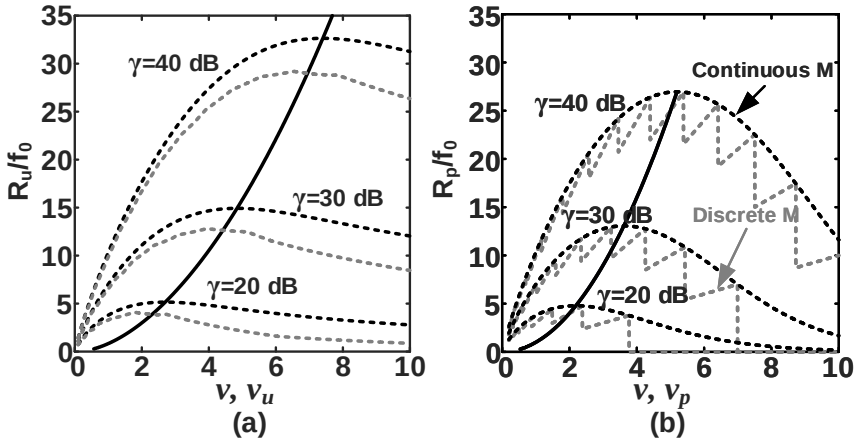

Figure 3.3: Normalized rate (dashed curves) achieved by (a) uniform loading and (b) pre-emphasis versus the normalized modulation bandwidth ν for link NPB γ of 20, 30 and 40 dB. The dashed-grey curves are for the case of discrete constellation sizes i.e. M = 2, 4, 8, ... Normalized maximum throughput (solid) by (a) uniform and (b) pre-emphasized loading versus optimum modulation bandwidth ν_u and ν_p, respectively. Every point on this solid curve corresponds to a different γ.

inverse of the LED response (3.9) for $0 < f < f_{\max}$, it feeds into the LED

$$S_p(f) = S_0 2^{\frac{f}{f_0}} = \kappa \frac{\sigma_{mod}^2}{f_{\max}} 2^{\frac{f}{f_0}}, \tag{3.47}$$

where the power spectral density $S_0 = S_p(0)$ incurs a pre-emphasis back-off κ, with $S_0 = \kappa\sigma_{mod}^2/f_{\max}$ to satisfy constraint (3.32). The back-off coefficient κ is calculated as

$$\kappa = \frac{\nu \ln(2)}{2^{\nu-1}}, \tag{3.48}$$

where $\nu = f_{\max}/f_0$ is the normalized modulation bandwidth. The normalized throughput $\Re_p$, with ($\Re_p = R_p/f_0$), can be derived from (3.29) and (3.47). So,

$$\Re_p(\nu) = \nu \log_2 \left(1 + \frac{\gamma \ln 2}{\Gamma\left(2^{\nu} - 1\right)}\right). \tag{3.49}$$

Fig. 3.3(b) shows that a pre-emphasized system is severely affected if the bandwidth is chosen too large. Discretization of the constellation causes sharp cuts in rate if the bandwidth exceeds certain values. Particularly for small link NPBs ($\gamma < 100$), choosing ν_p too large is detrimental. Moreover, even the envelope, which describes the theoretical rate if also non-integer numbers of bits can be loaded onto sub-carriers,

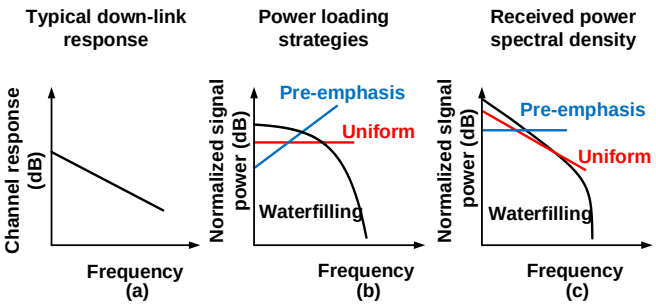

Figure 3.4: Illustration of the different power loading strategies. (a) Channel response, (b) allocated power versus frequency and (c) PSD at the output of the LED for waterfilling, uniform loading and pre-emphasis.

shows a steeper decline than with uniform power loading. For this envelope, the normalized optimum modulation bandwidth, denoted as ν_p, can then be found to maximize the throughput. Using $\frac{d\Re_p}{d\nu_p} = 0$ results in

$$\frac{\gamma \nu_p 2^{\nu_p} \ln 2}{\Gamma (2^{\nu_p} - 1)^2 + \gamma \ln 2 \, (2^{\nu_p} - 1)} = \log_2 \left(1 + \frac{\gamma \ln 2}{\Gamma \, (2^{\nu_p} - 1)} \right). \tag{3.50}$$

Regrettably this cannot be solved for ν_p in closed form. Nonetheless, for the given γ, the normalized ν_p can be calculated from (3.50) by iterative methods and inserted in (3.49) to calculate the throughput. The solid line in Fig. 3.3(b) shows the normalized throughput as a function of ν_p. That is, it connects all optima $dR_p/d\nu = 0$.

3.6 Comparison of Sub-carrier Loading Strategies

For the LED response as in (3.9) and Fig. 3.4(a), the transmit and receive power spectral densities are illustrated in Fig. 3.4(b) and (c), respectively, on a log-log scale. For waterfilling, we observe that, at least for low frequencies, the transmit power only exhibits a gentle roll-off, which is illustrated in Fig. 3.4(b). The power spectrum that falls on the receiving detector follows the channel frequency decline shown in Fig. 3.4(c).

For $H(f)$ being a monotonically decreasing function, as in (3.9), we have $\tau = \Gamma N_0 |H(f_{\max_w})|^{-2}$ in (3.35). Apparently, this constant τ dominates the shape of $S(f)$. In reasonable approximation, (3.35) becomes almost uniform with $S_w(f) \approx \Gamma N_0 / |H(f_{\max_w})|^2$ for $f < f_{\max_w}$ and zero otherwise, thus neglecting the smaller second, frequency-dependent term. We will see later that hence waterfilling and uniform loading theoretically have almost identical performance.

Fig. 3.5(a) shows that already at small link NPBs, the optimized bandwidth exceeds f_0, while $f_{\max}$ increases above an advised $10f_0$ for high link NPBs (higher than 40 dB), so signal-to-noise ratios may well be 10 dB less than our γ and Fig. 3.5(a) gives the conversion rate, as the noise bandwidth follows $f_{\max} = \nu f_0$. Yet, if we normalize not only γ, but also the bandwidth and the throughput to f_0 (Fig. 3.5(a) and (b), resp.), this allows us to plot generic curves without limiting the validity to any specific LED or bias current. Next, we translate the normalized γ to typical SNR values.

3.6.1 Signal-to-Noise Ratio

The normalized link NPB γ can be translated to a received SNR, which in engineering practice is mostly defined as the total received power divided by the noise power in the full signal bandwidth, i.e.,

$$SNR_x \triangleq \frac{\int_0^{f_{\max_x}} S_x(f)|H(f)|^2 df}{N_0 f_{\max_x}}. \tag{3.51}$$

Since this SNR depends on the power loading strategy, we use the system reference x to refer to waterfilling (w), uniform loading (u) or a pre-emphasis (p). In fact, solving the integral for all loading strategies, we get

$$SNR_w = \frac{\gamma}{\nu_w} \frac{-1 + 2^{\nu_w} - \ln(2)\nu_w}{1 - 2^{\nu_w} + \ln(2)\nu_w 2^{\nu_w}}, \tag{3.52}$$

$$SNR_u = \gamma \frac{1 - 2^{-\nu_u}}{\ln(2)\nu_u^2}, \tag{3.53}$$

and

$$SNR_p = \gamma \frac{\ln(2)}{2^{\nu_p} - 1}. \tag{3.54}$$

Here, as also seen in Fig. 3.5(a), ν_w, ν_u and ν_p are a function of γ, according to Eq. (3.38), (3.44) and (3.50), respectively. For a large γ (hence large ν_w and ν_u),

$$SNR_w = SNR_u \approx \gamma \frac{1}{\ln(2)\nu_w^2}. \tag{3.55}$$

3.6.2 Example

In our setup, a Digital-to-Analog Convertor (DAC) with an analog output of $V_{DAC}x(t)$, where $x(t)$ is the digital signal, is fed into a 50 Ω's power amplifier with 26 dB gain ($G_x = 400$). It drives the LED in series with a 50 Ω resistor to avoid that the mismatch to R_{LED} damages the amplifier. We calibrate our system by measuring the analog signal power $P_{TX,a} = G_x^{-1} i_{LED,rms}^2 (50\,\Omega + R_{LED}) = V_{DAC}^2 \sigma_x^2 / 50\Omega$ at the DAC

output. To ensure $\sigma_x = i_{LED,rms}$, we take $V_{DAC} = G_x^{-1/2}\sqrt{(50\,\Omega + R_{LED})50\,\Omega}$. A practical design will of course use a more efficient matching. Taking the optical efficiency of $\eta = 90\%$ for the LED used in our experiments the transmitted optical power (at low modulation frequencies) can be written as [27]

$$s_{o,rms} = \eta \frac{\langle E_p \rangle}{q} i_{LED,rms}, \tag{3.56}$$

where $\langle E_p \rangle = 4{\times}10^{-19}$ J is the average photon energy of blue light (with a Wavelength around 500 nm) and $q = 1.6 \times 10^{-19}$ C is the charge of electron. We take the example of a typical blue LED transmitting over a 1 m distance. This gives, for an emitter with a Lambertian mode, approximately, a path loss of 60 dB ($P_L = 1 \times 10^{-6}$) [10]. For low-frequency signals, (or if f_0 is large), the received signal $y(t)$ after the detector with sensitivity G_d (in V/W) is

$$y(t) = s_o(t) P_L G_d = \frac{\eta \langle E_p \rangle}{q} P_L G_d x(t), \tag{3.57}$$

thus, $H_0 = \eta \langle E_p \rangle P_L G_d / q$. To avoid that we have to limit our results for a specific propagation distance, light beam width, H_0, and transmit power, we take σ_x^2 and H_0^2/N_0 as lumped variables that jointly determine the link NPB. So, the link NPB is calculated as

$$\gamma = \frac{y_{rms}^2}{N_0 f_0} = \frac{\sigma_x^2 H_0^2}{N_0 f_0}, \tag{3.58}$$

and tested around 10^4 (40 dB). As we will confirm later, $f_0 \approx 10$ MHz. Practical receivers have an equivalent input (optical) noise of 5 nW in their 100 MHz electrical bandwidth [87]. At the output of the decoder,

$$N_0 = \frac{(G_d\, 5\text{ nW})^2}{100\text{ MHz}}. \tag{3.59}$$

To have $\gamma = 10^4$, $\sigma_{mod}^2 = 0.005$. In our example, that results in $i_{LED,rms} = 70$ mA and $P_{TX,a} = 0.6$ mW or -2.2 dBm. A NPB of 40 dB yields an optimum modulation bandwidth of 8.1, 7.4 and 5.2 times f_0 for waterfilling, uniform loading and pre-emphasis, respectively, assuming BER $= 10^{-4}$ (Γ of 7.39 dB). The received SNR from (3.52), (3.53) and (3.54) becomes 24.2 dB, 24.2 dB and 22.9 dB, respectively. Pre-emphasis excessively amplifies frequencies above f_0, that are deeply attenuated anyhow, thus that do not effectively contribute to the throughput. This is only possible by restricting $f_{\max}$ to lower values than used for waterfilling. Boosting high frequencies while fixing σ_x^2 implies poorer SNR at lower frequencies where the channel is good. Differences become particularly noticeable above NPBs of 40 dB, where $f_{\max_p}$ is several times larger than f_0. The maximum throughputs are plotted in Fig. 3.5(b) for a BER of 10^{-4}. The worst case modulation gap Γ for this BER used in the calculations of the throughput, Γ of 7.39 dB, obtained by assuming $M = 2$ in (3.28).

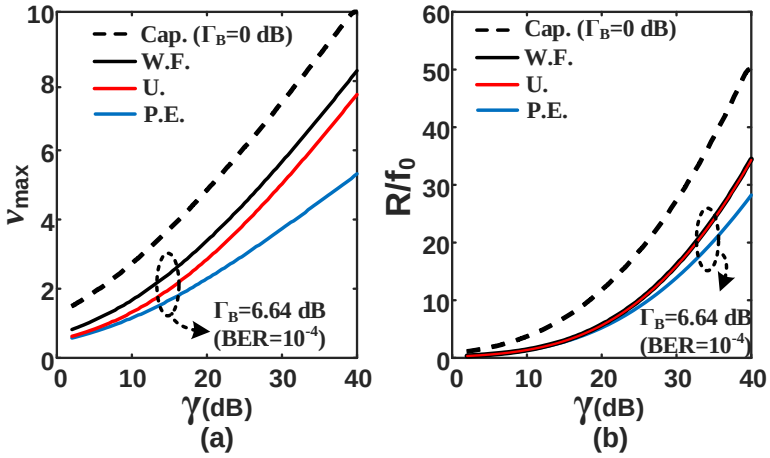

Figure 3.5: Theoretical (normalized) optimum modulation bandwidth $\nu_x = f_{\max_x}/f_0$ (x refers to w, u or p) and (normalized) maximum throughput as a function of NPB γ in (3.30) for waterfilling (dark), uniform loading (red) and pre-emphasis (blue) for BER $= 10^{-4}$. The throughput of the channel (using waterfilling strategy with Γ= 1) and the corresponding bandwidth are shown using dashed lines.

For comparison, Fig. 3.5 also contains the throughput and the corresponding modulation bandwidth for waterfilling with $\Gamma = 1$, shown with dashed-dark lines. Since waterfilling is the optimum power loading strategy calculated by employing Lagrangian method, the dashed plot in Fig. 3.5(b) corresponds to channel throughput and the required modulation bandwidth for this throughput is shown in Fig. 3.5(a). It can be seen that the waterfilling (dark) and the uniform approaches (red) achieve (almost) the same throughput for the given NPB γ and both outperform the pre-emphasis approach (blue). The required optimum modulation bandwidth of the waterfilling is the highest.

We define the relative maximum throughput difference for uniform loading and pre-emphasis strategy, compared with the waterfilling respectively, as

$$\Delta R_{wx}(\%) = 100\% \times \frac{R_w - R_x}{R_w}, \tag{3.60}$$

where the system reference x denotes either pre-emphasis (p) or uniform loading (u). Similarly, the relative bandwidth difference is defined as

$$\Delta f_{wx}(\%) = 100\% \times \frac{f_w - f_x}{f_w}. \tag{3.61}$$

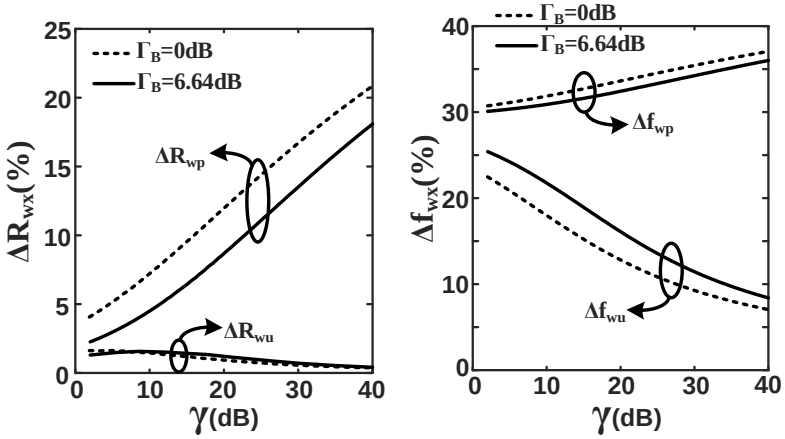

Figure 3.6: (a) Relative rate difference between waterfilling and uniform loading (ΔR_{wu}), and between waterfilling and pre-emphasis (ΔR_{wp}), (b) relative optimum bandwidth difference between waterfilling and uniform loading ($\Delta f_{\max,wu}$) and waterfilling and pre-emphasis ($\Delta f_{\max,wp}$) as a function of NPB γ (normalized to LED 3 dB BW).

These relative rate and required bandwidth differences are shown in Fig. 3.6. Waterfilling is seen to promise at most a 2% higher throughput than uniform loading, at low γ while the difference reduces to less than 0.3% at higher γ. Waterfilling continues to assign 'some' power at a 25% larger bandwidth (at low γ for Γ of 7.39 dB). Yet, this extension reduces to less than 10% at higher γ. Also, the bandwidth extension of waterfilling reduces for a lower Γ (higher BER). Waterfilling outperforms pre-emphasis, but at lower γ this is limited to, say, 5%, but it steadily grows beyond 20% at higher NPBs.

3.7 Experimental Verification

In order to validate to what extent practical loading schemes in previous sections stay short of the theoretical limits, we conducted experiments with OFDM transmission over a measured VLC channel as depicted in Fig. 3.7. The measurement setup is shown in Fig. 3.8. A 450 nm LXML-PB02-0023 blue LED with a measured 3-dB cut-off frequency of around $f_0 \approx 10$ MHz at I_{LED} =350 mA bias current was used at the transmitter. At the receiver side, we used a Silicon Avalanche Photo-Detector (Si-APD) with 100 MHz 3-dB bandwidth and 1 mm diameter active area followed by

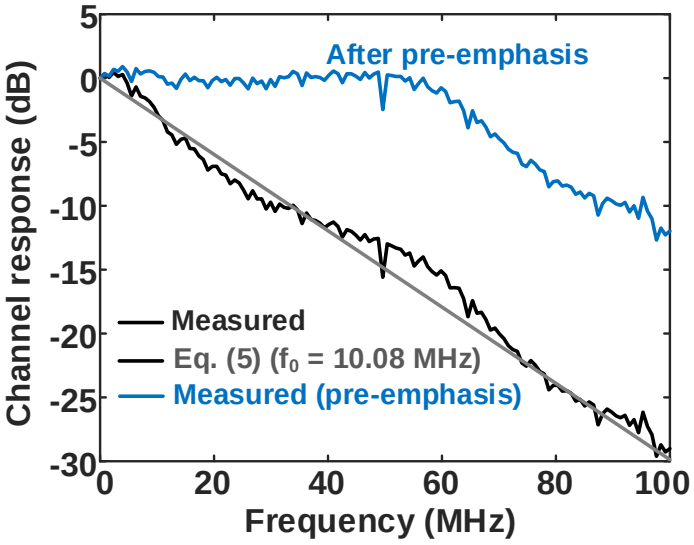

Figure 3.7: Measured response of the VLC link with Luxeon Rebel LXML-PB02-0023 blue LED (dark) and curve fitting (grey) with exponential curve ($f_0 = 10.08$ MHz), normalized to eliminate propagation attenuation ($H_0 = 1$). Channel response with a simple pre-emphasis (blue), given in (3.67), prior to the LED.

Table 3.1: OFDM parameters used for VLC measurements.

OFDM parameter	value
Maximum signal bandwidth	100 MHz
Sampling rate	200 Ms/s
Number of sub-carriers	128
Sub-carrier spacing	0.78125 MHz
IFFT/FFT size	256
Cyclic prefix length	26

a Trans-Impedance Amplifier (TIA). The normalized channel response was measured by directly modulating the LED with an OFDM signal having $N_s = 128$ sub-carriers within a bandwidth of $BW_X = 100$ MHz which allows us to implement a variable $f_{\max_w}$, $f_{\max_u}$ or $f_{\max_p}$ by assigning zero power to sub-carriers. The parameters are summarized in Table I. Adaptive allocation algorithms for discrete QAM constellations were used to validate the theoretical findings. The modulation parameter σ^2_{mod} was directly measured at the amplifier's input and to evaluate γ, given in (3.30), $H_0^2/N_0 f_0$ (Gain to noise ratio of the channel at DC normalized to f_0) was obtained from the received signal.

Initially, receiver estimates the SNR for each sub-carrier (SNR_n) and from the

allocated power to each sub-carrier ($S(n\Delta f)$) of the training sequence, the Gain to Noise Ratio (GNR) per sub-carrier can be determined as

$$GNR_n = \frac{SNR_n}{S(n\Delta f)} = \frac{S(n\Delta f)|H(n\Delta f)|^2}{N_0 \Delta f S(n\Delta f)} = \frac{|H(n\Delta f)|^2}{N_0 \Delta f}, \tag{3.62}$$

where Δf is a sub-carrier bandwidth.

To estimate γ, the 3 dB bandwidth f_0 needs to be estimated from the measured GNR. Plotting GNR in dB versus frequency in linear scale results in a straight line with a negative slope $\hat{a}$, that can be estimated via minimizing the Least Squares of the error:

$$\min_{\hat{a}} \sum_{n=1}^{N_s} \left\{10 \log_{10}\left[GNR_n\right] - \hat{a} n \Delta f\right\}^2. \tag{3.63}$$

Setting the derivative to zero results in

$$\hat{a} = \frac{10 \sum_{n=1}^{N_s} n \log_{10} GNR_n}{\Delta f \sum_{n=1}^{N_s} n^2} = \frac{60 \sum_{n=1}^{N_s} n \log_{10} GNR_n}{N_s(N_s+1)(2N_s+1)\Delta f}, \tag{3.64}$$

and from Eq. (3.9), we estimate the 3 dB cut-off frequency from the division $\hat{f}_0 = 10 \log_{10}(2)/\hat{a}$. On the measured channel, we saw $\hat{f}_0 = 10.08$ MHz. Some of the adaptive loading algorithms that we describe next also employ this estimation method as part of their adaptive loading.

3.7.1 Waterfilling

To resemble waterfilling, the Hughes-Hartogs (HH) algorithm [63] iteratively assigns one additional bit to the constellation of the particular sub-carrier that requires the lowest energy to increase its payload by one bit. Trying to accommodate an extra bit reflects an effort to further increase the throughput while spending the lowest extra possible energy for that extra bit. It can be interpreted as a discrete version of the Lagrangian derivation to make $dR_n/d\mathrm{E}\{|X_n^2|\}$ constant (similar to our τ), where R_n reflects the rate contributed by sub-carrier n, which utilizes the power $\mathrm{E}\{|X_n^2|\}$ on the nth sub-carrier. In fact, this algorithm converges to a loading with more or less equal partial derivatives at all frequencies, except for quantization effects caused by integer constellations. The average number of iterations to complete this algorithm is proportional to $O(B_{tot}N_s)$, where B_{tot} corresponds to the total number of loaded bits and N_s is the total number of sub-carriers. Since every active sub-carrier carries at least one bit, the complexity grows faster than with the square of N_s.

In our example, we let the algorithm target a BER of 10^{-4}, corresponding to a modulation gap of 7.39 dB. Fig. 3.9(a) shows the power loaded on each sub-carrier (normalized to modulation power) and the number of bits loaded on each sub-carrier

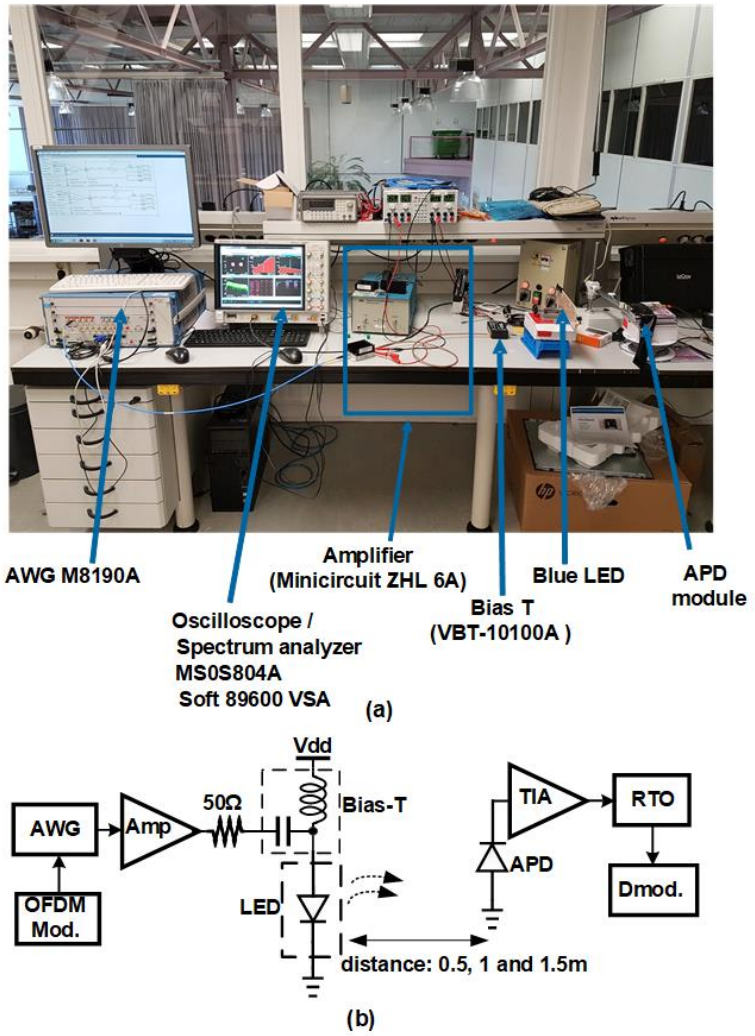

Figure 3.8: (a) Measurement Setup. (b) Schematic of the setup.

for NPB of 38.4 dB. Since only discrete number of bits can be loaded, the loaded power takes a sawtooth behavior around the ideal PSD, $S_w(f)$, illustrated in Fig. 3.4(b). For this NPB, 299.2 Mbit/sec is achieved in $f_{\max_w} = 71.9$ MHz ($N_{\max_w} = 92$). For the NPB of 38.4 dB and BER of 10^{-4}, our presented theory predicts a maximum throughput of 294.2 Mbit/sec in $f_{\max_w} = 76.7$ MHz. The small difference between the theoretical and experimental results are due to the small deviation of the channel response from the ideal exponential channel model shown in Fig. 3.7. Also the discrete constellation size (that needs to be used in practice) contributes to the difference.

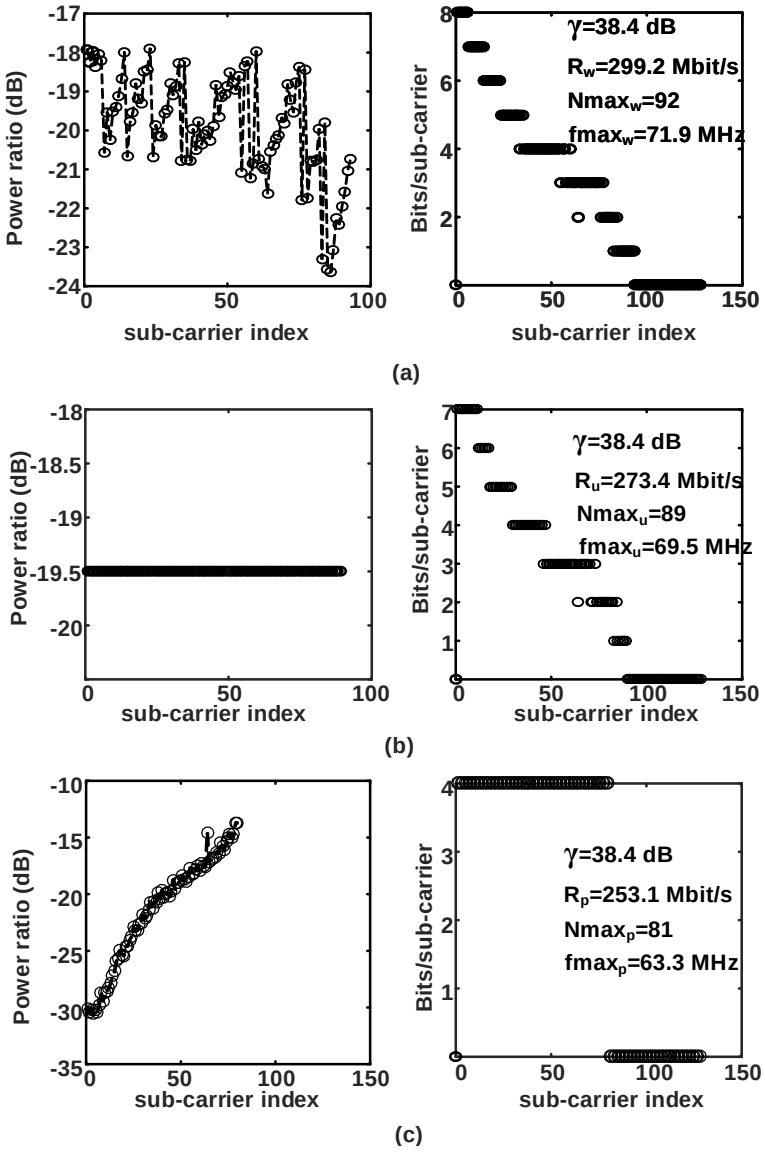

Figure 3.9: Experimental power (normalized to σ^2_{mod}) and number of bits loaded per sub-carrier for (a) waterfilling (HH algorithm [63]), (b) uniform loading after exhaustive search of the best $N_{\max}$ over VLC and (c) pre-emphasis employing strictly constant bit loading. For all three strategies $\mathrm{BER} = 10^{-4}$**.**

3.7.2 Uniform power loading

To uniformly load power, we need to find the optimum number of sub-carriers over which the uniform PSD extends. To examine to what extent the practical rates fall

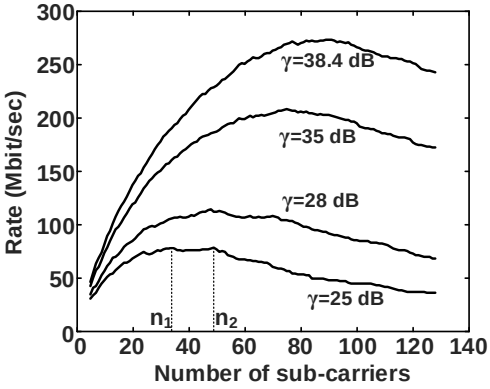

Figure 3.10: Rate R_u for uniform loading of the modulation power versus the number of used sub-carriers N_{max} for different values of γ over the measured channel of Fig. 3.7. Sub-carriers were loaded with discrete QAM constellations.

short compared to the theoretical derivations, a brute-force (but not necessarily efficient) approach was initially used to calculate R_u for all possible candidates for $N_{\max_u} \in (1, 2, ..N_s)$ and to pick the best. Fig. 3.10 shows the experimental throughput versus the number of sub-carriers for four different NPB values over the channel with the measured frequency response shown in Fig. 3.7. It differs from Fig. 3.3(a) in that it reflects a real measured channel and practical discrete constellation sizes.

Starting with a small number of sub-carriers, the system is very bandwidth limited, so the available power per sub-carrier is high. Theoretically, the rate grows in good approximation linearly, or more precisely, proportional to $N_{\max}$. Yet, in practice R_u is subject to jumps in suitable constellation size M. For example, for a γ of 38.4 dB using $N_{\max} = 5$ sub-carriers, each sub-carrier has a power budget allowing 2048-QAM (11 bits per sub-carrier). Using more sub-carriers, the available power for each sub-carrier reduces, but initially still 11 bits of payload are feasible. While doubling the number of sub-carriers to 10, the available power has reduced by a factor of 2, so at some point the payload needs to be reduced to 10 bits, but this results in one bit less (9% w.r.t. 11 bits). This jump causes non-monotonicity.

Only when the number of sub-carriers grows high, e.g. above 100 for γ of 38.4 dB, the effect that lower sub-carriers gradually reduce their payload is no longer compensated by having more sub-carriers, as the channel attenuation does not allow a significant payload at high frequencies. Fig. 3.10 confirms that for example for the NPB of 38.4 dB, the optimum rate is achieved at $N_{\max_u} = 89$. Fig. 3.9(b) plots the corresponding power and number of bits per sub-carrier. The throughput is 273.4 Mbit/sec over 69.5 MHz bandwidth. For this NPB, our theory predicts $f_{\max_u} =$ 69.8 MHz with an throughput of $R_u = 291.6$ Mbit/sec. Yet, in practice a discrete

constellation size must be loaded on each sub-carrier. The constellation size is always rounded down to an integer M in (3.26), which is seen to result in a slightly lower rate. Some sub-carriers contain up to 2 or 3 dB of extra power which cannot contribute to the rate. As the distribution of the utilized power overhead, expressed in dB, is in good approximation uniform, it corresponds to a loss of one half times the step in SNR required for two successive constellations (say, one half of 3 dB). Such waste is not experienced using HH. This explains why in theory waterfilling and uniform loading perform equally well, while in practice uniform loading lags about 1.5 dB.

Although Fig. 3.10 shows a good fit with the theory (say, as in Fig. 3.3(a)), due to the discretized M, the rate versus number of sub-carriers might not be unimodal, but exhibit multiple local peaks, e.g. n_1 and n_2 for γ around 25 dB. Non-convexity can be understood from discretization effects described before in this section. Formally, non-unimodality or non-convexity prevents us from using efficient search algorithms. However, one can exploit the observation that the peak is not sharp. An error in the estimation of $N_{\max_u}$ is unlikely to cause a major loss in the achieved rate. This allows us to use more efficient (than brute-force) approaches to approach the optimum number of sub-carriers to be used.

Search Approach

For a (sufficiently) unimodal function with one maximum, thus also for the case in Fig. 3.3(a), a simple golden search algorithm [131] can be implemented to find the optimum $N_{\max_u}$. In practice, due to discrete QAM constellation size, there can be local extremes, e.g. shown in Fig. 3.10 for γ of 28 dB and a local extreme is seen around 70 on the horizontal axis. Yet, we observed that the golden search algorithm nonetheless usually successfully detects the optimum $N_{\max_u}$. The golden search algorithm uses the golden number $G_r = \frac{1+\sqrt{5}}{2}$ and a simplified form of Golden search is given in Algorithm 1.

Algorithm 1 Golden search

Start with $n_l = 1$ and $n_u = 128$
for $n_u - n_l > 1$
  $n_1 = [n_u - \frac{n_u - n_l}{G_r}]$
  $n_2 = [n_1 + \frac{n_u - n_l}{G_r}] + 1$
  if $(R_u(n_1) > R_u(n_2))$ **then**
  $n_u = n_2$ **else** $n_l = n_1$
  end if
end for
Obtain the the optimum $N_{\max_u}$

Golden search algorithm takes two observation points n_1, n_2 with $n_2 > n_1$ between the boundary limits n_l and n_u using the golden number. The algorithm then compares

the throughput when n_1 and n_2 sub-carriers are used and limits the search range. One could take a more complex search algorithm with more observation points, but it more likely results into a unfavorable local optimum, which however is beyond the scope of this chapter.

Model-Based $N_{\max_u}$ Selection

In this section we propose to rely on the theory developed in this chapter. As discussed, there is a good agreement between the theoretical $f_{\max_u}$ and that obtained from brute-force approach for different γ. This motivated us to use our expression to obtain a suitable $f_{\max_u}$ in a single iteration.

As a first step the system must estimate f_0 and γ from the received signal, as described at the start of this section. Then for any γ, the $f_{\max_u}$ is obtained from a look up table based on (3.44) and the optimum number of sub-carriers follows a rounding form of $N_{\max_u} = [N_s \times \frac{f_{\max_u}}{BW_X}]$, where in our case $BW_X = 100$ MHz which is the maximum transmission bandwidth containing all N_s sub-carriers. In this example, an accuracy of ± 0.05 in normalized $f_{\max_u}$ results in an accuracy of ± 1 in $N_{\max_u}$. Hence, after finding the number of active sub-carriers, $N_{\max_u}$, we obtain the (fixed) transmit power $\mathbf{E}\{|X_n|^2\}$ per sub-carrier n as the constant $\mathbf{E}\{|X_n|^2\} = \sigma^2_{mod}/N_{\max_u}$.

Using receiver information about the actual channel gain for the nth sub-carrier, $H(n\Delta f)$, and the possibly frequency-dependent, noise levels N_{0_n}, the system calculates

$$\gamma_n = \mathbf{E}\{|X_n|^2\}|H(n\Delta f)|^2/N_{0_n}\Delta f.$$

Then, the maximum number of bits to meet the BER criterion is taken from a look-up table that records $b_n = [\log_2(1 + \gamma_n/\Gamma)]$. The number of bits b_n are rounded down to integer constellations, in particular 0, 1, 2, 3, ... corresponding to no data, BPSK, 4-QAM, 8-QAM, ... modulation levels, respectively. The total number of loaded bits is then summed to $B_{N_{\max_u}} = \Sigma_{n=1}^{N_{\max_u}} b_n$.

Table II compares the results obtained from brute-force, golden search and theory-based estimation using discrete QAM constellations. All three approaches estimate (almost) the same throughput for three different NPB values. The estimated number of sub-carriers for the golden search algorithm and the NPB of 25 dB is a bit off, compared to the theoretical expectations and the result of other algorithms. For this NPB, as shown in Fig. 3.10, there are two local extremes at n_1 (= 34) and n_2 (= 49) and the algorithm finds n_1 as the optimum number of sub-carriers. The rate penalty is negligible though. Further, we see that for 38.4 dB the choice of $N_{\max} = 89$ and 90 both give exactly the same $R_u = 273.4$ Mbit/s. Apparently the 90-th sub-carrier can carry 1 bit, but this is at the cost of 1 bit loss in the constellation for the 11^{st} sub-carrier that can no longer carry 7 bits.

Table 3.2: Comparison between the experimental results using proposed simplified algorithms for uniform loading, theoretical expectations and optimum experimental results for $\mathrm{BER} = 10^{-4}$**.**

		γ (dB)	$N_{\max_u}$	R_u (Mbps)
Theory		38.4	89	291.6
		29.5	60	142.4
		25	47	91.2
Experiment	Brute-force	38.4	89	273.4
		29.5	60	120.3
		25	49	75
	Golden search	38.4	90	273.4
		29.5	60	120.3
		25	34	74.2
	Model-based	38.4	89	273.4
		29.5	60	120.3
		25	47	73.4

The complexity of our simple uniform algorithms is linear with N_s. For the theory based approach, all sub-carriers are loaded in the first iteration. Golden search approach takes 10-12 iterations to converge. Since the power is uniform, another advantage is that the constellation mapping for M-QAM at the input of the transmit I-FFT can be done from a fixed set of points without a need for a weighing with an adaptive power level.

3.7.3 Pre-emphasis

The prime motivation for a pre-emphasis is to simplify the bit loading effort, limit the complexity of decoding, and minimize the exchange of system parameters between transmitter and receiver. Two approaches are compared in this chapter. A full-fledged method is, at every sub-carrier to digitally create a signal of the appropriate amplitude to guarantee a constant constellation. Since the constellation size is identical for all sub-carriers, the algorithm can simply try the effect of loading all sub-carriers with M bits, and pre-calculate the entire power loading for $M = 1, 2, 4, ...$ In pseudo code, this corresponds to Algorithm 2. That is, for a tested input constellation size, the algorithm assigns the corresponding required power for each sub-carrier, by step-wise increasing number of sub-carriers, and boosting their power by the inverse of the LED channel response. The loading stops when the distributed power tends to exceed the tolerable power σ^2_{mod} after the pre-emphasis. It selects the constellation size that achieves the highest rate.

From (3.22) and (3.23), the constellation size on n^{th} sub-carrier is

$$M(n\Delta f) = 1 + \frac{S(n\Delta f)|H(n\Delta f)|^2}{\Gamma N_0}. \tag{3.65}$$

Using the definition of GNR in (3.62), the constellation size can be written as

$$M(n\Delta f) = 1 + \frac{S(n\Delta f)\Delta f GNR_n}{\Gamma} = 1 + \frac{P[M,n]GNR_n}{\Gamma}, \tag{3.66}$$

where $P[M,n] = S(n\Delta f)\Delta f$ is the (normalized) power loaded on the sub-carrier n to carry a constellation size M. We have explicitly called $P[M,n]$ as the normalized power since its dimension is V^2 (at the IFF output) or A^2 (if the constraint is translated into current domain at LED input). The Algorithm 2 now readily follows.

Algorithm 2 Power and bits loading for pre-emphasis

```
Assess Γ and the channel GNR_n for all sub-carriers
    P = 0
for M = 2, 4, 8, 16, 32, 64
    n = 1
    while P < σ²_mod
    P[M,n] = Γ/GNR_n (M − 1) // Digital Pre-emphasis
    P = P + P[M,n] // LED Power constraint
    n++
    end while
    R(M) = n × M
end for
M_opt = arg max R(M)
```

Fig. 3.11 shows the experimental maximum modulation bandwidth and the rate as a function of the modulation order M. For a NPB of 38.4 dB, the optimum modulation order is 16-QAM ($M = 4$), for which the power and bit loading are plotted in Fig. 3.9(c). The throughput is 253.1 Mbit/sec, using 81 sub-carriers each loaded with 4 bits, and spanning 63.3 MHz. According to our presented theory, for the NPB of 38.4 dB, the modulation bandwidth to maximize the rate is 49.5 MHz and the throughput is 243.8 Mbits/s. The theoretical modulation order can also be readily calculated by dividing the throughput to the modulation bandwidth to be $2^{4.92}$. In practice, an integer modulation order, here 2^4 (16-QAM), is used which compared to theoretical (non-integer) counterpart requires a lower power per sub-carrier. Hence the algorithm extends the modulation bandwidth to make full use of the modulation power and modulating up to a larger $f_{\max_p}$ than predicted by continuous constellation sizes. This is seen by comparing the dashed-dark curves with their grey counterparts in Fig. 3.3(b). A slightly higher experimental rate than according to the theory is due to deviations of the channel from the exponential behavior.

A pragmatic pre-emphasis is to implement a fixed pre-filter of the form

$$H_p(f) = \kappa_r \frac{1 + j\frac{f}{f_0}}{1 + j\frac{f}{10f_0}}, \tag{3.67}$$

prior the LED driver. The constant κ_r is a backoff to satisfy the power constraint (3.32) at the LED input, taking the boosted high frequencies into account (similar to

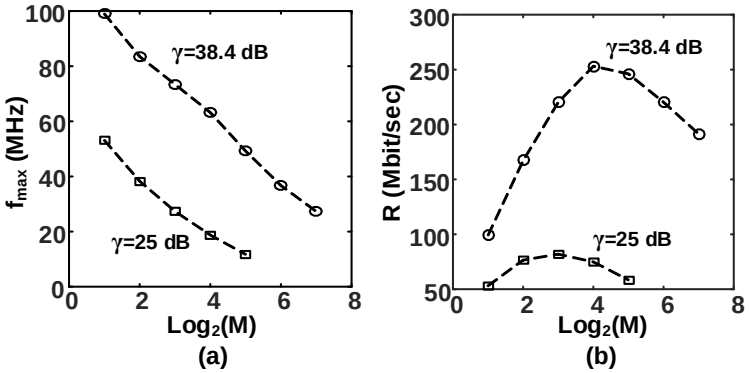

Figure 3.11: Experimental results for the (a) maximum modulation bandwidth ($f_{\max}$) and (b) the rate as a function of modulation order M for the pre-emphasis algorithm and two different NPB values for $\mathrm{BER} = 10^{-4}$**.**

(3.48)). The numerator acts as an intuitively appealing countermeasure against the low-pass effect of a junction capacitance [27], while the denominator avoids excessive boosting of very high frequencies. If f_0 is fixed and known in advance, an analog filter can consist of two resistors and a capacitor. If it is implemented digitally (in this work) as a single tap delay equalizer, it can adapt to variations in f_0 for instance due to temperature, dimming or aging [27]. The effect of this filter on the channel response is shown in Fig 3.7. Deviations occur particularly above 60 MHz (or $6f_0$), presumably because of APD limitations. Yet, for a NPB γ below 40 dB, the modulation bandwidth for optimized pre-emphasized power loading does not exceed $5f_0$ (Fig. 3.5(a)), so the deviation above 60 MHz may be less relevant. Note that the phase distortion by the channel as well as by the pre-emphasis filter is not affecting the power allocation per sub-carrier. For each sub-carrier the phase distortion can be considered as a constant phase offset which can be easily compensated at the receiver side.

In this scheme, the number of used sub-carriers and the choice of constellation is initially set to a discretized value obtained from the theoretical results. To be specific, one could use a look up table based on (3.49) and (3.50), with the available NPB γ as input, and a theoretical result for ν_p and $\Re_p$, respectively. This look-up table thus stores f_{max_p} and the optimum constellation size M (M_{opt}) as a function of γ. The resulting M_{opt} from the theory may not be an integer number (Table III) and the channel deviations from the theoretical exponential behavior also contribute to deviations from the theory. Therefore, the transmitter tries both $\lfloor M_{opt} \rfloor$ and $\lfloor M_{opt} \rfloor + 1$ as the constellation size. For example, in Fig. 3.3(b) and for γ of 30 dB, the optimum rate is at the cross point of the corresponding dashed-dark curve with the solid optimum rate curve. In practice, only rates on the saw-tooth curve are feasible, or, accepting sub-optimal operation, on the connecting straight lines to

Table 3.3: Comparison between the experimental results using proposed algorithms for the pre-emphasis loading and theoretical expectations for BER $= 10^{-4}$**.**

		γ (dB)	$N_{\max_p}$	M_{opt}	R_p (Mbps)
Theory		38.4	63	30.5	243.8
		29.5	45	11.6	125
		25	36	7.3	82.6
Experiments	FFT Channel Inversion (Alg. 2)	38.4	81	16	253.1
		29.5	50	8	117.2
		25	33	8	77.3
	Fixed Pre-filter	38.4	80	16	250
		29.5	52	8	121.9
		25	34	8	79.7

the origin. The saw-tooth upper dents show two local maximums at both sides of the theoretical optimum rate.

If a generic high-boost (3.67) is implemented, the outer-OFDM system sees a channel that is approximately flat. While a fixed constellation can presumably be applied, the bit error rates may differ slightly per subcarrier, due to model mismatch, aging, etc., or due to narrowband effects, possibly interference. Our results indicate that a small SNR margin, preferably with interleaved coding is likely to overcome this, unless major wideband deviations occur. In our example, the fall off above 60 MHz would require such further measures.

Table III compares the outputs of the approaches, Algorithm 2 and using the pre-filter, given in (3.67), with those resulting from the theory. The optimum modulation bandwidth (or equivalently $N_{\max_p}$) can be larger or smaller than that predicted by the theory depending on whether the practical M_{opt} is the lower integer number respectively higher integer number than the theoretical optimum value. Yet, the theoretical throughputs are very close to those predicted by the theory.

3.7.4 Experimental Comparison

Fig. 3.12 shows the measurement results of the previous subsections (on top of theoretical plots) for a BER $= 10^{-4}$ as a function of γ. Compared with Fig. 3.5, this figure shows the actual rates and compares them with the experimental results. Changing the NPB γ, can be seen as changing the distance between the transmitter and the receiver (hence the channel DC gain H_0) from the minimum distance (approximately) 0.5 m to 1 and 1.5 m. Yet as the channel transfer function appeared to predominantly depend on LED and photodiode properties but not on the light propagation channel, we extrapolated by keeping the shape of $H(f)$ constant, but just changed H_0. To be able to confirm our theoretical derivations, for uniform loading a brute-force approach was considered to obtain the optimum modulation bandwidth and the throughput. For the pre-emphasis the Algorithm 2 was used to truly implement the pre-emphasis.

The experiments confirm that waterfilling demands more bandwidth. We see a

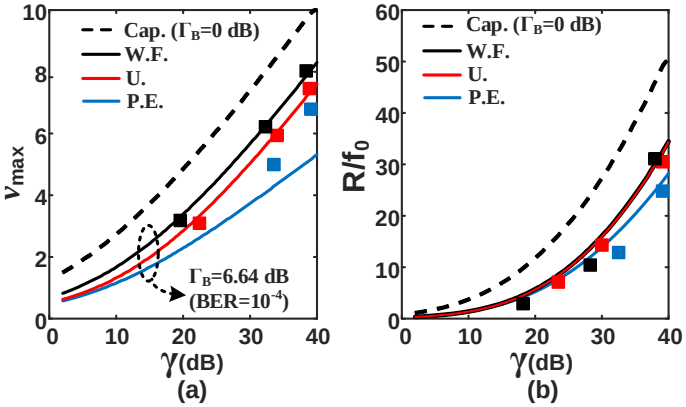

Figure 3.12: Theoretical (solid) and measured (squares) bandwidth ν_x and throughput $\Re_x$ as a function of NPB γ in (3.30). All parameters are normalized to LED 3 dB bandwidth f_0, BER $= 10^{-4}$ and are shown for waterfilling (dark), uniform loading (red) and pre-emphasis (blue). The throughput of the channel and the corresponding bandwidth are in dashed lines.

good fit between the measurements and the theoretical findings, although there are small deviations of the channel response from (3.9) and quantization of the number of loaded bits (see Fig. 3.9).

3.8 Conclusion

In this chapter, we compared the performance of three power loading strategies: waterfilling, uniform loading and applying a pre-emphasis in IM/DD systems for the specific illumination LED channel response, as experienced in VLC. We argued that it is an (extra) power-constrained channel. This allowed us to derive mathematical solutions for the throughput of various loading strategies. We proposed a suitable bandwidth normalization, that allows to plot a single power-budget-versus-rate curve that generically applies to any LED that adheres to the now commonly referred LED frequency response.

The results were validated experimentally with adaptive allocation algorithms. The obtained theoretical results reveal that waterfilling and uniform loading achieve almost the same data rate, while outperforming pre-emphasis. A waterfilling strategy is known to provide the highest possible throughput. However, in practice uniform loading, as used for instance in the ITU g.9991 standard, can be attractive for practical reasons. The uniform loading, in order to be near-optimum needs to be truncated at

an optimized frequency, which we quantified in this chapter. This optimum frequency depends on the LED 3 dB bandwidth and on the NPB. The imposed complexity of the implementation of waterfilling may not always be justified by the benefits from throughput, as uniform loading only loses less than 2% of the overall maximum rate. Furthermore, this deviation vanishes for higher NPBs and is already negligible for typical NPBs used in practice. This inspired us to study alternative algorithms, that exploit the prior knowledge of the LED channel driven by a constant power spectral density.

We saw that the modulation bandwidth optimized for waterfilling loads higher frequencies, while a pre-emphasis strategy to flatten the channel frequency response requires the minimum modulation bandwidth. Moreover, an algorithm that forces a strictly uniform power loses some performance because it can only load a discrete constellation with an integer number of bits.

Our throughput results show that there is a penalty for using pre-emphasis. This penalty may seem small if the bandwidth is well adapted to the link NPB. Yet, when pre-emphasis is applied over a pre-set, fixed, standardized bandwidth, very pronounced stepwise reductions in bit rates will be seen if the receiver moves away from the transmitter (declining SNR). We expect a hard, stepwise cut-off of the range, while uniform loading is expected to exhibit a more graceful degradation, even if bandwidth is not adapted.

Pre-knowledge of the modulation bandwidth, as we quantified analytically, can be used to find for instance preferred maximum bandwidths supported in a standard, or set the required sampling rate of the D/A and A/D converters as well as the optimum bandwidth of the filters at the receiver. These impact power consumption and the quality of the received signal at the receiver. Here we noticed that waterfilling may have the disadvantage that it may consume a bit more power in the electronics due to slightly higher clock speeds. Furthermore, the derivation of a theoretically optimum modulation bandwidth can be used as an input to algorithms that implement the power-bit loading, to improve the convergence rate or to simplify the algorithm while maintaining performance.

Chapter 4

Optimization and Comparison of M-PAM and Optical OFDM Modulation

In chapter 3, DCO-OFDM over VLC was discussed. For VLC only the extra power consumed for modulation is of interest (DC bias is dictated by illumination) and the modulation index is low enough to ensure energystar compliance. This low modulation index will not result in distortion/clipping in the LED current. For IR applications, however, the total electrical power is important. That is, the LED bias current may not be chosen such that it is much larger than the modulation rms, then distortion/clipping in the LED current is expected. This chapter studies the effect of such distortions/clipping in the system throughput employing DCO-OFDM and compares it with the throughput of a simpler (in implementation) Pulse Amplitude Modulation scheme. It is shown that the clipping limits the DCO-OFDM performance to the extent that PAM becomes more interesting.

4.1 Introduction

[1]The rapid growth of bandwidth-intensive mobile applications combined with the emerging Internet-of-Things (IoT) services are putting immense pressure on the Radio Frequency (RF) spectrum. Recently, Optical Wireless Communication (OWC) has gained research attention from both academia and industry to provide an alternative technology for the currently predominantly RF-based connectivity [13, 19, 104, 105].

[1]This chapter consists of material previously published in IEEE Open Journal of the Communications Society [73] which was re-structured for readability in thesis form.

OWC, employing visible light (denoted as Visible Light Communication, VLC) or the Infrared spectrum (denoted as IR communication), offers unique features, such as free access to huge amounts of unregulated but largely interference–free bandwidth, a high degree of spatial reuse, secure connectivity, and absence of electromagnetic interference.

The output optical flux of commercial Light Emitting Diodes (LEDs), illumination or IR LEDs, is modulated in an Intensity Modulation Direct Detection (IM/DD) OWC system. This optical channel, typically, exhibits a low–pass frequency response with a 3 dB bandwidth that is dominated by LED properties which are not optimized for communication purposes. This low–pass nature, in particular the LED junction capacitance attenuates higher frequencies in the intensity-modulated spectrum [40, 42, 45, 72, 105]. In this respect, line-of-sight OWC differs from Rayleigh or Rician distributions in radio communication where frequency-selective fades are sufficiently narrow to be overcome by coding and interleaving, employed in IEEE 802.11a/g standard. In OWC, excessive attenuation occurs in too wide portions of the bandwidth to rely on coding.

To handle the low-pass nature of LEDs, Orthogonal Frequency-Division Multiplexing (OFDM) yet adapted for optical applications (denoted as Optical OFDM, O-OFDM) is popular [55, 56]. There is a persistent debate on whether multi-carrier OFDM outperforms carrier–free modulation, such as Pulse Amplitude Modulation (PAM) over an OWC low-pass channel. In fact, O-OFDM allows one to optimize the distribution of the available modulation power among the sub-carriers and to select the bit load independently on every sub-carrier to maximize the data rate [72]. However, the OFDM composition of multiple frequency components has a high Peak to Average Power Ratio (PAPR) that increases the power consumption. A large DC bias needs to accommodate peaks in the signal. OFDM also requires highly linear amplifiers, which are inefficient. In an OWC link, a pre-emphasis filter can be used in front of the LED to flatten the channel frequency response. In this case, OFDM might no longer be needed. In such a flattened channel, using the simpler PAM modulation with lower PAPR reduces the biasing power waste [48, 54]. A comparison involves consideration of many aspects, which we further extend in this chapter.

Depending on the application, the constraint on the channel differs. For VLC, the DC power is already available for the illumination and the modern LEDs are designed to have a high wall-plug-to-lumen efficiency. However, modulation costs extra electrical power that can deteriorate the overall system efficiency and has to be limited. Thus, for VLC, *extra* consumed power is the key constraint, rather than total electrical power [133]. Particularly for IR, human eye safety can limit the average optical power to be transmitted by the LED [134].

To have a fair comparison of PAM and DC-biased Optical OFDM (DCO-OFDM) under certain constraints, one needs to operate both systems at their particular opti-

Table 4.1: Current work in comparison with the previously published works.

		[48]	[54]	[135]	[60]	[49]	[51]	**This work**
OFDM	Clipping noise	Filtered	Flat/white	Filtered	Filtered	Filtered/white	Flat	Filtered/colored
	Mod.[1] depth optimization	Numerically	Numerically	No[3]	Numerically	Yes	N.A.	Yes
	Bandwidth optimization	Numerically	Numerically	No	Numerically	Yes/No[6]	N.A.	Analytically
	Channel model	LPF /multipath	1^{st} LPF[2]	1^{st} LPF	Cosine	Dispersive[7]/flat	flat (1 Hz)	Exponential
	Power/bit loading	Waterfilling	Waterfilling	N.A.[4]	Waterfilling	Waterfilling	N.A	Waterfilling/P.E.[10]
	Throughput expressions	No	No	No	No	No	in 1 Hz	Expressions
PAM	Constellation optimization	No	Numerically	No	No[5]	N.A.	N.A.	Analytically
	Low-pass mitigation	Equalizer	Equalizer	Equalizer	No	N.A.	N.A.	Pre-emphasis
	Bandwidth optimization	No	Numerically	No	No	N.A.	N.A.	Yes
	Power constraint	Optical	Optical	N.A.	N.A.	Opt.[8]/Elec.[9] ($V_0 = 0$).	Opt/Elec.	Versatile

[1] Modulation. [2] Low pass filter. Briefly covered in numerical simulations. [3] PAM and OFDM variants are compared for 1, 2 and 3 bit/s/Hz of data rate. [4]Not Applicable. [5] Only OOK is discussed. [6] Yes for dispersive channels and No for flat channels. [7] Time domain impulse response was used. [8] Optical. [9] Electrical. [10] Pre-emphasis.

mum. A proper framework includes for OFDM:

- optimum sub-carrier–dependent bit and power loading,
- optimized total bandwidth, and
- optimum bias current and modulation depth, in relation to the optimally tolerated clipping level, considering a realistic non-linear LED model (clipping, static and dynamic higher–order terms),

includes for PAM:

- pre-emphasis, with associated back-off to adhere to the power constraint and
- optimum bandwidth and modulation order as, in contrast to non-dispersive AWGN channels adhering to Shannon limits, we see that for the LED channel, the optimum does not necessarily lies at the smallest constellation (e.g. 2-PAM) and using the corresponding large bandwidth,

and for both modulation methods addresses

- the type of (extra) electrical or optical power constraint imposed by the application, and
- the low-pass LED response.

The comparison of different modulation schemes was studied extensively. For instance, [48], [54], [135] and [60] compare OFDM variants with a PAM scheme, while [49,51] address OFDM variants. In fact, with respect to the above listed aspects, previous works known to us lack at least one aspect or do not generalize their findings into generic expressions that extend outside the simulation range. We summarize the comparison between prior art and this work in Table 5.1.

DCO-PAM, thus level-shifted, non-negative PAM was found in [48] to outperform all variants of OFDM in terms of optical power efficiency (including DC bias power) over a range of spectral efficiencies. In [48], a Decision Feedback Equalizer (DFE) was used to combat the LED low-pass nature and the optimization of the bit loading in OFDM could not revert this finding. However, the DFE has a high complexity, while we show that already with a simple pre-emphasis filter, PAM can become attractive, provided that also the constellation size is optimized for the LED response, in particular allowing $M = 8, ..$ for high Signal to Noise Ratio (SNR). In fact, [48] used 2 and 4-PAM only, presumably because of the DFE restrictions.

Numerical optimization for a constrained peak optical power in [54] showed that in a limited bandwidth, DCO-PAM performs better. However, in contrast to RF, the bandwidth in unregulated OWC is a design freedom that preferably is not a priori

restricted. We see that for the same transmit power constraint, different modulation methods and different constellations each have a different optimum bandwidth, and that it leads to different SNR profiles along the frequency axis. Hence SNR is not a preferred benchmark.

In DCO-OFDM, the modulation depth, relative to the DC-bias determines the amount of clipping. This may prohibit the use of larger modulation orders. In [54], clipping noise was assumed to have a flat spectrum at the receiver over all FFT outputs regardless of the actual signal bandwidth. However, we show that the clipping noise predominantly depends on the modulation bandwidth. That is, one cannot arbitrarily spread clipping noise outside the signal bandwidth by using faster, oversized FFT processing at the receiver. Moreover, the clipping artefacts further are subject to the low–pass LED frequency response. As shown in Table 5.1, this was simplified in previous works.

The work in [135] compares single–carrier (but frequency–domain equalized) M-PAM modulation to multiple OFDM variants, with a main focus on multi-path dispersion of the OWC propagation channel. M-PAM appeared to require a lower SNR to achieve the same Bit Error Rate (BER). Both LED clipping and low-pass memory effects are covered in numerical simulations. However, no further optimizations for modulation bandwidth nor for a (frequency–adaptive) modulation order are discussed. On-Off Keying (OOK) shows a better optical power efficiency than DCO-OFDM and unipolar Asymmetric Clipped Optical OFDM (ACO-OFDM) in single-mode fiber systems [60], where the DC bias and bandwidth optimizations were carried out by numerical simulations, considering clipping for low biases. In fact, at low available transmit power, ACO-OFDM can become more attractive than DCO-OFDM [48,57]. However, Section 4.7.B shows that PAM reaches higher throughput for the same power.

In [49], OFDM has been studied for VLC in flat and dispersive channels, addressing also clipping noise while optimizing the DC offset of OFDM. However, the practical limitations of a discrete modulation order and an optimization of the modulation bandwidth for OFDM were not discussed. On a pre-emphasized channel, the use of a fixed number of constellation bits over a fixed (non-optimized) bandwidth causes pronounced, abrupt discontinuities in the throughput, versus changes in the SNR [72]. That is, e.g., if the receiver gradually moves away from the transmitter, there will be a stepwise, non-graceful cut-off in throughput. In [51], throughput achieved by OFDM-based schemes were discussed. The clipping noise as well as the distortion introduced by the LED are modelled. However, the results of [51] did not include the frequency selectivity of the LED channel.

To optimize OFDM for frequency selective LED channels, different power and bit loading strategies have been discussed in the literature, e.g. [62–64, 72, 121, 136, 137]. Waterfilling and uniform bit loading (also known as pre-emphasized power loading)

are the two well-known strategies. Waterfilling is known as the optimum strategy that results in the maximum throughput in a frequency selective communication channel [62]. However, it requires a (relatively) complex algorithm [63, 64, 72]. The existing ITU g.9991 standard [65] simplifies this into assigning the same power level to all sub-carriers, but adapts the constellation per sub-carrier. Forcing a uniform constellation on all sub-carriers would further simplify the implementation to a great extent [137]. This is also considered in the current standardization of IEEE 802.11bb [66], as it can reuse approaches designed earlier for RF channels. In this work both waterfilling and pre-emphasis strategies are considered.

The main contributions of this work include the following:

- In many other communication channels, using a higher bandwidth enhances throughput. In contrast to this, we show that for an LED there exists an optimum modulation bandwidth beyond which the throughput reduces. Moreover, OWC standards that fix bandwidth, as radio standards typically do, abruptly fail to sustain a weakening link.

- To make a fair comparison among systems that optimize their transmit bandwidth, we introduce the Normalized Power Budget (NPB), defined as transmit power corrected for path loss, normalized to the noise in the 3 dB bandwidth of the LED. In fact, we cannot use the bandwidth of transmit signal as different modulation strategies optimize differently.

- We derive mathematical expressions for the throughput and the preferred modulation bandwidth for DCO-PAM and DCO-OFDM. Using the now commonly reported exponential OWC channel frequency response [26,58], we capture these in new expressions. Hitherto, the comparisons were mostly limited to simulations for specific settings, thereby did not give generic expressions for other settings. Furthermore, we derive expressions for the optimum modulation bandwidth for DCO-OFDM and for (DCO-) PAM, considering discrete modulation orders and optimizing for the LED low-pass response. Our optimization includes the impact of limiting the DC bias for an OFDM signal, by allowing clipping and by making a trade off with the resulting clipping noise.

- We quantify clipping for DCO-OFDM as it raises the perceived noise floor and thereby limits the usable modulation order, even in a further noise–free channel. Following arguments in [27, 48, 49, 72, 75], we conclude that for modern LEDs, a saturation peak limit does not accurately model the behavior. We use and extend the clipping noise model of [49] which considered one-sided clipping of the LED current. This extends our previous bit loading evaluations in [72], which assumed clipping-free DCO-OFDM, leading to more complete, realistic model.

- We compare constrained optical power (related to the average LED current), the extra electrical power (related to the variance of the current caused by modulation) and the total electrical power (related to a combination of DC current and AC variance, weighted by the LED (say, bandgap) voltage and the dynamic resistance, respectively). While previously published works, e.g., [48], [54], [135] and [60], often report outspoken preferences for the choice of modulation, we conclude that there is not always simple unique answer to the question whether OFDM and PAM is performing better, depending on which constraint applies.

- We show that in a VLC context, where the extra power needs to be far below the illumination power, there is no difference in performance between pre-emphasized DCO-OFDM and a DCO-PAM. However, DCO-OFDM with waterfilling outperforms DCO-PAM.

- For IR, where the bias or the mean DC light has to be paid for from the communication power budget, PAM with an appropriate high-boost and a carefully chosen bit rate and bandwidth outperforms pre-emphasized OFDM. Our model of the impact of clipping artefacts allows us to optimize the choice of the modulation depth for OFDM. In fact, one can intuitively interpret our results as a quantification that the power penalty incurred for the DC bias in pre-emphasized DCO-OFDM is not compensated by the ability to adaptively load sub-carriers over a certain NPB range. For high power budgets, say NPB above 30 dB, however, OFDM with waterfilling and optimum choice of LED bias current outperforms PAM. Here, OFDM can fully exploit the adaptive bit and power loading. For high power budgets one can afford a large back-off of the modulation depth to avoid clipping of the OFDM signal, the latter conclusion disagrees with [54]. We show that the crossover point where OFDM with waterfilling outperforms PAM moves to higher power budget values when LED is biased at higher currents. If, instead, more LEDs were used to boost coverage, this would not happen.

- We propose a simple rule of thumb and an algorithm to optimize the modulation order and the modulation bandwidth of M-PAM, which works for both VLC and IR applications.

The rest of the chapter is organized as follows. We start with a short introduction to the OWC link and the realistic LED channel model in section 4.2. Section 4.3 presents the DCO-PAM model, its performance over an OWC channel and the DC penalty required. DCO-OFDM is discussed in section 4.4. Both the continuous (for theoretical purposes) and discrete (practical case) modulation orders are discussed. This section also presents the optimum waterfilling approach results for the

comparison. The DC penalty and the clipping noise associated with DCO-OFDM is discussed in section 4.5. In section 4.6 a proper measure is given to choose a proper DC bias for the LED based on the modulation order. Furthermore, this section includes the distortion power due to clipping (to reduce the DC penalty) of the LED current in the throughput and modulation bandwidth requirement. Section 4.7 compares DCO-OFDM and DCO-PAM in three different contexts, VLC, IR and average–optical–power constrained channels. The computational complexity of DCO-OFDM and PAM is discussed in section 4.8. Finally, conclusions are drawn in section 4.9.

4.2 OWC Power Constraints

In this chapter three main power constraints in an OWC channel are discussed, optical power constraint in both IR and VLC applications, electrical power constraint in IR and extra power constraint in VLC. For more details we refer to section 3.3.

4.2.1 Channel Model

The low-pass frequency response of the LED channel from LED current to photodiode current can be modeled as a low-pass filter with exponential decay, discussed in chapter 2,

$$|H(f)|^2 = H_0^2 2^{-f/f_0}, \tag{4.1}$$

where H_0 and f_0 are the low frequency channel gain and the 3 dB cut-off frequency, respectively.

We focus on Line-of-Sight (LoS) channels. In fact, we increasingly see the creation of beam steering emitters and of angular diversity receivers. In such case, each resolved angular path is not likely to be subject to a significant delay spread. Hence, we believe that the reflection-free LoS assumption remains relevant. If nonetheless long delay spreads occur, a linear time–domain equalizer can become complex for PAM, and frequency–domain equalization may be preferred, as in OFDM [135].

4.2.2 Normalized Power Budget (NPB) Definition

Often, systems are compared based on the (frequency–average) SNR at the receiver, for a particular choice of the modulation bandwidth. However, this leads to an intrinsically unfair comparison as PAM and OFDM benefit differently from expanding the modulation bandwidth further beyond the LED 3 dB bandwidth. In fact, bandwidth is a parameter subject to modulation–specific optimization constrained by transmit power. This prohibits us to compare two systems just with the same bandwidth or with the same SNR. Although, it seemingly complicates the number of variables, we

must restrict a comparison to essential parameters that are not a design freedom. Similar to chapter 3, we use H_0, f_0, the modulation rms σ^2_{mod} and the noise spectral density N_0, represented in A^2/Hz, referenced to currents through the photodiode detector at the receiver and we define the NPB γ as

$$\gamma = \frac{\sigma^2_{mod} H_0^2}{N_0 f_0}. \tag{4.2}$$

In fact, normalizing to the LED bandwidth f_0 and not to signal bandwidth f_{max} allows us to plot generic curves for throughput. To optimally cope with the frequency-dependent channel response $H(f)$, we take the freedom to optimize the emitted spectral density $S_x(f)$ and the total bandwidth. The subscript x indicates the modulation strategy; PAM for DCO-PAM, p for DCO-OFDM with pre-emphasis and w for DCO-OFDM with waterfilling. The noise bandwidth is subject to dynamic adaptations and the SNR is frequency dependent:

$$\mathrm{SNR}(f) = \frac{S_x(f)|H(f)|^2}{N_0}. \tag{4.3}$$

We denote the frequency-domain spectral density of $i_{led}(t)$ by $S_x(f)$, expressed in A^2/Hz. Over the signal bandwidth, $S_x(f)$ integrates to σ^2_{mod}. That is,

$$\int_f S_x(f) df = \sigma^2_{mod}. \tag{4.4}$$

Here, σ^2_{mod} and γ address effective signal powers thus allow the calculation of link performance, but ignore DC-biasing power. We relate these to consumed power later when we invoke β weight factors, defined in section 3.3.

For a pre-emphasized spectrum, the received modulation spectrum after the photodiode, $S_x(f)|H(f)|^2$, is flat over frequency. To achieve this, $S_x(f)$ inverts $H(f)$ according to

$$S_x(f) = \kappa \frac{\sigma^2_{mod}}{f_x} 2^{f/f_0}, \tag{4.5}$$

where κ is the pre-emphasis back-off to satisfy the constraint (4.4) and f_x is the modulation bandwidth over which the $S_x(f)$ is spread. Inserting (4.5) into (4.4), the coefficient κ is calculated as

$$\kappa = \frac{\ln(2) f_x/f_0}{2^{f_x/f_0} - 1}. \tag{4.6}$$

If, for PAM, instead of a pre-filter, a linear post-equalizer is used, the transmit current density is uniform, or fully determined by the pulse shaping. However, the receive filter will then boost the noise in every sample by κ. That is, the SNR for every PAM sample is the same for either a pre or post equalization (κ applies).

4.3 Pulse Amplitude Modulation (PAM)

PAM requires a flat frequency response for Inter–Symbol Interference (ISI) free communication. To repair the low–pass LED frequency response, as in (4.1), a linear equalizer can be used to boost high frequency components [35, 138]. According to Nyquist theory, a baseband PAM signal with a bandwidth f_{PAM} can accommodate $2Tf_{\mathrm{PAM}}$ symbol dimensions in a time interval T. For a symbol duration T_s ($T_s = 1/(2f_{\mathrm{PAM}})$), we multiply the numerator of the SNR in (4.3) by $2T_s f_{\mathrm{PAM}}$, thus by unity, to get

$$\mathrm{SNR}_{\mathrm{PAM}}(f) = \frac{2S_{\mathrm{PAM}}(f)|H(f)|^2 f_{\mathrm{PAM}} T_s}{N_0} = \frac{2\epsilon_N}{N_0}. \tag{4.7}$$

where ϵ_N is the average received symbol energy per dimension. For PAM, the energy per symbol ϵ_s equals ϵ_N, while for two-dimensional QAM, as used in OFDM, $\epsilon_s = 2\epsilon_N$.

In (bi-polar) M-PAM, input data are mapped into a zero-mean sequence of symbols chosen from M discrete levels, uniformly spaced by distance $2d_M$, so

$$s_m = md_M, \quad m \in \{\pm(M-1), \pm(M-3), ..., \pm 1\}. \tag{4.8}$$

The average energy per symbol (at the receiver), ϵ_s, is

$$\epsilon_s = \epsilon_N = \frac{2d_M^2}{M} \sum_{m=1}^{M/2} m^2 = \frac{M^2-1}{3} d_M^2. \tag{4.9}$$

The distance d_M can then be expressed as a function of ϵ_N as follows:

$$d_M = \sqrt{\frac{3\epsilon_N}{M^2-1}}. \tag{4.10}$$

The BER is expressed as [61]

$$\mathrm{BER_M} = \frac{2}{\log_2 M} \left(\frac{M-1}{M}\right) Q\left(\sqrt{\frac{6\epsilon_N}{(M^2-1)\,N_0}}\right). \tag{4.11}$$

Thus, the average energy requirement of a M-PAM scheme, normalized to N_0 and denoted as $X(M)$ for a pre-determined $\mathrm{BER_M}$ is

$$X(M) = \frac{M^2-1}{6} \left(Q^{-1}\left(\frac{M\log_2 M}{2(M-1)}\mathrm{BER_M}\right)\right)^2. \tag{4.12}$$

We list $X(M)$ in Table 5.2 and extend it to M^2-QAM by interpreting QAM as just a 2D variant of M-PAM. We explicitly use a different symbol $X(M)$ to represent a fixed system property, while ϵ_N/N_0 is a property of the incoming signal, subject to optimization and may even be frequency dependent. Within a Nyquist bandwidth of f_{PAM}, a system reaches a throughput R_{PAM} of

$$R_{\mathrm{PAM}} = 2f_{\mathrm{PAM}}\log_2 M. \tag{4.13}$$

Table 4.2: Required received average energy per dimension normalized to N_0 for different constellation size (M) and the minimum normalized bias requirement z at BER=10^{-4}.

M	QAM order	$X(M)$	$X(M)$ in dB	z (OFDM)
2	4	6.92	8.4	1.11
4	16	33.23	15.2	1.69
8	64	134.61	21.3	2.15
16	256	527.49	27.2	2.57
32	1024	2055.6	33.1	2.95

4.3.1 PAM Bias Penalty

For PAM as in (4.8), a DC-bias of at least $(M-1)d_M$ is needed to make the LED signal non-negative. We define a parameter z to be the ratio of the bias current over the LED rms current. For PAM,

$$z = \frac{\mathrm{I_{LED}}}{\sigma_{mod}} = \frac{(M-1)d_M}{\sqrt{\frac{M^2-1}{3}}d_M} = \sqrt{3\frac{M-1}{M+1}}, \tag{4.14}$$

where the variance of the modulation σ_{mod} can be calculated from (4.8), as $\sigma_{mod} = d_M\sqrt{(M^2-1)/3}$. For such DCO-PAM, the parameter z depends on the modulation order M. It equals $z = 1$ for $M = 2$ and approaches $z = \sqrt{3}$ for $M \to \infty$. We will use this parameter in the later sections to compare PAM with OFDM.

4.3.2 Throughput of DCO-PAM over Low-Pass Channel

Inserting (4.5) into (4.3) with κ given in (4.6) and the channel model (4.1), the $\mathrm{SNR}(f)$ for PAM becomes

$$\mathrm{SNR_{PAM}}(f) = \frac{\sigma_{mod}^2 H_0^2}{N_0 f_0} \cdot \frac{\ln(2)}{2^{f_{\mathrm{PAM}}/f_0} - 1}. \tag{4.15}$$

To benchmark our results, we also relate it to the NPB defined in (4.2),

$$\mathrm{SNR_{PAM}}(f) = \gamma \frac{\ln(2)}{2^{f_{\mathrm{PAM}}/f_0} - 1}. \tag{4.16}$$

In (4.7), we derived an equivalent expression for the SNR as a function of ϵ_N. From (4.7) and (4.16), the achieved ϵ_N/N_0, expressed in terms of the NPB and the bandwidth in PAM modulation is

$$\frac{\epsilon_N}{N_0} = \gamma \frac{\ln 2}{2\left(2^{f_{\mathrm{PAM}}/f_0} - 1\right)}. \tag{4.17}$$

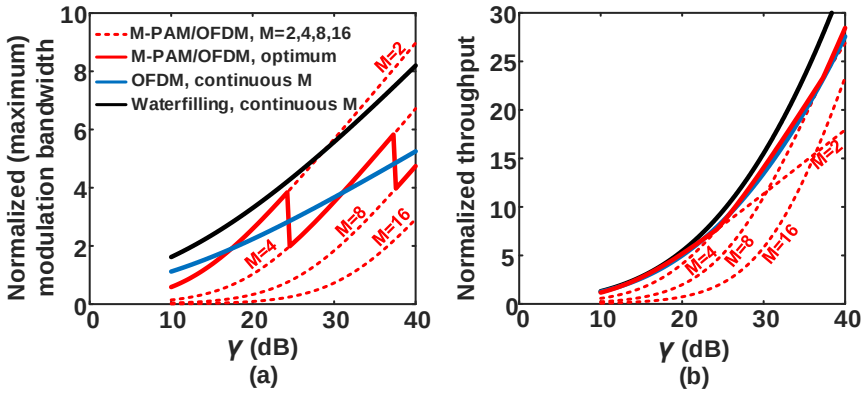

Figure 4.1: (a) (Optimum) normalized modulation bandwidth ($f_{\max_{PAM}}/f_0$, $f_{\max_p}/f_0$ and $f_{\max_w}/f_0$ for PAM, pre-emphasized OFDM and waterfilling, respectively) and (b) normalized throughput versus NPB used for modulation, γ, ignoring DC-bias power (VLC scenario). Dashed-red lines represent the performance for various constellation sizes M (for PAM and pre-emphasized DCO-OFDM) with the solid red being the choice of M optimized for maximum throughput. Solid blue and black lines represent the performance of OFDM with pre-emphasis and waterfilling, respectively, for continuous modulation order. For all plots $\mathrm{BER_M} = 10^{-4}$.

In order to support a constellation M, the ϵ_N/N_0 must exceed $X(M)$ (given in Table 5.2 and defined in (4.12)). So, we require

$$\gamma \geq \frac{2X(M)}{\ln 2}\left\{2^{f_{\mathrm{PAM}}/f_0} - 1\right\}. \tag{4.18}$$

This allows us, for any NPB γ and M, to find the modulation bandwidth,

$$f_{\mathrm{PAM}} \leq f_0 \log_2\left\{\frac{\ln 2}{2}\frac{\gamma}{X(M)} + 1\right\}. \tag{4.19}$$

For any M, we fully utilize the available power when f_{PAM} is set to reach an equality. For $\mathrm{BER_M} = 10^{-4}$ and $M = 2, ..., 32$, we use the $X(M)$ values of Table 5.2 to plot f_{PAM} as a function of γ_{PAM} in Fig. 4.1(a), shown with dashed red lines. We use (4.13) to plot the throughput in Fig. 4.1(b) for various M as the function of γ. Normalization to f_0 allows us to plot generic curves, not specific for the bandwidth of the chosen LED.

For each γ value, the optimum value of M is the one that gives the highest throughput, shown in Fig. 4.1(b) with a solid red line. The corresponding optimum (or maximum) normalized modulation bandwidth $f_{\max_{\mathrm{PAM}}}$ to achieve the maximum throughput is also shown in Fig. 4.1(a) with a solid red line. We learn from Fig. 4.1,

that for a NPB (γ) up to 24.3 dB and for $\mathrm{BER_M} = 10^{-4}$, the optimum modulation is OOK (2-PAM). In fact for a NPB below 24.3 dB, it is preferred to use a crude modulation method very far beyond the 3 dB bandwidth of the LED rather than to choose a higher constellation to stay within the LED bandwidth. This NPB also corresponds to a $f_{\mathrm{max_{PAM}}} = 3.85\ f_0$. This insight can be the basis for a practical algorithm to find, adapt and track the best compromise between bandwidth and M: initially search for the highest throughput that is possible with 2-PAM, by increasing the bit rate while adhering to the transmit power constant. If it turns out that for this throughput, the corresponding $f_{\mathrm{max_{PAM}}}$ exceeds 3.85 f_0, then the algorithm adopts 4-PAM, and searches for the new highest sustainable bit rate by scaling down f_{max}. The limits of $f_{\mathrm{max_{PAM}}}$ for which 8-PAM and 16-PAM are appropriate appear to be 5.8 f_0 and 7.7 f_0, respectively. For a total–power limited channel, similar numbers apply. When a communication link is operational, one preferably uses receiver feedback to change the symbol rate while keeping M fixed, but only switch up or down M at specific threshold symbol rates. Fig. 4.1(b) shows that the penalty for sticking to suboptimal M can be substantial. At higher NPB, sticking to 2-PAM or 4-PAM is not attractive. Similarly, sticking to a pre-configured, possibly sub-optimum f_{max}, thus only adapting M, can have a significant penalty and leads to a full collapse of the link at some low γ.

4.4 OFDM

OFDM can naturally handle the frequency selective LED behavior by dividing the input information over multiple sub-carriers, with an aggregate bandwidth that can be multiple times the channel 3-dB bandwidth. As each sub-carrier only occupies a small fraction of the modulation bandwidth, it sees a (relatively) flat channel frequency response. A sub-carrier at frequency f with a bandwidth Δf can accommodate $T\Delta f$ two dimensional M^2-QAM symbols in a time duration T. The duration of one OFDM block is $T_s = 1/\Delta f$. As the symbol energy equals $\epsilon_s(f) = S_x(f)|H(f)|^2 \Delta f T_s = S_x(f)|H(f)|^2$, we can rewrite the SNR as

$$\mathrm{SNR_{OFDM}}(f) = \frac{\epsilon_s(f)}{N_0} = \frac{2\epsilon_N(f)}{N_0}. \tag{4.20}$$

For OFDM, each sub-carrier symbol is received with a different energy, thus preferably it is loaded with its optimized constellation $M(f)$. Therefore, we explicitly write $\epsilon_N(f)$ as a function of frequency.

4.4.1 Throughput of DCO-OFDM over Low-Pass Channel

As discussed in section (3.4), for DCO-OFDM employing M^2-QAM modulation over its sub-carriers, the number of bits $b(f)$ per dimension that can be delivered is

$$b(f) = \log_2(M(f)) = \frac{1}{2}\log_2\left(1 + \frac{1}{\Gamma}\frac{S_x(f)|H(f)|^2}{N_0}\right), \tag{4.21}$$

where Γ is the modulation gap. The throughput[2] over a modulation bandwidth $[0, f_x]$ is obtained by integrating all the rate contributions, given by (4.21),

$$\begin{aligned} R &= \int_0^{f_x} 2b(f)df \\ &= \int_0^{f_x} \log_2\left(1 + \frac{1}{\Gamma}\frac{S_x(f)|H(f)|^2}{N_0}\right)df. \end{aligned} \tag{4.22}$$

The factor 2 reflects the two dimensions per second per Hz of QAM. This expression looks like a misused Shannon limit for AWGN channels, which repeatedly was argued not to be valid for optical channels. However, here (4.22) comes just as a consequence of inverting the BER expression.

4.4.2 OFDM with Waterfilling

In practice, the constellation size M can only take values from the discrete set $\{2, 4, 8, ...\}$. However, for theoretical derivations it is convenient to assume that M can take any arbitrary positive value, including a non-integer one. As argued in chapter 3, regardless of the choice of $\beta_{1,2,3}$ in (3.16), any optimized power spectral loading is equivalent to applying constraint (4.4) to choose the transmitted $S_x(f)$ to maximize the throughput (4.22). Lagrangian optimization leads to the well-known waterfilling solution with $S_x(f)$ adhering to [62]

$$S_w(f) = \Gamma\left(\frac{N_0}{|H(f_{\max_w})|^2} - \frac{N_0}{|H(f)|^2}\right)^+, \tag{4.23}$$

where the subscript w refers to waterfilling and $f_{\max_w}$ is the maximum modulation frequency for which $S_w(f)$ is non-zero. The optimal power allocation of (4.23) shows that low frequency sub-carriers that experience a good channel quality are assigned more power than those at higher frequencies. Section (3.5.1) derived the relation between $f_{\max_w}$, the NPB γ and the throughput:

$$\gamma = \frac{\Gamma}{\ln(2)}\left(1 + \left(\frac{\ln(2)f_{\max_w}}{f_0} - 1\right)2^{f_{\max_w}/f_0}\right). \tag{4.24}$$

[2] Gross rate before coding.

$$\frac{R_w}{f_0} = \frac{1}{f_0}\int_0^{f_{\max_w}} \log_2\left(\frac{|H(f)|^2}{|H(f_{\max})|^2}\right)df = \frac{1}{2}\left(\frac{f_{\max_w}}{f_0}\right)^2. \tag{4.25}$$

For a given γ, the optimum modulation bandwidth and the throughput are implicitly given by the inverse of (4.24) and by (4.25), respectively. Practical algorithms such as Hughes-Hartogs (HH) [63, 64] provide an iterative, discretized algorithm to calculate the optimum bit and power loading distribution. In chapter 3, a good match between the theoretical throughput and the throughput achieved by discrete constellations using HH is shown. It optimizes the throughput, however, with high complexity and large overhead in communicating the used constellation on all sub-carriers.

4.4.3 OFDM with Pre-emphasis

A simpler implementation is to pre-emphasize the channel and to use the same constellation for all sub-carriers. Pre-emphasizing implies a forced inversion of the channel response at the transmitter to compensate its low–pass behaviour. This is often referred to as a bandwidth extension, but comes at a penalty. Such pre-emphasis tends to defeat the advantage of OFDM to load every frequency bin optimally, thus is counterproductive. Nonetheless, we see IEEE 802.11bb standardization proposals to reuse WiFi-like OFDM schemes with constant constellations for OWC, to use existing IC designs. Our results will show that repairing the frequency response to support a fixed constellation can be reasonable in the lower NPB ranges, but the transmit bandwidth needs to be made adaptive to the NPB.

Arbitrary Modulation Constellations:

A filter inverts the LED low–pass response in the frequency range $[0, f_p]$. As shown in section 3.5.3, the throughput R_p is derived from (4.22) and (4.5) with the back-off κ given in (4.6):

$$\frac{R_p}{f_0} = \left(\frac{f_p}{f_0}\right)\log_2\left(1 + \frac{\gamma \ln 2}{\Gamma\left(2^{f_p/f_0} - 1\right)}\right). \tag{4.26}$$

The optimum modulation bandwidth, denoted by $f_{\max_p}$, to maximize the throughput is calculated from $dR_p/df_{\max_p} = 0$, which depends only on γ, f_0 and Γ. This was done in section 3.5.3.

Discrete Modulation Constellations

Using discrete M, in (4.26), we cannot get tractable expressions for the derivatives w.r.t. spectral density. As an alternative optimization track, we exploit the fact that all sub-carriers carry the same constellation size M. In the previous sub-section, we implicitly assumed a continuous-valued M, but in this section, we assume an

M^2-QAM modulation that can only take integer values of an even power of 2 ($M = 2, 4, 8, ..$) and identical on all sub-carriers. We use the relation (4.20) to express ϵ_N/N_0 in terms of SNR(f), as in (4.3) but with a pre-emphasized spectral density (4.5),

$$\frac{2\epsilon_N(f)}{N_0} = \frac{\sigma_{mod}^2 H_0^2}{N_0 f_0} \frac{\ln 2}{2^{(f_p/f_0)} - 1}. \tag{4.27}$$

Our optimization tests various M and for each M value, the optimum modulation bandwidth f_p is taken such that ϵ_N/N_0 just exceeds $X(M)$. This results in

$$\frac{f_p}{f_0} = \log_2 \left\{ \frac{\gamma \ln(2)}{2X(M)} + 1 \right\}, \tag{4.28}$$

which is identical to (4.19). The throughput for pre-emphasized OFDM employing M^2-QAM modulation scheme on all sub-carriers is calculated from

$$\frac{R_p}{f_0} = \frac{f_p}{f_0} \cdot \log_2 M^2, \tag{4.29}$$

which reduces to (4.13). In conclusion, for the same NPB γ, thus not yet considering the bias penalty on a pre-emphasized channel, both PAM and pre-emphasized OFDM schemes demand the same optimum modulation bandwidth and provide identical throughput and, therefore, the modulation bandwidth and throughput plots of Fig. 4.1 are also applicable for DCO-OFDM employing M^2-QAM.

Fig. 4.1 also includes the required modulation bandwidth and the throughput for pre-emphasized OFDM (blue lines) and for waterfilling (black lines) with continuous modulation order M at BER = 10^{-4}. As expected, waterfilling provides the maximum throughput. Pre-emphasis comes with a penalty in throughput, which increases with NPB but is small for low NPB. However, pre-emphasis requires less bandwidth. This can reduce the sampling rate, hence it consumes less power in analog-to-digital conversion and in digital signal processing. Furthermore, pre-emphasis avoids the need to exchange the bit loading profile, thus it reduces signalling overhead.

In Fig. 4.1(b), we see a small artefact due to simplifying Γ: OFDM with discrete M (red line) cannot outperform OFDM with continuous M (blue line). This artefact is small. Comparing the maximum normalized modulation bandwidth, continuous M does not show any jump in the optimized modulation bandwidth, which was also observed in [72].

Fixing the bandwidth means operating on a point on a horizontal line in Fig. 1(a). For operational points on this line, the link collapses if it is above the curves of the calculated maximum supportable $f_{\max}$. As an example, if a system with an LED of $f_0 = 10$ MHz fixes the transmit bandwidth to 40 MHz, it operates on the horizontal line of a normalized modulation bandwidth of 4. Below an NPB of about 25 dB, it uses a bandwidth broader than what PAM or pre-emphasized OFDM can support

(the point of operation is above the plotted curves). Nonetheless, a well-performing link would be feasible if the system were allowed to scale back the bandwidth, rather than to aggressively push symbol rates beyond the 3 dB LED bandwidth.

4.5 Clipping and Distortion Model

The modelling of clipping and distortion is subject to improving insights [75]. In the following we discuss three models

- Double sided clipping: In the early days, LEDs had to be designed for maximum power output. Above a certain current level, the LED would thermally break down. This justified a model in which the LED current is both non-negative and peak-limited [51].

- Clipping of the current: Today's LEDs are operated at a set point where the photon output per recombining electron-hole pair is the highest. This is far below any clipping point or breakdown rating. At higher currents, the LED efficiency only gradually reduces (LED droop). This justifies a single-sided (non-negative) clipping model [48,49,72,75]. Similarly, many practical electronic drivers do not allow a negative current through the LED.

- Droop: Above their most efficient point, the LED becomes somewhat less efficient. This 'droop' leads to invertible second–order distortion, inherent to non-linear photon generation rates [52, 53, 67].

In this chapter we focus on the second model, but we also discuss the consequences of droop, as in the third model. In OFDM, the LED AC current, $i_{led}(t)$, has in good approximation a Gaussian probability density. It has rms modulation depth σ_{mod}. To ensure that the signal remains in the linear region, a DC bias I_{LED} is needed for the LED. Further, the LED imposes a low-pass nature, but studying memory effects in distortion is beyond the scope of this chapter.

4.5.1 Current Clipping

The choice of z (defined in (4.14)) needs to ensure that the clipping noise stays below the maximum tolerable noise floor. From arguments in [49, 72, 75], we conclude that modern LEDs clip negative currents but are not peak limited in their operational range. The clipping noise per sample is zero if the signal $i_{led}(t) \geq -z\sigma_{mod}$ (or $I_{LED} \geq 0$) and equal to $i_{led} + z\sigma_{mod}$ otherwise. Using a Gaussian pdf for I_{LED} with mean value $z\sigma_{mod}$ and variance σ^2_{mod} and integrating over $\xi = i_{LED} - z\sigma_{mod}$, the i-th

moment of the clipping is

$$\mu_i = \int_{-\infty}^{-z\sigma} \frac{(\xi + z\sigma_{mod})^i}{\sqrt{2\pi}\sigma_{mod}} \exp\left(-\frac{\xi^2}{2\sigma_{mod}^2}\right) d\xi. \tag{4.30}$$

The effective noise variance of the distortion is $\sigma_D^2 = \mu_2 - \mu_1^2$ and is calculated as

$$\frac{\sigma_D^2}{\sigma_{mod}^2} = (z^2+1)Q(z) - zg(z) - (g(z) - zQ(z))^2, \tag{4.31}$$

where $Q(.)$ and $g(.)$ are the tail distribution function and pdf of the standard normal distribution, respectively. For ease of notation, we introduce $c_z = \sigma_D/\sigma_{mod}$.

Clipping also attenuates the signal, particularly if $z < 2$. Below $z = 1$, where the signal level is multiplied by $a_z = 0.84$ [49], the effect becomes pronounced. While we refer the reader to [49] for expressions that relate z and a_z, we use a_z in following throughput equations.

In contrast to the earlier works in [49, 54], We argue that the clipping spectrum is limited to f_x and does not significantly spill over to empty sub-carriers far above f_x: A signal spectrum limited to f_x, creates time–domain signals that are highly correlated in a period $f_x^{-1}/2$. Every clipping event causes an error signal that has a typical duration of about $f_x^{-1}/2$. By virtue of properties of Fourier Transforms and as we confirm by simulation, this leads to a clipping noise spectrum that is mainly restricted to $(0, f_x)$. Oversampling, and using an oversized FFT with broader bandwidth ($f_s \gg f_{max}$) sees clipping artefacts that span multiple time samples, but oversampling does not increase their bandwidth. Multiple independent clipping events add incoherently on a particular victim sub-carrier. Here, we refine the clipping noise model of [49, 54] that considers low-pass filtering of flat (spectrally white) clipping artefacts in the LED. Fig. 4.2 shows the PSD of 64-QAM ($M = 8$) on the 64 lower sub-carriers in an OFDM system with 128 sub-carriers thus with an IFFT size of 256. The PSD of the clipping noise is shown in Fig. 4.2 for $z = 0.5$ (overly aggressive clipping), $z = 1$ and $z = 2$. This plot confirms our argument that the clipping noise is mostly confined within the modulation bandwidth of the signal where it may have two or three dB variations. Also, the clipping PSD raises with lowering z. For the signal in Fig. 4.2, $z \geq 2.2$ is required to achieve a simulated BER of $< 10^{-4}$.

As clipping noise raises the noise floor, we model $N_0 \rightarrow N_0 + N_D(f)$. We approximate the simulated clipping spectra by a rectangular function within the modulation bandwidth f_x:

$$N_D(f) \approx \frac{\sigma_D^2}{f_x}|H(f)|^2 = \frac{c_z^2\sigma_{mod}^2|H(f)|^2}{f_x}. \tag{4.32}$$

A limitation of this model is that we modelled clipping of the input current. That is, we assumed that the input current cannot be negative. This is realistic if the electronic circuitry of the driver has limitations. The series transistor topology [50],

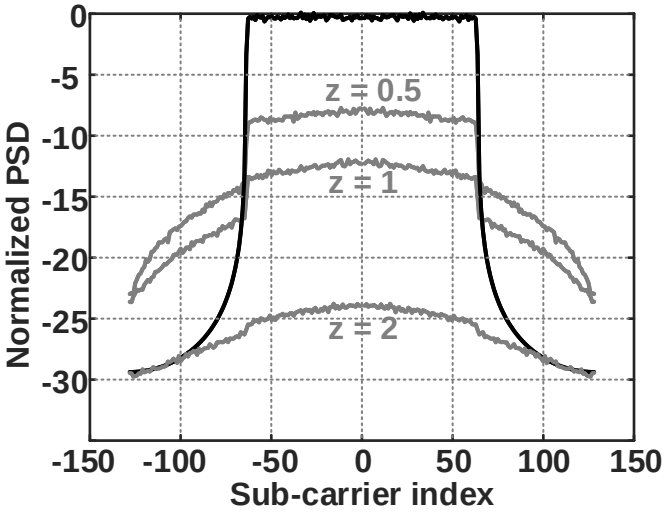

Figure 4.2: PSD of an OFDM signal (black) and clipping noise (gray), for bias ratio of 0.5, 1 and 2. LED low-pass response not included.

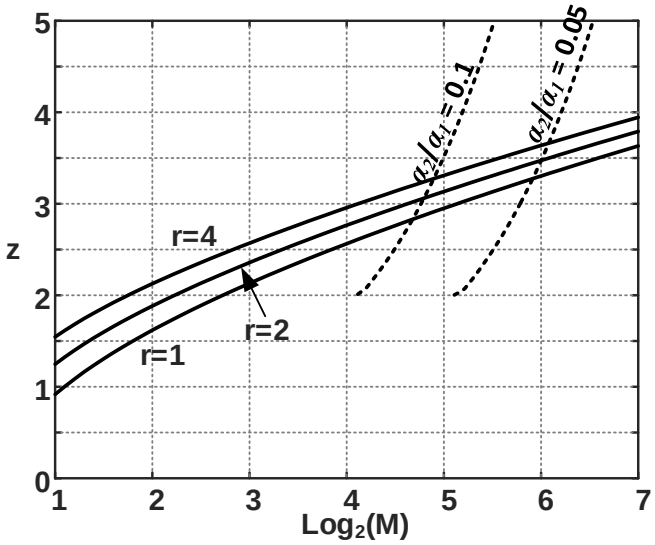

Figure 4.3: Bias ratio z versus number of bits $b = \log_2 M$ per sub-carrier in one dimension. Noise-free ($r = 1$) and leaving a 3 and 6 dB power margin ($r = 2$ and $r = 4$, respectively) to operate over a noisy channel. Solid line: clipping limit. Dashed line: invertible distortion limit. For distortion–limited z, we used $r = 1$.

for instance cannot deliver negative currents. On the other hand, a bias-T topology can extract a negative current during short periods of time. In such case the LED junction is discharged faster than only via recombination, e.g. photon generation. This speeds up the LED response, and does not necessarily lead to clipping as long a the numbers of holes and electrons stay positive [sweep out] [75]. In other words, one may argue that LEDs cause clipping particularly if the low-pass filtered signal would be driven into negative values. To acknowledge this, we use the term "current clipping", as opposed to light output clipping.

4.5.2 Invertible Distortion Model

The hard clipping model of the LED needs refinement as other (invertible) non-linearities may dominate for high z. Electrons and holes recombine at a rate governed by the ABC formula [52, 53, 67]. For a brief discussion here, we simplify the dynamic model [27, 53, 75] by describing the light output ϕ as a function of LED current,

$$\phi = \alpha_1 I_{LED} + \alpha_2 I_{LED}^2 + \alpha_3 I_{LED}^3.$$

Modulating with $I_{LED} = \mathrm{I}_{LED} + i_{led}$, the signal ϕ sees second–order distortion with a relative strength

$$\begin{aligned} \frac{\sigma_{2D}^2}{\sigma_{mod}^2} &= \frac{(\alpha_2 + 3\alpha_3 \mathrm{I}_{LED})^2 \mathrm{E}\{i_{led}^4\}}{(\alpha_1 + 2\alpha_2 \mathrm{I}_{LED} + 3\alpha_3 \mathrm{I}^2{}_{LED})^2 \mathrm{E}\{i_{led}^2\}} \\ &= \frac{3}{z^2} \frac{(\frac{\alpha_2}{\alpha_1} + \frac{3\alpha_3}{\alpha_1} \mathrm{I}_{LED})^2 \mathrm{I}^2{}_{LED}}{(1 + \frac{2\alpha_2}{\alpha_1} \mathrm{I}_{LED} + \frac{3\alpha_3}{\alpha_1} \mathrm{I}^2{}_{LED})^2} \end{aligned} \tag{4.33}$$

where σ_{2D}^2 is the variance of the second–order distortion and we used that, for a Gaussian distribution, $\mathrm{E}\{i_{led}^4\} = 3(\mathrm{E}\{i_{led}^2\})^2 = 3\sigma_{mod}^2$ and inserted $z^2 = \mathrm{I}_{LED}^2/\sigma_{mod}^2$. Based on our observations, the second–order distortion is the dominant distortion in LEDs for $z > 2$, hence we can neglect the term α_3 and the distortion caused by the third order non-linearity. The distortion i_{led}^2 is uncorrelated with the LED modulation current i_{led}, i.e., $\mathrm{E}\{i_{led}^2 \cdot i_{led}\} = 0$. Its spectrum, $N_{2D}(f)$ can be calculated by the convolution of the modulation spectrum of i_{led} by itself.

4.6 Effect of Clipping and Distortion on OFDM

In the following, we discuss two different approaches to handle the clipping noise.

4.6.1 Conservatively Choosing Low Modulation Depth

A pragmatic (but not optimum) approach is to ensure the clipping noise spectrum falls below the receiver noise level. This can be translated into a requirement on the

Signal-to-Distortion Ratio (SDR),

$$\text{SDR} = \frac{2\epsilon_N}{N_D} = \frac{a_z^2}{c_z^2} \geq 2rX(M), \tag{4.34}$$

for all f, where r is a design (power) margin. This, with (4.31) gives the maximum modulation order M that can be used for a given z. Thus, for a target modulation order M (for M^2-QAM), it specifies the minimum required LED bias. Fig. 4.3 shows the minimum z as a function of number of bits per sub-carrier in one dimension for margins $r = 1$, 2 and 4. It can be seen that for a typical modulation order of 64-QAM ($M = 8$), $z \geq 2.15$ (compared to the simulated $z \geq 2.2$ in section 4.5) and $z \geq 2.4$ are needed for $r = 1$ and $r = 2$, respectively.

The optimum modulation bandwidth and the throughput follow from (4.28) and (4.29), if the distortion can be assumed to be negligible compared to receiver noise. This requires the modulation depth and constellation size to satisfy (4.34) for the given z with an adequate margin factor $r \geq 1$. However, choosing the distortion power just below the noise level ($r = 1$) may not be adequate, as the distortion raises the noise level by 3 dB. Since the distortion also has a low–pass spectrum response, this affects mainly the lower sub-carriers. Nonetheless, to avoid that clipping effects the BER at any sub-carrier, a margin $r \geq 1$ is needed.

Considering a channel limited by second–order distortion, thus clipping– and noise–free channels, (4.34) can be written as

$$\text{SDR} = \frac{\sigma_{mod}^2}{\sigma_{2D}^2} \geq 2rX(M).$$

Dashed lines in Fig. 4.3 also show the minimum required z for margin $r = 1$ for two values of α_2/α_1 when $\text{I}_{\text{LED}} = 0.3$ A. It can be seen that for modulation order of $M \leq 16$, thus 256 QAM, the minimum z (for this specific example) is dominated by the clipping noise and the distortion is negligible. Values in the range of a Signal–to–Distortion–and–Noise Ratio (SNDR) around 40 dB are achieved in commercial ITU G.9991 systems, allowing up to 1024-QAM ($M = 32$), or 4096-QAM ($M = 64$) at maximum. The steep dashed curves confirm the practical experience that modulation orders above $M = 64$ are hard to achieve at reasonable z. In future systems, the distortion may be overcome by a pre or post-distortion compensation method, such as in [40]. Therefore, we do not elaborate on invertible distortion as limiting the throughput, so we focus on non-invertible clipping.

4.6.2 Optimizing for Throughput

In this section, we include the clipping distortion power in our optimization of the modulation bandwidth and the throughput. Recalling (4.20), the received QAM

symbol energy to noise plus distortion ratio (SNDR) is, using (4.32),

$$\mathrm{SNDR}_{\mathrm{OFDM}} = \frac{2\epsilon_N}{N_0 + N_D(f)} = \frac{a_z^2 S_x(f)|H(f)|^2}{N_0 + \frac{c_z^2 \sigma_{mod}^2}{f_x}|H(f)|^2}. \tag{4.35}$$

where x stands for pre-emphasis (p) or waterfilling (w).

Throughput of Pre-emphasis with Current Clipping

Inserting $S_p(f)$ and κ from (4.5) and (4.6), respectively,

$$\mathrm{SNDR}_{\mathrm{OFDM}} = \frac{\gamma \ln 2}{2^{f_p/f_0} - 1} \cdot \frac{a_z^2}{1 + \frac{c_z^2 \gamma 2^{-f/f_0}}{f_p/f_0}}. \tag{4.36}$$

For $z \to \infty$, $c_z \to 0$, $a_z \to 1$, and (4.36) reduces to (4.27) which was derived for clipping–free modulation. The above equations (4.35) and (4.36) are based on the effective energy emitted per symbol, thus do not reflect that with increasing z, more bias power is needed to achieve ϵ_N.

For a continuous modulation order M, one can replace the SNDR into (4.22) and solve the integral numerically for different f_p choices to optimize f_p for a given z. Pre-emphasis can achieve a normalized throughput of

$$\frac{R_p}{f_0} = \int_0^{f_p/f_0} \log_2 \left(1 + \frac{1}{\Gamma} \frac{\gamma \ln 2}{2^{f_p/f_0} - 1} \cdot \frac{a_z^2}{1 + \frac{c_z^2 \gamma 2^{-x}}{f_p/f_0}} \right) dx. \tag{4.37}$$

The above integral has a closed form solution,

$$\begin{aligned} \frac{R_p}{f_0} = & \frac{R_p(z \to \infty)}{f_0} + \\ & \frac{1}{(\ln 2)^2} \cdot \left(Li_2 \left(\frac{-c_{z_n}^2 \gamma}{f_p/f_0} 2^{-f_p/f_0} \right) - Li_2 \left(\frac{-c_{z_n}^2 \gamma}{f_p/f_0} \right) \right) - \\ & \frac{1}{(\ln 2)^2} \cdot \left(Li_2 \left(\frac{-c_z^2 \gamma}{f_p/f_0} 2^{-f_p/f_0} \right) - Li_2 \left(\frac{-c_z^2 \gamma}{f_p/f_0} \right) \right), \end{aligned} \tag{4.38}$$

where $R_p(z \to \infty)$ is the throughput for the case of no clipping noise, given in (4.26), $Li_2(.)$ is the Spence function defined as

$$Li_2(z) \triangleq \int_0^z \frac{\ln(1-u)}{-u} du, \tag{4.39}$$

and

$$c_{z_n} = \frac{c_z}{\sqrt{1 + \frac{a_z^2}{\Gamma} \frac{\gamma \ln 2}{2^{f_p/f_0} - 1}}}. \tag{4.40}$$

The optimum modulation bandwidth for pre-emphasis, $f_{\max_p}$, is normalized to f_0 to create versatile, generically applicable curves in Fig. 4.4(a) with blue lines for $z \to \infty$ (solid blue) and $z = 2.5$ (dashed blue). The corresponding normalized rates are shown in Fig. 4.4(b). Reducing z from ∞ (thus allowing unbounded biasing power) to 2.5 at a constant γ, increases the optimum modulation bandwidth to leverage the better SNDR at higher frequencies. Nevertheless, the throughput is experiencing a considerable penalty, which is about 25% for a γ of 50 dB. Increasing z from 2.5 to 3 reduces the penalty to about 10%.

More of practical use is a discrete constellation size M for M^2-QAM modulation. The calculated SNDR is an increasing function of frequency, that is, the minimum SNDR occurs at low frequencies. For the communication link to use the same constellation on all sub-carriers with the target BER, the choice of z needs to ensure that the required $X(M)$ can be satisfied at low frequencies,

$$\frac{\epsilon_N}{N_0 + N_D(0)} \geq X(M) \to \frac{\gamma \ln 2}{2^{f_p/f_0} - 1} \cdot \frac{a_z^2}{1 + \frac{c_z^2 \gamma}{f_p/f_0}} \geq 2X(M). \tag{4.41}$$

For a given γ and modulation order M, the optimum modulation bandwidth is the maximum f_p that satisfies (4.41). Unfortunately, a closed form expression for the optimum bandwidth cannot be derived. In the limiting case of clipping–free communication, our result reduces to (4.28). For a given γ and a given choice of z, the modulation bandwidth f_p is optimized from (4.41) as a function of M, so the throughput follows from (4.29). The optimum modulation order M is the one that gives the highest throughput and the corresponding normalized modulation bandwidth is the optimum, $f_{\max_p}$. The throughput and $f_{\max_p}$ are shown in Fig. 4.4(a) and (b) with red lines for $z = 2.5$ (dashed-red) and $z \to \infty$ (solid red) and in Fig. 4.4(c) and (d) for different z values.

The difference between the continuous and discrete constellation size M was discussed in Section 4.4 for distortion–free modulation ($z \to \infty$). Considering distortion with $z = 2.5$, as in Fig. 4.4(b), shows a considerable cut in throughput when using a discrete M, compared to a non-practical non-integer modulation order M. The throughput shows a reduction of about 40% at γ of 50 dB (see dashed red and dashed-blue lines).

We see a very substantial throughput penalty if one has to stick to discrete constellations M that are a power of 2, which is understood from the discussions that led to (4.41). In fact, while pre-emphasis equalizes the SNR (derived from (4.36) for $c_z = 0$), it does not generically equalize the SNDR, which, tends to be worse at lower frequencies.

To mitigate this gap while still using a common equal constellation M, the transmitter can adjust (lower) the power for the sub-carriers at higher frequencies with a better SNDR. This approach, however, requires an adaptive power loading algo-

rithm which increases the complexity. Another approach to recover the throughput of discrete M modulation scheme (compared to the theoretical dashed-blue line of Fig. 4.4(b)) is to use a higher DC current. Fig. 4.4(d) shows that increasing z from 2.5 to 3 can recover a big fraction of the loss; the penalty of using discrete M compared to continuous M is about 20% and compared to $z \to \infty$ is about 30%.

Fig. 4.4(c) and (d) show that for a fixed z and large γ, thus when distortion dominates over the noise and over invertible distortion, the modulation bandwidth converges to a constant. Having $\gamma \to \infty$ in (4.41),

$$\frac{(\ln 2) a_z^2 f_p/f_0}{c_z^2 (2^{f_p/f_0} - 1)} \geq 2X(M), \tag{4.42}$$

shows that f_p/f_0 only depends on M, irrespective of the NPB γ. The throughput in (4.29), which only depends on M and the modulation bandwidth, is also approaching to a constant at large γ values.

Waterfilling with Clipping

In section 3.5.1, it was shown that the presence of clipping noise does not affect the modulation bandwidth $f_{\max_w}$ that optimizes the throughput. Hence the modulation bandwidth versus NPB (4.24) also holds when there is clipping noise provided that the signal power is corrected for the attenuation factor a_z^2. Based on equations in this chapter, we quantify the throughput penalty due to distortion as

$$\begin{aligned}\frac{R_w}{f_0} = \frac{R_w(z \to \infty)}{f_0} + \frac{f_{\max_w}}{f_0} \log_2 \left(1 + \frac{c_z^2 \gamma}{f_{\max_w}/f_0} 2^{-f_{\max_w}/f_0}\right) + \\ \frac{1}{(\ln 2)^2} \left(Li_2 \left(\frac{-c_z^2 \gamma}{f_{\max_w}/f_0} 2^{-f_{\max_w}/f_0} \right) - Li_2 \left(\frac{-c_z^2 \gamma}{f_{\max_w}/f_0} \right) \right).\end{aligned} \tag{4.43}$$

The throughput and the associated optimum modulation bandwidth are shown in Fig. 4.4(a) and (b) as a function of the NPB γ. Waterfilling provides a better performance compared to pre-emphasis but uses a larger modulation bandwidth, for both clipping–free and clipped communication. Choosing $z = 2.5$ reduces the throughput of waterfilling approach by a gap that increases with γ and that is about 18% at γ of 50 dB compared to $z \to \infty$.

4.7 Comparison of DCO-PAM and DCO-OFDM

We compare the two modulation schemes, DCO-PAM and DCO-OFDM, for different power constraints at the transmitter side. For various power constraints at the transmitter, we calculate the portion of the power that contributes to the throughput

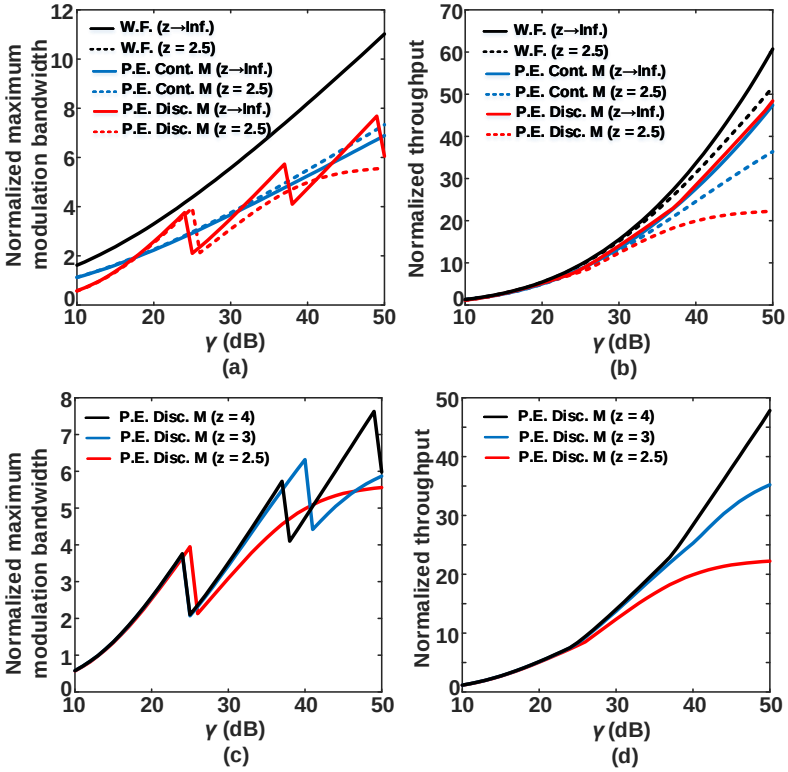

Figure 4.4: Normalized maximum modulation bandwidth and throughput for (a,b) waterfilling (W.F.), pre-emphasis (P.E.) with continuous (Cont.) and discrete (Disc.) modulation order M and (c,d) for pre-emphasis with discrete M, and different values of z as a function of γ. The BER is fixed at 10^{-4}.

versus biasing power. We redefine the NPB parameter that allows for a fair comparison of the schemes, considering that a particular σ_{mod} leads to different consumed powers.

4.7.1 Extra–Power Limited Channel

For VLC links, the illumination power is available already ($\beta_1 = 0$) and only the extra power which is needed for modulation is of interest. Extra power was shown to be directly related to the LED current variance through the factor R_{LED}. The LED resistance R_{LED} consists of two parts, $R_{LED} = V_T/\mathrm{I}_{LED} + R_s$, where the dynamic part is an inverse function of I_{LED} and the second part is the constant parasitic resistance R_s. For LEDs biased at a typical current of $\mathrm{I}_{LED} = 0.35$ A and with

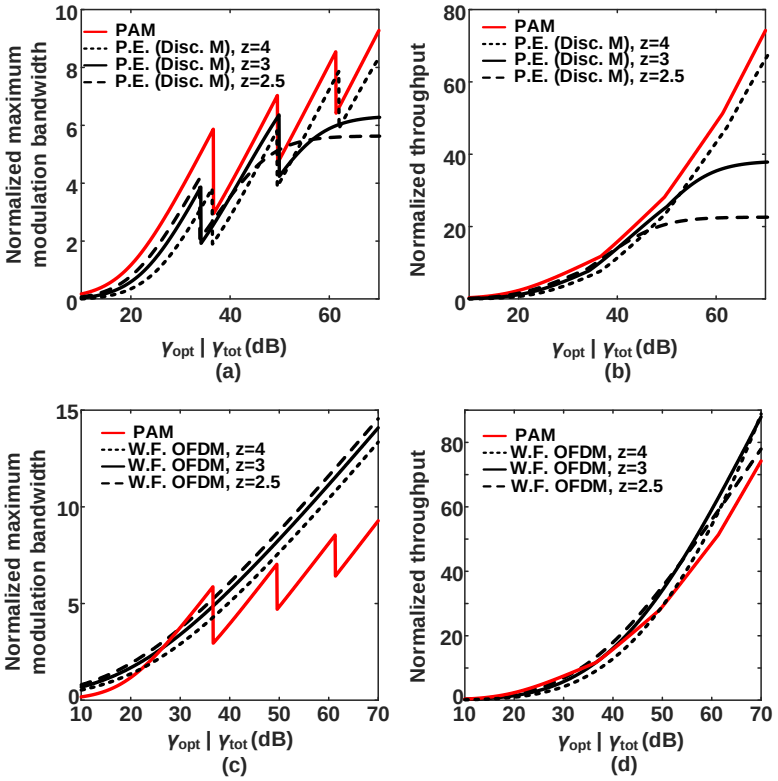

Figure 4.5: (a,c) Optimum (normalized) modulation bandwidth and (b,d) throughput versus optical NPB γ_{opt} for PAM (red lines) and OFDM (with pre-emphasis and with waterfilling) with different z choices. For all plots BER = 10^{-4}.

V_T being 25 mV, the dynamic resistance becomes approximately 70 mΩ which is negligible compared to the R_s which is typically in the order of $1-2\ \Omega$ [132]. As a result, identical extra power for both modulation schemes is translated into identical σ_{mod}, hence the same NPB for both schemes. In section 4.4 and Fig. 4.1, it was shown that for the same NPB, thus ignoring biasing power and taking adequate z (no significant distortion), both schemes achieve the same throughput in a pre-emphasized channel. In fact, one may interpret the FFT with Hermitian symmetry, as used in OFDM, as just a unitary rotation of the PAM time signals along the time-frequency domains. OFDM preserves the number of dimensions and the distances in the signal space, thus in a pre-emphasized channel has equal spectrum efficiency and BER as PAM.

4.7.2 Optical–Power Limited Channel

Optical power limitations can be induced for instance in VLC where illumination dictates the light level or in IR where eye-safety needs to be guaranteed. The average optical power of an LED can be written as [40]

$$P_{opt} = \frac{\langle E_p \rangle}{q} \mathrm{I}_{LED}, \tag{4.44}$$

where $\langle E_p \rangle$ is the average energy of the photons transmitted by the LED and q is the unit electron charge. According to (4.44), constraining the average optical power is equivalent to constraining the LED DC current via β_1 ($\beta_2 = 0, \beta_3 = 0$).

As we compare DCO-PAM and DCO-OFDM for the same LED DC current, their variances differ. The variance σ^2_{mod} is related to I_{LED} via z in (4.14). To reflect this, we use γ_{opt} as a variant of γ that addresses the optical power limit:

$$\gamma_{opt} = \frac{q^2 P^2_{opt}}{\langle E_p \rangle^2} \cdot \frac{H_0^2}{N_0 f_0}. \tag{4.45}$$

Then from (4.44), (4.45) and using the definition of z, the optical NPB relates to γ via

$$\gamma_{opt} = z^2 \gamma. \tag{4.46}$$

DCO-PAM has a lower PAPR, thus allows a smaller z than DCO-OFDM, hence gets a better γ for the same γ_{opt}. This implies a horizontal shift that differs per modulation setting. This changes the cross-over points for the choice of modulation that performs best for a given NPB. Using (4.14) for M-PAM with $M = 4, 8, 16$ and 32, $1/z^2$ is equivalent to horizontal shifts of 2.55, 3.68, 4.23, and 4.5 dB, respectively.

For OFDM, the bias ratio z is subject to optimization. We see in Fig. 4.5 that for pre-emphasized OFDM with a fixed z the throughput converges to a constant for large γ_{opt}, thus when clipping dominates over the noise floor. On the other hand for small γ_{opt}, when distortion is negligible, increasing z just leads to a reduction in the received SNR. Hence, at low γ_{opt}, the throughput curves of pre-emphasized DCO-OFDM are horizontally shifted copies of each other; the distance between the curves for $z = 2.5$ and $z = 4$ is significant: 4 dB.

High Normalized Power Budgets

As an example, for an LED with $f_0 = 10$ MHz bandwidth, to reach a throughput near a gigabit ($R_p/f_0 = 100$), $z = 4$ is needed, but that significantly jeopardizes the throughput for more distant receivers (with lower available NPBs) where $z < 3$ needs to guarantee range. In another example, to provide a throughput of $60 f_0$, DCO-PAM requires an about 2.5 dB lower NPB compared to pre-emphasized DCO-OFDM while $z = 4$ is used for OFDM. Keeping the bias ratio of OFDM at $z = 4$, at a

lower throughput of $10f_0$, the NPB difference between DCO-PAM and pre-emphasized DCO-OFDM increases to about 5 dB while a lower z, e.g. $z = 2.5$ shows only 1.6 dB NPB difference. We acknowledge that if pulse shaping of PAM is needed, the advantage shrinks, as z rises.

Interestingly, DCO-PAM also outperforms DCO-OFDM with waterfilling at low optical NPBs. Waterfilling performs better when the optical NPB increases, say γ_{opt} above 32 dB for $z = 2.5$ (equivalent to γ more than 24 dB) and above 50 dB for $z = 4$ (equivalent to a NPB γ of more than 38 dB[3]). The cross-over point for waterfilled DCO-OFDM to outperform PAM moves to higher NPBs when a higher z is selected. However, at large NPBs of 50 dB, the theoretically optimum modulation bandwidth for DCO-PAM is around $7f_0$. In practice, these large bandwidth extensions impose difficulties in the implementation.

Low Normalized Power Budgets

At low NPBs, it may be attractive to use dedicated non-negative OFDM variants, such as ACO-OFDM or Flip OFDM, to avoid the power losses in the DC bias. Flip OFDM carries the signal with variance σ^2_{mod}, however, samples with positive polarity are transmitted in a first block, negative samples are transmitted in flipped polarity in a second block. This ensures that a signal sample is always transmitted, thus it retains σ^2_{mod}, but the transmission time doubles. During reception, two blocks are folded back into one block to recover the full signal. It has been noticed [57,139–141], that this operation collects noise from two blocks, thus reduces the SNR by one half. This, to a large extent, defeats the gain obtained from trying to avoid the DC-bias.

At high NPBs, these non-negative OFDM variants are outperformed by DCO-OFDM, also because at high SNR, a spectrum efficiency loss is incurred in Flip-OFDM by transmitting a second block: This demands higher constellations to squeeze more bits into fewer dimensions [57]. At low NPBs, where LED bandwidth is adequate to carry a low-rate signal, the lower mean value of Flip-OFDM appears beneficial [57]. The signal in the collapsed block has an effective symbol energy jointly equal to σ^2_{mod} but is processed over a single block time. The mean value of the signal is $\sqrt{2/\pi}\sigma_{mod} \approx 0.80\sigma_{mod}$. Table 5.3 lists the resulting linear and quadratic factors in the power consumption, given in (3.16).

For optical–power limited channels, we take $\beta_2 = 0$. Flip OFDM[4] provides the maximum available σ_{mod} within a constrained β_1. Despite the 50% drop in the SNR of ACO/Flip OFDM, these appear to be slightly more attractive than PAM for large

[3] which is equivalent to a received electrical SNR of 23 dB in the modulation bandwidth of $f_{\max_w} \approx 7.5f_0$ [72].

[4] Alternatively one many argue that clipping halves the ACO-OFDM power by 50%. So, to compare for the same signal power, we boost the ACO power by a factor of two, and also arrive at full σ^2_{mod}.

Table 4.3: Quick comparison of the linear and quadratic terms in the power consumption and a penalty on the SNR for flat channel (low NPB, small modulation bandwidth).

	Linear	Quadratic	SNR
PAM	$\sqrt{3\frac{M-1}{M+1}}\sigma_{mod}$	σ^2_{mod}	
DCO	$z\sigma_{mod}$	σ^2_{mod}	reduced by a_z^2 and $N_D(f)$
Flip/ACO	$\sqrt{2/\pi}\sigma_{mod}$	σ^2_{mod}	reduced by 50%

M: The FFT shapes the almost uniform 2D PAM signal probability density into a one-sided Gaussian, which appears to be beneficial. However, large modulation order are not suitable for weak links, which demand small M. For small and moderate M, straight PAM appears better than ACO-OFDM. From Fig. 4.3, we further see that DCO-OFDM performs comparably; by choosing a very low z. It severely clips, but 4-QAM ($M = 2$) DCO-OFDM is nonetheless feasible.

4.7.3 Electrical–Power Limited Channel

Often, the total electrical power, given in (3.16), consumed is relevant. For a bias-T modulator, $\beta_1 = \mathrm{V}_0$ and $\beta_3 \approx R_s$ dominate (3.16), while $\beta_2\sigma^2_{mod}$ is much smaller. In fact, for a typical LED bias current of $\mathrm{I}_{LED} = 0.35$ A, $V_0 = 2.5$ V and $R_s = 1\ \Omega$, in the total electrical power equation (3.16), $\beta_1\mathrm{I}_{LED}$ =0.875, $\beta_2\sigma^2_{mod} = \beta_2\mathrm{I}^2_{LED}/z^2 = 0.1225/z^2$ and $\beta_3\mathrm{I}^2_{LED}$ =0.1225. For OFDM, typically $z > 2$, hence the term $\beta_2\sigma^2_{mod}$ is negligible. For PAM, however, z can be as low as 1 (for $M = 2$) and the approximation $\beta_2\sigma^2_{mod} \approx 0$ results in about 10% error (0.46 dB) in the total electrical power. The total electrical power can reasonably be approximated by the LED DC power consumption:

$$P_{tot} \approx \mathrm{V_{LED}}\mathrm{I}_{LED} = \mathrm{V_{LED}}z\sigma_{mod}. \tag{4.47}$$

To acknowledge that $z^2\sigma^2_{mod}$ rather than σ^2_{mod} itself is constrained, let us compare systems for the total NPB γ_{tot} including bias losses as

$$\gamma_{tot} = z^2\sigma^2_{mod} \cdot \frac{H_0^2}{N_0 f_0}. \tag{4.48}$$

This $\gamma_{tot} = z^2\gamma$ is identical to the definition of (4.45). In this case, the curves of Fig. 4.5 also apply to electrical-power limited channel if the x-axis is read as γ_{tot} axis. Alternatively, it can be shown that, the electrical power model by [49], taking $\beta_2 = \beta_3$ and $\beta_1 = 0$ would lead to $\gamma_{tot} = (z^2 + 1)\gamma$ which we do not consider in this work.

Design Choice for z

At constant total power, lowering z boosts the signal σ^2_{mod}, thus enhances ϵ_N and γ, but it also increases distortion. For example, systems optimized for large coverage spread their optical power over a large area, thus often have to operate with relatively small γ_{tot}, say of about 30 dB. Then $z = 2.5$ is more attractive than $z = 4$. The latter can improve the throughput for short range or for systems with narrow beams by 65% (from $4.2f_0$ to $6.9f_0$) and 50% (from $R = 4.2f_0$ to $6.2f_0$) improvement for waterfilling and pre-emphasis, respectively. The point where higher z (e.g. $z = 4$ to avoid clipping) preforms better than boosting the signal strength (say, $z = 2.5$) is around a γ_{tot} of 46 dB for pre-emphasis and of 62 dB for waterfilling. For a high speed link (several hundreds of Mbit/sec or several Gbit/sec) with an LED with a typical 3 dB bandwidth of $f_0 \approx 10$ MHz, a large γ_{tot} (e.g. more than 70 dB) is needed. In this range, a large fraction of the electrical power is burnt in DC biasing to limit the distortion. From Fig. 4.5(b) and (d), we learn that a z above 4 will be required to achieve a transmission rate of more than $80f_0$. Moreover, mitigating second-order distortion also becomes critical (see Fig 3).

A Typical Example

Consider an OWC system limited by total power, with the channel frequency response given in (4.1). At 1m distance, a gain-to-noise ratio of 70 dB in a 1 MHz sub-carrier bandwidth requires

$$\frac{H_0^2}{N_0 \times 10^6} = 10^7 \rightarrow N_0 \approx 10^{-19}(V^2/Hz).$$

A 450 nm LXML-PB02-0023 blue LED was measured. It has a 3-dB bandwidth around $f_0 \approx 10$ MHz at I_{LED} =350 mA bias current [72] with $V_0 \approx 2.5$ V. Since the dominant term in the total power consumption equation (3.16) is the DC power, from (3.12) we have

$$\mathrm{V}_{LED} = 2.5V + (1\Omega) \times (0.35A) = 2.85V,$$

and

$$P_{tot} \approx P_{DC} = (2.85V) \times (0.35A) \approx 1W.$$

The total NPB is calculated from (4.47) and (4.48) to be 1.6×10^5, thus approximately 52 dB. For the 52 dB of γ_{tot}, the throughput can be found in Fig. 4.5(b) and (d) for DCO-PAM and DCO-OFDM using waterfilling or pre-emphasis strategies. Fig. 4.6 shows the throughput versus the distance between the transmitter and the receiver for different z values. To include the impact of distance d, we used the 4th power law ("40 log d") path loss model of [142]. With $\gamma_{tot,dB} = 10\log_{10}(\gamma_{tot})$,

$$\gamma_{tot,dB}(d) = 52 - 40\log_{10}\left(\frac{d}{1\mathrm{m}}\right)$$

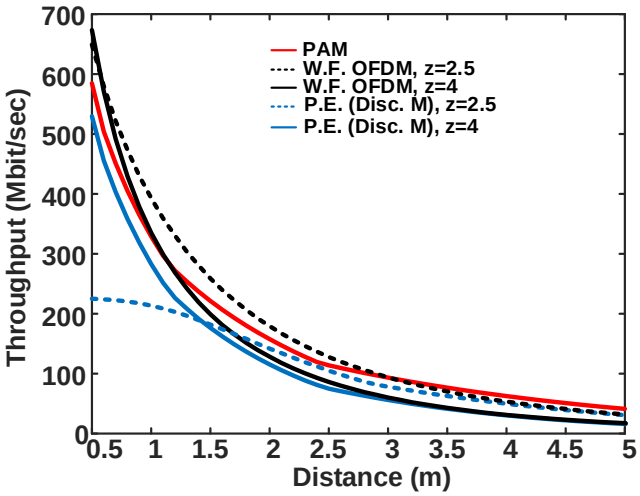

Figure 4.6: Throughput versus distance for PAM (red), pre-emphasized OFDM with $z = 2.5$ (dashed-blue) and $z = 4$ (solid-blue) and waterfilling with $z = 2.5$ (dashed-black) and $z = 4$ (solid-black). The total electrical power is limited to 1 W.

to ensure that at 1 m distance, γ_{tot} is 52 dB. Several relevant observations can be made. Waterfilling marginally outperforms DCO-PAM at distances below 1 m, while operating beyond 3 m, DCO-PAM provides the better performance. At a close distance (below 1 m for waterfilling and below 1.5 m for pre-emphasis), the received signal is sufficiently strong to focus merely on distortion. Therefore, a large z (e.g. $z = 4$ rather than a small $z = 2.5$) is required to provide the optimum performance. On the other hand, when the distance increases, the receiver noise floor becomes the dominant design concern and the transmitter has to boost the modulation depth, thereby compromising z and tolerating more clipping.

4.8 Computational Complexity

Another important aspect for the comparison is the computational complexity of modulation at the transmitter and detection in the receiver. The complexity in the OFDM transmit Inverse Fast Fourier Transform (IFFT) and in the receive (FFT) of size N is in the order of $4N \log_2 N$ per block. For PAM, the use of simple pre-emphasis eliminates the need for equalization if only the low-pass LED response needs to be compensated. One can repair ISI at the receiver more effectively by using a DFE equalizer [60]. The latter can simultaneously handle channel multipath, if it

occurs, and avoids too large noise enhancements, but at the cost of a complex Viterbi algorithm. Also frequency–domain, equalizers have been proposed, that place both an FFT and IFFT at the receiver. However, one may argue that the complexity of FFTs typically is small compared to other signal processing, such that the use of an FFT is not prohibitive. Possibly, the complexity of the signalling protocol, its over-head, and the number of memory operations in an OFDM system can be of concern. In this respect, waterfilling or uniform power loading may be less attractive as it places a different modulation order per sub-carrier, which needs to be negotiated between receiver and transmitter.

4.9 Conclusions

The two popular OWC modulation schemes, namely Orthogonal Frequency Division Multiplexing (OFDM) and Pulse Amplitude Modulation (PAM) were compared for use in an IM/DD system using LEDs, considering the minimally required DC biasing to ensure the non-negativity of driving LED current. To cope with the LED channel response, two well-known OFDM power loading strategies were discussed, namely, waterfilling and the correction of the attenuation of higher frequencies by a pre-emphasis.

We derived mathematical expressions for the throughput and the optimum modulation bandwidth to be used. Using a suitable Normalized Power Budget (NPB) definition and a normalization to the LED 3 dB bandwidth, generic results could be derived. It was shown that for the same extra modulation power, which is a suitable metric for VLC where the DC bias is already available for illumination, pre-emphasized OFDM and PAM at a reduced modulation depth showed no difference in throughput and in required modulation bandwidth. Waterfilling, which is the optimum power allocation strategy, outperforms pre-emphasized systems, but occupies a larger required bandwidth.

The conclusions and optimally recommended choices, however, differ for channels that are limited by their optical power or by their electrical power. Optical power can be confined by limits to the illumination level in VLC or by eye safety precautions in IR. In IR communication, particularly with battery–powered devices, the total available electrical power may be limited. Here, the DC bias can be minimized, just to carry the data signal in an undistorted manner. OFDM suffers from a large peak-to-average ratio. The non-negativity constraint forces the use of an unattractively large bias. Compromising for a practical bias current for OFDM, peaks in the current have to be clipped before being applied to the LED. We quantified and modeled the resulting distortion and its impact on performance, which allows for an optimization of the modulation depth depending on, for instance, NPB. In this chapter, we generalized

derivations for OFDM, both for waterfilling and for pre-emphasis, by including the clipping noise in the throughput and bandwidth optimization. We showed that for an IR channel, more precisely, for optical–power limited channels, under moderate modulation bandwidth, M-PAM with a linear high-boost filter is able to provide a higher data transmission rate than any sub-carrier loading scheme, optimized for DCO-OFDM. When a large NPB is available, OFDM preferably with bit loading that follows waterfilling principles outperforms M-PAM.

The best LED bias setting depends on the NPB. Moreover, the cross point for the NPB at which waterfilling DCO-OFDM starts to outperform PAM moves towards higher NPB values when a higher bias current of the LED is selected. Therefore, an OFDM system with a fixed LED bias current which is designed to operate for a range of NPBs might underperform compared to PAM, if OFDM is optimized for low NPB range or for large coverage. Preferably, an adaptive setting of the LED bias current, optimized for the NPB is used to yield the highest DCO-OFDM throughput.

Chapter 5

LED Nonlinear Distortion Mitigation

In chapters 3 and 4, the LED communication channel was assumed to be linear, except the current clipping at the LED input to ensure non-negativity constraint. In section 4.5.2, it was discussed that even if the bias to rms ratio of the LED current becomes so high that the current clipping is negligible, the invertible distortions become dominant limiting the system throughput. In this chapter, a novel non-linear equalizer is proposed to tackle the LED induced distortions. The effectiveness of the proposed equalizer is shown for both DCO-OFDM and PAM schemes.

5.1 Introduction

[1]The rapidly growing demand to communicate wirelessly creates spectrum scarcity that poses pressure on Radio Frequency (RF) systems. Optical Wireless Communication (OWC), including Infrared (IR) or Visible Light Communication (VLC) offers a promising alternative to relieve the congested RF spectrum [13, 19, 104, 105]. Collimation and beam sectorization allow denser spectrum reuse to serve more users at high bit rates. For instance, OWC appears attractive to provide simultaneous connections to passengers in airline or railway cabins. As OWC can ensure interference-free links, these suffer less from latency jitter. This appears attractive for latency-critical transportation systems or autonomous vehicles.

However, LEDs have bandwidth limitations and exhibit non-linearities [75, 104]. Multiple non-linear mechanisms, including imperfections in the LED electronics cir-

[1]This chapter consists of material previously published in IEEE Transactions on Vehicular Technology [74] which was re-structured for readability in thesis form.

cuitry, contribute to the distortion of the IR or VLC signals. Effects in the LED junction itself typically are dominant [27]. Distortion due to the LED driver electronics, Digital-to-Analog Converters (DACs), Analog-to-Digital Converters (ADCs), Photo-Diodes (PDs) have been extensively studied in the past and can mostly be avoided [40, 42].

To also repair LED-induced distortion, we start with a system identification via an appropriate LED model. Static non-linearities were modeled in [45–47]. However, for high–speed applications using a large–signal bandwidth, the inclusion of memory effects in distortion can significantly improve performance, as the LED photon generation depends not only on instantaneous non-linear effects, but also on the build–up of hole–electron concentrations in the (recent) past [33, 42]. In this regard, Volterra series are very generic, thus can be applied for LEDs. However, this technique involves a large number of the parameters that all must be extracted and updated [42–44]. For example, for a Volterra series with a memory length N, N^p coefficients must be estimated for the pth kernel function. One needs an appropriate choice for the number of the memories taps and for the order of the distortion to avoid the use of an overly parameter-rich model. With a large set of Volterra parameters, its complexity makes Volterra series identification and distortion mitigation hard to implement for high-speed real-time applications. Nonetheless, we saw successful offline approaches in [43, 44].

LED models by Hammerstein and Wiener [76, 106] can be seen as an aggressively simplified subset of Volterra series. These models cascade a Linear Time-Invariant (LTI) low-pass filter with a separate memoryless non-linear block. However, [40] argues that such models fail to model the different fall and rise time constants. Moreover, eye diagrams show a level-dependent position of the optimum PAM sampling moment, which can be modelled only by considering non-linear operations on time–delayed signals.

Recently, the models for the dynamic behaviour of LEDs have been refined in literature as the light output responses are described by non-linear dynamic differential equations [75]. We study the use of Double Hetero-structured (DH) LEDs. For this structure both the carriers and the optical field are confined in a central recombination region to achieve high optical efficiency [33]. The ABC model for hole-electron recombination in the Quantum Well (QW) was used in [33, 40, 41, 71] to describe the photon output as a function of the dynamic carrier concentrations. It can be extended to LED input–current–to–output–power relations. This method can model the LEDs with a lower computational complexity than generic Volterra approaches that lack a restriction to physical phenomena.

Using an equivalent discrete-time model for DH-LEDs, both the distortion and the low-pass behavior of the LEDs can be inverted, either before the LED emitter [40] or at the receiver [41]. However, full elimination of the distortion caused by the LED in

Table 5.1: Summary of coefficient number for non-linear models in literature

Ref., Year	Non-linear Models	Functions	Coefficient Number	Others
[44], 2011	Volterra model	LED model	very large	Continuous parameter sweep for kernels
[43], 2013	Volterra model	Predistorter in VLC	144	Only for the second kernel
[76], 2014	Memory polynomial model	Postdistorter in VLC	6-24	Two delays and varying order nonlinearity
[108], 2015	Volterra model	Postdistorter in VLC	625	Only for the second kernel
[109], 2016	Memory polynomial model	Predistorter in VLC	8-10	One delays and varying order nonlinearity
[110], 2017	Volterra model in frequency	Postdistorter in VLC	1024-7168	Only for the second kernel
[41], [40], 2018	Rate-equation-based model	Post/Predistorter in VLC	5	Delay and noise enhancement
This work	Rate-equation-based model	Postdistorter in VLC	3	Improve the noise performance

a Zero-Forcing (ZF) manner, leads to excessive noise enhancements at the receiver, or excessively large high–frequency components in the LED driving signal.

In this chapter, we study a Minimum Mean Square Error (MMSE)-based trade-off of noise enhancement versus minimizing residual distortion artefacts left at the receiver. Based on a pre–determined training sequence, the receiver estimates the equalizer parameters to minimize the total noise–plus–distortion power. LED parameter variations are caused for instance by aging, temperature drifts and different operating biases. As these do not change rapidly, parameter estimation is needed but does not need to be frequent so it may not necessarily impose significant additional communication overhead. The contributions of this chapter can further be summarized as follows:

- Following the work in [41], we start with the physical model of photon generation and consider a discrete–time equivalent that can be inverted into a ZF non-linear equalizer. We modify this in two ways: We simplify the ZF structure to reduce the number of unknown coefficients from five (in [41]) to three, plus an overall gain parameter. We show that the model error stays well below the typical receiver noise floor.

- Secondly, we estimate the coefficients to minimise the Mean Square Error (MSE), considering also noise.

- For the simplified equalizer, we develop a model to study the effect of noise on the coefficients estimation and on the equalizer performance for random i.i.d. Gaussian signals. Comparisons with the ZF approach are also provided. We show that the model results in a simpler set of equations for the estimation of equalizer coefficients.

- We show that the resulting, simplified equalizer can be interpreted as a heavily pruned Volterra series. In fact, it only considers the coefficients that reflect dominant physical hole-electron recombination mechanisms. Evidently, a richer, more generic Volterra model with more degrees of freedom can not be less effective in addressing the static and dynamic distortion than our solution, as the latter by default forces many coefficients that do not represent a known physical mechanism to zero. Nonetheless, by bounding the room for improvement, we show that the gain to be expected for the generic Volterra solution is negligible and may not justify the added complexity, slower coefficient estimation and the higher power consumption.

- We simulate our algorithms and experimentally verify these with real measurement signals to quantify and benchmark the performance over a range of Signal-to-Noise Ratios (SNRs). That is, measurement results in this chapter

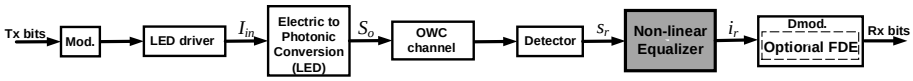

Figure 5.1: Block diagram of optical wireless system including our non-linear equalizer.

demonstrate that a single-tap second-order non-linear equalizer is able to mitigate the distortion and Inter-symbol Interference (ISI) in LED channels.

- We show that the non-linear equalizer can effectively widen the measured eye diagram of a Pulse Amplitude Modulation (PAM) signal [107]. For DC–offset Optical Orthogonal Frequency Division Multiplexing (DCO-OFDM) [55,56] our non-linear equalizer can reduce the power consumption by 70% while maintaining constant system throughput. Alternatively, we can improve the system throughput by more than 50% at a constant LED power consumption.

A comparison with the state of art is given in Table I, including a summary of coefficient numbers for non-linear models and other information.

The rest of the chapter is organized as follows. Section 5.2 presents the dynamic behavior of the LEDs. Section 5.3 presents the non-linear LED inverse (ZF equalization) and its (proposed) simplified form. In Section 5.4, the MMSE-based equalizer parameter estimation is discussed. The effect of noise on the equalizer parameter estimation and its performance is analyzed in Section 5.5. This chapter examines the proposed equalizer in both simulation and experimental setup. The setup is described in Section 5.6. The effect of LED-induced distortion on the signal and thereafter the performance of the non-linear equalizer are shown in simulations and experiments using PAM, in Section 5.7, and DCO-OFDM, in Section 5.8, schemes and using single-tone sinusoidal signal in Section 5.9. Finally, conclusions are presented in Section 5.10.

5.2 System Description and LED Model

The overall block diagram of our OWC system is shown in Fig. 5.1. A modulator (Mod.) creates time–domain waveforms from incoming data symbols. The LED driver converts these waveforms into LED current $I_{in}(t)$ for transmission over the wireless OWC channel, in the form of optical intensity modulation with power $S_o(t)$. The optical signal is then detected and converted back into the electrical domain $s_r(t)$ at the receiver. As the LED distorts the signal, we use a non-linear equalizer in the receiver chain to avoid that LED–induced distortion degrades the link performance.

Finally, a demodulator (Dmod.) converts the distortion–free signal $i_r(t)$ into bits for error correction and decoding.

For OFDM transmission, it may have advantages not to repair the LED low-pass nature, but only to remove the distortion. In fact, bit and power loading algorithms can optimize the throughput over the low-pass channel. Inverting the LED frequency response is known not to be optimum [72], so we allow adaptive bit loading and waterfilling approaches that anyhow have a Frequency–Domain Equalizer (FDE) in the form of an FFT followed by per–sub-carrier processing.

Typically, the detector and certainly the propagation channel are linear, but these may not necessarily have a flat frequency response. A generic Volterra series equalizer can simultaneously handle the cascade of the non-linear LED and such other, linear filtering effects. However, the complexity benefits of our design are possible by focusing on the LED in isolation. If, for instance in a system with wide beams, multipath propagation is also significant, one may have to use a more complicated structure. Alternatively, one could consider to first separately repair linear channel effects and use our non-linear single–tap compensation in a dedicated stage to address LED distortion.

In this section, we briefly review the LED physics and discuss the dominant phenomena that govern the dynamic relations among the input current, the carrier concentrations in the QW and the output optical power. The dynamic behavior of an LED can be modeled by the ABC expression, which has become increasingly accepted in physics literature [33, 40, 52, 53, 67–71]. For a typical LED used in IR communication or in illumination, the number of carriers $N_c(t)$ in the quantum well changes according to,

$$\frac{dN_c(t)}{dt} = \frac{I_{in}(t)}{qA_w t_w} - \left\{(A + p_0 B)N_c(t) + BN_c^2(t) + CN_c^3(t)\right\}, \tag{5.1}$$

where $I_{in}(t)$ is the injected current, q is the elementary charge of $q = 1.6 \times 10^{-19}$ coulomb, A represents the defect-related Shockley-Read-Hall recombination constant, B is the radiative recombination constant, C is the Auger recombination coefficient, A_w and t_w are the LED area and thickness, respectively, and p_0 is the doping concentration in the active layer. The QW carrier concentration $N_c(t) = \mathrm{N_c} + n_c(t)$ contains a DC bias $\mathrm{N_c}$ and a small–signal variation $n_c(t)$. In this chapter, we adhere to the following notation convention: capital *italic* font for total instantaneous quantities such as N_c, capital roman font for DC bias quantities, such as $\mathrm{N_c}$ and small characters for modulation around DC, such as n_c.

The large-signal LED model described by (5.1) is a generic expression suitable for instance for Pulse Amplitude Modulation (PAM) or Asymmetrically Clipped Optical-OFDM (ACO-OFDM). For DC-centered modulation, such as DCO-OFDM, it can be more insightful to split the DC term from the AC variations. That is, injecting a

current $I_{in}(t) = \mathrm{I_{in}} + i_{in}(t)$, yields a DC bias setting of

$$\frac{\mathrm{I_{in}}}{qA_w t_w} = (A + p_0 B)\mathrm{N_c} + B{\mathrm{N_c}}^2 + C{\mathrm{N_c}}^3, \tag{5.2}$$

and the DC-free signal modulation adheres to

$$\begin{aligned}\frac{dn_c(t)}{dt} = \frac{i_{in}(t)}{qA_w t_w} &- (A + p_0 B + 2B\mathrm{N_c} + 3C{\mathrm{N_c}}^2)n_c(t) \\ &- (B + 3C\mathrm{N_c})n_c^2(t) - Cn_c^3(t).\end{aligned} \tag{5.3}$$

So, in fact the response to modulation depends on the bias $\mathrm{N_c}$. The optical power of the output light is [33]

$$S_o(t) = A_w t_w \langle E_p \rangle B\left(p_0 N_c(t) + N_c^2(t)\right), \tag{5.4}$$

where $\langle E_p \rangle$ is the average photon energy. The DC light output $\mathrm{S_o}$ and the light modulation s_o in the optical output power are, respectively,

$$\mathrm{S_o} = A_w t_w \langle E_p \rangle B\mathrm{N_c}(p_0 + \mathrm{N_c}), \tag{5.5}$$

and

$$s_o(t) = A_w t_w \langle E_p \rangle B\left[(2\mathrm{N_c} + p_0)n_c(t) + n_c^2(t)\right]. \tag{5.6}$$

We can observe that N_c is related to I_{in} by a first-order non-linear differential equation, i.e., one in which only first derivatives occur, and the output power is a non-linear function of N_c. That makes the output optical power to exhibit both static (that is, memoryless) and dynamic non-linear effects as a function of input current I_{in}.

5.2.1 Low–Frequency (Quasi–Static) LED Model

For slowly varying (or DC) signals, the term $dN_c(t)/dt$ in (5.1) is negligible and we have the quasi-static expression as

$$\frac{I_{in}(t)}{qA_w t_w} = (A + p_0 B)N_c(t) + BN_c^2(t) + CN_c^3(t). \tag{5.7}$$

The term C is responsible for the efficiency droop in high power LEDs which causes a gradual saturation of output power with increased input current. The optical power output is also given by (5.4).

For high-efficiency LEDs, such as so-called non-resonant cavity (NRC) LEDs, the two efficiency droop coefficients C and A (compared to Bp_0) can be neglected [33]. The carrier concentration given in (5.7) is simplified into

$$\frac{I_{in}(t)}{qA_w t_w} = (p_0 B)N_c(t) + BN_c^2(t). \tag{5.8}$$

Combining (5.8) and (5.4), the output optical power as a function of input current would reduce to

$$S_o(t) = \frac{\langle E_p \rangle}{q} I_{in}(t). \tag{5.9}$$

This shows that for a slowly varying signal and for $A \ll Bp_0$ and negligible term C, the LED is (statically) linear, while memory effects and bandwidth limitations are not relevant for slow modulation.

5.2.2 Discrete-Time LED Dynamic Model with Normalization

Converting the expressions (5.3) and (5.6) for DC-free signal variations into discrete time n sampled at T_s intervals, thus at $t = t_0 + nT_s$, the concentration $n_c(n)$ can be described recursively from the previous states, as

$$n_c(n+1) = a_0 i_{in}(n) + a_1 n_c(n) + a_2 n_c^2(n) + a_3 n_c^3(n), \tag{5.10}$$

and

$$s_o(n) = a_4 n_c(n) + a_5 n_c^2(n). \tag{5.11}$$

We retain the structure of this system, but we simplify the notation into parameters that can be estimated by the receiver. To this end, we introduce the normalization parameter ξ:

$$\begin{aligned} a_0 &= \xi \tfrac{T_s}{q t_w A_w}, \\ a_1 &= 1 - T_s(A + p_0 B + 2B\mathrm{N_c} + 3C\mathrm{N_c^2}), \\ a_2 &= -\xi^{-1} T_s(B + 3C\mathrm{N_c}), \\ a_3 &= -\xi^{-2} T_s C, \\ a_4 &= \xi^{-1} A_w t_w \langle E_p \rangle B(p_0 + 2\mathrm{N_c}), \\ a_5 &= \xi^{-2} A_w t_w \langle E_p \rangle B. \end{aligned} \tag{5.12}$$

Choosing $\xi = q t_w A_w T_s^{-1}$ simplifies fixed–point implementation of an FPGA LED emulator while it does not affect the input-to-output relation of the LED model. Thereby, we eliminate a_0 in the equalizer model, thus ensure that our algorithm unambiguously determines $a_1, ..a_5$. This discrete–time non–linear dynamic representation (5.10) and (5.11) is illustrated in Fig. 5.2. This diagram consists of two stages: the first stage relates the injected current i_{in} into carrier concentrations n_c in the LED junction and the second stage expresses the photonic output power s_o. In the remainder of this chapter, we use this discrete–time model of the LEDs.

For an analysis without separating the DC-bias from the AC modulation, the same LED structure of Fig. 5.2 can be used, but with coefficients that follow from (5.1) and (5.4). In fact, one can obtain the a_i $(i = 0, 1, ..., 5)$ coefficients by setting $\mathrm{N_c} = 0$ from (5.12). We will show that an accurate simplification in a suitable non-negative range can also be obtained as a best fit with fewer coefficients.

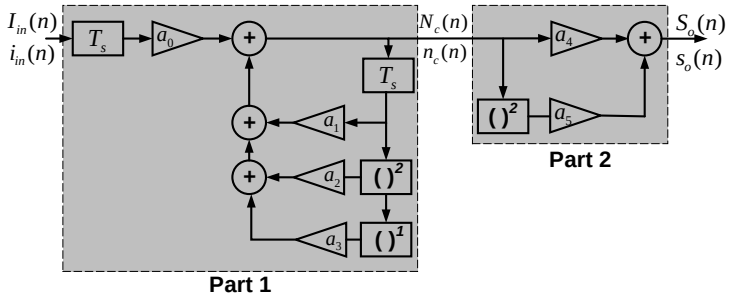

Figure 5.2: Discrete-time non-linear LED model. For a DC-free modulation and for non-negative e.g. PAM, the same structure applies, but coefficients may take slightly different values.

5.3 Post-Distorter (Equalizer) Structure

In the Appendix A, we derive a structure for our equalizer, namely a post–distorter that inverts the LED model to eliminate the LED–induced distortion, as in Fig. 5.3(a). The (Infinite Response, feedback) structure in Part 1 of Fig. 5.2 can be inverted by a (Finite Response, feed-forward) structure. The inverse of the second stage ($n_c \rightarrow s_o$) involves a square–root operation. To simplify the computational complexity, we propose to approximate the square–root operation by a (preferably second–order) polynomial. Fig. 5.3(b) shows the resulting equalizer with coefficients c_i ($i = 1, ..., 4$). As we show in Sections 5.7 - 5.9, the second-order non-linear equalizer effectively compensates nonlinearity and non–linear memory effects of the LED.

We verify that the same structure (Fig. 5.3(b)) can also operate effectively as an equalizer that reduces the MSE, if we appropriately select the parameter setting. We introduce and evaluate an approach that updates the coefficients c_is of the equalizer using MMSE criteria. That is, we use values of incoming signals in our analysis, while the MMSE estimator in the receiver has the task to estimate c_is by correlation of incoming signals with a known training sequence.

This simplified structure reduces the number of independent coefficients from five to three, as elaborated in the Appendix. Since the LED parameters are subject to process spread, to biasing N_c, and may drift over time, these need to be estimated per device and repeatedly. This reduction in model parameters accelerates the acquisition and makes tracking more reliable. Sections 5.7 and 5.8 show that both for PAM and OFDM signals, the simplified equalizer structure substantially improves performance over an approach without equalizer, and is not substantially worse than a more ideal equalization. We simulate and experimentally test over which range of SNR this approach works. Since the equalizer parameters are extracted at the receiver, it can

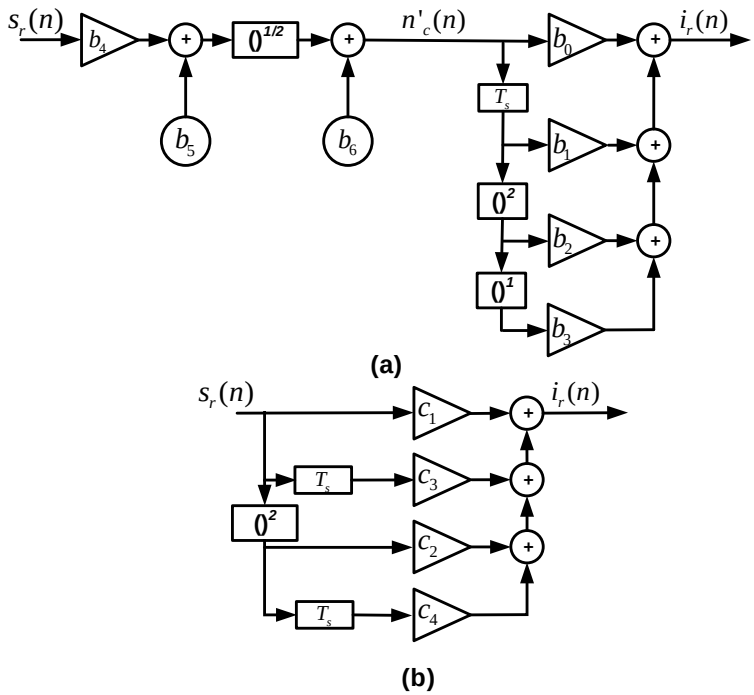

Figure 5.3: (a) Exact inverse of LED model (post-distorter), (b) The proposed simplified structure. The input to the equalizer can be DC-free (s_r employing e.g. OFDM modulation scheme) or can be accompanied by a DC component (S_r employing e.g. PAM modulation).

be done repeatedly to account for effects such as channel variation and device aging.

5.3.1 Single-Tap Second-Order Non-linear Equalizer

One approach to simplify the square-root operation is a Taylor expansion around the signal mean, which conceptually applies to the concept of DCO-OFDM with a signal probability mass centered near the DC bias. Another approach is a best fit in the range between the LED turn-on current and the maximum signal level used, which conceptually better suits the concept of PAM with equally probable constellation points in the signal range.

Following the latter, Appendix B expresses the equalized receive signal $i_r(n)$ as a function of the optical input $s_r(n)$ in Fig. 5.3(a). The square–root operation appears in two forms, $f(x) = \sqrt{x}$ and $g(x) = (\sqrt{x})^3$, where x resembles the signal input argument to the functions. Appendix B further evaluates the accuracy of approximating $f(.)$ and $g(.)$ as second-order polynomials. Section 5.4 discusses an estimation pro-

cedure to find best fits for the equalizer coefficients, based on a training sequence. Appendix B shows that the equalizer output can then be written as

$$i_r(n) \approx c_1 s_r(n) + c_2 s_r(n)^2 + c_3 s_r(n-1) + c_4 s_r(n-1)^2, \tag{5.13}$$

where, the parameters $c_1..c_4$ are the equalizer parameters to be estimated. The overall gain is a redundant parameter since it has the same function as a normalization or gain in the symbol slicer, following the equalizer, typically even after the OFDM FFT. Therefore, and without loss of generality, we can normalize (5.13) to c_1, thus take $c_i := c_i/c_1$ which leaves all signal-to-noise ratios unaffected.

We use two successive samples and their squares as four input values to (5.13). One important observation from (5.13) is that the second–order non–linear one–delay–tap polynomial model adequately covers the dominant LED characteristics.

The diagram of the equalizer, described by (5.13), is shown in Fig. 5.3(b). This structure only addresses second–order distortion, however, for our application, it can perform equally well as the exactly inverting post-distorter shown in Fig. 5.3(a). It has negligible error. In fact, our structure (shown in Fig. 5.3(b)) can be seen as a special, heavily pruned instantiation of a Volterra-series equalizer, where we have no cross terms of signals with various delays and in which we only use a single delay and second-order terms.

5.3.2 Special Case: Very Small–Signal Excitation

For very small–signal excitation, $|i_{in}(n)| \ll \mathrm{I_{in}}$, the distortion components n_c^2 and n_c^3 are negligible, so the optical output power s_o is a linear function of i_{in}. However, the LED exhibits a first–order low–pass roll off, with a 3 dB bandwidth that depends on I_{in}, discussed in section 2.4. In the discrete–time LED model of Fig. 5.2 with the a_i $(i = 0, 1, ..., 5)$ parameters given in (5.12), the non–linear paths can be discarded and the LED model reduces to a forward path with a gain factor and a delayed feedback path with gain a_1 that determines the 3 dB bandwidth. The transfer function of Part 1 becomes

$$H(z = e^{-j\omega T_s}) = \frac{a_0}{1 - a_1 z^{-1}}. \tag{5.14}$$

The 3 dB bandwidth can be derived as

$$\omega_{3dB} = \frac{1}{T_s} \sin^{-1}\left(\frac{1 - a_1^2}{2a_1}\right), \tag{5.15}$$

Replacing a_1 from (5.12), in the limit of $T_s \to 0$ the 3 dB bandwidth reduces to (2.20).

For a small signal at the input of the simplified equalizer of Fig. 5.3(b), $s_r^2(n)$ and $s_r^2(n-1)$ are also negligible and the equalizer structure is simplified into a feed–forward path with a gain of $c_3 = -a_1$ and a single delay tap to compensate the first-order low pass behavior of the LED.

5.4 Training–Sequence Based Estimation

To configure the equalizer, the parameters $\boldsymbol{c}_{1\times 4} = [c_1, c_2, c_3, c_4]$ need to be determined. In this section, we formulate a model for a training-sequence-based approach and its performance. It extends typical use of preambles in communication links used to estimate linear channels.

A training reference of the form of a known current $i_{in,t}(n)$ is offered to the input of the LED, in addition to a DC bias. The transmit optical signal is denoted by $s_{o,t}$. The signal at the input and the output of our simplified equalizer are $s_{r,t}$ and $i_{r,t}$, respectively. Our objective is to minimize the MSE, defined as

$$\mathbf{E}\{|e(n)|^2\} = \mathbf{E}\{(i_{in,t}(n) - i_{r,t}(n))^2\}. \tag{5.16}$$

Using our equalizer structure (5.13), its output $i_{r,t}$ is re-written in vector form as,

$$i_{r,t}(n) = \boldsymbol{c}.\boldsymbol{s_{r,t}}(n), \tag{5.17}$$

where two successive samples of the incoming signal are denoted as the vector

$$\begin{aligned}\boldsymbol{s_{r,t}}_{4\times 1}(n) &= [s_1, s_2, s_3, s_4]^T \\ &= [s_{r,t}(n), s^2_{r,t}(n), s_{r,t}(n-1), s^2_{r,t}(n-1)]^T.\end{aligned}$$

Here, $(\cdot)^T$ denotes the matrix transpose operation. For simplicity of notation and readability, we drop the index term n for all variables on discrete time n. The expected value of the error is

$$\begin{aligned}\mathbf{E}\left\{|e|^2\right\} &= \mathbf{E}\{(i_{in,t} - \boldsymbol{c}\boldsymbol{s_{r,t}})(i_{in,t} - \boldsymbol{c}\boldsymbol{s_{r,t}})^T\} \\ &= \mathbf{E}\{i^2_{in,t}\} - 2\boldsymbol{c}\mathbf{E}\{\boldsymbol{s_{r,t}} i_{in,t}\} + \boldsymbol{c}\mathbf{E}\{\boldsymbol{s_{r,t}}\boldsymbol{s^T_{r,t}}\}\boldsymbol{c}^T,\end{aligned} \tag{5.18}$$

where $\mathbf{E}\{i^2_{in,t}\}$ is the autocorrelation of the training sequence, $\mathbf{E}\{\boldsymbol{s_{r,t}} i_{in,t}\}$ is a 4×1 matrix containing the cross correlation of the training sequence and the elements of $s_i (i = 1, 2, 3, 4)$ and $\mathbf{E}\{\boldsymbol{s_{r,t}}\boldsymbol{s^T_{r,t}}\}$ is a 4×4 correlation matrix with elements

$$\mathbf{E}\{\boldsymbol{s_{r,t}}\boldsymbol{s^T_{r,t}}\} = \mathbf{E}\begin{pmatrix} s_1^2 & s_1 s_2 & s_1 s_3 & s_1 s_4 \\ s_2 s_1 & s_2^2 & s_2 s_3 & s_2 s_4 \\ s_3 s_1 & s_3 s_2 & s_3^2 & s_3 s_4 \\ s_4 s_1 & s_4 s_2 & s_4 s_3 & s_4^2 \end{pmatrix}. \tag{5.19}$$

The cost function in (5.18) must be minimized with respect to the coefficient vector $\boldsymbol{c}$, so

$$\frac{\partial \mathbf{E}\left\{|e|^2\right\}}{\partial \boldsymbol{c}} = -2\mathbf{E}\{\boldsymbol{s_{r,t}} i_{in,t}\} + 2\mathbf{E}\{\boldsymbol{s_{r,t}}\boldsymbol{s^T_{r,t}}\}\boldsymbol{c}^T = 0. \tag{5.20}$$

Hence, the coefficients $\boldsymbol{c}$ of our simplified equalizer are determined from

$$\boldsymbol{c}^T = \left(\mathbf{E}\{\boldsymbol{s_{r,t}}\boldsymbol{s_{r,t}^T}\}\right)^{-1}\mathbf{E}\{\boldsymbol{s_{r,t}}i_{in,t}\}. \tag{5.21}$$

The proposed approach measures the matrix and vectors from the incoming signals, during a training period, but uses prior knowledge that we have about its structure. For coefficients $\boldsymbol{c}$, it involves an inverse operation of a matrix. For long sequences, its complexity can be challenging. We can adopt adaptive algorithms such as Recursive Least Squares (RLS) to solve the above problem. As we do not see it as a task of the equalizer to control the gain, we normalized $\boldsymbol{c}$, without loss of performance, to c_1. In fact, we expand the matrix form (5.21) and obtain the four elements $\boldsymbol{c}$ and normalize those elements to unity c_1. After normalization, we get $c_1 = 1$ and three closed-form expressions for c_2/c_1, c_3/c_1 and c_4/c_1, respectively. In fact, $i_{r,t}$ will differ from $i_{in,t}$ by only a constant factor while distortion is mitigated.

5.5 Effect of Noise

In this section, we study the effect that Additive White Gaussian Noise (AWGN) has on the estimation of the equalizer coefficients c_i $(i = 1, 2, 3, 4)$. In addition to numerical simulations, we derive a mathematical model with reasonable simplifications to develop a further intuition. Later, we justify these approximations and assumptions by comparing these with numerical simulations. We show that for a randomly chosen i.i.d. Gaussian training sequence, the simplifications lead to a simpler set of equations for the equalizer, which facilitates the implementation.

5.5.1 Estimation of Non-linear Equalizer Coefficients

To consider the effect of noise on parameters c_i $(i = 1, 2, 3, 4)$, we assume the presence of AWGN with variance σ_z^2 and independent of signal $s_{r,t}$. The received signal vector is rewritten as $\boldsymbol{s_{r,t}}_{4\times 1}(\boldsymbol{n})$ as

$$\begin{aligned}\boldsymbol{s_{r,t}}_{4\times 1}(n) &= [s_1, s_2, s_3, s_4]^T \\ &= \begin{bmatrix} s_{r,t}(n) + z_r(n) \\ (s_{r,t}(n) + z_r(n))^2 \\ s_{r,t}(n-1) + z_r(n-1) \\ (s_{r,t}(n-1) + z_r(n-1))^2 \end{bmatrix}.\end{aligned} \tag{5.22}$$

In this analysis, for simplicity, we take a random i.i.d. Gaussian signal as training sequence $i_{in,t}$. Such sequence would resemble an OFDM signal. Nonetheless, such training sequence can also estimate the channel to equalize for a PAM signal. Later on, we will show that a random PAM sequence can also work well, in practice. We

leave it to further work to find appropriate specific sequences that work better than random sequences. Writing (5.20) in matrix format, for row 1 and 3 we have

$$c_1\mathbf{E}\{s_1^2\} + c_2\mathbf{E}\{s_1s_2\} + c_3\mathbf{E}\{s_1s_3\} + c_4\mathbf{E}\{s_1s_4\} = \mathbf{E}\{s_1 i_{in,t}(n)\} \tag{5.23}$$

$$c_1\mathbf{E}\{s_1s_3\} + c_2\mathbf{E}\{s_2s_3\} + c_3\mathbf{E}\{s_3^2\} + c_4\mathbf{E}\{s_3s_4\} = \mathbf{E}\{s_3 i_{in,t}(n)\}. \tag{5.24}$$

If the distortion is sufficiently small to approximate $s_{r,t}(n)$ as (Jointly) Gaussian, $s_{r,t}(n)$ has an even distribution. Then,

$$\mathbf{E}\{s_1s_2\} = \mathbf{E}\{(s_{r,t}(n) + z(n))^3\} = 0. \tag{5.25}$$

Similarly, $\mathbf{E}\{s_3s_4\} = 0$. To show that also cross-variances are near-zero, we use the well-known property of jointly Gaussian random variables (JG r.v.'s) that these variables can be decomposed into a set of independent Jointly Gaussian random variables. That is, without loss of generality, we can write

$$\begin{bmatrix} s_{r,t}(n) \\ s_{r,t}(n-1) \end{bmatrix} = \begin{bmatrix} 1 & 0 \\ \rho & \sqrt{(1-\rho^2)} \end{bmatrix} \begin{bmatrix} s_{r,t}(n) \\ \xi(n) \end{bmatrix}. \tag{5.26}$$

where $s_{r,t}(n)$ and ξ are i.i.d. random variables. In fact, the correlation coefficient ρ follows from $\mathbf{E}\{s_{r,t}(n)s_{r,t}(n-1)\} = \rho\mathbf{E}\{s_{r,t}^2(n)\}$. It plays a specific role in the equalizer parameters, but initially, we just argue that for any pair of JG r.v.'s, a ρ exists. Writing out $\mathbf{E}\{s_1s_4\} = \mathbf{E}\{s_1s_3^2\}$ and using (5.26) result in

$$\mathbf{E}\{s_1s_4\} = \mathbf{E}\{(s_{r,t}(n) + z_r(n)) \cdot (\rho s_{r,t}(n) + \sqrt{1-\rho^2}\xi(n) + z_r(n-1))^2\} \tag{5.27}$$

Expanding (5.27), all the terms contain an odd moment, thus all are zero for zero-mean Gaussian random variables. Similarly, $\mathbf{E}\{s_2s_3\} = 0$ regardless of ρ. Hence, we expect that an estimation algorithm based on correlating the received signal $s_{r,t}$ with the local reference copy has a benign convergence behavior, which we will experimentally verify later.

A Gaussian signal with second-order distortion formally is non-Gaussian, but artefacts are typically 20 to 30 dB below the main signal, such that a Gaussian approximation of the distorted signal may be reasonable. Moreover, in the following sections, we verify whether an estimator inspired by this Gaussian model in practice also works for signals with significant distortion. Using these properties, the set of equations (5.23) and (5.24) can be simplified into

$$c_1\mathbf{E}\{s_1^2\} + c_3\mathbf{E}\{s_1s_3\} = \mathbf{E}\{s_1 i_{in,t}(n)\} \tag{5.28}$$

$$c_1\mathbf{E}\{s_1s_3\} + c_3\mathbf{E}\{s_3^2\} = \mathbf{E}\{s_3 i_{in,t}(n)\}. \tag{5.29}$$

The channel estimator measures the correlations in the above expression, and estimates the best fit for c_1 and c_3 to be used by the receiver.

Next, we will argue that ρ plays a specific role in the equalizer structure. We can derive that

$$\frac{c_3}{c_1} = \frac{k(\mathrm{SNR_r}+1) - \rho.\mathrm{SNR_r}}{\mathrm{SNR_r}+1-k.\rho.\mathrm{SNR_r}}, \tag{5.30}$$

where we used

$$\mathbf{E}\{i_{in,t}z_r\} = \mathbf{E}\{s_{r,t}z_r\} = \mathbf{E}\{z_r(n)z_r(n-1)\} = 0,$$

$$\mathbf{E}\{s_{r,t}(n)s_{r,t}(n-1)\} = \rho\mathbf{E}\{s_{r,t}^2(n)\}$$

and defined $\mathbf{E}\{s_{r,t}^2\} = \sigma_{s_r}^2$, $\mathbf{E}\{z_r^2\} = \sigma_z^2$ and the signal–to–noise ratio at the input of the equalizer as $\mathrm{SNR_r} = \sigma_{s_r}^2/\sigma_z^2$. The parameter k in (5.30) is defined as

$$k = \frac{\mathbf{E}\{s_{r,t}(n-1)i_{in,t}\}}{\mathbf{E}\{s_{r,t}(n)i_{in,t}\}}. \tag{5.31}$$

Since the LED output at time instant index n only depends on the input current at the current and previous time instants, we have $\mathbf{E}\{s_{r,t}(n-1)i_{in,t}(n)\} = 0$, so (5.30) reduces to

$$\frac{c_3}{c_1} = -\rho\frac{\mathrm{SNR_r}}{1+\mathrm{SNR_r}}. \tag{5.32}$$

Equation (5.32) gives the linear first memory tap coefficient of the equalizer as a function of ρ and a factor to mitigate excessive noise enhancements. In fact, the term c_3 is responsible for boosting high frequencies, thus the noise enhancements. For $\mathrm{SNR_r} \gg 1$, $c_3/c_1 = -\rho$ and the memory tap coefficient only depends on the received signal correlation with its delayed samples. This is expected as c_3 is compensating the filtering effect of the LED which attenuates higher frequencies. Eq. (5.32) confirms that if the SNR reduces, the equalizer reduces the term c_3 (to limit noise enhancement) and in the limit of $\mathrm{SNR_r} \to 0$, $c_3 = 0$ to minimize the error.

Having c_1 and c_3, c_2 and c_4 are estimated from rows 2 and 4 of equation (5.20), and we get

$$\begin{aligned} c_2\mathbf{E}\{s_2^2\} + c_4\mathbf{E}\{s_2s_4\} = \\ \mathbf{E}\{s_2i_{in,t}(n)\} - c_1\mathbf{E}\{s_2s_1\} - c_3\mathbf{E}\{s_2s_3\} \end{aligned} \tag{5.33}$$

$$\begin{aligned} c_2\mathbf{E}\{s_2s_4\} + c_4\mathbf{E}\{s_4^2\} = \\ \mathbf{E}\{s_4i_{in,t}(n)\} - c_1\mathbf{E}\{s_4s_1\} - c_3\mathbf{E}\{s_4s_3\}. \end{aligned} \tag{5.34}$$

One can write the above linear expressions in matrix form, which can be inverted to obtain values for c_2 and c_4. We will discuss the effect of noise on c_2 and c_4 in the next section, with simulations.

To estimate c_3/c_1, we discussed that $s_{r,t}$ can be considered as Gaussian and

$$\mathbf{E}\{s_1 s_2\} = \mathbf{E}\{s_2 s_3\} = \mathbf{E}\{s_4 s_1\} = \mathbf{E}\{s_3 s_4\} = 0.$$

Intuitively speaking this was a reasonable assumption because c_3/c_1 is compensating linear distortion (filtering effect) introduced by the LED and for this purpose the Gaussian approximation for $s_{r,t}$ can be justified. c_3 is predominantly determined by the main signal while distortion is second–order effect.

5.5.2 Summary of Equalizer Algorithm

In practice, the equalizer has to estimate the coefficients by measuring cross and auto–correlations on the incoming signals. That is, expectation values are not known, but can be estimated using local averaging. To distinguish between theoretical performance evaluation, as mainly done in the previous section, and the real-time execution of the algorithm here, we use the averaging operand "$\langle x \rangle$" and use the overhead $\hat{x}$ for estimates. Using our algorithm (5.32)-(5.34) can be rewritten into

$$\frac{c_3}{c_1} = -\hat{\rho}\frac{\hat{\mathrm{SNR}}_\mathrm{r}}{1+\hat{\mathrm{SNR}}_\mathrm{r}}, \tag{5.35}$$

where $\hat{\rho}$ is an estimation of ρ, obtained from

$$\hat{\rho} = \frac{\langle s_{r,t}(n) s_{r,t}(n-1)\rangle}{\left\langle s_{r,t}^2(n)\right\rangle}$$

and $\hat{\mathrm{SNR}}_\mathrm{r}$ is the estimated SNR at the receiver. The estimated $\hat{\mathrm{SNR}}_\mathrm{r}$ is taken from Error Vector Measurements (EVM) once the system is in tracking mode,

$$c_2\left\langle s_2^2\right\rangle + c_4\left\langle s_2 s_4\right\rangle = \langle s_2 i_{in,t}(n)\rangle - c_1\left\langle s_2 s_1\right\rangle - c_3\left\langle s_2 s_3\right\rangle \tag{5.36}$$

$$c_2\left\langle s_2 s_4\right\rangle + c_4\left\langle s_4^2\right\rangle = \langle s_4 i_{in,t}(n)\rangle - c_1\left\langle s_4 s_1\right\rangle - c_3\left\langle s_4 s_3\right\rangle. \tag{5.37}$$

The above Equations (5.35)-(5.37) give a recipe to obtain the coefficients. These are accurate under Gaussian assumptions on the received signal. However, a Gaussian signal, say an OFDM signal, with second-order distortion would, strictly speaking, violate this simplification. Since numerical operations in a real-time system must be limited in complexity, we test whether these can nonetheless be used also for distorted signals. In the simulations, we verify whether for modest amounts of distortion, this approach works adequately.

Table 5.2: Parameters for the LED model

Parameter	Interpretation	Value
q	Charge of Electron	1.6×10^{-19}
A	SRH recombination coefficient	1×10^{6}
B	Radiative recombination coefficient	2×10^{-11}No./s/cm^3
C	Auger recombination coefficient	1×10^{-27}
t_w	Active layer thickness	30×10^{-6}cm
A_w	Active layer area	0.0139cm^2
p_0	Doping concentration	2×10^{17} No./cm^3
$\langle E_p \rangle$	Energy of photon (650nm)	3.06×10^{-19}J
T_s	Sampling period in simulation	1ns

5.5.3 Noise and Signal Distortion Power

The equalizer aims at reproducing an undistorted replica of the signal $i_{in}(n)$ at its output. Then, the expected value of the squared error, defined in (5.16), is the variance of noise plus distortion,

$$\mathbf{E}\{|e(n)|^2\} = \sigma_d^2 + \sigma_{z_{eff}}^2 \tag{5.38}$$

where σ_d^2 is the residual distortion power and $\sigma_{z_{eff}}^2$ is the effective noise power at the equalizer output. Taking the definition (5.22) of $\boldsymbol{s_{r,t}}$ and importing (5.17) into (5.16) result in

$$\begin{aligned}\sigma_d^2 =& \mathbf{E}\{(i_{in,t}(n) - c_1 s_{r,t}(n) - c_2 s_{r,t}^2(n) \\ & - c_3 s_{r,t}(n-1) - c_4 s_{r,t}^2(n-1))^2\}\end{aligned} \tag{5.39}$$

and

$$\sigma_{z_{eff}}^2 = \sigma_z^2 \left(1 + c_3^2 + 3(c_2^2 + c_4^2)\sigma_z^2 + 4(c_2^2 + c_4^2)\sigma_s^2 + 2c_2 c_4 \sigma_z^2\right) \tag{5.40}$$

where we assumed that the noise samples $z_r(n)$ and $z_r(n-1)$ are i.i.d. Gaussian r.v.'s with zero mean that are independent of the received signal.

In the ZF approach, the equalizer parameters c_{2-4} aim at $\sigma_d^2 = 0$. However, it can be seen that this setting of c_3 inappropriately boosts noise while the other terms in the right hand side of (5.40) are negligible. For this analysis, we only considered noise in the signal bandwidth. Pre-filtering suppresses out-of-band noise. The MMSE approach, on the other hand, tolerates some distortion whenever fully eliminating $\sigma_d^2 = 0$ would boost the noise too much.

5.5.4 A simulation Example

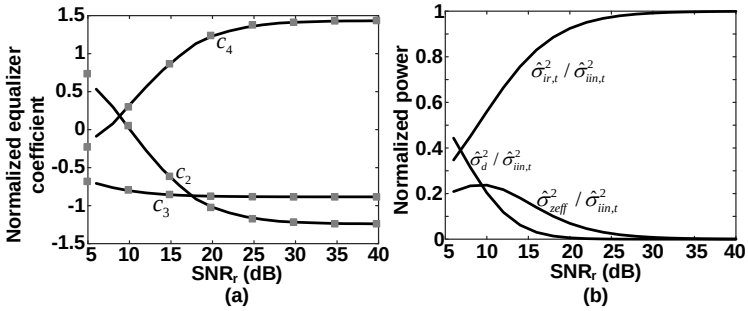

Figure 5.4: (a) Normalized c_{2-4} using (5.35) to (5.37) (grey squares) and using (5.21) (solid dark curves). (b) Normalized (estimated) output signal, distortion and noise power at the equalizer output.

In this section, we examine the performance of our simple equalizer and its parameter estimation by simulating an LED with parameters given in Table II. We assumed a random i.i.d. Gaussian current with mean and AC Root-Mean-Square (RMS) of 0.5 and 0.1 A ($\sigma_{i_{in,t}} = 0.1$ A), respectively, at the input of the LED with 10k samples taken at $1/T_s = 1$ GHz. Since the equalizer aims to reduce the output error, ideally, $\mathbf{E}\{i_{r,t}^2\} = \mathbf{E}\{i_{in,t}^2\} = 0.01$ A^2. We calculated the parameters a_i for the LED parameters given in Table II, and used Matlab to find the optical output power $s_{o,t}(n)$. We corrected for the channel pass loss and assumed $s_{r,t}(n) = s_{o,t}(n)$.

Having $s_{r,t}(n)$, we calculated $\left\langle \boldsymbol{s_{r,t}} \boldsymbol{s_{r,t}^T} \right\rangle$, $\langle \boldsymbol{s_{r,t}} i_{in,t} \rangle$ and $\left\langle s_{r,t}^2(n) \right\rangle$ from incoming signals, which were our local estimates of $\mathbf{E}\{\boldsymbol{s_{r,t}} \boldsymbol{s_{r,t}^T}\}$, $\mathbf{E}\{\boldsymbol{s_{r,t}} i_{in,t}\}$ and $\mathbf{E}\{s_{r,t}^2(n)\}$, respectively. We also defined $\hat{\sigma}_{i_{r,t}}^2 = \left\langle i_{r,t}^2(n) \right\rangle$, $\hat{\sigma}_s^2 = \left\langle s_{r,t}^2(n) \right\rangle$ and for a specific value of SNR$_\mathrm{r}$, the variance of the AWGN noise was estimated from $\hat{\sigma}_z^2 = \hat{\sigma}_s^2 / \mathrm{SNR_r}$.

For the MMSE equalizer, the normalized parameters c_{2-4} are estimated from (5.35) to (5.37) (grey squares) and compared to those obtained from (5.21) (solid dark curves), shown in Fig. 5.4(a) as a function of received SNR. The power of the signal at the equalizer output, power of the distortion (5.39) and noise (5.40) are also shown in Fig. 5.4(b), all normalized to $\sigma_{i_{in,t}}^2$. Several observations can be made. Firstly, the grey squares and solid lines in Fig. 5.4 are at almost identical values. This verifies the accuracy of the simplifications that resulted in the simpler sets of equations (5.28), (5.29), (5.33) and (5.34). As discussed, we can approximate $s_{r,t(n)}$ as being Gaussian for sufficiently small distortion. To further determine at what level distortion was preset, we applied a single–tone, sinusoidal signal with a frequency of 10 MHz, an amplitude of 0.4 A and a DC level of 0.5 A. Simulation showed a total harmonic distortion at approximately -23 dB.

Secondly, at high SNR$_r$, the non-linear coefficients c_2 and c_4 are non-zero and

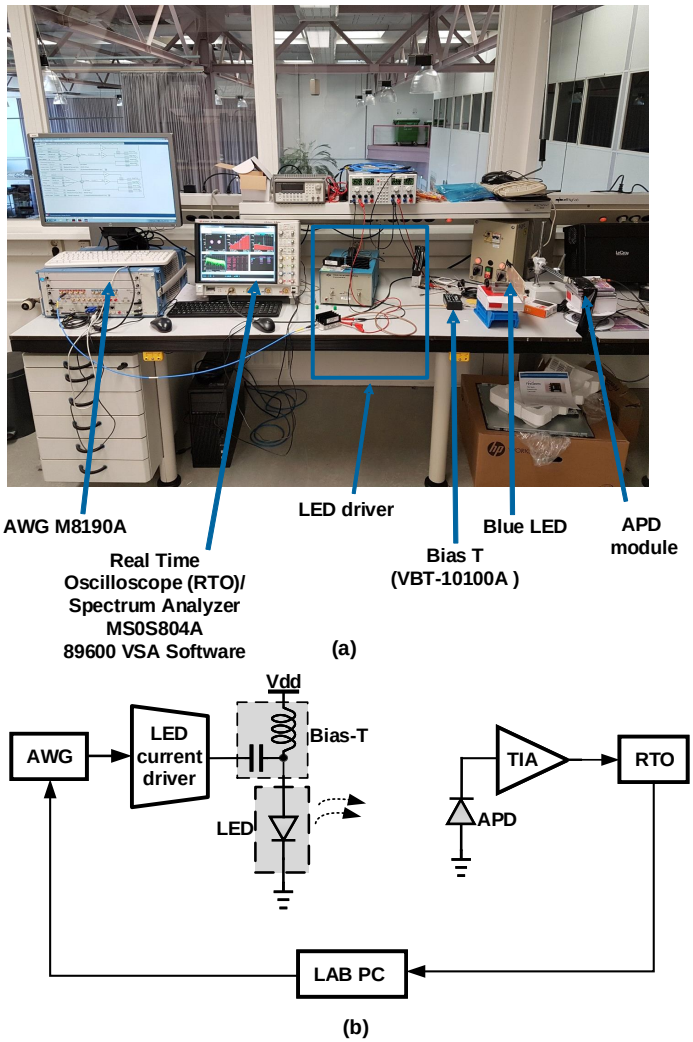

Figure 5.5: (a) Measurement Setup. (b) Schematic of the setup.

fully cancel the distortion power, resulting in $\hat{\sigma}^2_{i_{r,t}} = \mathbf{E}\{i^2_{in,t}\} = 0.01$ while the noise power is already negligible. When the received SNR drops, the equalizer keeps the balance between the output noise and distortion power to minimize the total error.

5.6 Simulation and Practical Verification Setup

We examine the performance of the equalizer structure proposed in Fig. 5.3(b), with the two commonly used signaling methods: PAM and OFDM, in section VII and

VIII, resp. Finally, in Section IX, we use a single-tone sinusoidal signal to show the effectiveness of the proposed structure in reducing harmonic distortion.

The experimental setup is shown in Fig. 5.5(a) with its simplified schematic in Fig. 5.5(b). An Arbitrary Waveform Generator (AWG) created the modulated signal which was converted into current domain by a custom–made LED current driver based on a Minicircuit ZHL-6A amplifier. A bias-T network was used to separately inject the LED DC and AC current components. A resistor was interposed between the amplifier and the Bias-T. The resistor was inserted intentionally not only to protect the power amplifier from being damaged by a mismatching LED load of too low impedance, it also ensures that the amplifier drives the LED with a specific current that is linear with the desired signal waveform. In fact, the resistor ensures that the LED current is not subject to any LED I-V non-linearity. The Bias-T was configured to operate adequately over the entire band, even with an LED dynamic resistance load of less than one Ohm. For practical driver circuits, we refer to [50, 79].

A LXML-PB02-0023 blue LED with a measured 3-dB cut-off frequency of 10 MHz at I_{in} = 350 mA bias current was used at the transmitter. At the receiver, we used a Silicon Avalanche Photo-Detector (Si-APD) with 100 MHz 3-dB bandwidth and 1 mm diameter active area [87] followed by a Trans-Impedance Amplifier (TIA). The distance between the LED and the APD was fixed at 1 m. The output signal of the TIA was sampled using a Real Time Oscilloscope (RTO) and delivered to a lab PC for equalization and BER measurement.

In the simulations, we implemented the discrete model of Fig. 5.2 with parameters given in Table 5.2. For a specific transmit power, the quality of the received signal (SNR) at the receiver is limited due to the presence of (AWGN) noise coming from the background ambient light and thermal noise of the receiver. In simulations, the LED input current was directly modulated, the path loss, APD and the TIA were replaced by a normalized unity gain block and the AWGN noise was added in the entire signal bandwidth of the LED output signal, referenced to the simulated (target) SNR at the receiver. Equalizer parameters were estimated in the presence of AWGN using (5.21).

5.7 Non-linear Equalizer in PAM Signaling

For PAM, we numerically simulated to what extent the equalizer improved the Symbol Error Rate (SER) of 4-PAM and 8-PAM. Additionally, using real signals obtained from a hardware setup, we also tested the effect of the equalizer on the eye-diagram of 4-PAM.

5.7.1 Simulation Results

Different symbol rates with raised-cosine pulse shaping were applied to an LED specified by the parameters given in Table II. By proper DC biasing, the minimum LED current was limited to 0.02 A, i.e., as low as possible but avoiding to fully deplete the LED junction charge, at which more severe non-linear mechanisms kick in. The peak current was set not to exceed 0.4 A. The dynamic discrete-time LED model, discussed in Section 5.2 was employed with a numerical solver in MATLAB to calculate the output optical signal. The sampling frequency in the solver was chosen to be 16 times of the symbol rate hence $T_s = T_{sym}/16$ where T_{sym} is a symbol duration in time, although in principle practical receiver systems can process data at rates much closer to the Nyquist rate for pulse shaped data.

We considered three different scenarios. The initial scenario involved no equalization at the receiver. The received noisy signal (after scaling to the original signal level) was directly used for SER calculation. In the second scenario, the non-linear terms in the equalizer was forced to zero, hence a first-order MMSE-based linear equalizer was retained. Finally, we tested our non-linear MMSE-based equalizer. The results are given in Fig. 5.6(a) for 20 Msym/sec symbol rate. It can be seen that, due to the non-linear low–pass behavior of the LED, without any equalization the SER is too large for any practical communication system to handle. Using a linear equalizer can extend the LED bandwidth limitation. However, the BER exceeds the theoretical curve for a flat linear channel at SNRs above 10 dB for 20 Msym/sec symbol rate. This becomes worse at higher rates. For reference, we compare these with an ideal (flat and low-pass) AWGN Linear Time-Invariant (LTI) channel. Using the non-linear equalizer, we reach almost the same performance as in a distortion–free AWGN LTI channel. This observation also indicates that the expected improvement by any other generic and optimized solutions such as Volterra-based compensation is limited and the potential added complexity is not justified. At higher rates, the compensation of the low-pass LED junction inevitably leads to some noise penalty (Fig. 5.6(b)). This is quantified in Fig. 5.6(b), where dotted and dashed lines represent the performance of a fixed MMSE first–order linear equalizer to mitigate ISI in a first–order low–pass LTI channel with 10 MHz bandwidth. Fig. 5.6(a), shows that distortion compensation is critical to support 8-PAM.

Fig. 5.7 plots the performance of the parameter estimation for 4-PAM. Here, we used uniform random PAM levels as training sequence, that is, to estimate the equalizer coefficients $\boldsymbol{c}$, we used the generic derivation (5.21) instead of the simplified derivations (5.35)-(5.37). Multiple SER simulations show that the parameters converge (in worst case) in around 50 symbols for SNRs better than 18 dB, where uncoded bit rates are in typically preferred range of 10^{-4} to 10^{-3}. At poorer SNR, not only the SER deteriorates (Fig. 5.6) but also convergence and number of symbols

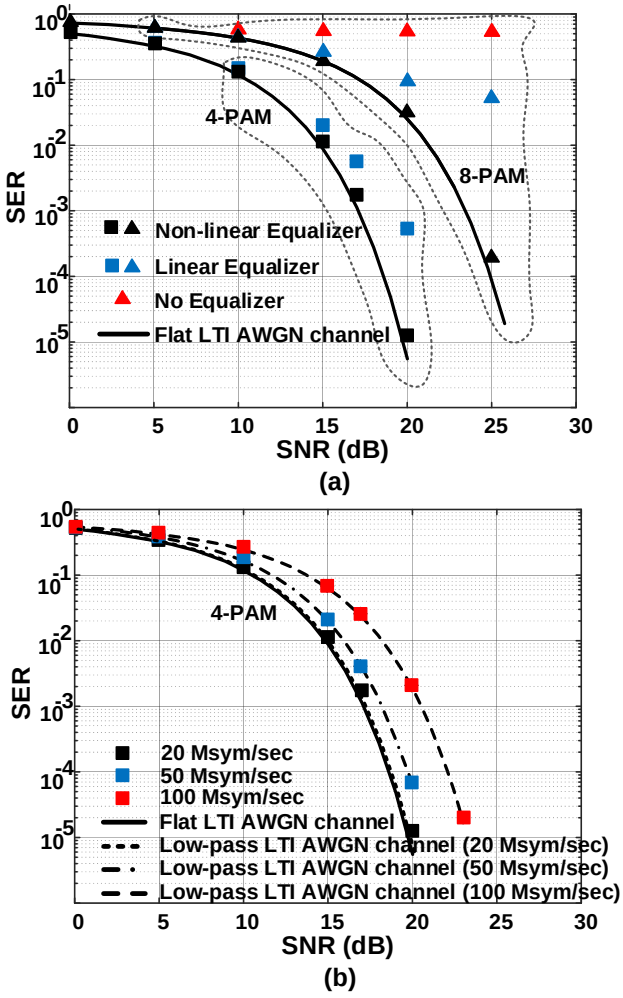

Figure 5.6: (a) Simulated SER performance for 4-PAM and 8-PAM signaling at 20 Msym/sec symbol rate. Red triangles (only for 8-PAM) show the SER for the case of no equalization at the receiver. Blue and dark triangles/squares show the SER for having a first–order linear equalizer and for having the proposed non-linear equalizer, respectively. The theoretical limit for uncoded SER for AWGN frequency–flat LTI channel is shown with a solid black line. (b) Simulated SER performance of 4-PAM for 20, 50 and 100 Msym/sec using the proposed non-linear equalizer (squares). Bound: SER for distortion-free frequency–flat (solid line) and distortion–free first–order low–pass LTI channel (dotted lines).

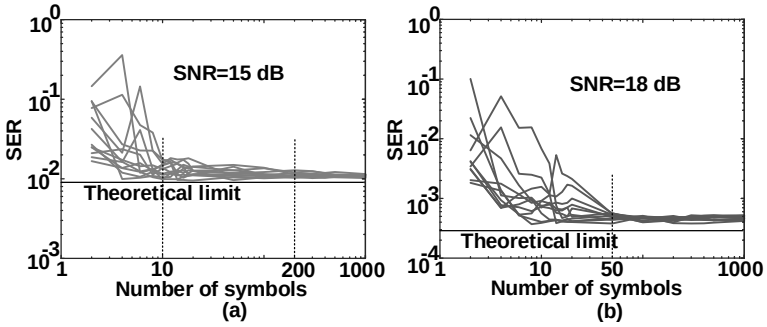

Figure 5.7: Simulated 4-PAM SER vs training sequence length for SNR of 15 dB (a) and 18 dB (b).

needed for training increase (Fig. 5.7).

In the eye diagrams of Fig. 5.8, to exaggerate the effect for visual illustration, we plot square-shaped waveforms. Eye diagrams of the received signal (after scaling) before equalization, after applying a linear equalizer and after applying our non-linear equalizer are shown in Fig. 5.8 for 20 Msym/sec input to the LED. From Fig. 5.8(a), it can be observed that the received signal has a right skew due to non-linear memory effects of the LED. In fact, this behavior is equivalent to the LED responding faster at a higher input current level, or equivalent to shorter rise times than fall times. Due to efficiency droop at higher input currents (non-zero term C), PAM levels of the received signal gets closer.

The use of just a linear equalizer can also improve performance and it can result in a wider eye, shown in Fig. 5.8(b). However, as the equalizer structure misses non-linear terms, the spacing of PAM levels is not uniform, but is narrower at higher levels. Inclusion of the non-linear terms, shown in Fig. 5.8(c), mitigates the issue of non-uniform spacing between PAM levels and results in a much better eye opening compared to linear equalizer.

5.7.2 Experimental Results

To further validate our proposed equalizer structure, the effectiveness of the non-linear equalizer on the eye opening of a 4-PAM signal over optical communication was examined in a real measurement. Fig. 5.9 shows the eye diagrams of the 4-PAM modulating signal for 5 Msym/s before and after non-linear equalization. It can be seen that the eye diagram of the received 4-PAM signal before non-linear equalization has a right skew, but after applying the non-linear equalization the eye is open and

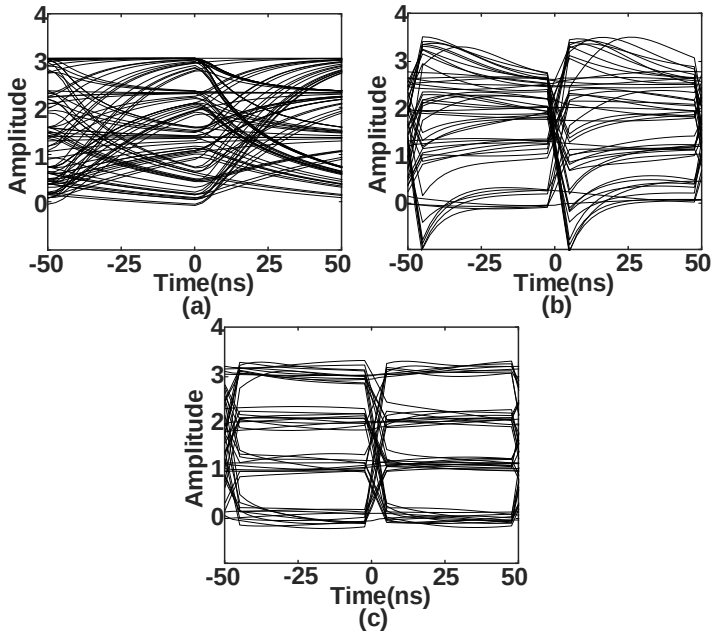

Figure 5.8: Simulated 4-PAM eye diagrams with rectangular waveform shaping and symbol rate of 20 Msym/s before (a), after linear (b) and non-linear equalization (c). The sample rate is taken 16x of the symbol rate, the training sequence includes 20 symbols (320 samples) and noise is absent.

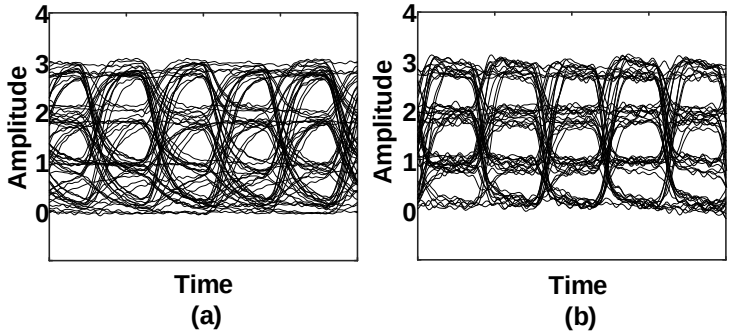

Figure 5.9: Experimentally measured 4-PAM eye diagrams with raised cosine waveform shaping, symbol rate of 5 Msym/s and 30 dB SNR. before (a) with $\mathrm{BER} = 10^{-2}$ and after (b) non-linear equalization. The initial 25 symbols of the PAM signal was used to estimate the equalizer parameters.

levels are clearly distinguishable.

5.8 Non-linear equalizer in OFDM Signaling

For OFDM, we examine the rate increase that can be achieved for a given SER (or BER) target. For the experimental validation of the proposed equalizer with an OFDM modulation scheme, 64 sub-carriers were used in a 100 MHz bandwidth. The time–domain training sequence of the signal was measured and compared to the original signal to estimate our equalizer vector coefficients (c_i for $i = 1, 2, 3, 4$).

The communication channel gain/loss can be described by a constant factor, independent of the transmit signal [81–83]. The distorted signal was received by an APD and then amplified by a TIA. We verified that the APD and the TIA did not distort the received signal. The proposed post-distorter (or non-linear equalizer) was used after the TIA (in digital domain) to eliminate or mitigate the distortion caused by the LED to enhance the communication performance. Instead of measuring the BER versus SNR curve for a fixed predetermined bit loading, we used an approach that is more commonly used for OFDM over the low-pass OWC channel. Per sub-carrier, we used an adaptive power and bit loading to maximize the overall communication rate. We selected the largest possible vector of constellations while adhering to the conditions that 1) the total modulation power is constrained and 2) that on every sub-carrier the uncoded BER remains below 10^{-4} [72]. Similar to Hughes-Hartogs [63], the algorithm takes an uncoded BER target and as long as the BER remains below that target BER, it iteratively increases the modulation load with steps of one extra bit, selecting the sub-carrier where adding that extra bit requires the lowest extra power.

In our system, we concatenated our non-linear equalizer, that reduces distortion, with an OFDM system that inherently applies a frequency-domain (linear) equalization. The latter may compensate any frequency filtering earlier in the chain before its FFT, such as by c_1 and c_3. However, c_3 needs to be set such that it is matched by c_2 and c_4 in the distortion cancelling path. That is, one can omit tap c_3, to build just a distortion remover that leaves adaptation to the LED frequency response as a task for the FFT-based OFDM system. Of course, taking $c_3 = 0$, implies that c_2 and c_4 must adapt according to suppress the then differently filtered distortion.

The end-to-end bit loading algorithm optimizes the sub-carrier payload. Fig. 5.10(a) shows the SNR measured at the receiver for two different LED DC currents, 100 mA and 350 mA, with and without enabling the non-linear equalizer. A communication LED, biased at 100 mA with a non-linear equalizer enabled in the receiver, is seen to achieve a better received signal quality than a system without the non-linear equalizer, even if the latter is biased at 350 mA, where more linearity can be expected. That is, the non-linear equalizer saves a significant amount of power (more than 71%

reduction in biasing power).

Bringing the bias current back to 350 mA, the non-linear equalizer allows more modulation power and more bits on the sub-carriers: at 40 MHz, the signal-to-noise-plus-distortion is improved by more than 6 dB, allowing the use of 64-QAM modulation, compared to only 8-QAM without the equalizer. The bit-loading profiles with and without running the non-linear equalizer are shown in Fig. 5.10(b), which are limited by detector noise and no longer by distortion. The non-linear equalizer improves the data rate from 303 Mbits/sec to 464 Mbits/sec (more than 53% improvement). Although the non-linear equalizer also compensates the low-pass frequency response, this of course does not improve the signal-to-noise ratio at high frequency as also noise is enhanced. The beneficial effects of the non-linear equalizer are in reducing the distortion, while the OFDM signaling handles the frequency selectivity, after linearization.

5.9 Harmonic Distortion

In order to see the effectiveness of the proposed non-linear equalizer, a single–tone signal was fed into the LED while harmonics were determined and measured at the output, before and after applying the non-linear equalizer. The frequency and amplitude of the tone is selected such that it triggers the LED non-linear dynamic operation. For a very small input amplitude (discussed in section 5.3.2) or a slow input variations (low-frequency input discussed in sections 5.2.1) LED works in a linear regime.

The DC current of the LED was set to 0.2 A and the amplitude of the modulating AC current to 0.15 A, i.e., the LED current swings from 0.05 A to 0.35 A at 10 MHz. It was sampled at 100 MHz. The received harmonic levels at the receiver, normalized to the fundamental, are shown in Table 5.3 with and without operating the non-linear equalizer. The number of periods used in our measurements for FFT calculation and also for equalizer parameter estimation was set to 10. The received SNR at the receiver was around 30 dB.

We observe that the second harmonic is dominant at the LED output and that it is reduced below the receiver noise floor, such that it is indistinguishable from the noise. The third harmonic, which anyhow is of less concern, is also suppressed below the noise floor.

5.10 Conclusions

Mitigation of non-linear distortion is crucial in the design of future high-speed VLC systems. The LED is the major source of nonlinearity in a VLC system that limits the

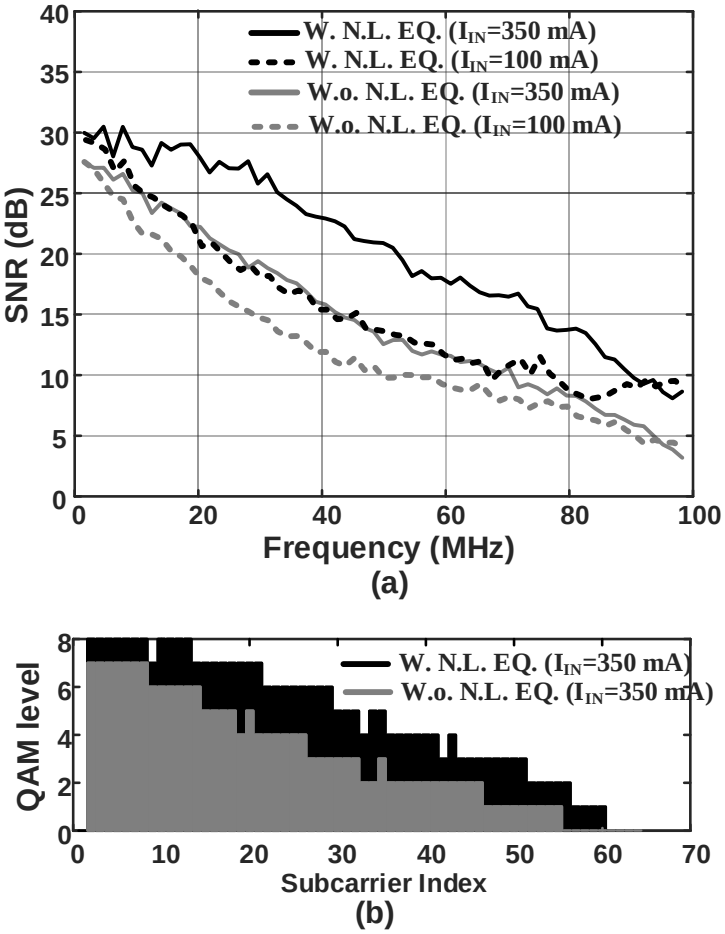

Figure 5.10: (a) **Measured SNR versus frequency for** $I_{IN} = 100$ **mA (dashed) and** 350 **mA (solid) with (W.) and without (W.o.) non-linear (N.L.) equalizer (EQ.), (b) Sub-carrier bit loading for** $I_{IN} = 350$ **mA to ensure** $BER \leq 10^{-4}$ **with (dark) and without (grey) enabling the non-linear equalizer.**

Table 5.3: Measured harmonics of the LED output w/o non-linear equalizer and with non-linear equalizer for received SNR of 30 dB.

Harmonic #	W/o equalizer	With equalizer
1	0 dBc	0 dBc
2	−20.7 dBc	< -45 dBc
3	−39.3 dBc	< -43 dBc

achievable bit rate. The recombination rates of photon generation in Double Heterostructure (DH) LEDs give a mixture of nonlinearities and memory effects. Their mathematical model can be translated into an equivalent discrete-time circuit, that can be inverted. In order to effectively track and compensate for the nonlinearity and memory effects we proposed an MMSE equalizer. This equalizer gives an estimation of the transmitted signal using a single delay tap: sample of the received signal, a previous sample and squares of these are used as four inputs to our design.

The equalization requires to be updated regularly because of variations in LED nonlinearity with time, temperature and different operating regimes, biases, and so on. The alternative of a blind Volterra equalization is computationally complex and time consuming in practical systems. The work in this chapter has shown that the MMSE equalizer with a single tap of memory and second–order nonlinearity can mitigate the LED distortion efficiently.

The performance of the non-linear equalizer technique was tested in a DCO-OFDM system with an adaptive bit and power loading algorithm. For a required Bit Error Rate (BER), more than 50% higher data rate was achieved. We expect that on less noisy channels, the gains can be higher. We also saw that the non-linear equalizer can be used to substantially reduce biasing power.

Using Pulse Amplitude Modulation (PAM), the widening of the eye diagram was experimentally validated and the expected improvement of the equalizer on the SER performance was quantified by simulation.

Finally, for single-tone sinusoidal modulation of the LED, the harmonic distortion was measured at the receiver. The second harmonic appeared dominant. The non-linear equalizer can mitigate the harmonics to levels below the receiver noise floor, as more than 20 dB mitigation of the second harmonic appeared feasible, even under realistic noise considerations.

Chapter 6

Conclusions and Recommendations for Future Research

The presented dissertation dealt with different challenges for efficient communication over the LED channels.

6.1 Conclusions and Original Contributions

Based on the detailed discussions in this dissertation, a few general conclusions are highlighted:

- LED channel is a low-pass communication channel.
- In a distortion/clipping free regime, OFDM (Orthogonal Frequency Division Multiplexing) can maximize the link throughput. This is achieved by employing an optimum yet complex power and bit distribution over the sub-carriers. It was shown that the simpler (in the implementation) uniform power loading and adapting the constellations (bit distributions) or fixing the constellation size and adapting the power are also interesting. The throughput penalty of both approaches were quantified to be acceptable and it was shown that fixing the constellation is vulnerable to channel response variations.
- When the current clipping noise is present, the PAM (Pulse Amplitude Modulation) scheme could also be considered to replace the OFDM. When the channel gain drops (far receiver), boosting the signal at a constant bias introduces more

clipping noise limiting the throughput achieved by OFDM. There, it was shown that PAM outperforms OFDM.

- LED induced distortions are another source of throughput limitations in LED communication channel. Compensating the non-linearities, it was shown that a better throughput could be achieved at a constant LED bias or at a constant link throughput, the LED bias current can be reduced significantly.

Original contributions of this dissertations include,

- The exponential channel model, reported in the literature, was verified and compared to the theoretical model derived from the LED physics.

- Optical blue filters were modeled and experimentally verified. The presented model answered the contradictory conclusions reported in the literature on the effectiveness of these filters in an LED communication link.

- For the first time, the throughput expressions were derived for the exponential LED channel. The derivations include two modulation schemes, OFDM with three different power and bit loading strategies and PAM.

- The optimum modulation bandwidth to be used by the transmitter was theoretically derived for the exponential channel, for OFDM and PAM, and verified experimentally (only for OFDM).

- Novel algorithms were presented to choose the optimum modulation order for the single-carrier PAM and for the sub-carriers of OFDM while optimizing the total bandwidth.

- The most comprehensive platform was built to to make a fair comparison between OFDM and PAM. A new system parameter, the Normalized Power Budget, was introduced to draw the conclusions based on the fixed system parameters; the available modulation power, channel DC gain and 3 dB bandwidth and the receiver noise floor. The comparisons were made for three different power constraints at the transmitter; constraint on the total or the extra (due to modulation) electrical power or on the average optical power. A general equation was proposed for the LED total power consumption to cover all three power constraints in a single formula.

- The clipping noise model was refined in the dissertation and verified using simulations. We discussed that the clipping noise spectrum is confined to the modulation bandwidth.

- A novel and simple non-linear equalizer was presented based on the LED physics, hence complexity-wise efficient. The presented equalizer had the least unknown parameters w.r.t. the state of the art competitors.
- An MMSE approach was developed to estimate the unknown parameters of the equalizer.
- More than 70% reduction in the LED power at a constant signal quality was achieved by employing the proposed equalizer. At a constant LED power, more than 50% improvement in the link throughput was shown experimentally.

6.2 Recommendations for Future Research

In this section, a few points are highlighted where that the limited time did not allow to address them thoroughly.

- The experimental LED channel decays faster than the theoretical first-order model at high frequencies. For a high data rate where the modulation bandwidth exceeds the LED 3 dB bandwidth significantly, the faster decay impacts the throughput. It was discussed that this is coming from the 2^{nd}-order effects in the communication link such as APD/TIA limited bandwidth or parasitics due to wiring and interconnection of the LED and the driver. For further improvement of the data rate, the source of these second-order effects should be identified and resolved by a proper design.
- Uniform power loading showed a penalty of about 1.5 dB in the Normalized Power Budget (NPB). That is, 1.5 dB of the available NPB is lost due to rounding down the constellation sizes to the nearest integer. The left-over power can still be distributed over the sub-carriers to enhance the throughput.
- There are other power-bit-loading algorithms targeting waterfilling. The work in [143] provides the optimal solution with less complexity compared to Hughes-Hartogs algorithm. In [143], a search algorithm has been developed to find the operating point of each sub-carrier on the rate-vs-allocated-power graph that results in the same slope for all sub-carriers. There, the results of this work in chapter 3 can be used to provide with the correct operation point for each sub-carrier and to find the number of sub-carriers to be used in order to speed up the algorithm.
- The DC to rms ratio of PAM scheme, in practice, and due to pulse shaping is higher than the theoretical derivation given in chapter 4. This results in a penalty in the PAM throughput over the LED channel. A proper theoretical

model is needed to calculate the ratio to be able to predict the impact on the throughput.

- A pre-emphasizer was used in front of the LED to make the LED communication channel flat (for PAM). Simulations showed that DC to rms ratio of the signal can change when passing through the pre-emphasizer. This might further jeopardize the benefit of the PAM over the OFDM.
- In section 2.3.3, it was shown that the non-linearities in the LED cause a sharp/slow rise/fall time. That is, the eye diagram is wider when the PAM level is changing to a higher current levels. This information can be used in the signal design at the transmitter to use a symbol-specific pulse width. For example in an OOK modulation, the pulse width of the symbol 0 can be made wider than that for symbol 1. Using this technique, the ISI impact on the eye diagram can be reduced and a wider eye is expected.

Bibliography

[1] Inside Innovation: Philips breaks 200 lumens per watt barrier. Available: https://www.signify.com/en-sg/our-company/news/press-release-archive/2013/inside-innovation-philips-breaks-200-lumens-per-watt-barrier.

[2] B. Bowers, Lengthening the Day: a History of Lighting Technology, Oxford University Press, UK, 1998.

[3] D. DeLaura, A brief history of lighting, Opt. Photonics News (September 2008) 23.

[4] R. Fouquet, P.J.G. Pearson, Seven centuries of energy services: the price and use of light in the United Kingdom (1300–2000), Energy J. 27 (2006) 139.

[5] F. R. Gfeller and U. Bapst, "Wireless in-house data communication via diffuse infrared radiation," in Proceedings of the IEEE, vol. 67, no. 11, pp. 1474-1486, Nov. 1979, doi: 10.1109/PROC.1979.11508.

[6] Z. Ghassemlooy, W. Popoola and S. Rajbhandari, Optical Wireless Communications, CRC Press Boca Raton, FL, 2012.

[7] A. M. Seybold, Using Wireless Communications in business, John Wiley Sons Inc., 1994.

[8] G. Pang, Ka-Lim Ho, T. Kwan and E. Yang, "Visible light communication for audio systems," in IEEE Transactions on Consumer Electronics, vol. 45, no. 4, pp. 1112-1118, Nov. 1999, doi: 10.1109/30.809190.

[9] S. Mardanikorani, A. Khalid, F. M. J. Willems and J. P. Linnartz, "Effect of Blue Filter on the SNR and Data Rate for Indoor Visible Light Communication System," 2017 European Conference on Optical Communication (ECOC), Gothenburg, 2017, pp. 1-3.

[10] Joseph M. Kahn, John R. Barry, "Wireless Infrared Communications", Proceedings of the IEEE, Vol. 85, No. 2, pp. 265-298, 1997

[11] T. A. Khan, M. Tahir and A. Usman, "Visible light communication using wavelength division multiplexing for smart spaces," 2012 IEEE Consumer Communications and Networking Conference (CCNC), Las Vegas, NV, 2012, pp. 230-234, doi: 10.1109/CCNC.2012.6181092.

[12] N. Saha, M. S. Ifthekhar, N. T. Le and Y. M. Jang, "Survey on optical camera communications: challenges and opportunities," in IET Optoelectronics, vol. 9, no. 5, pp. 172-183, 10 2015, doi: 10.1049/iet-opt.2014.0151.

[13] Visible Light Communication (VLC) - A Potential Solution to the Global Wireless Spectrum Shortage, GBI Research, Tech. Rep., 2011. [Online]. Available: http://www.gbiresearch.com/

[14] J. B. Carruthers, "Wireless infrared communications," in Encyclopedia of Telecommunications, 1st ed. Hoboken, NJ, USA: Wiley, 2003.

[15] M. Kavehrad, "Sustainable energy-efficient wireless applications using light," IEEE Commun. Mag., vol. 48, no. 12, pp. 66–73, Dec. 2010.

[16] H. Haas, L. Yin, Y. Wang, and C. Chen, "What is LiFi?," J. Lightw. Technol., vol. 34, no. 6, pp. 1533–1544, Mar. 2016.

[17] T. Komine and M. Nakagawa, "Fundamental analysis for visible light communication system using LED lights," IEEE Trans. Consum. Electron., vol. 50, no. 1, pp. 100–107, Feb. 2004.

[18] L. Hanzo, H. Haas, S. Imre, D. O'Brien, M. Rupp, and L. Gyongyosi, "Wireless myths, realities, and futures: From 3G/4G to optical and quantum wireless," Proc. IEEE, vol. 100, pp. 1853–1888, May 2012.

[19] L. Grobe et al., "High-speed visible light communication systems," IEEE Communications Magazine, vol. 51, no. 12, pp. 60–66, 2013.

[20] J. Eberspacher, HJ. Vogel, C. Bettstetter, C. C Hartmann, "GSM Architecture, Protocols and Services" Wiley, West Sussex, UK, 2009.

[21] A. Goldsmith, Wireless Communications, Cambridge University Press, Cambridge, UK, 2005.

[22] H. Holm, A. Toskala, WCDMA for UMTS: HSPA Evolution and LTE, Wiley, West Sussex, UK, 2007.

[23] J. Korhonen, Introduction to 4G Mobile Communications, Artech House, London, UK, 2014.

[24] A. Zaidi, F. Athley, J. Medbo U. Gustavsson, G. Durisi and X. Chen, 5G Physical Layer: Principles, Models and Technology Components, 1^{st} Edition, Academic Press, 2018.

[25] M. Lotfy Rabeh, M. I. Gabr and T. Hosny, "Data Transmission via Visible Light Communication (VLC) Technique" in International Journal of Innovative Research in Science, Engineering and Technology, 2016, 16473-16481. 10.15680/IJIRSET.2016.0509133.

[26] H. Le Minh et al., "100-Mb/s NRZ Visible Light Communications Using a Postequalized White LED," in IEEE Photonics Technology Letters, vol. 21, no. 15, pp. 1063-1065, Aug.1, 2009, doi: 10.1109/LPT.2009.2022413.

[27] S. Mardanikorani, Anton Alexeev, and Jean-Paul Linnartz, "Modeling and compensating dynamic nonlinearities in LED photon-emission rates to enhance OWC," *Proc. SPIE 10940, Light-Emitting Devices, Materials, and Applications*, 109400U (1 March 2019).

[28] J. Grubor, S. C. J. Lee, K. Langer, T. Koonen and J. W. Walewski, "Wireless High-Speed Data Transmission with Phosphorescent White-Light LEDs," 33rd European Conference and Exhibition of Optical Communication - Post-Deadline Papers (published 2008), Berlin, Germany, 2007, pp. 1-2.

[29] H. Le Minh et al., "High-Speed Visible Light Communications Using Multiple-Resonant Equalization," in IEEE Photonics Technology Letters, vol. 20, no. 14, pp. 1243-1245, July15, 2008, doi: 10.1109/LPT.2008.926030.

[30] Hamamatsu, LED datasheet, Compact SMD type high output LED, L12171-0087G Infrared LED, Aug. 2019.

[31] S. B. Park, D. K. Jung, H. S. Shin, D. J. Shin, Y.-J. Hyun, K. Lee, and Y. J. Oh, "Information Broadcasting System based on Visible Light Signboard". Proc. Wireless and Optical Communications 2007, Montreal, Canada, 5/30/2007 - 6/1/2007 2007.

[32] S. Watson et al., "High speed visible light communication using blue GaN laser diodes", in Advanced Free-Space Optical Communication Techniques and Applications II, vol. 9991, pp. 60-66, 2016.

[33] R. Windisch et al., "Large-signal-modulation of high-efficiency light emitting diodes for optical communication," IEEE J. Quantum Electron., vol. 36, no. 12, pp. 1445–1453, Dec. 2000.

[34] Z. Ghassemlooy, S. Arnon, M. Uysal, Z. Xu and J. Cheng, "Emerging Optical Wireless Communications-Advances and Challenges," in IEEE Journal on Selected Areas in Communications, vol. 33, no. 9, pp. 1738-1749, Sept. 2015, doi: 10.1109/JSAC.2015.2458511.

[35] X. Huang, J. Shi, J. Li, Y. Wang, and N. Chi, "A Gb/s VLC transmission using hardware pre-equalization circuit," IEEE Photon. Technol. Lett., vol. 27, no. 18, pp. 1915–1918, Sep. 15, 2015.

[36] P. A. Haigh, Z. Ghassemlooy, S. Rajbhandari, I. Papakonstantinou and W. Popoola, "Visible Light Communications: 170 Mb/s Using an Artificial Neural Network Equalizer in a Low Bandwidth White Light Configuration," in Journal of Lightwave Technology, vol. 32, no. 9, pp. 1807-1813, May1, 2014, doi: 10.1109/JLT.2014.2314635.

[37] Y. S. Cho, J. Kim, W. Y. Yang, C. G. Kang, "Introduction to OFDM," in MIMO-OFDM Wireless Communications with MATLAB® , IEEE, 2010, pp.111-151, doi: 10.1002/9780470825631.ch4.

[38] A. M. Khalid et al., "1-Gb/s Transmission over a Phosphorescent White LED by Using Rate-Adaptive Discrete Multitone Modulation," IEEE Photon. J., vol. 4, no. 5, Oct. 2012, pp. 1465–73.

[39] G. Cossu, A. M. Khalid, P. Choudhury, R. Corsini, and E. Ciaramella, "3.4 Gbit/s visible optical wireless transmission based on RGB LED," Opt. Express 20(26), B501–B506 (2012)..

[40] X. Deng et al., "Mitigating LED Nonlinearity to Enhance Visible Light Communications," in IEEE Transactions on Communications, vol. 66, no. 11, pp. 5593-5607, Nov. 2018.

[41] X. Deng, S. Mardanikorani, K. Arulandu, and Jean-Paul M. G. Linnartz, "Novel Post-distortion to Mitigate LED Nonlinearity in High-speed Visible Light Communications", in Dec 2018 IEEE Globecom Workshops (GC Wkshps).

[42] K. Ying, Z. Yu, R. J. Baxley, H. Qian, G. Chang and G. T. Zhou, "Nonlinear distortion mitigation in visible light communications," in IEEE Wireless Communications, vol. 22, no. 2, pp. 36-45, April 2015.

[43] G. Stepniak, J. Siuzdak, and P. Zwierko, "Compensation of a vlc phosphorescent white led nonlinearity by means of volterra dfe," IEEE Photonics Technology Letters, vol. 25, no. 16, pp. 1597–1600, 2013.

[44] T. Kamalakis, J. W. Walewski, and G. Mileounis, “Empirical volterra-series modeling of commercial light-emitting diodes,” Journal of Lightwave Technology, vol. 29, no. 14, pp. 2146–2155, 2011.

[45] D. Tsonev, S. Sinanovic, and H. Haas, ”Complete Modeling of Nonlinear Distortion in OFDM-Based Optical Wireless Communication,” J. Lightwave Tech., vol. 31, no. 18, Sept. 2013, pp. 3064–76.

[46] I. Neokosmidis, T. Kamalakis, J. W. Walewski, B. Inan and T. Sphicopoulos, ”Impact of Nonlinear LED Transfer Function on Discrete Multitone Modulation: Analytical Approach,” in Journal of Lightwave Technology, vol. 27, no. 22, pp. 4970-4978, Nov.15, 2009.

[47] H. Elgala, R. Mesleh and H. Haas, ”Predistortion in Optical Wireless Transmission Using OFDM,” 2009 Ninth International Conference on Hybrid Intelligent Systems, Shenyang, 2009, pp. 184-189.

[48] D. J. F. Barros, S. K. Wilson, and J. M. Kahn, ”Comparison of orthogonal frequency-division multiplexing and pulse-amplitude modulation in indoor optical wireless links,” IEEE Trans. Commun., vol. 60, no. 1, pp. 153–163, Jan. 2012.

[49] X. Ling, J. Wang, X. Liang, Z. Ding and C. Zhao, ”Offset and Power Optimization for DCO-OFDM in Visible Light Communication Systems,” in IEEE Transactions on Signal Processing, vol. 64, no. 2, pp. 349-363, Jan.15, 2016.

[50] K. Arulandu, J.-P. MG Linnartz, and X. Deng, “Enhanced visible light communication modulators with dual feedback control,”IEEE Journal of Emerging and Selected Topic in Power Electronics, Early Access, 2019.

[51] S. Dimitrov and H. Haas, ”Information rate of OFDM-based optical wireless communication systems with nonlinear distortion,” J. Lightw. Technol., vol. 31, no. 6, pp. 918–929, Mar. 2013.

[52] J. Piprek, ”Efficiency droop in nitride-based light-emitting diodes,” Phys. Status Solidi A, vol. 207, no. 10, pp. 2217–2225, Oct. 2010.

[53] Q. Dai et al., ”On the symmetry of efficiency-versus-carrier concentration curves in GaInN/GaN light-emitting diodes and relation to droop-causing mechanisms,” Appl. Phys. Lett., vol. 98, no. 3, p. 033506, 2011.

[54] J. Lian, M. Noshad and M. Brandt-Pearce, ”Comparison of Optical OFDM and M-PAM for LED-Based Communication Systems,” in IEEE Communications Letters, vol. 23, no. 3, pp. 430-433, March 2019.

[55] J. Armstrong, "OFDM for Optical Communications," IEEE/OSA Journal on Lightwave Technology (IEEE/OSA JLT), vol. 27, no. 3, pp. 189–204, Feb. 2009.

[56] J. Lee, "Discrete multitone modulation for short-range optical communications," Eindhoven: Technische Universiteit Eindhoven, 2009.

[57] X. Deng, S. Mardanikorani, G. Zhou, and J.P. Linnartz, "DC-bias for Optical OFDM in Visible Light Communications," IEEE Access, 7, 98319-98330.

[58] C. Chen, D. A. Basnayaka and H. Haas, "Downlink Performance of Optical Attocell Networks," in Journal of Lightwave Technology, vol. 34, no. 1, pp. 137-156, Jan.1, 1 2016.

[59] Jean-Paul M.G. Linnartz and Xiong Deng, "Continuous phase Flip-OFDM in optical wireless communications," Signal Processing, Volume 182, 2021.

[60] D. Barros, and J. M. Kahn, "Comparison of orthogonal frequency-division multiplexing and on-off keying in amplified direct-detection single-mode fiber systems," Journal of lightwave technology 28.12 (2010): 1811-1820.

[61] S. Haykin, Communication Systems, 3rd edition, New York, Wiley, 1994.

[62] R. G. Gallager, Information Theory and Reliable Communication. New York: Wiley, 1968.

[63] D. Hughes-Hartogs, "Ensemble modem structure for imperfect transmission media," U.S. Patent 4, July 1987.

[64] D. Hughes-Hartogs, The capacity of a degraded spectral Gaussian broadcast channel, Ph.D. thesis, Stanford University, July 1995.

[65] https://www.itu.int/md/T17-SG15-181008-TD-PLEN-0291

[66] http://www.ieee802.org/11/Reports/tgbb-update.htm

[67] H. Zhao, G. Liu, J. Zhang, R. A. Arif, and N. Tansu, "Analysis of internal quantum efficiency and current injection efficiency in III-nitride light-emitting diodes," J. Display Technol., vol. 9, no. 4, pp. 212–225, Apr. 2013.

[68] G. B. Lin et al., "Method for determining the radiative efficiency of GaInN quantum wells based on the width of efficiency-versus-carrier concentration curve," Appl. Phys. Lett., vol. 101, no. 24, p. 241104, 2012.

[69] R. N. Hall, "Recombination processes in semiconductors," Proc. IEE-B, Electron. Commun. Eng., vol. 106, no. 17S, pp. 923–931, 1959.

[70] K. Ikeda, S. Horiuchi, T. Tanaka, and W. Susaki, "Design parameters of frequency response of GaAs—(Ga,Al)As double heterostructure LED's for optical communications," IEEE Trans. Electron Devices, vol. ED-24, no. 7, pp. 1001–1005, Jul. 1977.

[71] A. Alexeev, "Characterization of light emitting diodes with transient measurements and simulations", Ph.D. dissertation, Department of Electrical Engineering, Technical university of Eindhoven, May 2020.

[72] S. Mardanikorani, X. Deng and J. M. G. Linnartz, "Sub-Carrier Loading Strategies for DCO-OFDM LED Communication," in IEEE Transactions on Communications, vol. 68, no. 2, pp. 1101-1117, Feb. 2020, doi: 10.1109/TCOMM.2019.2953612.

[73] S. Mardanikorani, X. Deng and J. -P. M. G. Linnartz, "Optimization and Comparison of M-PAM and Optical OFDM Modulation for Optical Wireless Communication," in IEEE Open Journal of the Communications Society, vol. 1, pp. 1721-1737, 2020, doi: 10.1109/OJCOMS.2020.3034204.

[74] S. Mardanikorani, X. Deng, J. -P. Linnartz and A. Khalid, "Compensating Dynamic Nonlinearities in LED Photon Emission to Enhance Optical Wireless Communication," in IEEE Transactions on Vehicular Technology, doi: 10.1109/TVT.2021.3050862.

[75] J. P. Linnartz, X. Deng, A. Alexeev, and S. Mardani, "Wireless Communication over an LED Channel," *IEEE Communications Magazine*, December, 2020.

[76] H. Qian et al., "Adaptive post-distortion for nonlinear leds in visible light communications,"IEEE Photonics Journal, vol. 6, no. 4, pp. 1–8, 2014.

[77] A. Farid and S. Hranilovic, "Capacity of optical intensity channels with peak and average power constraints," in Proc. IEEE Int. Conf. Commun., Dresden, Germany, Jun. 14–18, 2009, pp. 1–5.

[78] J. Cho, E. F. Schubert, and J. K. Kim, "Efficiency droop in light-emitting diodes: Challenges and countermeasures,"Laser Photonics Reviews, vol. 7, no. 3, pp. 408–421,2013.

[79] X. Deng, K. Arulandu, Y. Wu, S. Mardanikorani, G. Zhou and J. M. G. Linnartz, "Modeling and Analysis of Transmitter Performance in Visible Light Communications," in IEEE Transactions on Vehicular Technology, vol. 68, no. 3, pp. 2316-2331, March 2019, doi: 10.1109/TVT.2019.2891639.

[80] K. Arulandu, X. Deng and J.-P. M. G. Linnartz, "Efficient Amplitude Modulator and Ripple Canceller for Visible Light Communication", in Dec 2018 IEEE Globecom Workshops (GC Wkshps).

[81] H. Yang, J.W.M. Bergmans, T.C.W. Schenk, J.P.M.G. Linnartz, R. Rietman, "An analytical model for the illuminance distribution of a power LED", Optics Express, Vol. 16 (2008), No. 26, pp. 21641-21646.

[82] Y. Qiu, H. Chen, and W. Meng, "Channel modeling for visible light communications- a survey," Wirel. Commun. Mob. Comput 16(14), 2016–2034 (2016).

[83] V. Jungnickel, V. Pohl, S. Nonnig and C. von Helmolt, "A physical model of the wireless infrared communication channel," in IEEE Journal on Selected Areas in Communications, vol. 20, no. 3, pp. 631-640, April 2002.

[84] M. Uysal, F. Miramirkhani, O. Narmanlioglu, T. Baykas and E. Panayirci, "IEEE 802.15.7r1 Reference Channel Models for Visible Light Communications," in IEEE Communications Magazine, vol. 55, no. 1, pp. 212-217, January 2017.

[85] M. Poenot, A. Tsiatmas, J.P.M.G. Linnartz, "Wireless Infrared Propagation in Dense Cellular Sensor Networks" ICT Open 2013.

[86] A. Tsiatmas, F. M. Willems, J. P. M. Linnartz, S. Baggen and J. W. Bergmans, "Joint illumination and visible-Light Communication systems: Data rates and extra power consumption," 2015 IEEE International Conference on Communication Workshop (ICCW), London, 2015, pp. 1380-1386.

[87] Hamamatsu, "APD modules ," C12702 series datasheet, Sept. 2017.

[88] B. Razavi, Design of Integrated Circuits for Optical Communications, McGraw-Hill, 1st Edition, 2002.

[89] A. Alexeev, et al. "Optical Wireless Communication Model for LED Bandwidth Based on Electrical Small Signal Response Analysis". 16th International Symposium on the Science and Technology for Lighting, 2018.

[90] A. David et al., "Carrier dynamics and coulomb-enhanced capture in iii-nitride quantum hetero structures, "Applied Physics Letters, vol. 109, no. 3, p. 033504, 2016.

[91] A. Al Bastami, M. R. Belic, and N. Z. Petrovic, "Special solutions of the Riccati equation with applications to the Gross–Pitaevskii non- linear PDE," Electron. J. Differ. Equ., vol. 2010, no. 66, pp. 1–10, 2010.

[92] E. Fred Schubert, "Light-Emitting Diodes", CAMBRIDGE UNIVERSITY PRESS, 2nd eddition, 2006.

[93] Justel T., Nikol H., and Ronda C. R. "New developments in the field of luminescent materials for lighting and displays", Angewandte Chemie (International Edition) 37, 3084 (1998).

[94] Olga V. Ivanova, Laura Marcu, Michael C. K. Khoo, "Estimation of optical fluorescent impulse response kernel in combined time and wavelength spaces", Proc. SPIE 4955, Optical Tomography and Spectroscopy of Tissue V, (29 July 2003); doi: 10.1117/12.478213.

[95] S. Hranilovic, "Wireless Optical Communication Systems", New York, NY, USA: Springer-Verlag, 2005

[96] E. A. Lee and D. G. Messerschmitt, "Digital Communication", Kluwer Academic Publishers, Boston, MA, 2nd edition, 1994.

[97] S. B. Alexander, "Optical Communication Receiver Design", Institution of Electrical Engineers, SPIE Optical Engineering Press, London, UK, 1997.

[98] S. Karp, E. L. O'Neill, and R. M. Gagliardi, "Communication theory for the free-space optical channel", Proceedings of the IEEE, 58(10):1611–1626, October 1970.

[99] S. Mardanikorani and J. P. Linnartz, "Capacity of the First-Order Low-Pass Channel with Power Constraint," Proceedings of the 2018 Symposium on Information Theory and Signal Processing in the Benelux, Enschede, pp. 149-153, May 2018.

[100] J. G. Proakis, Digital Communications, 4th Edition, McGraw-Hill, New York, 2001.

[101] Hoa Le Minh et al., "80 Mbit/s Visible Light Communications using pre-equalized white LED," 2008 34th European Conference on Optical Communication, Brussels, Belgium, 2008, pp. 1-2.

[102] J.-Y. Sung, C.-W. Chow, and C.-H. Yeh, "Is blue optical filter necessary in high speed phosphor-based white light LED visible light communications?" Optics express, vol. 22, no. 17, pp. 20 646–20 651, 2014.

[103] S. C. Tokgoz, N. Anous, S. Yarkan, A. Boyacı and K. A. Qaraqe, "Performance Evaluation of White LED-based OFDM-VLC Systems with Blue Filters: Experimental Study," 2019 16th International Multi-Conference on Systems, Signals Devices (SSD), Istanbul, Turkey, 2019, pp. 686-690, doi: 10.1109/SSD.2019.8893211.

[104] H. Elgala, R. Mesleh and H. Haas, "Indoor optical wireless communication: potential and state-of-the-art," in IEEE Communications Magazine, vol. 49, no. 9, pp. 56-62, September 2011.

[105] A. Jovicic, J. Li and T. Richardson, "Visible light communication: opportunities, challenges and the path to market," in IEEE Communications Magazine, vol. 51, no. 12, pp. 26-32, December 2013.

[106] M. Schetzen, "Nonlinear system modeling based on the Wiener theory," Proc. IEEE, vol. 69, no. 12, pp. 1557–1573, Dec. 1981.

[107] M. S. Islim and H. Haas, "Modulation techniques for LiFi," ZTE Commun, vol. 14, no. 2, pp. 29–40, 2016.

[108] Y. Wang, T. Li, H. Xingxing, S. Jianyang and C. Nan, "8-Gb/s RGBY LED-based WDM VLC system employing high-order CAP modulation and hybrid post equalizer," IEEE Photonics Journal 7, no. 6 (2015): 1-7.

[109] W. Zhao, G. Qinghua, T. Jun, X. Jiangtao, Y. Yanguang, N. Pingjuan, and S. Xiaohong, "Orthogonal polynomial-based nonlinearity modeling and mitigation for LED communications." IEEE Photonics Journal 8, no. 4 (2016): 1-12.

[110] G. Zhang, Z. Junwei, H. Xuezhi, and H. Sailing, "Low-complexity frequency domain nonlinear compensation for OFDM based high-speed visible light communication systems with light emitting diodes." Optics express 25, no. 4 (2017): 3780-3794.

[111] Joel G. Smith, "The information capacity of amplitude- and variance-constrained scalar gaussian channels", Information and Control, Volume 18, Issue 3, April 1971, Pages 203-219

[112] X. Li, R. Mardling, and J. Armstrong, "Channel throughput of IM/DD optical communication systems and of ACO-OFDM," in Proc. IEEE 2007 Int. Conf. Commun. (ICC), Glasgow, U.K., Jun. 2007, pp. 2128–2133.

[113] J. Zhou and W. Zhang, "A Comparative Study of Unipolar OFDM Schemes in Gaussian Optical Intensity Channel," IEEE Trans. Commun., vol. 66, no. 4, pp. 1549-1564, Apr. 2018.

[114] A. Lapidoth, S. M. Moser, and M. Wigger, "On the capacity of free-space optical intensity channels," IEEE Trans. Inf. Theory, vol. 55, no. 10, pp. 4449-4461, Oct. 2009.

[115] H. Elgala, R. Mesleh, H. Haas and B. Pricope, "OFDM Visible Light Wireless Communication Based on White LEDs," *2007 IEEE 65th Vehicular Technology Conference*, Dublin, 2007, pp. 2185-2189.

[116] J. B. Carruthers and J. M. Kahn, "Multiple-subcarrier modulation for nondirected wireless infrared communication," in *IEEE Journal on Selected Areas in Communications*, vol. 14, no. 3, pp. 538-546, Apr 1996.

[117] S. Mardanikorani, X. Deng and J.P. Linnartz, "Efficiency of Power Loading Strategies for Visible Light Communication," 2018 *IEEE Globecom Workshops (GC Wkshps)*, Abu Dhabi, United Arab Emirates, 2018, pp. 1-6.

[118] J. Campello, "Practical bit loading for DMT," presented at the *IEEE Int. Conf. Commun., Vancouver*, Canada, 1999.

[119] H. E. Levin, "A complete and optimal data allocation method for practical discrete multitone systems," presented at the *IEEE Global Telecommun. Conf.*, San Antonio, TX, USA, 2001.

[120] P. S. Chow, J. M. Cioffi and J. A. C. Bingham, "A practical discrete multitone transceiver loading algorithm for data transmission over spectrally shaped channels," in *IEEE Transactions on Communications*, vol. 43, no. 2/3/4, pp. 773-775, Feb./March/April 1995.

[121] B. Cardiff, M. F. Flanagan, F. Smyth, L. P. Barry, and A. D. Fagan, "On bit and power loading for OFDM over SI-POF," *Journal of Lightwave Technology*, vol. 29, no. 10, pp. 1547–1554, May 15, 2011.

[122] D. Bykhovsky and S. Arnon, "An Experimental Comparison of Different Bit-and-Power-Allocation Algorithms for DCO-OFDM," in *Journal of Lightwave Technology*, vol. 32, no. 8, pp. 1559-1564, April15, 2014.

[123] S. D. Dissanayake and J. Armstrong, "Comparison of ACO-OFDM, DCO-OFDM and ADO-OFDM in IM/DD systems," J. Lightw. Technol., vol. 31, no. 7, pp. 1063-1072, Apr. 1, 2013.

[124] B. Ranjha and M. Kavehrad, "Hybrid asymmetrically clipped OFDM-based IM/DD optical wireless system," in IEEE/OSA Journal of Optical Communications and Networking, vol. 6, no. 4, pp. 387-396, April 2014.

[125] Q. Dai, et al. "Carrier recombination mechanisms and efficiency droop in GaInN/GaN light-emitting diodes." *Applied Physics Letters*, 97.13, 133507, 2010.

[126] S. Dimitrov, S. Sinanovic and H. Haas, "A comparison of OFDM-based modulation schemes for OWC with clipping distortion," 2011 IEEE GLOBECOM Workshops (GC Wkshps), Houston, TX, 2011, pp. 787-791.

[127] "Energy star program requirements for lamps (light bulbs)," Eligibility Criteria Version 2.1, Tech. Rep., 2017.

[128] J. Armstrong and A. J. Lowery, "Power efficient optical OFDM," in Electronics Letters, vol. 42, no. 6, pp. 370-372, 16 March 2006.

[129] J. M. Cioffi, G. P. Dudevoir, M. V. Eyuboglu and G. D. Forney, "MMSE decision-feedback equalizers and coding. II. Coding results," in *IEEE Transactions on Communications*, vol. 43, no. 10, pp. 2595-2604, Oct 1995.

[130] G. D. Forney and G. Ungerboeck, "Modulation and coding for linear Gaussian channels," in *IEEE Transactions on Information Theory*, vol. 44, no. 6, pp. 2384-2415, Oct 1998.

[131] J. Kiefer, "Sequential minimax search for a maximum", *Proceedings of the American Mathematical Society*, vol. 4, no. 3, pp. 502-506, Jun., 1953.

[132] "Advance electrical design led model," application brief AB20-3A, Lumileds, Tech. Rep., 2002.

[133] S. Dimitrov, S. Sinanovic, and H. Haas, "Signal shaping and modulation for optical wireless communication," J. Lightw. Technol., vol. 30, no. 9, pp. 1319–1328, May 2012.

[134] Photobiological Safety of Lamps and Lamp Systems, BSI British Standards Std., BS EN 62471:2008, Sep. 2008.

[135] A. Nuwanpriya, et al. "PAM-SCFDE for optical wireless communications," Journal of Lightwave Technology 33.14 (2015): 2938-2949.

[136] J. A. C. Bingham, "Multicarrier modulation for data transmission: An idea whose time has come," IEEE Commun. Mag., pp. 6–14, May 1990.

[137] L. Goldfeld, V. Lyandres, and D. Wulich, "Minimum BER power loading for OFDM in fading channel," IEEE Trans. Commun., vol. 50, pp. 1729-1733, Nov. 2002

[138] S. Yoo et al., "A 10 Gb/s 4-PAM transceiver with adaptive pre-emphasis," ISIC, Singapore, 2011, pp. 258-261.

[139] N. Fernando, Y. Hong and E. Viterbo, "Flip-OFDM for optical wireless communications," 2011 IEEE Information Theory Workshop, Paraty, 2011, pp. 5-9.

[140] N. Fernando, Y. Hong, and E. Viterbo, "Flip-ofdm for unipolar communication systems," IEEE Transactions on Communications, vol. 60, no. 12, pp. 3726–3733, 2012.

[141] Z. Yu, R. J. Baxley and G. T. Zhou, "Achievable data rate analysis of clipped FLIP-OFDM in optical wireless communication," 2012 IEEE Globecom Workshops, Anaheim, CA, 2012, pp. 1203-1207.

[142] A. Tsiatmas, C. P. M. J. Baggen, F. M. J. Willems, J. M. G. Linnartz and J. W. M. Bergmans, "An illumination perspective on visible light communications," in IEEE Communications Magazine, vol. 52, no. 7, pp. 64-71, July 2014.

[143] B. S. Krongold, K. Ramchandran and D. L. Jones, "Computationally efficient optimal power allocation algorithms for multicarrier communication systems," in IEEE Transactions on Communications, vol. 48, no. 1, pp. 23-27, Jan. 2000.

Appendix A

Equalizer Derivations

A.0.1 Zero Forcing (ZF) equalizer

The ZF equalizer (post-distorter) consists of two sections, shown in Fig. 5.3(a) with seven parameters b_i ($i = 0, 1, ..., 6$). The received signal to the post distorter is denoted by s_r and the output of the post-distorter is i_r. The first part resembles an inversion of equation (5.11) to have

$$n'_c(n) = k_n n_c(n). \tag{A.1}$$

where k_n is a(n arbitrary) constant. We can derive that

$$b_4 = \frac{k_n^2}{a_5}, \tag{A.2}$$

$$b_5 = (\frac{k_n a_4}{2a_5})^2, \tag{A.3}$$

$$b_6 = -\frac{k_n a_4}{2a_5}. \tag{A.4}$$

The second part is used to inverse equation (5.10) and to have $i_r(n) = k_i i_{in}(n-1)$, where k_i is a(n arbitrary) constant. The parameters b_is ($i = 0, 1, 2, 3$) can be derived as

$$b_0 = \frac{k_i}{k_n a_0}, \tag{A.5}$$

$$b_1 = -\frac{k_i a_1}{k_n a_0}, \tag{A.6}$$

$$b_2 = -\frac{k_i a_2}{k_n^2 a_0}, \tag{A.7}$$

$$b_3 = -\frac{k_i a_3}{k_n^3 a_0}. \tag{A.8}$$

To implement the inverse of LED, seven parameters b_i $(i = 0, 1, ..., 6)$ seem to be required. However, to eliminate the LED-induced distortion, the parameters b_0 and b_4 can be freely chosen (e.g. $b_0 = b_4 = 1$ that results in $k_n = \sqrt{a_5}$ and $k_i = k_n a_0$) and the other parameters must be chosen according to (A.2) to (A.8). It can be shown that this approach will eliminate the distortion and will result in an $i_r(n)$ that is different from $i_{in}(n)$ only by a constant factor $k_i = a_0\sqrt{a_5}$. As a conclusion, only 5 independent parameters are required to implement the pre/post-distorter of Fig. 5.3(a). In [40], for this purpose, six parameters a_0-a_5 were estimated, firstly, through a parameter estimation phase.

A.0.2 The simplified equalizer structure

The equalizer of Fig. 5.3(a) contains a compute-intensive square-root operation. In a low-power implementation, it is attractive to avoid this. Therefore, we try to remove the distortion by using the structure of 5.3(b) that only uses a single squaring operation, eventhough this does not fully invert higher-order terms. Next, we address the penalty for reducing the complexity. As illustrated in Fig. 5.3(a), the inverse of the channel can be written as the concatenation of

$$\sqrt{b_4 s_r[n] + b_5} + b_6 = n_c'[n], \tag{A.9}$$

and

$$\begin{aligned} i_r[n] = b_0 n_c'[n] + b_1 n_c'[n-1] + b_2 (n_c'[n-1])^2 + \\ b_3 (n_c'[n-1])^3. \end{aligned} \tag{A.10}$$

Inserting (A.9) into (A.10) results in the equalized signal

$$\begin{aligned} i_r[n] = & b_0 \left(\sqrt{b_4 s_r[n] + b_5} + b_6 \right) + \\ & b_1 \left(\sqrt{b_4 s_r[n-1] + b_5} + b_6 \right) + \\ & b_2 \left(\sqrt{b_4 s_r[n-1] + b_5} + b_6 \right)^2 + \\ & b_3 \left(\sqrt{b_4 s_r[n-1] + b_5} + b_6 \right)^3 \end{aligned} \tag{A.11}$$

Expanding the square and the cubic terms, the optical-to-current conversion needs to be of the form

$$\begin{aligned} i_r[n] = & \left(b_0 b_6 + b_1 b_6 + b_2 b_5 + b_2 b_6^2 + b_3 b_6^3 + 3 b_3 b_5 b_6 \right) + \\ & b_0 \sqrt{b_4 s_r[n] + b_5} + (b_2 b_4 + 3 b_3 b_4 b_6) s_r[n-1] + \\ & \left(b_1 + 2 b_2 b_6 + 3 b_3 b_6^2 \right) \sqrt{b_4 s_r[n-1] + b_5} + \\ & b_3 \left(\sqrt{b_4 s_r[n-1] + b_5} \right)^3. \end{aligned} \tag{A.12}$$

Here, we preferably replace the square root operations by a simpler-to-compute polynomial.

Series expansion around DC

For a series expansion,

$$\sqrt{b_4 s_r + b_5} \approx \sqrt{b_5} + \frac{b_4}{2\sqrt{b_5}} s_r - \frac{b_4^2}{4 b_5^{1.5}} s_r^2 + .. \tag{A.13}$$

and

$$\sqrt{b_4 s_r + b_5}^3 \approx {b_5}^{1.5} + \frac{3 b_4 \sqrt{b_5}}{2} s_r + \frac{3 b_4^2}{4\sqrt{b_5}} s_r^2 + .. \tag{A.14}$$

Employing the second-order series approximations (A.13) and (A.14) into (A.12) derives (5.13), where we find the equalizer coefficients

$$c_1 = \frac{b_0 b_4}{2\sqrt{b_5}}, \tag{A.15}$$

$$c_2 = -\frac{b_0 b_4^2}{4 b_5^{1.5}}, \tag{A.16}$$

$$c_3 = b_2 b_4 + 3 b_3 b_4 b_6 + \frac{b_4(b1 + 2 b_2 b_6 + 3 b_3 b_6^2)}{2\sqrt{b_5}} + \frac{3 b_3 b_4 \sqrt{b_5}}{2}, \tag{A.17}$$

and

$$c_4 = \frac{-b_4^2(b1 + 2 b_2 b_6 + 3 b_3 b_6^2)}{4 b_5^{1.5}} + \frac{3 b_3 b_4^2}{4\sqrt{b_5}}. \tag{A.18}$$

Replacing b_{0-6} from (A.2) to (A.8), the equalizer parameters c_{1-4} can be readily derived as a function of LED parameters a_{0-4}. Furthermore, it can be shown that the dc terms cancel out. A practical receiver may have to estimate coefficients from incoming signals, as discussed in the paper.

Best fit approximation

In the previous subsection, we justified the simplification that led to the proposed equalizer. In this subsection, we discuss a more generic approach than the series expansion, best fit approximation. We take $f(x) = \sqrt{x}$ and $g(x) = (\sqrt{x})^3 = x\sqrt{x}$ and find the best second order polynomial fits $y_f(x) = v_0 + v_1 x + v_2 x^2$ and $y_g(x) = u_0 + u_1 x + u_2 x^2$ to minimize the error signals $\mathbf{E}\{e_f^2\} = \mathbf{E}\{(f(x) - y_f(x))^2\}$ and $\mathbf{E}\{e_g^2\} = \mathbf{E}\{(g(x) - y_g(x))^2\}$. The linear terms of the polynomials $y_f(x)$ and $y_g(x)$ are proportional to the received signal $s_r(n)$, but which is accompanied by noise. If the error due to the approximation falls below the noise power, we can neglect the error.

Table A.1: Estimation of $f(x) = \sqrt{x}$ with a second order polynomial and the residual error.

x range		$\mathbf{E}\{(v_1 x)^2\}$	$\mathbf{E}\{e_f^2\}$	$10\log_{10}\left(\frac{\mathbf{E}\{e_f^2\}}{\mathbf{E}\{(v_1 x)^2\}}\right)$
min	max			
0	10	6.27	4.1×10^{-3}	−31.9 dB
0	5	3.14	2.1×10^{-3}	−31.8 dB
0.1	5	2.86	1×10^{-3}	−34.5 dB
0.1	0.4	0.18	1.6×10^{-6}	−50.3 dB
0.01	0.4	0.226	7.3×10^{-5}	−34.9 dB

We tested this estimation for different ranges of the input parameter x with a uniform distribution over the range. The results are summarized in Table A.1 and Table A.2. Several observations can be made. Firstly, the accuracy of the estimation is higher when the input argument range has an offset from 0, i.e., the LED minimum output optical power and the input driving current stay above a minimum offset from zero. For high–speed communication, in [33], it has been suggested not to push the LED into its completely–off region, to avoid full depletion of LED junction from the carriers. Secondly, limiting the input range of the square–root argument improves the accuracy. Even in the extreme case of an input range between 0 and any arbitrarily high number, the error signal power, normalized to signal power does not exceed ≈-32 dB. In our experimental results as well as in simulations, we see that for the received SNR of (best case) 30 dB, LED–induced distortion is already limiting the performance. In conclusion, we expect that the error caused by the approximation of a square root by a second-order polynomial will not affect the equalizer performance considerably.

Inserting the expansions

$$\sqrt{b_4 s_r + b_5} \approx v_0 + v_1 s_r + v_2 s_r^2 \tag{A.19}$$

and

$$\sqrt{b_4 s_r + b_5}^3 \approx u_0 + u_1 s_r + u_2 s_r^2 \tag{A.20}$$

into (A.12) derives (5.13) where,

$$c_1 = b_0 v_1, \tag{A.21}$$

$$c_2 = b_0 v_2, \tag{A.22}$$

$$c_3 = b_2 b_4 + 3 b_3 b_4 b_6 + (b1 + 2 b_2 b_6 + 3 b_3 b_6^2) v_1 + b_3 u_1, \tag{A.23}$$

and

$$c_4 = (b1 + 2 b_2 b_6 + 3 b_3 b_6^2) v_2 + b_3 u_2. \tag{A.24}$$

Table A.2: Estimation of $g(x) = x\sqrt{x}$ with a second order polynomial and the residual error.

x range		$\mathbf{E}\{g(x)^2\}$	$\mathbf{E}\{e_g^2\}$	$10\log_{10}\left(\frac{\mathbf{E}\{e_g^2\}}{\mathbf{E}\{(u_1 x)^2\}}\right)$
min	max			
0	10	69.66	0.0227	-34.9 dB
0	5	8.71	0.0028	-34.9 dB
0.1	5	9.39	0.0021	-36.4 dB
0.1	0.4	0.009	8×10^{-8}	-50.6 dB
0.01	0.4	0.005	1×10^{-6}	-36.7 dB

For example, for the simulation setup in Section 5.5.D, the LED parameters given in Table 5.2 and neglecting AWGN noise (for simplicity), the ZF equalizer of Fig. 5.3(a) perfectly eliminates distortion, resulting in $\mathbf{E}\{|e(n)|^2\} = 0$. The definition of the residual distortion at the equalizer output, $\mathbf{E}\{|e(n)|^2\}$, is given in (5.38). For the equalizer of Fig. 5.3(b), from (A.15) to (A.18) and after normalization to c_1, $\{c_1, c_2, c_3, c_4\} = \{1, -2.505, -0.891, 3.015\}$, the Signal to (residual) Distortion Ratio (SDR) at the equalizer output, calculated as SDR $= \mathbf{E}\{(i_r(n))^2\}/\mathbf{E}\{|e(n)|^2\}$, is (almost) 40 dB.

Trying the best-fit approach, after normalization to c_1, we get $\{c_1, c_2, c_3, c_4\} = \{1, -1.218, -0.886, 1.474\}$ and the SDR is more than 60 dB. Finally, using the MMSE approach results in $\{c_1, c_2, c_3, c_4\} = \{1, -1.217, -0.886, 1.474\}$ and SDR of more than 70 dB. The results of the simulations strongly indicate that MMSE approach and the best-fit approximation give the same equalizer coefficients.

Appendix B

Uniform Power allocation: Derivations

The rate for the uniform power loading was derived in (3.43). Using the definition of $u(x)$ of

$$u(x) = -\frac{\gamma}{\Gamma\nu}2^{-x}, \tag{B.1}$$

the normalized rate $\Re_u = R_u/f_0$ is

$$\Re_u = \int_0^{\nu} \log_2\left(1 - u(x)\right)dx. \tag{B.2}$$

Now we wish to obtain the ν (ν_u) which maximizes the achievable rate for such a power allocation strategy. This is done by using Leibniz's rule as follows

$$\frac{d\Re_u}{d\nu} = \int_0^{\nu} \frac{d}{d\nu}\log_2\left(1 - u(x)\right)dx + \log_2(1 - u(v)) = 0. \tag{B.3}$$

The integral in (B.3) can be calculated as following

$$\int_0^{\nu} \frac{d}{d\nu}\log_2\left(1 - u(x)\right)dx = \frac{-1}{\ln 2}\int_0^{\nu} \frac{du(x)/d\nu}{(1 - u(x))}dx \tag{B.4}$$

$$= \frac{-1}{\nu \ln 2}\int_0^{\nu} \frac{\frac{\gamma}{\Gamma\nu}2^{-x}}{1 + \frac{\gamma}{\Gamma\nu}2^{-x}}dx = \frac{1}{\nu \ln 2}\log_2\left(1 + \frac{\gamma}{\Gamma\nu}2^{-x}\right)\Big|_0^{\nu}$$

$$= \frac{1}{\nu \ln 2}\left(\log_2\left(1 + \frac{\gamma}{\Gamma\nu}2^{-\nu}\right) - \log_2\left(1 + \frac{\gamma}{\Gamma\nu}\right)\right). \tag{B.5}$$

Replacing (B.4) in (B.3) for $\nu = \nu_u$ (the optimum ν) results in (3.44).

Now, we drive the achievable rate equation given in (3.46). Using $\log_2(.) =$

$\ln(.)/\ln 2$ and employing u-substitution method, Eq. (B.2) can be written as

$$\Re_u = -\frac{1}{(\ln 2)^2}\int_{u_1}^{u_2}\frac{\ln(1-u)}{u}du, \tag{B.6}$$

where $u_1 = \frac{-\gamma}{\Gamma\nu_u}$ and $u_2 = \frac{-\gamma}{\Gamma\nu_u}2^{-\nu_u}$. The achievable rate can then be simplified to

$$\Re_u = \frac{1}{(\ln 2)^2}\left(-\int_0^{u_2}\frac{\ln(1-u)}{u}du - \left(-\int_0^{u_1}\frac{\ln(1-u)}{u}du\right)\right), \tag{B.7}$$

which results in the rate equation (3.46).

Acknowledgments

This milestone would not have come to its end if I did not have support from so many great people during this journey.

First of all, I would like to express my gratitude to my patient and supportive supervisor Jean-Paul M.G. Linnartz for providing me with the opportunity to do research in his group. It was the happiest moment in my professional carrier when I received the positive feedback with the PhD offer from him and I truly believe that it was the best decision to accept it. His knowledge, enthusiasm, and invaluable expertise were of great help to formulate the research questions and methodology. His insightful feedback always pushed me to sharpen the ideas to bring my work to a higher level. Beside the technical support, I have also learned a lot from him to develop my soft skills. Jean-Paul was also very supportive during my maternity leave and after the birth of my first son. I could not submit, finalize and publish my first journal paper if you did not help me. A big thank you for being such a wonderful supervisor.

I gratefully acknowledge my copromotor dr. Xiong Deng for all the insightful discussions we had. I am also thankful for the effort and the support you provided for the publication of my journal papers. Xiong was also a great colleague to work with, a truly hard-working person.

My sincere thanks go to Jan W. M. Bergmans, the chair of the Signal Processing Systems (SPS) group. His insightful questions truly challenged our non-linear equalizer idea and helped to improve the work substantially. He was also very kind and supportive during my maternity leave and afterward; thank you Jan.

I would like to thank the committee of this thesis for being part of my doctorate committee and for taking the time to read and comment the thesis; prof. Steve Hranilovic (McMaster University, Canada), prof. dr. Marion Matters-Kammerer (Eindhoven University of Technology), dr. Volker Jungnickel (TU Berlin, Institut für Telekommunikationssysteme) and dr.ir. C. W. (Joanne) Oh.

I would like to acknowledge the SPS secretary, Carla Schaafstra, for the administrative assistance, on-boarding at the beginning of my PhD work and planning my defense.

I would like to also thank my colleagues at Signify, Michel Germe, Kumar Arulandu, Fernand Courtois, David Derrien, Walter Jaudard, Amir Khalid and Conrad Dandelski for offering me a desk and for the insightful discussions and support I received during my time at Signify. A special thank to Amir Khalid for his kind support during the experimental verifications of my ideas.

Many thanks to my colleagues in our Intelligent Lighting group, Anton, Chara, Jochem and Mahmoud. I enjoyed having brain storming sessions with you and the discussions during our weekly meetings.

During my time in the Netherlands I had wonderful friends from Iran. Our occasional/weekly gathering is always cheering me up and thanks to them, I have never become homesick. Many thanks to Behnaz and Bagher, Faegheh and Mohammad-Reze, Mina and Vahid, Zahra and Alireze, Maryam and Hamed, Hajar and Meisam, Maliheh and Hamed, Elnaz and Saeid, Maryam and Milad, Mana and Naseh, Farideh and Mohsen, Shayesteh and Alireza and Mahta and Saeid. My special thanks go to Maryam for designing the cover page.

I would like to also mention my parents, Rahdar and Morvarid, for sacrificing many things in their own life to raise seven children. Leaving them was a difficult decision and I am grateful for their continuous support.

And, last but not least, I owe thanks to a very special person, my husband Ali. Your valuable support and the insightful discussions we had during my PhD helped me to improve my ideas. I greatly value your contribution and deeply appreciate your belief in me. Without your everyday support, it would not have been possible to accomplish this journey. I love you and I feel fortunate to have you and our lovely sons Nickan and Ayeen.

List of publications

- **S. Mardanikorani**, A. Khalid, F. M. J. Willems and J. P. Linnartz, "Effect of Blue Filter on the SNR and Data Rate for Indoor Visible Light Communication System," 2017 European Conference on Optical Communication (ECOC), Gothenburg, 2017, pp. 1-3.

- **S. Mardanikorani**, Anton Alexeev, and Jean-Paul Linnartz, "Modeling and compensating dynamic nonlinearities in LED photon-emission rates to enhance OWC," *Proc. SPIE 10940, Light-Emitting Devices, Materials, and Applications*, 109400U (1 March 2019).

- **S. Mardanikorani** and J. P. Linnartz, "Capacity of the First-Order Low-Pass Channel with Power Constraint," Proceedings of the 2018 Symposium on Information Theory and Signal Processing in the Benelux, Enschede, pp. 149-153, May 2018.

- **S. Mardanikorani**, X. Deng and J.P. Linnartz, "Efficiency of Power Loading Strategies for Visible Light Communication," 2018 *IEEE Globecom Workshops (GC Wkshps)*, Abu Dhabi, United Arab Emirates, 2018, pp. 1-6.

- **S. Mardanikorani**, X. Deng, J. -P. Linnartz and A. Khalid, "Compensating Dynamic Nonlinearities in LED Photon Emission to Enhance Optical Wireless Communication," in IEEE Transactions on Vehicular Technology.

- **S. Mardanikorani**, X. Deng and J. M. G. Linnartz, "Sub-Carrier Loading Strategies for DCO-OFDM LED Communication," in IEEE Transactions on Communications, vol. 68, no. 2, pp. 1101-1117, Feb. 2020..

- **S. Mardanikorani**, X. Deng and J. -P. M. G. Linnartz, "Optimization and Comparison of M-PAM and Optical OFDM Modulation for Optical Wireless Communication," in IEEE Open Journal of the Communications Society, vol. 1, pp. 1721-1737, 2020.

- X. Deng, **S. Mardanikorani**, G. Zhou, and J.P. Linnartz, "DC-bias for Optical OFDM in Visible Light Communications," IEEE Access, 7, 98319-98330.
- X. Deng, **S. Mardanikorani**, K.Arulandu, and Jean-Paul M. G. Linnartz, "Novel Post-distortion to Mitigate LED Nonlinearity in High-speed Visible Light Communications", in Dec 2018 IEEE Globecom Workshops (GC Wkshps).
- X. Deng, K. Arulandu, Y. Wu, **S. Mardanikorani**, G. Zhou and J. M. G. Linnartz, "Modeling and Analysis of Transmitter Performance in Visible Light Communications," in IEEE Transactions on Vehicular Technology, vol. 68, no. 3, pp. 2316-2331, March 2019.
- J. P. Linnartz, X. Deng, A. Alexeev, and **S. Mardanikorani**, "Wireless Communication over an LED Channel," *IEEE Communications Magazine*, December, 2020.